

COMBUSTION CHARACTERISTICS OF A1  
NANOPARTICLES AND NANOCOMPOSITE

A1+MoO<sub>3</sub> THERMITES

by

JOHN JOSEPH GRANIER, B.S.M.E., M.S.M.E.

A DISSERTATION

IN

MECHANICAL ENGINEERING

Submitted to the Graduate Faculty  
of Texas Tech University in  
Partial Fulfillment of  
the Requirements for  
the Degree of

DOCTOR OF PHILOSOPHY

Approved

Michelle Pantoya  
Chairperson of the Committee

Walt Oler

Valery Levitas

Jordan Berg

Padmanabhan Seshaiyer

Accepted

John Borrelli  
Dean of the Graduate School

May, 2005

## ACKNOWLEDGEMENTS

May all of my accomplishments be to the benefit of the Lord. I am blessed with an array of talents and gifts that provide the tools and motivation for every challenge that I have completed. In the disturbed irony that man's progression of scientific knowledge has actually led to improved destruction of humankind, I realize that this is God's plan. I truly believe that modern medicine is causing a weaker human immunity, we have selfishly consumed unrenewable resources such as extinct animal species and hydrocarbon fuels and we have invented great weapons of mass destruction that make us more efficient killers and less conscious of our actions. I hope that the Father takes my work as a valuable contribution to man's scientific breadth such that his goals can be achieved.

I would like to thank my advisor, Dr. Michelle Pantoya. Our journey on this project started together as I started on the energetic material work as an undergraduate senior when you were beginning to form the Combustion Lab. Because of this, I have a lot of pride and *project ownership* in the lab and my work, which I hope I have repaid in my self-motivation and dedication. I do not believe that another advisor could have instilled such a deep feeling of *project ownership* that I have acquired for most of the experimental systems and designs. Thank you for the opportunities, support and intellectual freedom. I owe much of my professional growth and professional opinions to you and my experiences as a researcher and graduate student.

I would like to gratefully acknowledge the Army Research Office (Contract Number DAAD19-02-1-0214) and our program manager, Dr. David Mann for financial support through the progression of this project.

I would also like to acknowledge my dissertation committee, Dr. Jordan Berg, Dr. Valery Levitas, Dr. Walt Oler, Dr. Padmanabhan Seshaiyer, and my graduate dean's representative Dr. Moira Ridley for the time and consideration you have invested in helping me achieve my graduate requirements. I have chosen your participation based on the respect and admiration that I have for each of you.

Thanks for collaborative assistance from:

Keith Plantier – die designs, pressing iterations, technical conversations

Thomas Mullen – die designs and pressing iterations, experimental assistance  
with Pre-heating thermite study

Kevin Moore – SEM images from LANL (taken by Ed Roemer under the  
direction of Dr. Steve Son), technical conversations

Mark Grimson – SEM images at TTU

David Thomas – Calorimetry experiments at CSC (Calorimetry Science Corp.)

Jack Henderson, Rob Campbell – thermal property experiments with Netzsch

Kurt Schroder, Darrin Willauer and Dennis Wilson for the donation of the nm-  
Al powders from Nanotechnologies Inc.

Climax for the donation of the nanocrystalline  $\text{MoO}_3$

Thank you to my beautiful wife, Sara for helping me to keep the balance of  
enjoyment and productivity. Thank you for allowing my unusual schedule and habits in  
recreation and work. In my current period of stressful decision and life alterations, I hope  
our path is well defined and happiness is easily achieved. May our next life segment  
always be an improvement from our current stage?

## TABLE OF CONTENTS

ACKNOWLEDGEMENTS .....	ii
ABSTRACT .....	x
LIST OF TABLES .....	xiii
LIST OF FIGURES .....	xiv
NOMENCLATURE .....	xx
Chapter	
I. BACKGROUND .....	1
1.1 Thermite Reactions .....	1
1.2 Nanocomposite Thermites .....	3
1.2.1 Decreased Diffusion Lengths and Improved Heterogenity .....	5
1.2.2 Increased Surface Area to Volume Ratio of Nanoparticles .....	7
1.2.3 Decreased Melting Temperatures of Nanoparticles .....	8
1.2.4 Inherent Instability of nano-sized Aluminum .....	9
1.3 Theoretical Studies of Al Combustion .....	11
II. PRESSING OF ENERGETIC MATERIALS .....	12
2.1 Introduction .....	12
2.2 Symmetrical Steel Cylinder Dies .....	12
2.3 Unsymmetrical Acrylic Cylinder Dies .....	13
2.4 Harrick Scientific Evacuatable Pellet Press .....	15



2.5 Custom Steel Cylinder Dies .....	17
2.6 Carver Steel Die .....	21
2.7 Split Steel Die.....	22
2.8 Custom Steel Vacuum Die .....	24
III. DENSIFICATION EFFECTS ON NANOCOMPOSITE	
THERMITE COMBUSTION .....	27
3.1 Introduction .....	27
3.2 Literature Review .....	27
3.4 Composite Sample Fabrication .....	30
3.5 Experimental Setup .....	36
3.6 Combustion Performance Results .....	37
3.7 Discussion and Summary .....	42
3.7.1 Composite Pore Structure .....	43
3.7.2 Thermal Properties of Porous Composites .....	45
IV. PRE-HEATING EFFECTS ON NANO-COMPOSITE	
THERMITE COMBUSTION .....	49
3.1 Introduction .....	49
3.2 Experimental Setup .....	51
3.2.1 Sample Fabrication .....	52
3.2.2 Equipment System .....	53
3.2.3 Measuring Ignition.....	53
3.2.4 Measuring Flame Propagation .....	54
3.3 Results .....	55
3.3.1 Volumetric Preheating .....	55

3.3.2 Variable Laser Power.....	58
3.4 Discussion .....	64
3.5 Summary .....	66
V. TG/DSC REACTION ANALYSIS .....	69
5.1 Introduction .....	69
5.2 Literature Review .....	69
5.3 Theory of a Heat Flux DSC.....	73
5.4 Instrument and Sample Preparation .....	74
5.4.1 Sample Properties .....	77
5.5 Representative TG/DSC results .....	79
5.6 Chemical Kinetic Analysis.....	85
5.6.1 Arrhenius Equation .....	86
5.6.2 First-Order Arrhenius Reaction Kinetics Analysis .....	86
5.6.3 Kissinger Reaction Kinetics Analysis.....	87
VI. AL OXIDATION TG/DSC ANALYSIS .....	89
6.1 Literature Review .....	89
6.1 TG/DSC Results.....	91
6.2 Kinetic Parameter Approximation .....	100
6.2.1 Reaction Parameters Calculated by Peak Temperatures.....	100
6.2.2 Reaction Parameters Calculated by Onset Temperatures .....	103
6.4 Summary .....	107

VII.	AL/MO <sub>3</sub> THERMITE TG/DSC ANALYSIS .....	112
	7.1 TG/DSC Results .....	112
	7.2 Kinetic Parameter Approximation .....	115
	7.2.1 Reaction Parameters Calculated by Onset Temperatures .....	116
	7.2.2 Reaction Parameters Calculated by Peak Temperatures .....	118
	7.3 Reaction Product Analysis .....	121
	7.4 Summary .....	124
VIII.	TEMPERATURE DEPENDENT AL+MO <sub>3</sub> REACTION MECHANISMS .....	126
	8.1 Introduction .....	126
	8.2 nm-Al+MoO <sub>3</sub> Reactions .....	126
	8.3 μm-Al+MoO <sub>3</sub> Reactions .....	132
	8.4 Summary .....	136
IX.	TWO-DROP CALORIMETER THERMITE EXPERIMENTS .....	138
	9.1 Introduction .....	138
	9.2 Experimental Design .....	138
	9.3 Results .....	142
	9.4 Summary .....	145
X.	CONCLUSIONS .....	149
XI.	FUTURE WORK .....	154
	11.1 Fabrication .....	154

11.2 Nanocomposite Al/MoO <sub>3</sub> Reaction	
Characteristics .....	154
11.3 DSC experiments.....	157
REFERENCES .....	159
APPENDIX.....	165
A.    Compressed Composite LFA 447 data .....	165
A.1 50nm-Al+MoO <sub>3</sub> Thermal Properties .....	165
A.2 4.5-7μm-Al+MoO <sub>3</sub> Thermal Properties.....	166
B.    DSC System Diagram .....	167
C.    DSC Temperature Calibration .....	170
D.    DSC Sensitivity Calibration.....	172
E.    Aluminum Oxidation DSC/TGA Curves.....	174
E.1 50nm Al + O <sub>2</sub> Gas .....	174
E.2 1-3μm Al + O <sub>2</sub> Gas.....	178
E.3 4.5-7μm Al + O <sub>2</sub> Gas.....	182
E.4 20μm Al + O <sub>2</sub> Gas .....	187
F.    Aluminum Oxidation DSC/TGA Results	
Plotted by $\beta$ .....	193
G.    Aluminum + Molybdenum Trioxide	
Thermite DSC Curves .....	198
G.1 50nm Al + MoO <sub>3</sub> .....	199
G.2 80nm Al + MoO <sub>3</sub> .....	200
G.3 120nm Al + MoO <sub>3</sub> .....	201
G.4 1-3μm Al + MoO <sub>3</sub> .....	202

	G.5 3-4 $\mu\text{m}$ Al + MoO <sub>3</sub> .....	204
	G.6 4.5-7 $\mu\text{m}$ Al + MoO <sub>3</sub> .....	206
	G.7 10-14 $\mu\text{m}$ Al + MoO <sub>3</sub> .....	208
	G.8 20 $\mu\text{m}$ Al + MoO <sub>3</sub> .....	212
H.	SEM Images of DSC Samples .....	216
I.	2-Drop Calorimeter Calibration Data .....	217

## ABSTRACT

Scientific advances in material synthesis such as exploding wire technology, plasma nucleation and wet precipitation have enabled industrial manufacturers to produce metal and metal oxide powders with nanometer-sized particles. These processes have enabled better overall quality control (i.e. more definitive particle size, smaller particle size distributions, oxide coating control and decreased contaminate concentration) and faster production rates.

Much interest has been formed in the science and application of nano-sized aluminum (nm-Al) combustion. A thermite (or aluminothermic) reaction is an oxidation reaction between aluminum and a metal oxide with highly exothermic energy release. Thermite reactions of traditional Al powder (typically micron-sized particles) and Iron-oxide have been used for decades in welding and other intense heat applications. Nano-thermite reactions, have shown unique properties in ignition sensitivity and deflagration (flame propagation) speeds which have propelled thermites to new realms of applications. The decrease in required ignition stimuli of nano-thermites is an improvement for many payload critical applications, but the ignition sensitivity also creates various hazards during material handling and seems to be a factor in decreased reactivity of aged nano-thermites. Nano-thermites have displayed reaction rates near detonation speeds presenting applications as more efficient incendiary devices. The precise particle size control of nano-thermites is leading researchers to develop highly-tunable energy release mechanisms that can be applied as heat signature flare decoys.

Studies have shown that the thermite reaction of nm-Al+MoO<sub>3</sub> has a large theoretical energy density [19], increased ignition sensitivity [23][8], and near detonation flame propagation speeds [5][6] in comparison to traditional micron-particle thermites. This work will present macroscopic combustion behaviors (such as flame speed) along with experimental results focusing on the molecular reactions and thermal properties of nanocomposite Al+MoO<sub>3</sub> thermite materials

This work will outline the successes and precautions of several nm-Al+MoO<sub>3</sub> powder mixing methods and several cold-pressing techniques used to form compressed

solid samples. A general relationship of sample density as a function of pressing force and with a systematic methodology is presented to allow other researchers to produce similar samples for future comparison.

Second, results from laser experiments performed to determine flame speeds of nano and micron-sized Al+MoO<sub>3</sub> composites through a range of sample densities. Flame propagation speeds were measured using high-speed digital video. Samples were also tested to determine thermal conductivity, specific heat and thermal diffusivity as a function of compressed sample density. Theories are presented for the unique trends of the nano and micron-composite results.

Third, experimental work is presented analyzing the effects of pre-heated compressed nm-Al+MoO<sub>3</sub> samples. Sample pre-heating is achieved by volumetric heating using an isothermal oven and by varying the applied laser power to allow conductive heating. Both methods of preheating show unique behaviors and elevated flame propagation speeds compared to previous results. Results and discussion of this work also discuss the difficulties and critical time response of using bare-wire thermocouples to accurately measure nano-thermite reaction temperatures.

Fourth, a series of DSC/TGA experiments were performed on the reaction of Al and gaseous oxygen to analyze the purest and ‘simplest’ form of the Al oxidation (void of any reaction mechanisms dependent on the metal-oxide decomposition). Results are presented showing unique reaction onset temperatures, oxidation rates and activation energies for nano and micron-Al reacting in a gaseous oxygen environment.

Fifth, a series of DSC/TGA experiments were performed on the reaction of Al and nano-MoO<sub>3</sub>. Results are presented for reaction onset temperatures, peak temperatures, heat of reaction values, and activation energies for Al+MoO<sub>3</sub> composites with Al particles ranging from 50 nm to 20  $\mu$ m.

A final set of experiments was designed using the DSC/TGA to determine reaction duration and reaction self-propagation criteria for Al particle sizes ranging from 50 nm to 20  $\mu$ m. Heating programs were manipulated for micron and nano-Al+MoO<sub>3</sub> samples to determine the relationship between sample heating rate and reaction mechanisms. DSC tests were done using isothermal time intervals displaying that the nm-Al+MoO<sub>3</sub>

reactions are temperature dependent and not self-sustaining. Isothermal time intervals applied to  $\mu\text{m-Al}+\text{MoO}_3$  reactions displayed a delayed peak temperature.

Finally, all of the results and experiments are combined as evidence in support of a single theory of the oxidation reaction of spherical Al particles. The presented results portray unique evidence in support of the nano and micron-sized Al reaction characteristics.



## LIST OF TABLES

1.1: Literature Review of Studies Analyzing Melting Point Depression of Nanoparticles .....	9
3.1: Literature Review of Combustion Experiments of Composite.....	28
3.2: ThermiteAl+MoO <sub>3</sub> composite constituent densities.....	32
3.3: Density, propagation velocity and analysis data.....	41
4.1: Ignition time and burn rates for various Al particle diameters (Granier & Pantoya, 2003) [24] .....	49
5.1: Literature Review of DSC/TG Thermal Analysis .....	70
5.2: Literature Review of DSC Kinetic Parameter Studies.....	72
5.3: Thermite Composite Reactants used in DSC analysis.....	78
6.1: Literature Review of Al Oxidation Models and Theory.....	90
6.2: DSC data from Al and O <sub>2</sub> gas reactions .....	96
6.3: Activation energy for Al+O <sub>2</sub> reactions calculated from DSC and TGA data .....	106
6.4: Pre-exponential factor for Al+O <sub>2</sub> reactions calculated from DSC and TGA data .....	107
7.1: DSC data from Al/MoO <sub>3</sub> thermite reactions.....	112
7.2: Activation energy for Al+MoO <sub>3</sub> reactions calculated from DSC data .....	119
8.1: Isothermal reaction data for 10-14µm-Al+MoO <sub>3</sub> (from Figures 8.6 and 8.8) .....	136
9.1: Nichrome wire blank heat adjustment values .....	142
9.2: Al+MoO <sub>3</sub> Calorimeter peak integration areas .....	143
9.3: Two-drop calorimeter Al+MoO <sub>3</sub> heat of reaction results.....	144
10.1: Comparison remarks for micron and nano-Al reactions.....	150

## LIST OF FIGURES

1.1: Diagram of Heat of Reaction and Activation Energy .....	2
1.2: Heat of reaction of Thermites [19] and Conventional Explosives [52] .....	3
1.3: SEM images of a nanocomposite thermite: 120nm-Al (Nanotechnologies)+ nm-MoO <sub>3</sub> (Climax) .....	5
1.4: SEM image of micron-composite thermite: 10-14µm Al (Alfa Aesar) + nm-MoO <sub>3</sub> (Climax).....	6
1.5: Plot of calculated surface area to volume ratio for nano-sized particles.....	7
1.6: Plot of calculated oxide layer thickness for nano-sized particles .....	10
2.1: Diagram of LANL symmetrical load cylinder die.....	13
2.2: Photographic images of acrylic die with steel plungers and shims .....	14
2.3: Dimensional diagram of acrylic die and steel plungers.....	14
2.4: Photographic images of purchased ½in. ID Harrick- Scientific vacuum die[27] .....	16
2.5: Two samples pressed with the Harrick-Scientific vacuum die.....	16
2.6: Photographic images of custom ¼ in. ID cylinder die.....	18
2.7: Diagram of pressing sequence for custom cylinder die.....	19
2.8: Photographic images of custom ½ in. ID cylinder die.....	20
2.9: Photographic images of purchased ¼ in. ID Carver die (4000 lb) [11] .....	21
2.10: Photographic images of split steel die with external clamp.....	23
2.11: Photographic images of formed pellets in split steel die .....	24
2.12: Photographic images of custom ¼ in. ID vacuum die .....	26
3.1: Thermite composite sample density as a function of die pressure and applied load.....	33

3.2: Light Microscope and SEM images of 3-4.5 $\mu\text{m}$ Al+nm-MoO <sub>3</sub> compressed samples.....	34
3.3: Diagram of experimental mounting of compressed cylindrical pellet.....	36
3.4: Diagram of experimental equipment system .....	37
3.5: Sequence of still images captured as digital high-speed video.....	38
3.6: Flame propagation velocity of 80nm and 3-4 $\mu\text{m}$ Al+MoO <sub>3</sub> composites as a function of sample density .....	40
3.7 SEM image of fractured MoO <sub>3</sub> crystals in 75% TMD Al+MoO <sub>3</sub> sample .....	43
3.8: Composite specific heat as a function of bulk sample density .....	46
3.9: Composite thermal diffusivity as a function of bulk sample density .....	47
3.10: Composite thermal conductivity as a function of bulk sample density .....	48
4.1: Ignition time as a function of Al particle diameter (Granier & Pantoya, 2003) [24].....	50
4.2: Burn rate (propagation velocity) as a function of Al particle diameter (Granier & Pantoya, 2003) [24] .....	50
4.3: Cylindrical pellet on Stand with wedged between TC1 and TC2 in heated oven. ....	52
4.4: Ignition time as a function of preheat temperature 40nm Al + MoO <sub>3</sub> .....	55
4.5: Temperature as a function of preheat temperature 40nm Al + MoO <sub>3</sub> .....	56
4.6: Propagation velocity as a function of preheat temperature 40nm Al + MoO <sub>3</sub> .....	57
4.7: Volumetrically preheated nanocomposite flame speed plotted with ambient initial state nano and micron composite data.....	58
4.8: Temperature histories for 40 and 10W laser powers .....	59

4.9: Magnified temperature history of 40W laser power	
<i>Ignition Zone</i> .....	60
4.10: Ignition time as a function of laser power 40nm	
Al + MoO <sub>3</sub> .....	61
4.11: Flame and ignition temperatures as a function of laser	
power 40nm Al + MoO <sub>3</sub> .....	62
4.12: Propagation velocity as a function of laser power 40nm	
Al + MoO <sub>3</sub> .....	63
4.13: Laser preheated nanocomposite flame speed plotted with	
ambient initial state nano and micron composite data .....	64
4.14: Estimated thermite propagation speeds for nanocomposite	
thermites tested by laser igniton and DSC heating .....	68
5.1 DTA/DSC thermocouple diagram .....	74
5.2: TG-DTA/DSC instrument diagram [44] .....	75
5.3: Sample carrier showing sample and reference crucibles [44] .....	76
5.4: TG/DSC curves of 120 nm Al melt and MoO <sub>3</sub> Sublimation	
(both at 10 Kpm) .....	80
5.5: TG/DSC curves of 1-3 μm-Al oxidation (10 K/min in O <sub>2</sub>	
environment) .....	81
5.6: TG/DSC curves of 40nm-Al+MoO <sub>3</sub> reactions (10 K/min	
in argon) .....	82
5.7: TG/DSC curves of 3-4.5 μm-Al+MoO <sub>3</sub> reactions (10 K/min	
in argon) .....	83
5.8: DSC curves of 40nm, 50nm, 80nm, 120nm, 1-3μm, 3-4.5 μm,	
4.5-7μm, 10-14μm and 20μm-Al+MoO <sub>3</sub> reactions (10 K/min	
in argon) .....	83
6.1: TGA, DSC and reference temperature curves of 50nm-Al	
in O <sub>2</sub> (β=10Kpm) .....	91

6.2: TGA, DSC and reference temperature curves of 1-3 $\mu$ m-Al	
in O <sub>2</sub> ( $\beta$ =5Kpm) displaying three basic oxidation stages .....	94
6.3: DSC Onset temperature as a function of Al particle size .....	97
6.4: TGA Onset temperature as a function of Al particle size.....	97
6.5: Peak-1 DSC temperature as a function of Al particle size .....	98
6.6: Total mass gain as a function of Al particle size .....	99
6.7: Peak mass rate of change as a function of Al particle size .....	100
6.8: Slope plot to determine activation energy based on $T_{\text{peak-1}}$	
using Arrhenius method (see Section 5.6.2) .....	101
6.9: Slope plot to determine activation energy based on $T_{\text{peak-1}}$	
using Kissinger method (see Section 5.6.3).....	101
6.10: Activation energy ( $E_a$ ) calculated by $T_{\text{peak-1}}$ as a function	
of particle diameter .....	102
6.11: Slope plot to determine activation energy based on $T_{\text{onset-DSC}}$	
using Arrhenius method (see Section 5.6.2) .....	104
6.12: Slope plot to determine activation energy based on $T_{\text{onset-TGA}}$	
using Arrhenius method (see Section 5.6.2) .....	104
6.13: Slope plot to determine activation energy based on $T_{\text{onset-DSC}}$	
using Kissinger method (see Section 5.6.3).....	105
6.14: Slope plot to determine activation energy based on $T_{\text{onset-TGA}}$	
using Kissinger method (see Section 5.6.3).....	105
6.15: Activation energy ( $E_a$ ) calculated by $T_{\text{onset}}$ as a function of	
particle diameter.....	106
6.17: SEM Image of 3-4.5 $\mu$ m-Al manufactured by Alfa Aesar .....	109
7.1: Onset temperature as a function of Al particle size for various	
heating rates .....	113
7.2: Peak temperature as a function of Al particle size for various	
heating rates .....	114
7.3: DSC Heat of reaction as a function of Al particle size for various	
heating rates .....	115

7.4: Slope plot to determine activation energy based on $T_{\text{onset}}$ based on Arrhenius equation analysis Kissinger method (see Section 5.6.2).....	116
7.5: Slope plot to determine activation energy based on $T_{\text{onset}}$ based on Kissinger method (see Section 5.6.3) .....	117
7.6: Activation energy ( $E_a$ ) calculated by $T_{\text{onset}}$ as a function of particle diameter.....	117
7.7: Slope plot to determine activation energy based on $T_{\text{peak}}$ based on Arrhenius equation analysis Kissinger method (see Section 5.6.2).....	118
7.8: Slope plot to determine activation energy based on $T_{\text{peak}}$ based on Kissinger method (see Section 5.6.3) .....	118
7.9: Activation energy ( $E_a$ ) calculated by $T_{\text{peak}}$ as a function of particle diameter.....	119
7.10: SEM Images of 20 $\mu\text{m}$ -Al+MoO <sub>3</sub> before (A) and after (B) combustion.....	122
7.11: SEM Images of 10-14 $\mu\text{m}$ -Al+MoO <sub>3</sub> before (A) and after (B) combustion.....	123
8.1: 80nm Al+MoO <sub>3</sub> DSC results plotted versus Time (A) and Temperature (B).....	127
8.2: Reaction time duration and energy (area under DSC curve) versus heating rate for 80nm-Al+MoO <sub>3</sub> .....	128
8.3: Temperature dependence DSC testing for 80nm-Al+MoO <sub>3</sub> .....	129
8.4: Partial reaction threshold testing for 120nm-Al+MoO <sub>3</sub> .....	130
8.5: 40Kpm violent reaction of 80nm-Al+MoO <sub>3</sub> .....	131
8.6: Partial reaction threshold testing for 10-14 $\mu\text{m}$ -Al+MoO <sub>3</sub> .....	134
8.7: Decrease reactivity based on MoO <sub>3</sub> sublimation and sample stoichiometry for 10-14 $\mu\text{m}$ -Al+MoO <sub>3</sub> .....	135
8.8: Isothermal reaction data for 10-14 $\mu\text{m}$ -Al+MoO <sub>3</sub> .....	136
9.1: Two-drop calorimeter system schematic [43] .....	139

9.2: Sample vial with nichrome wire igniter.....	140
9.3: Sample vial, ignition system and calorimeter orientation.....	141
9.4: Experimental data for the 3 nichrome wire blanks tested.....	142
9.5: Experimental data for Samples 1-3.....	143
9.6: Two-drop calorimeter Al+MoO <sub>3</sub> heat of reaction results.....	144
9.7: Heat of Reaction determined by DSC Al+MoO <sub>3</sub> experiments.....	146
9.8: Heat of reaction comparison between instruments and cited source.....	147

## NOMENCLATURE

### Variable

$A$	Air or oxidizer
$B$	y-intercept
$C_p$	Specific-heat [J/kgK]
$d$	diameter
$E_a$	Activation energy
$F$	Fuel
$h, H$	Specific enthalpy [W/g] or Enthalpy [W] ( $\Delta H$ change in enthalpy)
$k$	Specific reaction rate constant
$M$	Linear slope
$n$	Reaction Order
$O$	Oxidizer
$P$	Pressure
$Q$	Heat of Reaction [cal/cm <sup>3</sup> or cal/cc] or [cal/g]
$r$	radius
$R_u$	Universal gas constant
$RR$	Reaction rate
$SA, SSA$	Surface area [m <sup>2</sup> ], Specific surface area [m <sup>2</sup> /g]
$t$	Time
$T$	Temperature
TMD	Theoretical Maximum Density (Define in Eq. 3.4)
$V$	Volume
$X$	Concentration of passivated Al powder in a composite sample
$Y$	Pure Al concentration
$Z$	Pre-exponential factor or steric factor

### Greek

$\alpha$	Thermal diffusivity
$\beta$	Heating Rate
$\varepsilon$	Porosity



$\Delta x$	Change in quantity x
$\phi$	Equivalence ratio (Define in Eq. 4.1)
$\lambda$	Thermal Conductivity [W/mK]
$\rho$	Density [ $\text{m}^3/\text{g}$ ]
$\sigma$	Surface tension

### Subscripts

ign	Ignition (ie. $t_{\text{ign}}$ indication time to ignition)
iso	Isothermal (constant temperature)
$l$	Liquid (ie. $\sigma_{lv}$ indicating liquid to vapor interface)
onset	Indicating initiation of an event (i.e. $T_{\text{onset}}$ indicating onset temperature)
$mp$	Melting point (ie. $T_{mp}$ indicating melting temperature)
peak	Critical point in DSC curve (max or min point of endo or exotherm)
$s$	Solid (ie. $\sigma_{sl}$ indicating solid to liquid interface)
$v$	Vapor

### Units

Kpm	Kelvin per minute (equivalent to $^{\circ}\text{C}$ per minute)
nm	nanometer ( $1 \times 10^{-9}$ m) – also referred to by nano
$\mu\text{m}$	Micrometer ( $1 \times 10^{-6}$ m) – also referred to by micron

## CHAPTER I

### BACKGROUND

#### 1.1 Thermite Reactions

By definition a thermite reaction is a chemical reaction in which aluminum metal (Al) is oxidized by a different metal-oxide, most commonly iron-oxide ( $\text{Fe}_2\text{O}_3$ ) [26]. Fischer and Grublich [19] presented a thorough listing of thermite reactions of Al with  $\text{Bi}_2\text{O}_3$ ,  $\text{Cu}_2\text{O}_3$ ,  $\text{Fe}_2\text{O}_3$ ,  $\text{MoO}_3$ ,  $\text{Pd}_2\text{O}_3$ ,  $\text{WO}_3$ , and many others. As indicated by the Latin root “*therm*” meaning heat, the main contribution of a thermite reaction is the exothermic heat production.

The exothermic properties of thermite reactions were discovered by Hans Goldschmidt in 1895 [13][26]. Goldschmidt’s main contributions to the science of alumino-thermics were the implementation of a fuse to stimulate ignition and a method to prevent explosion upon ignition. He also developed a method to generate molten metal for the welding of large iron or steel parts. In the mid 1900’s, thermites became the primary method of welding carbon-free metals such as railroad and streetcar rails [26].

Due the large heat production, thermites have been used as grenades and bombs in military combat as incendiary devices. Thermite devices are able to burn through combat armor and fireproof barriers. Thermite reactions have also been used to purify metal ores such as uranium [63].

Exothermic (or endothermic) heat release (or heat absorption) from a chemical reaction is quantified by a reaction property known as the heat of reaction ( $\Delta H_{\text{rxn}}$  or  $\Delta h_{\text{rxn}}$ ). A second important factor for any chemical reaction is the activation energy ( $E_a$ ) which quantifies the minimum amount of energy required for a reaction to initiate and go to completion. Both of these reaction parameters are symbolically shown in Figure 1.1. The heat of reaction is the enthalpy change from the reactant state to the product state. A negative  $\Delta H_{\text{rxn}}$  indicates an exothermic energy release while a positive  $\Delta H_{\text{rxn}}$  indicates an endothermic energy absorption. The activation energy for a specific reaction is an energy threshold that constitutes exciting the reactants enough to stimulate a chemical reaction.

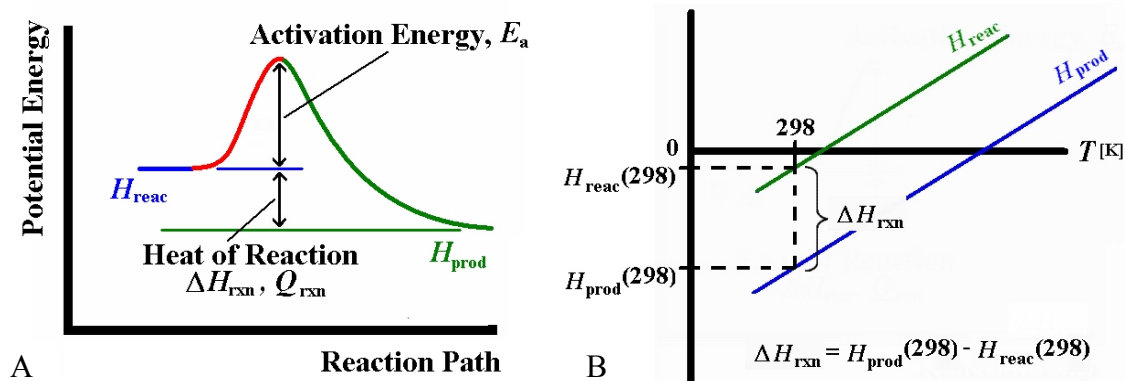
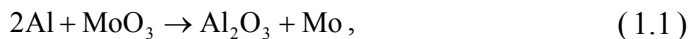


Figure 1.1: Diagram of Heat of Reaction and Activation Energy

Figure 1.2 shows the heat of reaction ( $\Delta h_{\text{rxn}}$ ) for four common thermite reactions and four common high-explosives (HE). As shown, all four thermite samples show higher exothermic energy release than traditional HE. A significant difference in HE reactions and thermite reactions is the rate of energy release. A sample of TNT may release its total reaction energy of 300 cal/g on the order of picoseconds ( $10^{-12}$ ), while a traditional thermite sample of Al+MoO<sub>3</sub> may release its total reaction energy of 4279 cal/g through a time interval of a few seconds. Majority of the work in this document will be on the thermite reaction between Al and MoO<sub>3</sub> shown below.



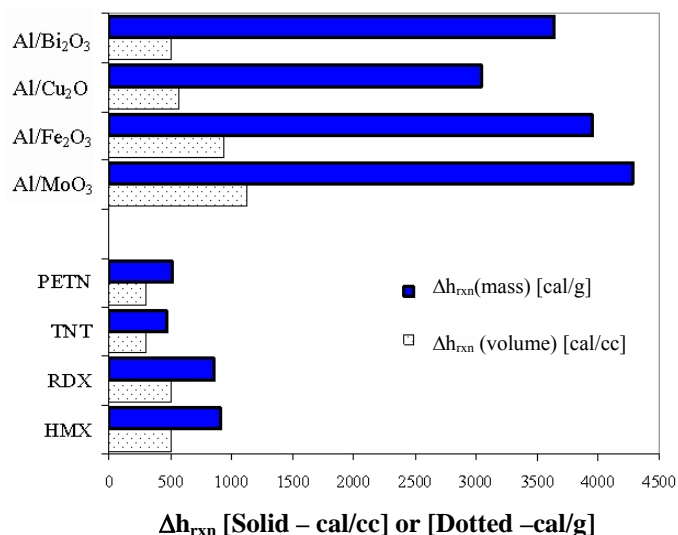


Figure 1.2: Heat of reaction of Thermites [19] and Conventional Explosives [52]

## 1.2 Nanocomposite Thermites

As mentioned earlier, a crucial difference in thermites and explosives is the time for the reaction to reach completion. Thermites are bimolecular reactions and reaction rates are limited by diffusion times between reactants. Whereas HE are typically monomolecular and reaction rates occur more rapidly only limited by chemical conversion rates. Thermite mixtures of nano-sized reactants reduce the critical diffusion length thus increasing the overall reaction rate. Numerous studies [4][7][23][25][49][52][53][56][57] have shown that nanocomposite thermites are much more reactive (i.e. increased ignition sensitivity and faster burn rates) than tradition micron-sized thermite mixtures.

Traditionally the exothermic properties of thermite reactions used for welding applications contained micron-size or larger reactant particles. The technology to develop nano-sized particles (also called ultra fine particles or super-fine particles) of metals such as gold and nickel have been around since the early 1950's [28]. In the last decade, these two technology fields have merged to allow large volume, quality controlled and cost effective production of nanocomposite thermite mixtures.

Manufactures such as Clark Manufacturing, LLC (Newman Lake, WA); Climax Molybdenum Co. (Pheonix, AZ); Firefox Enterprises, Inc. (Pocatello, ID); Nanotechnologies, Inc (Austin, TX); Nanophase Technologies Corp. (Romeoville, Il); Skylighter, Inc (Round Hill, VA); Technanogy, Inc (Santa Ana, CA) and many more companies have been producing nanosized metals and metal-oxides for use in thermite applications. Development of chemical process to produce nano-sized reactants and nano-sized thermite mixtures (e.g Sol-gel, Xerogel, etc.) has been tested at Lawrence Livermore National Lab (LLNL), Los Alamos National Lab (LANL) and Texas Tech University (TTU).

There are several advantages to nanocomposite thermites reactants that are still being tested to better explain observed phenomenon. A few advantages of nano-particles influence on thermite reactions are listed below (it is noted that there are several characteristics of nanoparticles that are not listed that may contribution to faster and hotter thermite reactions).

- 1) decreased diffusion distances between fuel and oxidizer particles promoting faster reaction rates
- 2) improved heterogeneity of fuel and oxidizer particles promoting more complete and stoichiometric reactions (producing  $\Delta h_{\text{rxn}}$  values closer to theoretical calculations based on ideal conditions)
- 3) increased surface to volume ratio promotes more simultaneous reaction locations thus decreasing the global reaction time
- 4) decreased melting temperatures of nanoparticles induces earlier phase transition promoting increased ignition sensitivity
- 5) inherent surface energy instability of nanoparticles require less energy to stimulate ignition
- 6) thinner and more homogeneous aluminum oxide atering diffusion properties
- 7) more homogeneous porosity and a wider range of porosity control in compressed composite samples.

### 1.2.1 Decreased Diffusion Lengths and Improved Heterogeneity

Figure 1.3 shows two SEM images of a nanocomposite Al+MoO<sub>3</sub> loose powder sample. Figure 1.3A shows the larger MoO<sub>3</sub> crystals surrounded by small Al spheres.

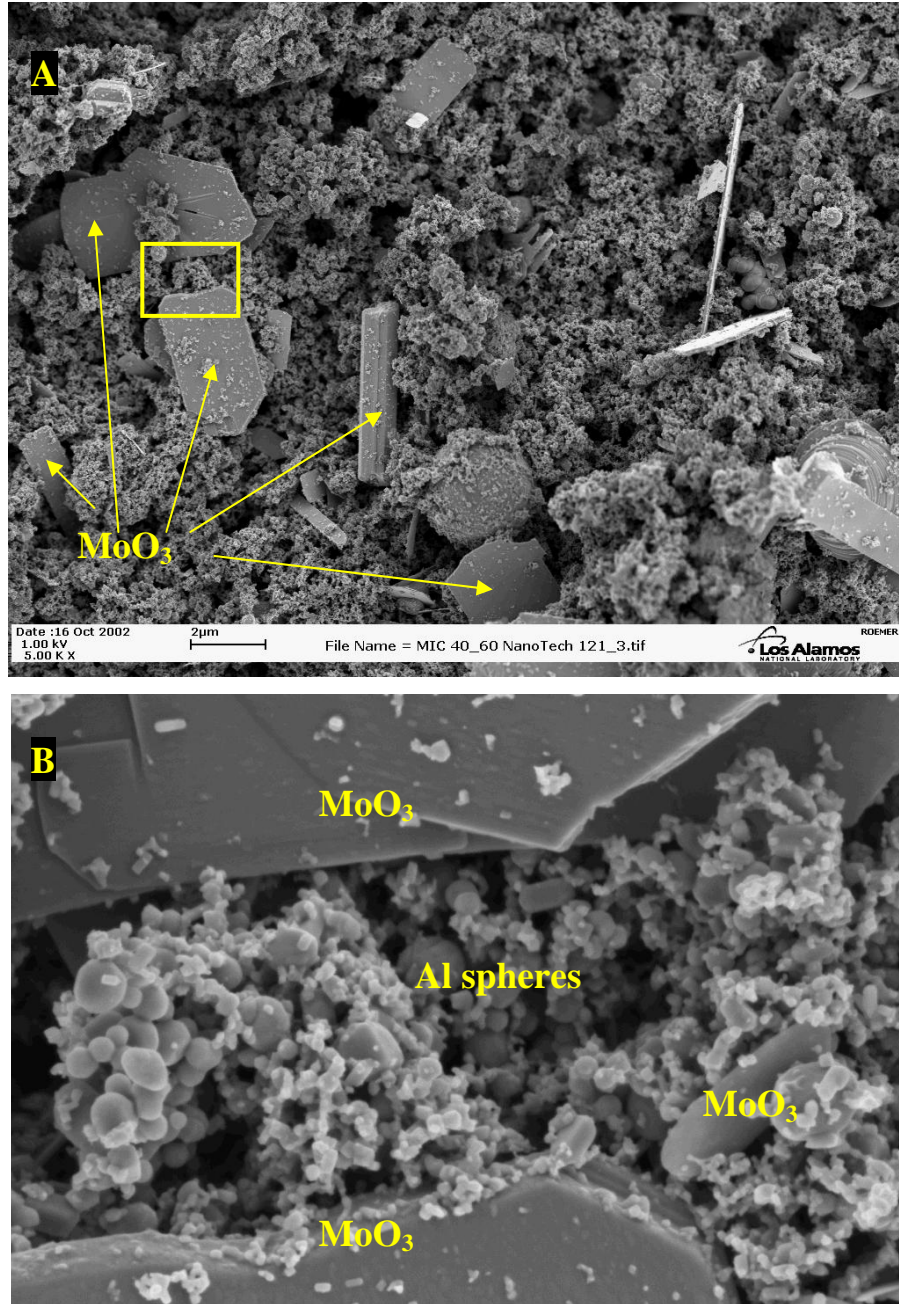


Figure 1.3: SEM images of a nanocomposite thermite: 120nm-Al (Nanotechnologies)+ nm-MoO<sub>3</sub> (Climax)

Taken by Ed Roemer under direction of Dr. Steve Son, LANL

Figure 1.3B is zoomed image of the outlined region in Figure 1.3A showing the 120nm Al spheres more distinctly mixed with smaller MoO<sub>3</sub> crystals. Figure 1.4 shows two SEM images of a micron-composite Al+MoO<sub>3</sub> loose powder sample.

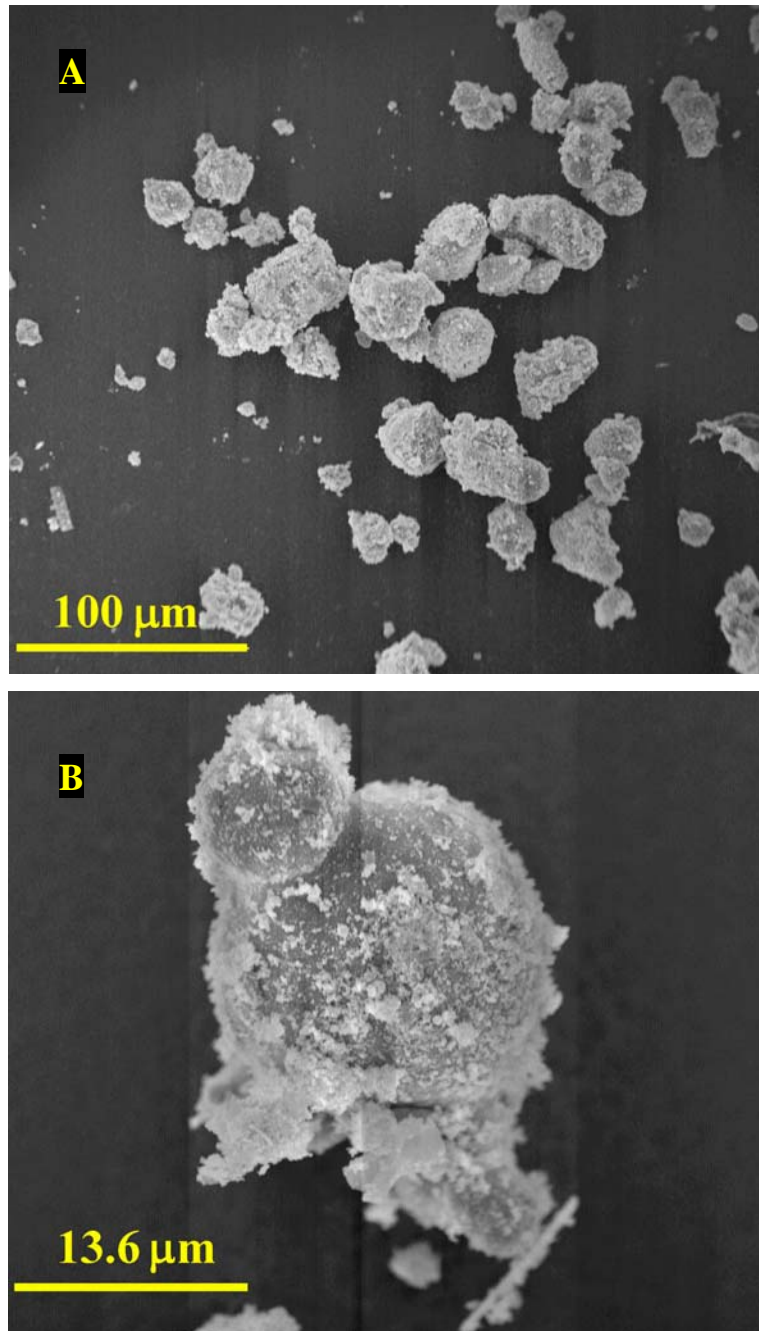


Figure 1.4: SEM image of micron-composite thermite: 10-14μm Al (Alfa Aesar) + nm-MoO<sub>3</sub> (Climax)

Figure 1.4A shows several 8-16  $\mu\text{m}$  masses (approximately spherical). Figure 1.4B shows the a micron-Al sphere coated in the nano-sized  $\text{MoO}_3$  crystals. In comparing Figures 1.3 and 1.4, the nanocomposite samples are more heterogeneously mixed and display shorter inter-crystalline voids (diffusion distances between fuel and oxidizer) than micron-composite samples.

### 1.2.2 Increased Surface Area to Volume Ratio of Nanoparticles

Using simple geometric calculations, one can generate the plot shown in Figure 1.5. Nanotechnologies' 50nm Al product has a specific surface area (SSA) of  $39.9\text{m}^2/\text{g}$  while Suvaci et. al [59] presented data for a 2-5 $\mu\text{m}$  Al powder with a SSA of  $1.24\text{m}^2/\text{g}$ . This is a 3000% increase in SSA from micron to nano-sized Al and this trend will only increase for larger micron-sized Al particles. Many models (see literature review in Table 6.1) of Al combustion discuss that the oxidation reaction occurs at the outer surface of the Al spheres. Models described by of Cabrera et al. [10] and Dreizen et al. [60] state that the oxidation reaction of Al is directional proportional to oxygen-aluminum contact surface area. For this reason the increased surface area of the nm-Al spheres allow much faster burn rates than micron-Al spheres [6].

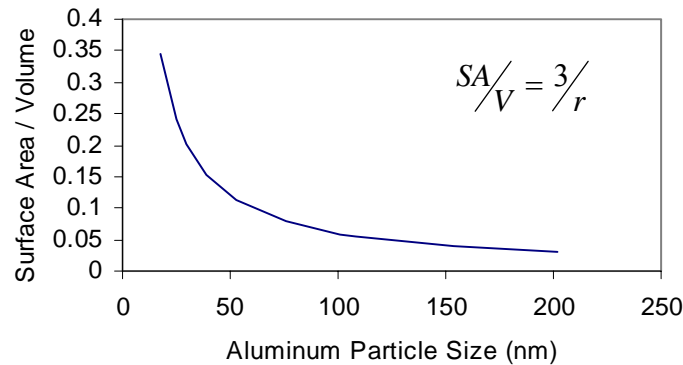


Figure 1.5: Plot of calculated surface area to volume ratio for nano-sized particles



### 1.2.3 Decreased Melting Temperatures of Nanoparticles

Several theoretical models supported by experimental results explain the melting point depression of small particles. One model for melting temperature depression is based on a thermodynamic approach in which a molten shell surrounds a solid particle core and the two phases are in thermal equilibrium. Based on this theory, Wronski [65] developed the following relationship for the particle-size dependent melting temperature ( $T_{mp}(r)$ ).

$$\Delta T_{mp} = T_{mp}(\infty) - T_{mp}(r) = \frac{2T_{mp}(\infty)}{\Delta H_{fus}} \left\{ \frac{\sigma_{sl}}{\rho_s(r-\tau)} + \frac{\sigma_{lv}}{r} \left( \frac{1}{\rho_s} - \frac{1}{\rho_l} \right) \right\} \quad (1.2)$$

Wronski [65] used his analysis of Eq. 1.1 to predict the melting temperature of tin particles and compared his theoretical results to experimental results from Takagi [60] and Blackman and Curzon [4]. A similar melting point depression has been shown experimentally and theoretically for many other metals as well as shown in Table 1.1. Eckert et al. [16] present data showing a melting point depression for Al which was followed by a comparison theoretical model for Al by Zhang et al. [66].

Due to the solid-solid interface of all thermite composites, theory of traditional micron composites attributed the onset of combustion to the phase change of one or both of the reactants. The solid-solid thermite reaction is known to be diffusion controlled and the migration of liquid state Al will occur more readily than solid Al simply based on a comparison of diffusion coefficients. The advantage of reduced melting temperatures of nano-sized particles is that the solid-liquid phase transformation will begin at lower energy levels (lower temperatures) allowing the onset of a diffusion controlled ignition to occur at lower temperatures. Nanocomposite mixtures of Al+MoO<sub>3</sub> have shown increased ignition sensitivity in experiments performed by Granier and Pantoya [24].

Table 1.1: Literature Review of Studies Analyzing Melting Point Depression of Nanoparticles

Author(s)	Element	Citation
<b>Theoretical Studies</b>		
Buffat, Ph. And Borel, J-P.	Au	<i>Physical Review</i> Vol.13 No.6 pp.2287-2298 (1976)
Castro, T., and Reifengerger, R.	Au, Ag	<i>Physical Review B</i> Vol.42 No.13 pp.8548-8556 (1990)
Dippel, M., Maier, A., Gimple, V., Wider, H., Evenson, W.E., Rasera, R.L. and Schatz, G.	In	<i>Physical Review Letters</i> Vol.87 No.9 (2001)
Wautelet, M.	71 elem.	<i>J. Phys. D: Appl. Phys.</i> Vol.24 pp.343-346 (1991)
Zhang, Z., Lu, X.X., and Jiang, Q.	Al	<i>Physica B</i> Vol.270 pp.249-254 (1999)
<b>Experimental Studies</b>		
Dick, K., Dhanasekaran, T., Zhang, Z., and Meisel, D.	Au	<i>J. Am. Chem. Soc.</i> Vol.124 No.10 pp.2312-2317 (2002)
Eckert, J., Holzer, J.C., Ahn, C.C., Fu, A. and Johnson, W.L.	Al	<i>Nanostructured Materials</i> Vol.2 No.4 pp.407-413 (1993)
Lai, S.L., Guo, J.Y., Petrova, V., Ramanath, G., and Allen, L.H.	Sn	<i>Physical Review Letters</i> Vol.77 No.1 pp.99-102 (1996)
Peters, K.F., Cohen, J.B., and Chung, Y-W.	Pb	<i>Physical Review B</i> Vol.57 No.21 pp.13430-13438 (1998)

Note that Table 1.1 is a short list of studies on particle-size dependent melting temperatures and that many more works exists pertaining to other elements.

#### 1.2.4 Inherent Instability of nano-sized Aluminum

Nano-scale aluminum is pyrophoric in air and must be stabilized for handling. An oxide passivation layer is ‘grown’ around the core aluminum particles by controlling the pressure, temperature, oxygen concentration and exposure time to achieve a uniform and precisely controlled oxide layer. This shell provides an air stable nano-aluminum particle. Campbell et al. [9] performed a molecular dynamic simulation on a 20 nm aluminum particle and showed that the oxide layer reached an equilibrium thickness of 3.3 nm after 260 picoseconds. These results are consistent with the 1-4 nm thick oxide shells that are typical of the nano-aluminum particles on the market today [47].

Because the surface area to volume ratio increases dramatically as particle diameter decreases, the aluminum-oxide shell becomes a larger portion of the total material (by mass and volume). Figure 1.6 shows the variation in active aluminum content as a function of particle diameter for an oxide thickness shell thickness ranging from 2-4 nm.

These calculations were generated assuming spherical particles with a uniform oxide shell thickness. As particle size is reduced, the active aluminum content is decreased such that a trade-off may exist between the benefits of the nano-scale and diminished purity of the Al particle.

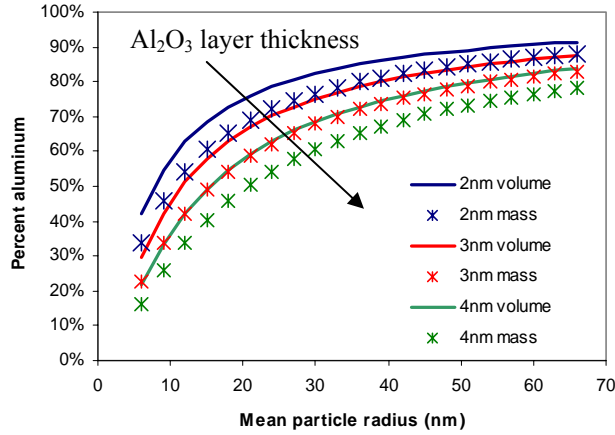


Figure 1.6: Plot of calculated oxide layer thickness for nano-sized particles

Jones et al. [33][37] studied the effect of the thickness of the passivation layer on the reactivity of Al nano-powders in air using thermal analysis techniques. Their results suggest that the thickness of the passivation layer does not significantly influence the reactivity of the material; but other factors play an important role such as particle size distribution, degree of agglomeration and composition of the passivation layer. Although the reactivity of the particle may not be strongly influenced by the thickness of the oxide shell, the increased  $\text{Al}_2\text{O}_3$  content of the nano-powders may significantly influence the microstructure and macroscopic properties of combustion-synthesized alloys [25].

Another important property of Al nanoparticles is the increased surface tension and mechanical stress due to the sharp curvature of the nano-spheres. The effects of this property will be discussed further in later chapters.

### 1.3 Theoretical Studies of Al Combustion

The most critical segment of a thermite reaction is the interaction between the Al and oxygen atoms on a molecular scale (or atomic scale). The solid-liquid phase and energy state of the reactants are secondary to the physical meeting of Al and O atoms that govern the diffusion-limited reactions.

Cabrera & Mott [10] specifically state that aluminum oxide will not dissolve oxygen but will dissolve metals (such as  $\text{Al}^{3+}$  ions). This supports the theories of Driez [61][62] and Shimizu [54] that Al ions diffuse from the pure Al core, through the  $\text{Al}_2\text{O}_3$  shell to react with oxygen at the outer radius of the oxide shell. A brief description of several theoretical models on Al combustion are presented in Table 6.1.

The transition of the metal-oxides to release free oxygen atoms is not well known. Most of the data analysis and theories available on Al combustion deal with Al and air reactions to eliminate variables created by the destruction of various metal oxide molecules. This work will present comparisons between the  $\text{Al}+\text{O}_2$  and  $\text{Al}+\text{MoO}_3$  reactions.

## CHAPTER II

### PRESSING OF ENERGETIC MATERIALS

#### 2.1 Introduction

Many applications of micron and nanocomposite thermites involve application of compressed powder samples simply because of volume constraints. Because nanocomposite powders are extremely ignition sensitive to heat, friction and electric spark, a safe and consistent method of pressing nanocomposite powders is desired. At least five major steel die designs were used to compress nanocomposite mixtures of Al+MoO<sub>3</sub>. The goal of this chapter is to present the progression of pressing techniques used on nanocomposite energetic materials.

#### 2.2 Symmetrical Steel Cylinder Dies

The first attempts of pressing nanocomposite Al+MoO<sub>3</sub> powders were done by researchers at Los Alamos National Lab (LANL). The LANL die designs and pressing problems were shared with the author and expanded upon for future designs at Texas Tech University. In 2001, Jim Busse (DX2-Los Alamos National Lab) was pressing nm-Al+MoO<sub>3</sub> using a steel die designed similar to Figure 2.1. The basic procedure of pressing was:

1. measure out shims to insert between the plunger heads and the barrel (based on plunger length and barrel length) to ensure a specific pellet length
2. partially insert the bottom plunger to form a loose seal with the barrel
3. pour a measured mass of loose Al+MoO<sub>3</sub> powder into the barrel
4. guide the top plunger into the barrel and inserting the shims
5. load into a press and apply a given load to adequately eliminate any spaces between the shims
6. remove one plunger by hand (usually the top)
7. remove the shims and extrude the pellet sample out of the barrel end.

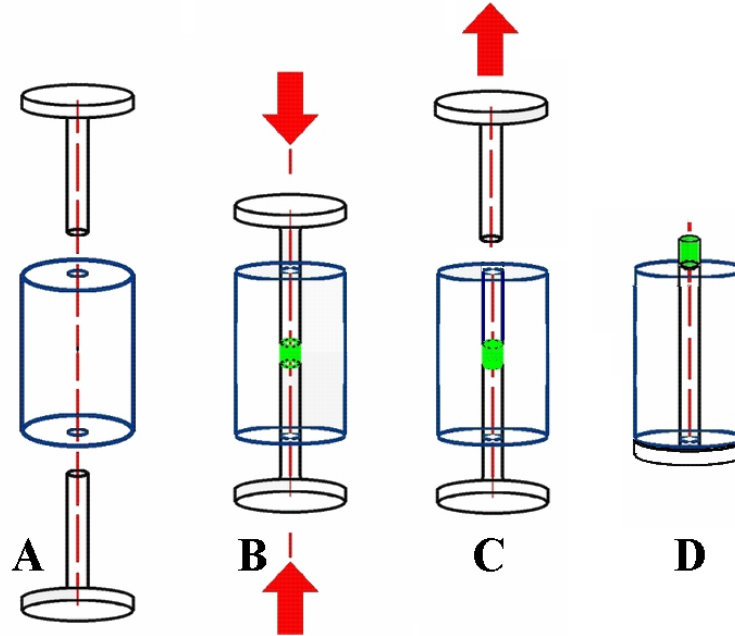


Figure 2.1: Diagram of LANL symmetrical load cylinder die

This die design provided many problems associated with the plunger travel distances and plunger/barrel tolerances. After compression the sample would ignite during extrusion or the plungers would become wedged in the die. The wedged plungers would require huge forces to remove causing deformation of the plunger ends or barrel walls and sometimes causing ignition of the small energetic mass still in the die

### 2.3 Unsymmetrical Acrylic Cylinder Dies

Expanding on LANL's design, techniques of pressing sensitive energetic powders were being developed at Texas Tech University using acrylic dies. Granier and Pantoya [24] presented experimental results using samples made from the die in Figure 2.2. Figure 2.2 shows A) 1018 steel top plunger head machined with a set screw and brass insert to clamp the plunger rod, B) oil/water quenchable hardened drill rod, C) U-shaped spacing shims, D) acrylic barrel with funneled top and reamed bore and E) large diameter base plunger. Acrylic was used for the barrel material based on cost and ease of machining. Acrylic is cheaper than steel (approximately \$0.75 for material costs) and several barrel pieces could be machined in one hours time. It was quickly observed, that

the barrel took the most wear when used for multiple samples. The barrel pieces were usually used to compress 4 to 6 samples and then discarded.

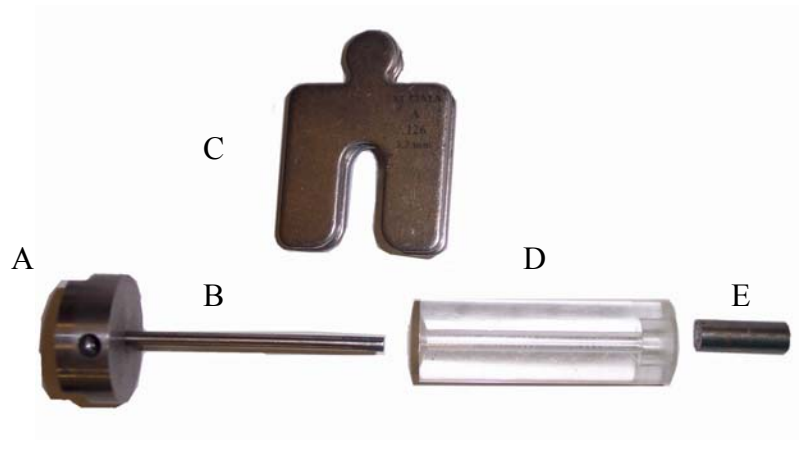


Figure 2.2: Photographic images of acrylic die with steel plungers and shims

Figure 2.3 is a diagram of the photograph in Figure 2.2.

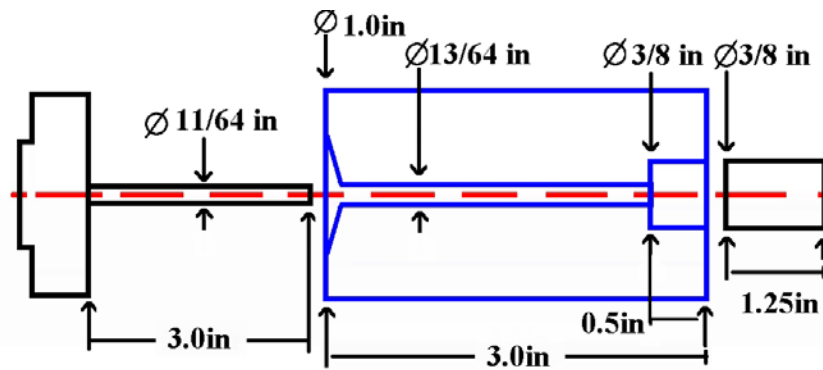


Figure 2.3: Dimensional diagram of acrylic die and steel plungers

There are two major advantages of the acrylic die/steel plunger design:

1. Acrylic softness: the softness of the acrylic compared to the steel plungers allowed the plungers to deform the barrel without damaging the plunger or rigidly resisting plunger movement causing ignition
2. Minimal extrusion length: in the acrylic die the compressed pellet is form at the top of the 3/8in. plunger. Even at low compression loads, the bore (inner surface) of the barrel will slightly expand. It is suggested that the constant bore diameter of die in Figure 2.1 causes ignition by forcing the expanded pellet in the smaller

diameter bore (where the top plunger was). The die shown in Figures 2.2 and 2.3 allows the expanded pellet to extrude into an even larger 3/8 in. diameter bore. One disadvantage of the acrylic cylinder dies is the low hoop stress strength of the acrylic. The acrylic dies only allowed enough compression force to achieve an average 1.47g/cc density nm-Al+MoO<sub>3</sub> sample or 38% TMD. TMD is the theoretical-maximum-density determined as a weighted average of the three components (Al, Al<sub>2</sub>O<sub>3</sub>, and MoO<sub>3</sub>) (discussed in more detail in Chapter III). Higher compression loads would cause the powder sample to expand and crack the acrylic barrel. Note that the actual die load was not recorded because shims were used to determine the pellet volume and density. Note that data from [24] shows 1.47 g/cc density samples as an average only (actual densities ranging between 1.18 and 1.82 g/cc or 30 to 47% TMD). Higher densities at the top of the range were not consistent, were more damaging to the acrylic barrel and were often structurally weak and unusable in experiments.

#### 2.4 Harrick Scientific Evacuatable Pellet Press

Soon after experiments were completed using the acrylic dies in Figure 2.2, efforts were made to manufacture high density samples more consistently and with more structural integrity. High density samples could be achieved by a more rigid barrel wall (like steel) that would prevent die wall deformation and simultaneously allowing higher die loads for increased powder compression. Improved structural strength could be achieved by using a vacuum die. Because of particle agglomeration and minimal individual particle mass, nanopowders are naturally “airy” and low density powders. For this reason, a vacuum die should remove gases from the interstitial spaces in the powders, allowing more compact organization of particles prior to plunger loading.

Figure 2.4 shows an *evacuatable pellet press* (as referred to by the manufacturer – also called a die) manufactured by Harrick Scientific (Ossining, NY) [27]. Both the top and bottom plungers are manufactured with a rubber o-ring which seals with a larger inner diameter wall of the barrel cylinder. A vacuum was drawn through a small port in the barrel cylinder attached to rubber hose and mechanical vacuum pump. Both the top and bottom plungers have a cross-sectional diameter of 12.7mm (1/2in.) and the barrel



cylinder allows approximately 10mm height for the initial loose powder. Because the overall short internal die dimensions only a small mass of loose nanopowder could fit in the die barrel prior to pressing (the mass would vary between 200 and 350 mg for different size nm-Al particles because of the varying powder density). Higher mass samples could be formed by compressing the initial volume, opening the die and adding more powder but this technique forms discontinuities in the compaction between multiple layers.



Figure 2.4: Photographic images of purchased 1/2in. ID Harrick-Scientific vacuum die[27]

Figure 2.5 shows two samples formed by the die in Figure 2.4. Both samples have a cross-sectional diameter of 12.7mm with a mass of 275.0 and 326.7mg for A and B respectively due to the initial powder mass allowance.



Figure 2.5: Two samples pressed with the Harrick-Scientific vacuum die

A) 153.8nm-Al+MoO<sub>3</sub> 1.31g/cc 33.7% TMD

B) 76nm-Al+MoO<sub>3</sub> 2.33g/cc 60% TMD

The Harrick-Scientific vacuum die did produce higher density samples that were structurally stronger but the dimensions were not optimal for laser ignition experiments or flame propagation measurements. Laser ignition experiments are based on uniform

cross-sectional heating which is more difficult for the large cross-sectional diameter (compared to  $\frac{1}{4}$  in diameter) shown in Figure 2.5. Flame propagation velocity measurements with axially lengths of 0.93 and 1.97mm for Figure 2.5A and B respectively is almost impossible and highly inaccurate using high-speed video.

## 2.5 Custom Steel Cylinder Dies

Figure 2.6 shows a custom steel die designed and fabricated by the author. The die properties and dimensions are as follows:

- A. Top plunger head: stainless steel, diameter  $d = 2$  in., overall length  $L = 1.25$  in., composed of two separate discs, the bottom piece with a 0.25 in. diameter hole and 0.375 in. diameter, 0.125 in. deep inset to fit the plunger head. The two discs were joined by two  $\frac{1}{4}$ -20 allen-head bolts.
- B. Top (long) plunger: M2 hardened tool steel, headed (0.375 in. dia. 0.125 in. length) and polished, 0.25 in. diameter shaft, overall shaft length of 2 or 2.5 in.. Purchased from McMaster-Carr, part number 93770A210 or 93770A310 (2 and 2.5 in. length respectively).
- C. Barrel: stainless steel, cold-rolled carbon steel, and chromemoly steel were used, outer diameter of 1 to 2 in., inside diameter (bore) drilled and reamed to 0.255 in., overall length of 1.5 or 2 in. based on plunger shaft length.
- D. Bottom plug: stainless steel, plug diameter of 0.25 in., plug length of 0.1 in. or less, overall disc diameter of 2 in., disc length of 0.5 in.



Figure 2.6: Photographic images of custom 1/4 in. ID cylinder die

Figure 2.7 is a diagram of the three major steps to complete the pressing of the powder samples using the die in Figure 2.6.

- A. The barrel is seated on the bottom plug to form a seal with the bore and the loose powder is poured into the top of the bore. The top plunger is inserted by hand (and in some instances shims were used between the top flat barrel surface and the top plunger head).
- B. The three pieces now joined are inserted into a hydraulic press and a specified load is applied to axially compress the powder inside the barrel.
- C. The load is released off of the die. The bottom plug is removed and the barrel and top plunger assembly are vertically flipped such that the formed pellet is at the top end of the barrel. A hollow-center spacer is placed above the bore hole and pellet and the assembly is reinserted into the hydraulic press. The pellet is carefully extruded into the hollow spacer.

Once these steps are completed the cylindrical pellet samples were collected, weighed and measured to calculate the sample density. The top plunger was either removed by hand (if possible) or extruded out of the barrel by a 0.1875in pin.

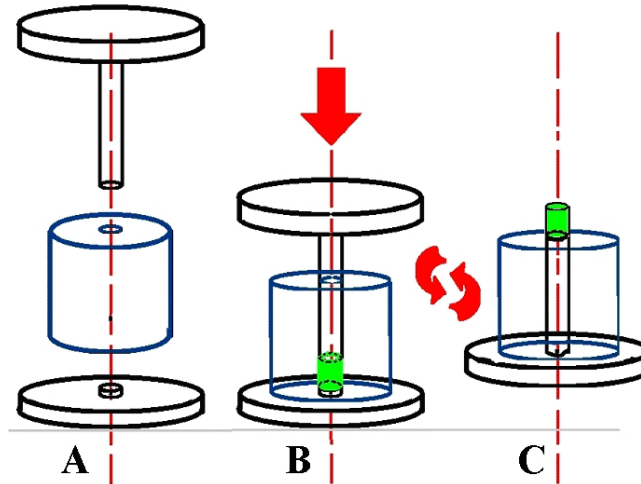


Figure 2.7: Diagram of pressing sequence for custom cylinder die

Normally 10-20mg of powder would lodge between the plunger and bore walls creating a tight and ignition sensitive wedge. Removing the plunger at a distance with the hydraulic press is less dangerous to personnel. The bore and plunger would then be cleaned with acetone or isopropanol and a round brass brush. The die would be allowed to dry and then reused. As many as 50 samples could be made with a single barrel piece before significant deformation was observed.

After considering design and material flaws of the three previous dies and pressing techniques several modifications were included in the custom die shown in Figure 2.6.

1. Samples were formed at one end of the barrel to minimize extrusion distance. After several samples were formed and bore diameter expanded, the barrel could be vertically flipped to press samples at the undeformed end.
2. The top plunger of M2 steel from McMaster-Carr was a harder material than the barrel allowing the barrel to take the deformation, which allowed easier extrusion of the samples and extraction of the plunger.
3. The top plunger had a diameter of 0.25in and the barrel bore holes were drilled and reamed to 0.255in to allow a slightly loose fit. Tighter fitting dies displayed

ignition more often during compression due to residual power between the plunger and bore wall.

4. The barrel material was finally optimized using chromemoly steel, which was softer than the plunger but strong enough to confine the compressed powder. The stainless steel barrel proved to be too hard or the wrong surface properties because pellets would often crack during extrusion. The cold-rolled carbon steel barrels proved to be too soft because the bore diameter would quickly expand in response to the radial stress during compression.

The ¼ inch diameter custom die shown in Figure 2.6 was used to fabricate most of the samples presented in Chapters III and IV of this document.

Special dimension samples were manufactured at Texas Tech University for experiments done by the Netzsch laboratory in Burlington, MA. A 12.7 mm (½ in.) diameter die with a similar design to Figure 2.6 was used to fabricate wafer like cylindrical samples. This die (shown in Figure 2.8) was used to fabricate various density samples with a 12.7 mm diameter and 2 mm length to be tested in the Netzsch LFA 447 (laser flash analyzer) instrument to determine thermal properties of compressed nano and micron Al+MoO<sub>3</sub> composites (results are shown in Chapter III, Section 3.7.2).



Figure 2.8: Photographic images of custom ½ in. ID cylinder die

Since the sample lengths were governed by the LFA instrument, shims were used to guarantee the sample length and the mass was incrementally varied to alter the sample

density. The wafer samples formed were very similar to the samples formed by the Harrick Scientific die in Figure 2.4 (wafers shown in Figure 2.5). The die in Figure 2.4 could not be used to guarantee the final sample dimensions or density.

For the die shown in Figure 2.8, the top plunger (left) is a headed pin blank of M2 tool steel purchased from McMaster-Carr (part number 93770A430). The barrel (center) was reamed to 0.505 in. diameter and the bottom plunger (right) was machined to a 0.500 in. diameter and 0.25 in. length. The top plunger head, barrel and bottom plunger were all made of stainless steel.

## 2.6 Carver Steel Die

Simultaneous to testing of the custom die in Figure 2.6, tests were also being done on the press capabilities of a similar steel cylinder die purchased from Carver Inc. (Wabash, IN) [11] (Figure 2.7). The dimensions of the plungers are very similar to the custom die in Figure 2.6. The plunger diameter is 0.25 in. and the bottom plug length is 0.25 in. The Carver die presented one major design improvement in the shape of the top plunger.



Figure 2.9: Photographic images of purchased 1/4 in. ID Carver die (4000 lb) [11]

The top plunger actually has two diameters. The end of the plunger ( $L_1$ ) is exactly 0.25 in. diameter with an axial length of 0.375 in. The mid length the plunger ( $L_2$ ) is approximately 0.245 in. diameter. This feature simplifies the extraction of the plunger after compression because the residual powder between the bore and plunger surfaces only interferes for a short length ( $L_1$ ) of the plunger.

The main disadvantage of the Carver die is that it is manufactured out of a mild-strength steel. The die is guaranteed to only withstand loads of 4000lbs. This load limit is relatively low and only produces samples at approximately 55% TMD for a 0.25in diameter. Tests were done to push the loads and sample densities higher in the Carver die which did in fact deform (expand) the inner bore diameter and mushroom the bottom plug.

## 2.7 Split Steel Die

Efforts were made to address the problems of pellet extrusion and plunger extraction in the steel dies. Figure 2.10 shows a split steel die fabricated at Texas Tech University. Basically the barrel piece shown in Figure 2.6 was replaced by a two-piece barrel with an external clamp. The goal of this design was to allow the sample to be compressed, the two halves of the barrel assembly would be removed and the top plunger and pellet sample could be removed without any axial motion induced friction.

Figure 2.11 shows several stages of pressing using the split barrel design. Figure 2.11A shows the compressed sample, top plunger and base plug immediately after compression with one side of the barrel remove. Figure 2.11B shows just the cylindrical sample from Figure 2.11A still remaining in the semi-cylindrical bore. Figure 2.11C shows a different sample that fractured across the same plane as the two halves of the barrel. Many pellets were formed using the split barrel die at different pressures and densities and the samples would most often fracture similar to the two pieces shown in Figure 2.11C. Even the solid sample shown in Figure 2.11B proved to be very difficult to remove with tweezers due to the adhesion-like bonding between the curved surface of the cylindrical sample and metal surface of the semi-cylindrical bore wall.

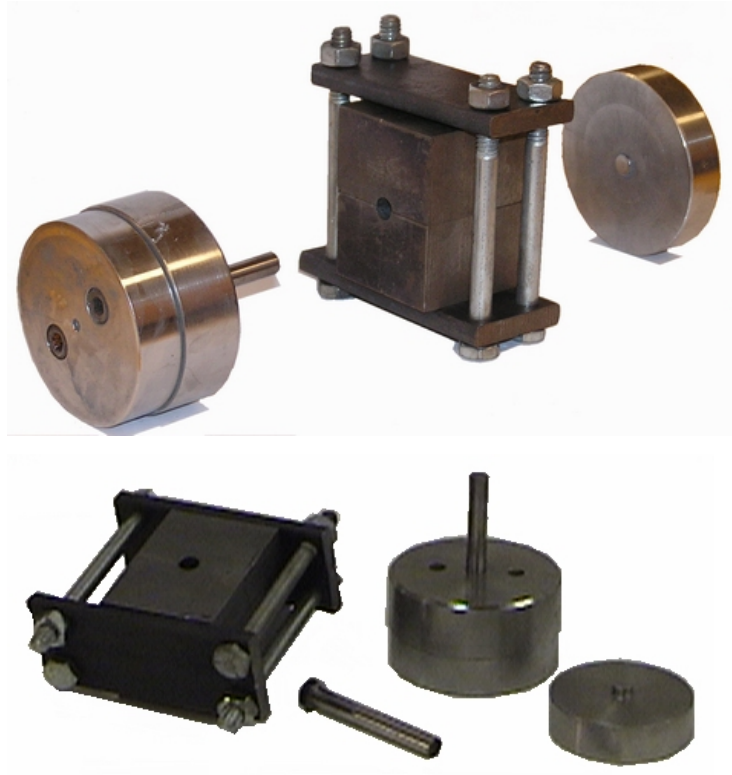


Figure 2.10: Photographic images of split steel die with external clamp



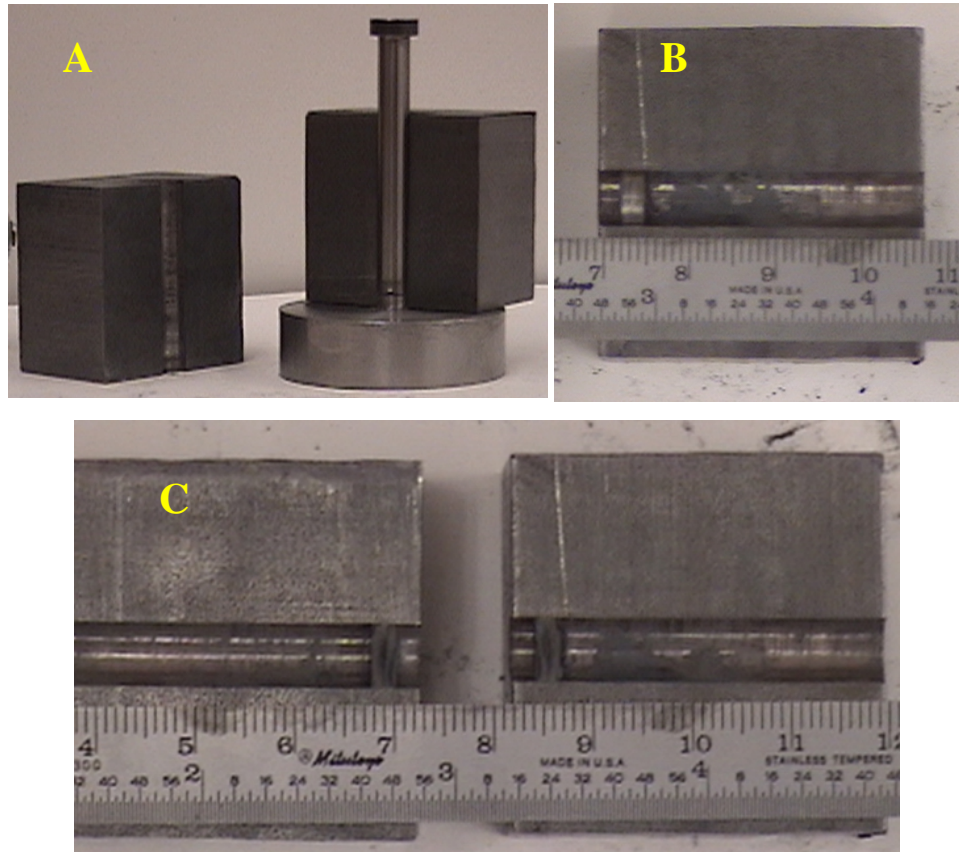


Figure 2.11: Photographic images of formed pellets in split steel die

A) first step of pellet extraction, B) single formed pellet, and  
C) two pellet halves: one in each split die piece

## 2.8 Custom Steel Vacuum Die

Combustion experiments presented in Chapters III and IV provided some indication that the porosity and interstitial air filled voids within the compressed samples may contribute to the flame propagation behaviors. To test this theory, a custom vacuum die was constructed to create the same dimension samples as the die shown in Figure 2.6. The goal of the 0.25 in. diameter vacuum die shown in Figure 2.12 was to reduce the oxygen (air) concentration inside the void spaces of the final porous solid. As mentioned previously, the vacuum may also cause a more organized powder bed prior to die loading that will produce either stronger samples or higher density samples.

The custom vacuum die dimension and parts are very similar to the die shown in Figure 2.6 with a few modifications.

1. Three rubber o-rings were introduced to create a sealed chamber: one above and below the location of the loose powder bed around the top plunger and bottom plug, the third o-ring is between the two discs of the top plunger head forming a seal around the replaceable plunger head.
2. The barrel bore was fabricated with a two stage diameter (similar to the Harrick Scientific vacuum die, Figure 2.4). The 1in. bore diameter forms a seal with the top plunger o-ring and the 0.25 in. bore diameter is where the powder bed is poured and the pellet compressed.
3. A 0.5 mm diameter port is drilled into the side wall of the barrel leading to a brass fitting for attaching a vacuum hose and pump.



Figure 2.12: Photographic images of custom  $\frac{1}{4}$  in. ID vacuum die

The goal of the custom vacuum die in Figure 2.12 was to create a die that would allow a 0.75 in. bed height of loose powder prior to compression (allowing higher mass samples) and produce 0.25 in. diameter samples.

The main disadvantage of the custom vacuum die shown in Figure 2.12 was the concentric alignment of the top plunger and bore. The bottom plug was joined to the barrel by two bolts that compressed the o-ring between the barrel and bottom disc flat surfaces. A compression fit is formed between the top plunger o-ring and 1 in. bore diameter to form a sealed chamber. The round cross-sectional o-ring allowed the top plunger and head assembly to roll and pivot and the operator could not visually see the 0.25 in. end of the top plunger shaft nor could the operator see the 0.255 in. bore hole to concentrically align the two pieces. This difficulty in alignment caused the pressing to be very time consuming and rendered the die unusable.

## CHAPTER III

### DENSIFICATION EFFECTS ON NANOCOMPOSITE THERMITE COMBUSTION

#### 3.1 Introduction

Many works have been published testing combustion behaviors of nanocomposite thermite powders [3][5][6][23][24][41][52][56][57] (see literature review, Table 3.1). The nanocomposite thermite mixtures (especially Al+MoO<sub>3</sub>) are extremely ignition sensitive thus making the powder handling hazardous. For safety and productivity reasons even fewer works have been presented on combustion behaviors of compressed solid nano-thermites [23][24][41][52] (see literature review, Table 3.1).

In 2004, Granier and Pantoya [24] tested nano and micron Al+MoO<sub>3</sub> thermite mixtures in compressed cylindrical pellet form. The pellet samples were pressed to 38% TMD or 1.48 g/cc using a steel and acrylic die in a hydraulic press [24]. The 38% TMD samples were highly porous and brittle with a high aptitude to break, crack and chip.

Attempts were made to prepare a denser sample with improved physical strength but the hydraulic press load (and density) was limited by the strength of the acrylic die. Designs were used incorporating a steel die that allowed safe pressing of denser and stronger samples. These high and mid-density samples were examined and preliminary observations of acoustics, light emission intensity, sensitivity and propagation speeds indicated that higher density nanocomposite samples were less reactive. This chapter presents results of pressing sensitive energetic materials and the effect of density on the combustion behaviors of micron and nanocomposite thermites.

#### 3.2 Literature Review

Table 3.1 tabulates a list of experimental results of physical combustion behaviors (i.e. ignition times, ignition temperatures, flame propagation velocities...) of several Al reactions.

Table 3.1: Literature Review of Combustion Experiments of Composite Thermite Energetic Materials

Author(s)/Date	Samples	Experiment	Results
Balakhir, Bushuev, Bareskov, Kosyakin, Kudryavtsev, & Fedorova (1974) [3]	Al + Metal Oxides	NiCr ignition of pressed pellets	Combustion rate [ $\text{g}/\text{cm}^2\cdot\text{sec}$ ] for varying metal oxides displaying $\text{WO}_3$ as the fastest burner and $\text{Cr}_2\text{O}_3$ as the slowest (2.82 and 0.23 $\text{g}/\text{cm}^2\cdot\text{sec}$ ) respectively
Bockmon, Son, Asay, Busse, Mang, Peterson & Pantoya (2002) [5]	Nm Al + $\text{MoO}_3$	Open tray loose powder burn, pressure cell	Propagation velocity and pressurization rate as function of stoichiometry (optimum found at 45% nano-Al), SANS/SAXS particle size distribution analysis, velocities as high as 1000m/s
Bulian, Kerr, & Puszynski (2004) [8]	nm Al + CuO	Open tray burn, pressure cell	Propagation velocities and ignition delay with aging effects and coating Al with Z6124 Silane and Oleic acid
Dreizin (1996) [14][15]	Al+Air	Single droplet combustion	Micron Al ignites above Al melt ( $T_{\text{mp}}=660^\circ\text{C}$ ) and closer to Al boiling ( $T_{\text{bp}}=2520^\circ\text{C}$ ), combustion time, 3 stage combustion
Granier & Pantoya (2004) [23]	Al (17nm-20 $\mu\text{m}$ ) + $\text{MoO}_3$	Laser ignition of compressed pellets	Optimum fuel rich stoichiometry ( $\phi=1.2$ ) determined by minimum $t_{\text{ign}}$ and maximum propagation velocity Increased sensitivity (decreased ignition delay) of nanocomposites, faster burn rates of micron samples contributed to preheating of 6s $t_{\text{ign}}$
Il'in, Gromov, Vereshchagin, Popenko, Surgin & Lehn (2001) [29]	Al (UFAP $\approx$ 0.1 $\mu\text{m}$ ) + Air	NiCr wire ignition in sealed bomb	Forced reaction with excess N in sealed vessel, AlN product concentrations, product mass change, list of elementary reactions between Al and Air, reaction enthalpy diagram of Al+O <sub>2</sub> +N <sub>2</sub>
Il'in, Popenko, Gromov, Shamina & Tikhonov (2002) [30]	Al (UFAP $\approx$ 0.1 $\mu\text{m}$ ) + Air	Sealed bomb	Comparing agglomerated and un-agglomerated nano-Al, SSA, Al purity, and initial powder density, 5-7 wt% absorbed surface gases, combustion time and $T_{\text{max}}$ for various bomb pressures
Moore, Pantoya, Son (2004)[41]	Bimodal Al (80nm + 4,20 nm) + $\text{MoO}_3$	Laser ignition of pellets, unconfined powder channel,	Ignition delay, propagation velocity, maximum pressure of bimodal pellet and powder samples, 20% nm-Al increases ignition sensitivity, 70% nm-Al to present maximum propagation speeds,

Author(s)/Date	Samples	Experiment	Results
Kwon, Gromov, Ilyin, Popenko, Rim (2003) [38]	Al (UFAP≈0.1μm) + Air	NiCr ignition of cone powder pile	$T_{\text{ign}} = 750\text{-}820\text{K}$ , slow first stage of combustion ( $T_{\text{max}} = 1400\text{ K}$ ), fast second stage of combustion ( $T_{\text{max}} = 2500\text{-}2800\text{ K}$ ), XRD and SEM of products displaying needle-like poly-crystals
Ostmark & Roman (1993) [45]	Mg + $\text{NaNO}_3, \text{BaO}_2$	Laser ignition of pressed pellets	Influence of pulse width, beam radius, particle size and gas pressure, determined $E_a$ , pre-exponential factor and absorption coefficient
Popenko, Il'in, A.M. Gromov, Kondratyuk, Surgin, A.A. Gromov (2002) [48]	Al (0.25-80μm) + Air	NiCr wire ignition of 3g cone	SEM analysis of reactants and products, Two stage combustion with $T_{\text{max}}$ of 1200 and 2400°C respectively, Products concentration analysis consisting of $\alpha\text{-Al}_2\text{O}_3$ , $\gamma\text{-Al}_2\text{O}_3$ , AlON, AlN, and $\text{Al}^0$
Puszynski (2004) [49]	Al (50&80 nm)+ CuO	Aging of Al, Unconfined channel burn	Al purity with aging in air, effects of aging with silane coating, optimum stoichiometry by propagation velocity in air and argon, coating Al with silane effects on propagation velocity
Sanders, Busse & Son (2003) [52]	Al + $\text{MoO}_3$ , $\text{Fe}_2\text{O}_3$ , $\text{WO}_3$ + HE	Percussion primers	Pressurization rates, maximum pressure
Sandstrom, Oschwald & Son (2004) [53]	Al (25nm – 14μm) + Air	Laser ignition of powders	Ignition delay (ms), Ignition energy ( $\text{J}/\text{cm}^2$ )
Son, Asay, Busse, Jorgensen, Bockmon & Pantoya (2001) [56]	Al + $\text{MoO}_3$	Open and confined channel burns, powder and pellet	Pressure and illumination time traces for powders and pellets, channel propagation speeds showing unsteady acceleration
Son, Dye, Busse, Sandstrom, Oschwald, Janicke (2003) [57]	nm Al + Air, $\text{N}_2$ , Ar, $\text{O}_2$	Open channel burns, laser ignited powder	Al particle size distribution by SAXS, Two stage burn with forming oxides, nitrides and aluminum oxynitrides, Ignition delay for varying laser flux

### 3.4 Composite Sample Fabrication

Sample powders were made of the nano and micron thermite and then cold pressed into cylindrical pellets. Passivated 75.9 and 80 nm aluminum powder provided by Technanogy (Santa Anna, CA) and Nanotechnologies (Austin, TX) respectively were mixed with dry MoO<sub>3</sub> powder provided by Climax (Phoenix, AZ). The mass ratio was calculated to create a 1.2 equivalence ratio mixture based on the stoichiometric reaction shown in Eq. (1.1). Equivalence ratio is calculated by Eq. (3.1) and (3.2).

$$\phi = \frac{F / A|_{actual}}{F / A|_{stoich}} \quad (3.1)$$

$$F / A|_{stoich} = \frac{2(MW_{Al})}{MW_{MoO_3}} \quad (3.2)$$

The stoichiometric fuel to oxidizer ratio was computed neglecting the oxygen contribution from the air environment. Based on the Al+MoO<sub>3</sub> reaction (Eq. 1.1) and Eq. 3.2,  $F / A|_{stoich}$  is 0.5625. The optimum equivalence ratio of 1.2 was determined based on the highest ignition sensitivity and burn rates for nm-Al+MoO<sub>3</sub> burning in an air environment [24]. For the 75.9 to 80 nm Al powders used the active Al concentration was quoted to be 80.4% and this value was used to determine mass ratios of fuel and oxidizer powders. The mass percentage of Al powder (Al with oxide coating) is determined by Eq. (3.3).

$$X = \frac{\phi \cdot F / A|_{stoich}}{Y + (\phi \cdot F / A|_{stoich})} \quad (3.3)$$

Passivated nm-Al powder was mixed at a mass ratio of 45.6% ( $X$ ) with 54.4% ( $1 - X$ ) MoO<sub>3</sub>. The  $\mu$ m-Al used for this study was 3-4 $\mu$ m particle diameter (Alfa Aesar) with an active Al concentration of 98%. This led to micron Al mass ratio of 40.78% Al to 59.22% nm-MoO<sub>3</sub>.

The dry powder mixtures of passivated Al and MoO<sub>3</sub> were suspended in a hexanes solution at a ratio of 1.5 gram powder to 60 mL of solvent. Agglomerates were destroyed and mixing was achieved by sonication. A ½ in. (12.7mm) diameter sonic probe

(Misonix 3000) was submerged approximately 1 in. (2-3cm) below the liquid level of 60 ml (1.5 grams of powder) and actively sonicated for 60 sec by an alternating duty cycle of 10 sec on/off intervals. The wet solution was then dried on a 40°C hot plate in a Teflon coated steel pan under a fume hood. After allowing the hexanes to evaporate for 12 min, a fine dry powder settled to the bottom of the drying pan. The dry mixture was brushed out of the pan using a conductive brush (Thunderon 22 bristle – Gordon Brush) electrically grounded to the actual drying pan. This loose powder sample was stored under standard grade argon until it was pressed into cylindrical pellets.

Loose powders were pressed into compact cylindrical pellets by two methods: 1) pressing to a critical load and 2) pressing to a specific volume constrained by shims. Both methods are discussed in more detail in Section 2.5. The steel die shown in Figure 2.6 was used with a 50 ton manual hydraulic press (Carver Inc. Model No. 3925) as outlined on Chapter II.

A series of dial gauges were alternated to allow load measurements between 200 and 17000 lbs. Nanocomposite pellets actually begin to form at loads lower than 200 lbs or (4 ksi for the ¼ in. diameter die used). The die pressure is not actually measured inside the die, but measured by the hydraulic pressure and calculated for the head of the top plunger. The available pressure gauges were not able to realize a load below 200 lbs. The higher pressure dial gauges show less precision than lower limit gauges; therefore the precise repeatability of the *load pressing* technique is not guaranteed. It is noted that some of the loading errors may have been avoided by using a digital pressure gauge.

The TMD was computed as the mass average of the individual components of the thermite mixtures. For example, the TMD of the 1.2 equivalence ratio nanocomposite Al+MoO<sub>3</sub> was calculated to be 3.886 g/cc using Eq. (3.4).

$$\rho_{\text{TMD}} = X \cdot (Y \cdot \rho_{\text{Al}} + (1 - Y) \cdot \rho_{\text{Al}_2\text{O}_3}) + (1 - X) \cdot \rho_{\text{MoO}_3} \quad (3.4)$$

Similarly the TMD was computed for the micron thermite mixtures as 3.888 g/cc only varying by the concentration of inert Al<sub>2</sub>O<sub>3</sub>. The density of each mixture component was taken as shown in Table 3.2.



Table 3.2: ThermiteAl+MoO<sub>3</sub> composite constituent densities

	Al	Al <sub>2</sub> O <sub>3</sub>	MoO <sub>3</sub>	
Density	2698.4	3860	4692	kg/m <sup>3</sup>

Using the *load pressing* method discussed previously, the press load was varied incrementally from 200 to 17000 lbs for the nanocomposite samples to achieve densities ranging from 1.9 to 2.8 g/cc respectively. The micron thermite mixtures were pressed under 500 to 7000 lbs to achieve a similar density range of 2.13 to 2.90g/cc. The die load and densities were recorded at each increment and are shown in Figure 3.1. Figure 3.1 shows that both the nano and micron composite samples have a logarithmic relation between the sample densities and die pressure. Figure 3.1 also shows that the micron samples are much easier to press than nano powders. Nano-powders are naturally airy and almost triple the force (as used on micron powder) is required to achieve the same 70 to 75% TMD. Table 3.3 shows the range of achieved densities. The data points in Table 3.3 and shown in Figures 3.1 and 3.6 are the average of 1-3 samples. Multiple samples were made at each die load to test repeatability. As the density increased, fewer samples were averaged due to die destruction or poor sample strength. At high densities the samples would break into layered strata upon extrusion rendering them undetermined density and useless for burning measurements (see Section 2.3).

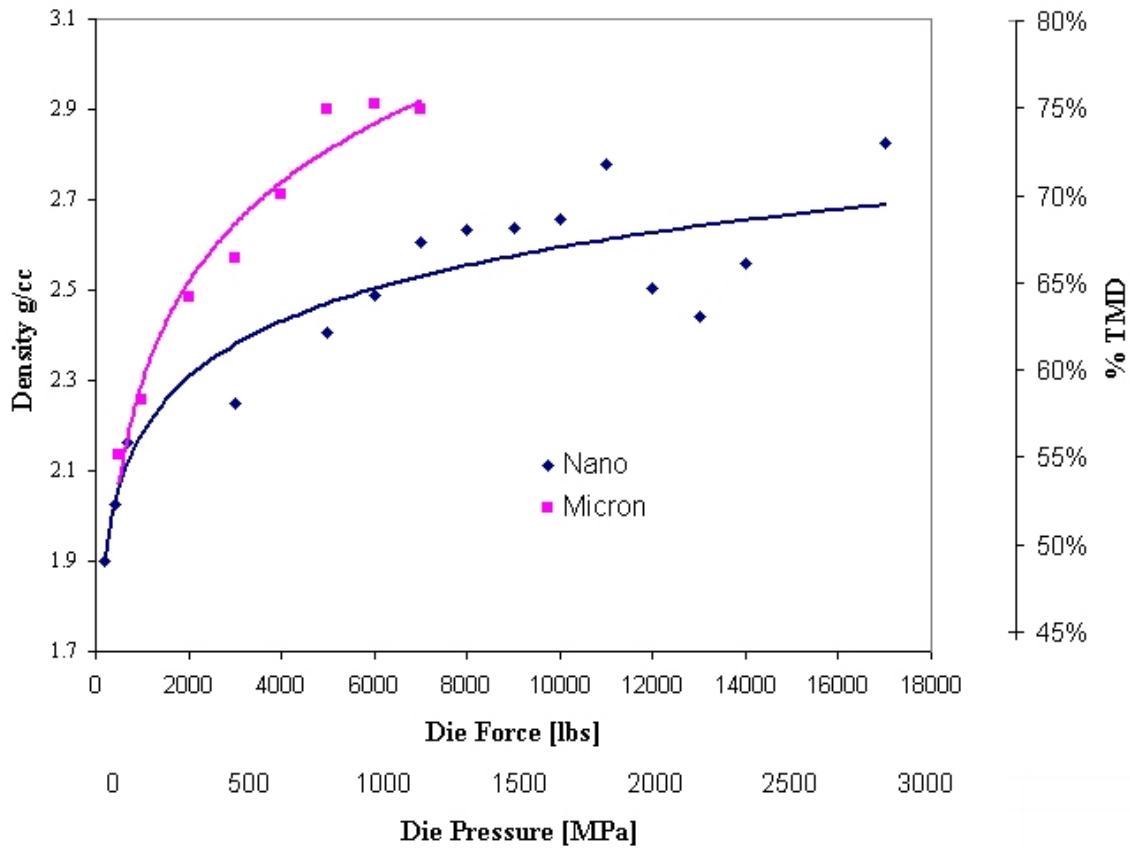


Figure 3.1: Thermite composite sample density as a function of die pressure and applied load

An empirical relation was derived based on the data trends shown in Figure 3.1 to allow predictions of density using the load pressing cold compaction technique.

	Figure 3.1 Trend Representation
nm Thermite	$\rho = 0.3202 \cdot \ln(P) + 1.3026 \pm 8.1\% *$
$\mu\text{m}$ Thermite	$\rho = 0.3202 \cdot \ln(P) + 0.7109 \pm 3.1\% *$

\*  $\rho$  in g/cc and  $P$  in MPa

where  $\rho$  and  $P$  have the units of g/cc and psi respectively. Andrievski [1] showed a logarithmic trend for the density versus pressure relationship for nickel (Ni) similar to Figure 3.1. Similar graphs have been made for metal-oxides and ceramics which present a dual linear trend separated by a critical pressure [35]. Figure 3.1 suggests that the Al spheres are the critical component for compressing the energetic materials (since the  $\text{MoO}_3$  samples are the same for the nm and  $\mu\text{m}$ -Al+ $\text{MoO}_3$  composites in Figure 3.1). The

critical pressure shift in metal oxides and ceramics is contributed to fracturing of the large agglomerates [35]. SEM images of the Al+MoO<sub>3</sub> mixtures have shown that the MoO<sub>3</sub> actually do fracture during compaction (Figure 3.2-C2 and Figure 3.7)

Figure 3.2 shows a series of light microscope and SEM images of a mid and high density 3-4.5  $\mu$ m-Al+MoO<sub>3</sub> thermite sample. The images in the left column are different magnifications of a 35% TMD (1.36 g/cc) and the right column images are 75% TMD (2.92 g/cc).

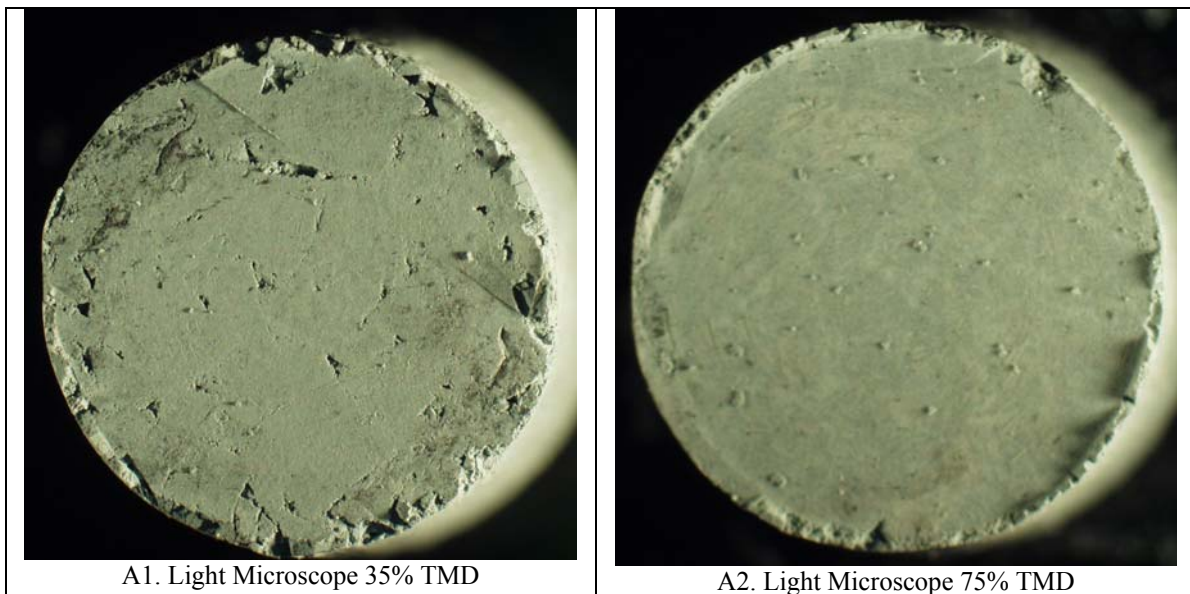
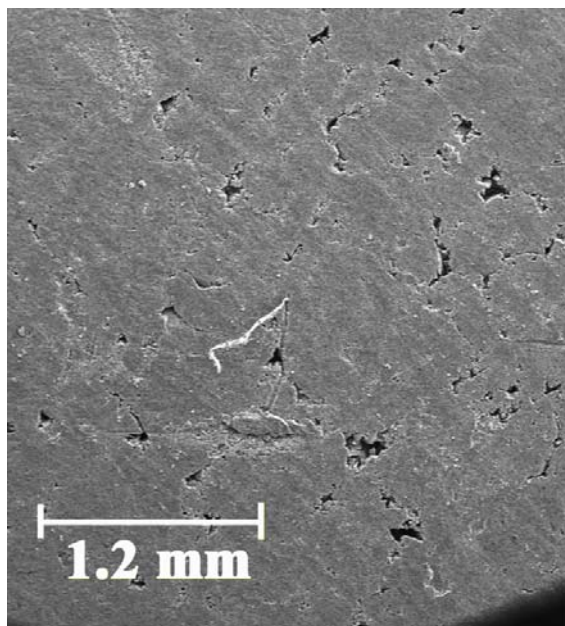
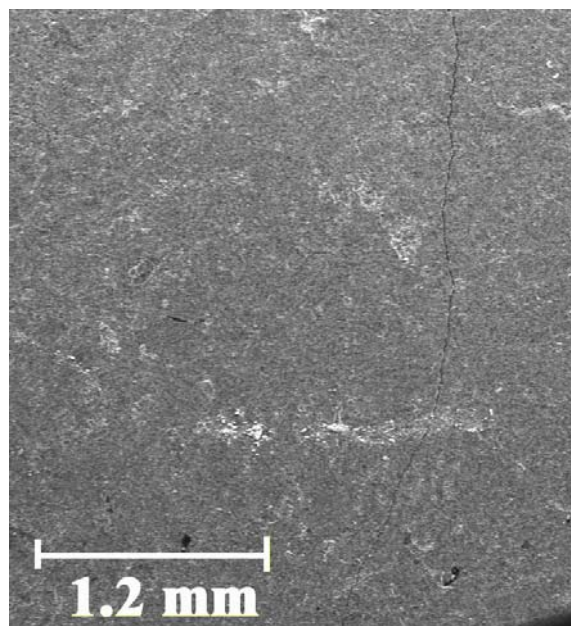


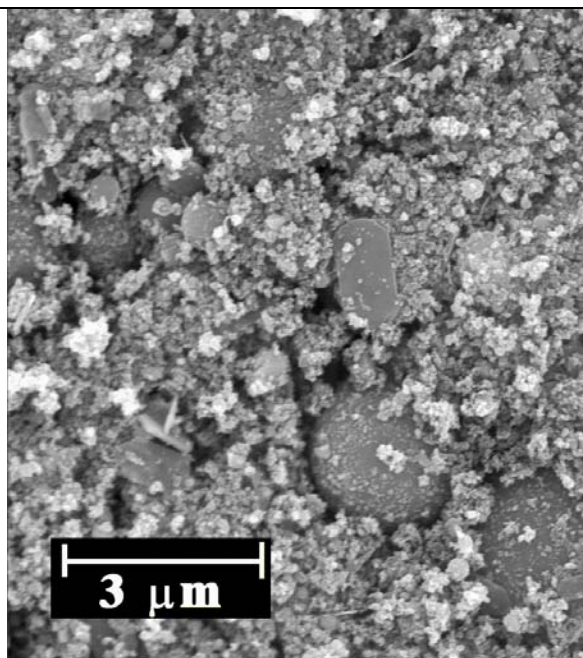
Figure 3.2: Light Microscope and SEM images of 3-4.5  $\mu$ m Al+nm-MoO<sub>3</sub> compressed samples



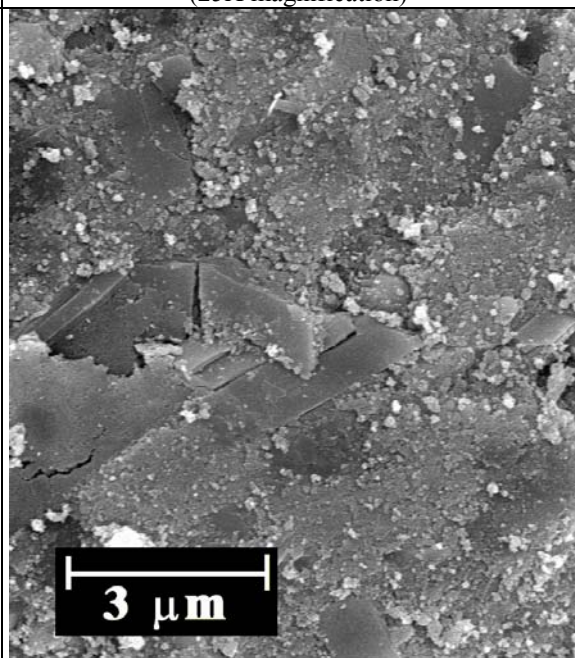
B1. SEM Image of 35% TMD  
(25X magnification)



B2. SEM Image of 75% TMD  
(25X magnification)



C1. SEM Image of 35% TMD  
(15kX magnification)



C2. SEM Image of 75% TMD  
(15kX magnification)

### 3.5 Experimental Setup

All of the compressed pellets were suspended on a copper rod stand (to minimize insulation or heat removal) and ignited with a 50 W continuous wave CO<sub>2</sub> laser at 10.6  $\mu\text{m}$  wavelength.

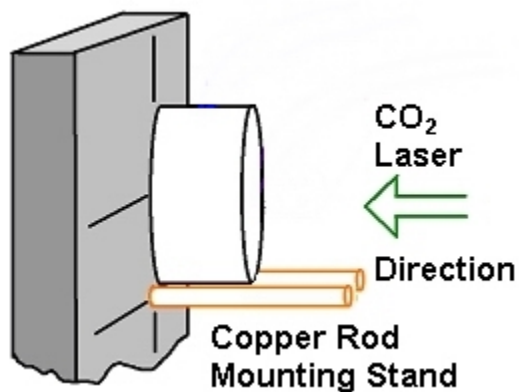


Figure 3.3: Diagram of experimental mounting of compressed cylindrical pellet

An electro-mechanical shutter controlled the laser exposure. A high-speed monochromatic visible light camera (Phantom IV) was triggered to record the sample burn at the moment of laser exposure. The camera recorded the event at 32,000 frames per second at a resolution of 128 x 32 pixels, with a 15 $\mu\text{s}$  exposure interval, 22 or 32 f-stop and two ND filters in series to allow 2.5% transmission into the camera optics. A schematic of the experimental setup is shown in Figure 3.4.

Nanocomposite mixtures at densities less than 0.5 g/cc and micron composite samples less than 1.3 g/cc were loose powder open-channel burns. Since the loose powder could not be suspended in air, the powder was poured into a 7 cm long rectangular channel in an acrylic block. The lowest density samples were simply poured then evenly distributed axially throughout the channel. The density was slightly modified by tamping and vibration to allow the powder to settle into a more uniform packing pattern. The powder mass, height inside channel and axial length were all measured to approximate the bulk density of the sample. The burn event was recorded identical to the pellets except the ignition source was a spark discharge from a piezoelectric crystal.

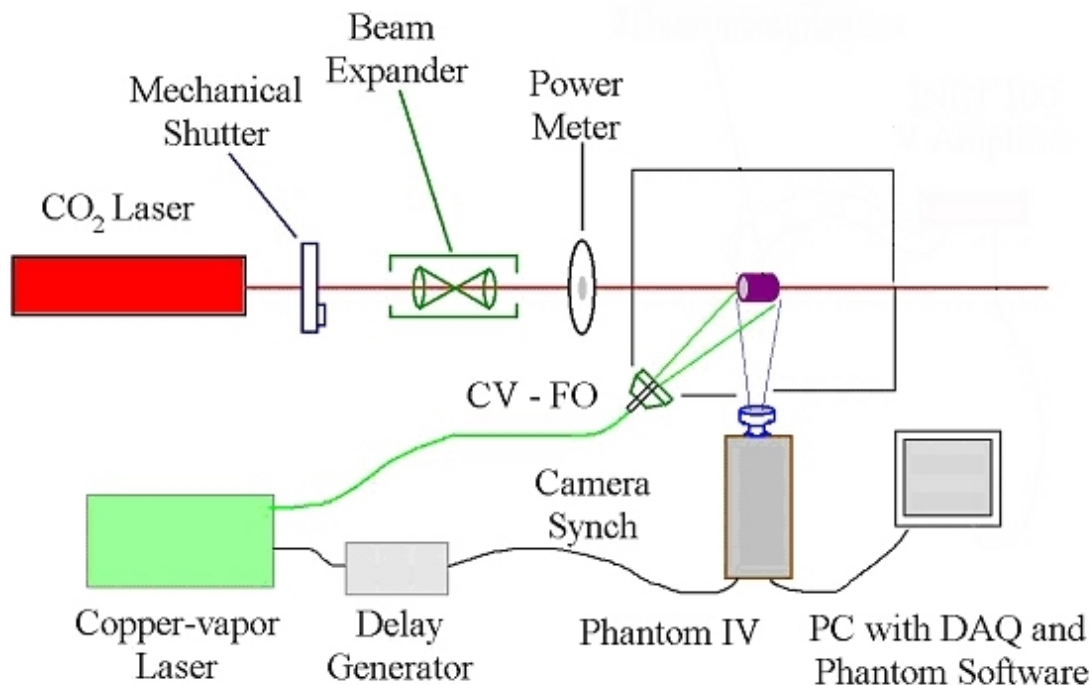


Figure 3.4: Diagram of experimental equipment system

### 3.6 Combustion Performance Results

For each of sample densities shown in Figure 3.1, the burn event was recorded as discussed in the previous section. The combustion wave was observed propagating through the compressed samples as shown in Figure 3.5. Indicating frame 11170 as time zero, ignition is recognized by a *first-light* criteria at the center of the pellet. Then combustion wave then propagates from right to left. An estimate of axial propagation velocity can be made by a reference distance between pixels divided by the time difference between sequential frames. Using a ruler reference in the high-speed video, the Phantom software allows one to estimate a linear propagation velocity.

Figure 3.5 shows two series of still images taken from the high speed imaging of the Al+MoO<sub>3</sub> composites. Sequence A shows a typical high-speed video series of frames. Note that the images are naturally dark due to the light absorption during the short exposure time for each frame. Ignition is determined by a *first light* criteria shown in the first images in sequence A and B.



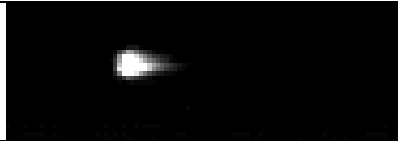

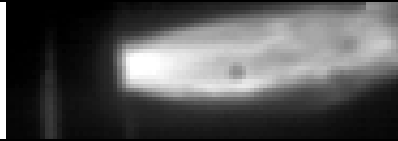


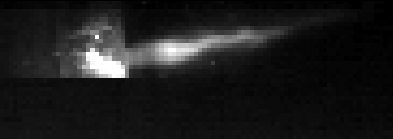
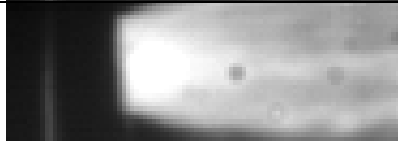



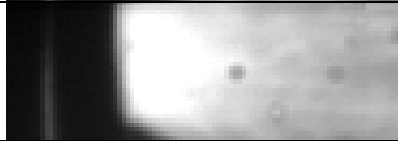

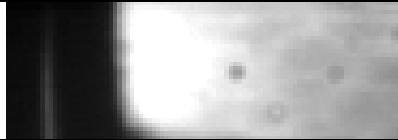
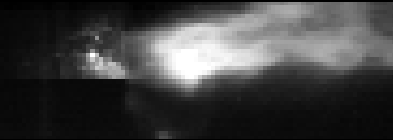
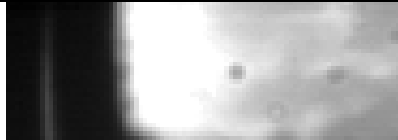
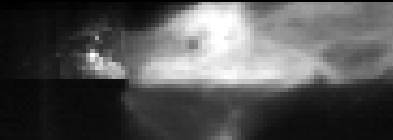
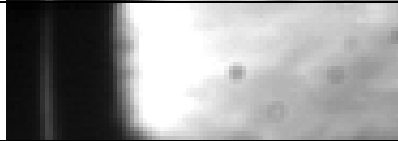
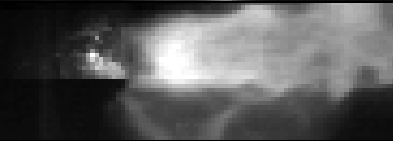
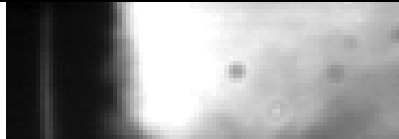

<b>Sequence A</b> 67.01% TMD 32 f-stop, 2.5% ND transmission		<b>Sequence B</b> 68.4% TMD 4 f-stop, Split CV image (CV on top of image)	
	Frame# t [ms]		Frame# t [ms]
	11170 0.0		12276 0.0
	11180 0.3125		12286 0.3125
	11190 0.6250		12296 0.6250
	11200 0.9375		12306 0.9375
	11210 1.2500		12316 1.2500
	11220 1.5625		12326 1.5625
	11230 1.8750		12336 1.8750
	11240 2.1875		12346 2.1875
	11250 2.5000		12356 2.5000
	11260 2.8125		12366 2.8125

Figure 3.5: Sequence of still images captured as digital high-speed video

The flame propagates radially across the front surface of the cylindrical pellet and then propagates axial through the length of the pellet.

Sequence B shows an alternate method of high-speed video using illumination from a synchronized copper-vapor (CV) laser. Basically the yellow/green CV laser beam was used to strobe a 10 ns pulse on the burning sample. The goal was to use a green wavelength bandpass filter on the high-speed camera lense to view the CV illumination and block the light emission from the flame. This was not possible due to the CV laser reflecting from the particulate cloud during the reaction. Because the camera was digital, information from the CCD array is recorded in a series of pixels and lines from the bottom of the image to the top. Sequence B, takes advantage of this property by altering the strobe synchronization of the CV laser. Basically, the camera scans the bottom 16 lines with normal high-speed illumination (with the notch filter) and then the CV laser pulses allowing a CV illuminated image for the top 16 lines of each image. Thus sequence B allows simultaneous viewing perspectives of the same event.

The combustion wave velocity was measured for all of the compressed samples shown in Figure 3.1. Lower density compressed pellets were manufactured using the Shim Press method due to the minimum gauge limit of our press. As discussed in the previous section, loose powder experiments were also burned. Compiling the three sets of samples, Figure 3.6 was generated to compare the wave velocity as a function of bulk sample density. The density axis of Figure 3.6 ranges from 6.5% to 73% TMD as shown in Table 3.3. Figure 3.6 shows the unique trends specific to the nano thermite samples versus the micron thermite samples.



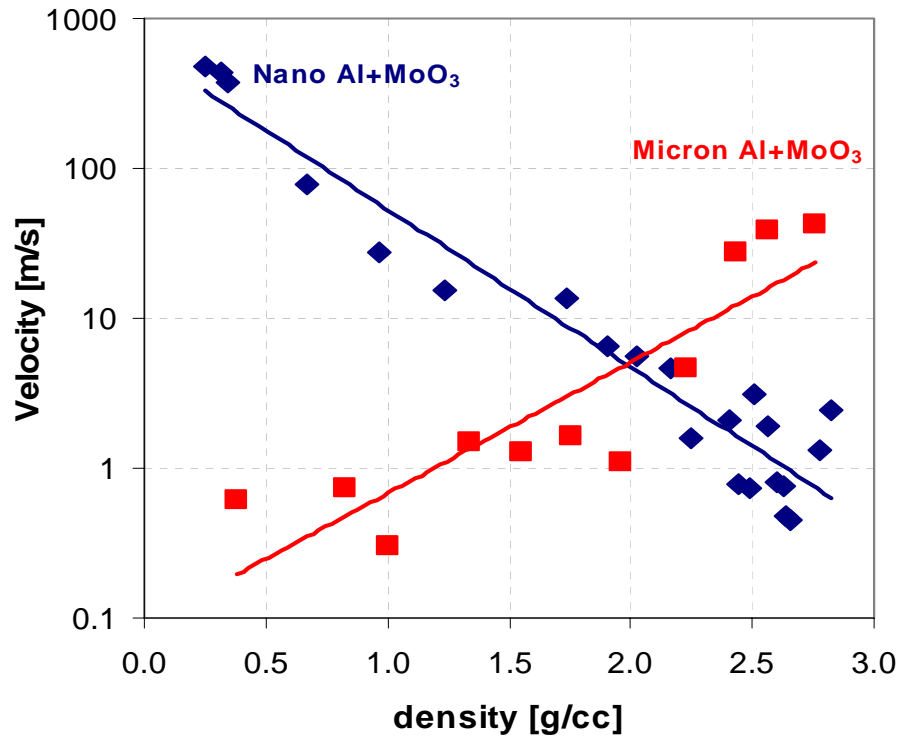


Figure 3.6: Flame propagation velocity of 80nm and 3-4 $\mu$ m Al+MoO<sub>3</sub> composites as a function of sample density

The nano-thermite samples show an exponential decrease on the order of a -2.5 exponent with respect to sample density. The micron thermite samples show an exponential increase on the order of a +2.0 exponent with respect to sample density. The coefficient  $A$  is not the same for both trendlines

	Figure X Trend Representation
nm Thermite	$v[\text{m/s}] = A \cdot \exp(-2.5\rho_{\text{sample}}[\text{g/cc}])_*$
$\mu\text{m}$ Thermite	$v[\text{m/s}] = A \cdot \exp(+2.0\rho_{\text{sample}}[\text{g/cc}])_*$

The porosity ( $\varepsilon$ ) and hydraulic pore diameter ( $d_h$ ) in Table 3.3 were calculated by the following equations.

$$\varepsilon = \frac{V_{\text{void}}}{V_{\text{solid}} + V_{\text{void}}} = \frac{V_{\text{void}}}{V_{\text{sample}}} \quad (3.5)$$

$$d_h = \frac{4 \cdot V_{\text{void}}}{SA} \quad (3.6)$$

where SA is complete surface area of the porous media calculated based on an approximation of actual Al and MoO<sub>3</sub> particle populations, dimensions and geometries.

Table 3.3: Density, propagation velocity and analysis data

75-80 nm Al + 44 nm MoO <sub>3</sub>					
	Sample Density g/cc	% TMD	Velocity m/s	Porosity $\epsilon$	Hydraulic Pore Diameter $d_h$ [nm]
Pwdr	0.252	6.48%	476.03	0.935	317.99
	0.319	8.20%	440.92	0.918	246.35
	0.343	8.84%	369.04	0.912	227.18
Pellet	0.673	17.32%	77.28	0.827	105.08
	0.969	24.94%	27.62	0.751	66.28
	1.235	31.78%	15.59	0.682	47.27
	1.739	44.75%	13.53	0.553	27.19
	1.901	48.92%	6.60	0.511	22.99
	2.026	52.14%	5.53	0.479	20.21
	2.162	55.63%	4.62	0.444	17.56
	2.247	57.82%	1.56	0.422	16.06
	2.406	61.90%	2.09	0.381	13.55
	2.443	62.85%	0.79	0.372	13.02
	2.489	64.04%	0.74	0.359	12.32
	2.505	64.46%	3.13	0.355	12.14
	2.559	65.85%	1.93	0.342	11.42
	2.604	67.00%	0.82	0.315	10.15
	2.632	67.72%	0.76	0.323	10.49
	2.639	67.90%	0.48	0.321	10.41
	2.658	68.39%	0.46	0.316	10.18
	2.777	71.45%	1.30	0.286	8.80
	2.825	72.69%	2.42	0.273	8.27

3-4 $\mu\text{m}$ Al + 44 nm MoO <sub>3</sub>					
	Sample Density g/cc	% TMD	Velocity m/s	Porosity $\epsilon$	Hydraulic Pore Diameter $d_h$ [nm]
Pwdr	0.379	9.76%	0.60	0.902	249.34
	0.828	21.29%	0.74	0.787	99.64
	1.003	25.80%	0.30	0.759	85.02
Pellet	1.341	34.49%	1.50	0.655	51.14
	1.549	39.84%	1.30	0.608	41.79
	1.758	45.21%	1.63	0.548	32.69
	1.962	50.46%	1.09	0.494	26.36
	2.226	57.25%	4.62	0.429	20.28
	2.433	62.57%	27.66	0.378	16.41
	2.563	65.91%	38.72	0.340	13.90
	2.759	70.95%	42.17	0.292	11.14

### 3.7 Discussion and Summary

While compressing the samples in Figures 3.1 and 3.6, the main physical alteration is in the porosity and pore structure of the composite. Obviously the loose powders will have an unorganized pore structure with pore sizes governed by the size of particle agglomerates and geometry. Whereas with high-density pellets, the agglomerates may be smaller, the crystalline  $\text{MoO}_3$  particles may be smaller (due to fracturing) and the interparticle void spaces (or pores) are definitely reduced and perhaps more homogeneous. A sample can be viewed as three component system (air volumes, aluminum spheres and  $\text{MoO}_3$  crystals) of random media. In a loose powder sample, the particles and air gaps are randomly formed and achieve random proximity. On the other hand, compressed samples are less random and compaction occurs following a movement of particles into a system of least resistance. Basically, as the powder samples are compressed, the air constantly moves between connected pores until escaping the sample or becoming pressurized in a defined cavity until a threshold pressure is achieved causing the cavity to rupture equilibrating the stored volume. The solid particles will also move in a more organized structure under loading to allow tighter geometry with less force resistance.

Porosity can be defined as the ratio of pore volume to the total volume of a material (Eqn. (3.5)). The key to explaining the unique burn velocity trends for nm and  $\mu\text{m}$ -Al in Figure 3.6 is analyzing the difference in overall pore structure and the effects of porosity on reaction behaviors.

Figure 3.7 shows that under extreme loading to compress the Al+ $\text{MoO}_3$  samples, the crystalline  $\text{MoO}_3$  will fracture. This fracture indicates that the geometry and dimensions of the  $\text{MoO}_3$  are not necessarily constant during compression. This suggests that porosity and method of compaction cannot be well predicted due to the altering properties of the composite particles under extreme pressure (forces).

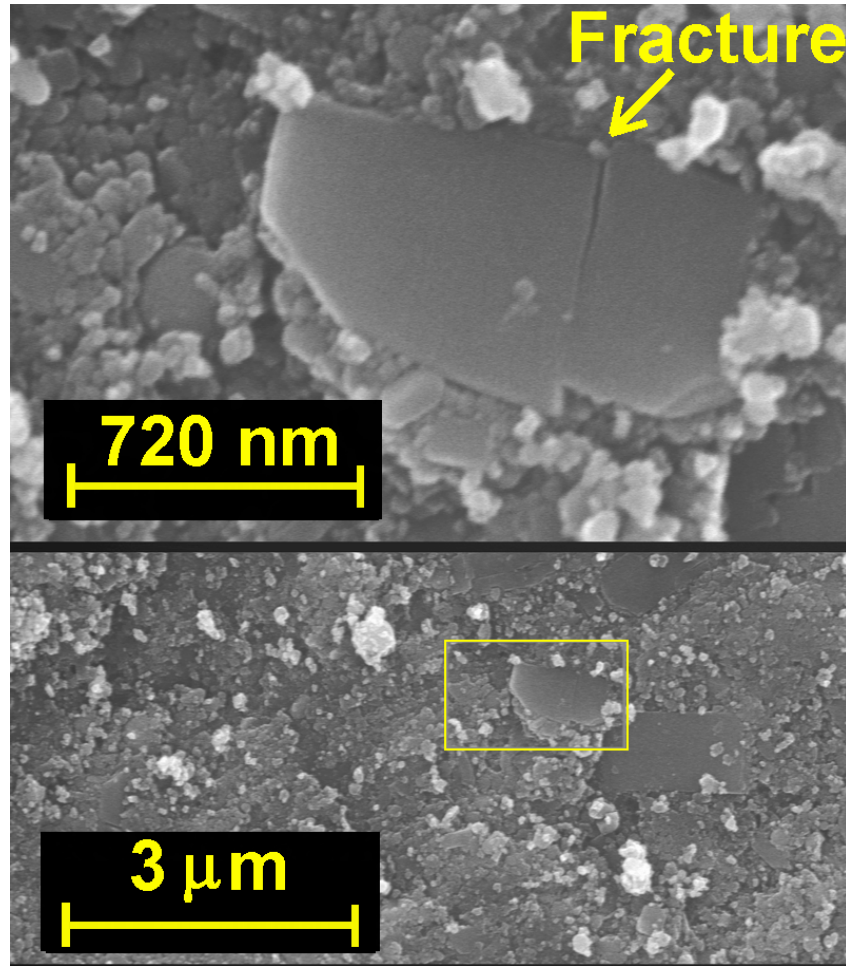


Figure 3.7 SEM image of fractured  $\text{MoO}_3$  crystals in 75% TMD Al+ $\text{MoO}_3$  sample

### 3.7.1 Composite Pore Structure

Based on the definition of TMD and how the experimental densities were determined in Figure 3.6 and Table 3.3, it can be shown that the nm and  $\mu\text{m}$ -Al samples of equal sample density have the same porosity. The pore volume is constant and independent of composite particle geometry. The average pore size and number of pores will inherently adjust based on the composite particles to achieve the same overall pore volume for equal density samples. Assuming that agglomerates exist in nano and micron composites and knowing that agglomeration geometry and size are difficult to measure or

classify with an average representative size and geometry, only single particles will be discussed in building a description of the entire composite.

It has been shown by simple geometry, that smaller (nanometer) spherical particles will form smaller and more numerous pores than larger spherical particles [1][12]. The pore volume is divided into more individual cavities in proportion to the surface area of the spherical solid particles. The minimum void space formed by larger (micron) spherical particles will always be greater than smaller (nanometer) spherical particles.

Results from DSC and TGA experiments in Chapter VI show that the nm-Al and gaseous oxygen reaction is two orders of magnitude faster than micron Al and gaseous oxygen (Figure 6.7). Results suggest that the gaseous O<sub>2</sub> (from the air pores) and Al reaction is the governing diffusion reaction that accounts for the nanocomposite burn velocity measurements shown in Figure 3.6. It is difficult to discern if the video determined burn velocities in Figure 3.6 are truly a measurement of an Al+MoO<sub>3</sub> reaction or Al+O<sub>2</sub> reaction around the pore sites. It is probable that the nanocomposite reactions are a combination of both reactions (due to the high affinity for the gaseous O<sub>2</sub> reaction and equivalent diffusion distances for the MoO<sub>3</sub> and O<sub>2</sub> molecules) and that any connected porosity will enhance flame propagation. Results suggest that the gaseous O<sub>2</sub> contained in the pores and on the surface of the samples may provide critical ignition sites that stimulate the Al+MoO<sub>3</sub> reaction. Flame propagation can be described by a sequence of local ignition points through a series of axial locations. Thus the low density nanocomposite samples are sure to have improved connected porosity and increased gaseous O<sub>2</sub> concentrations generating minimal resistance to flame propagation. High density nanocomposite samples have reduced porosity generating less gaseous O<sub>2</sub> reaction sites and reducing the overall simultaneous ignition sites. Results from the  $\mu$ m-Al+O<sub>2</sub> reactions using TG/DSC do not indicate the same affinity for gaseous O<sub>2</sub> as nm-Al. Thus the  $\mu$ m-Al composites will not be effected by the porosity in the same manner.

### 3.7.2 Thermal Properties of Porous Composites

The flame propagation speeds of the  $\mu\text{m-Al}+\text{MoO}_3$  composites shown in Figure 3.6 can best be described by comparing the porosity effects on thermal transport properties. Experiments were designed and conducted using a Netzsch LFA 447 (Laser Flash Apparatus) to determine the thermal diffusivity, specific heat, and thermal conductivity of micron and nanocomposite samples as a function of density (or porosity). These experiments were performed by Rob Campbell under the direction of Dr. Jack Henderson at the Netzsch labs in Burlington, MA.

Operation of an LFA device can be described as a Xenon flash lamp fires an energy pulse at one side of a thin wafer sample while an infrared detector measures the temperature of the opposite side of the wafer. The specific heat is measured by comparing the sample temperature to a reference sample of known specific heat. The thermal diffusivity is measured by the transient temperature response of the material. Once  $c_p$ ,  $\alpha$ , and  $\rho$  are known the thermal conductivity ( $\lambda$ ) can be back calculated by the product of the three.

$$\lambda = \alpha \rho c_p \quad (3.7)$$

The LFA 447/2 allows the user to heat the sample with a furnace to make thermal property measurements from ambient temperatures to 300°C.

The sample geometry is predefined by the LFA system as 12.7 mm diameter by 2mm length. Powder mixtures of 50nm-Al and 4.5-7 $\mu\text{m-Al}+\text{MoO}_3$  were made by suspending the powder in hexane, sonicating and drying off the liquid solvent. Four compressed wafers were fabricated using the 12.7 mm die in Figure 2.8 with premeasured shims to create the correct sample length. Since the sample volume was well defined, the powder mass was varied during pressing to generate a range of sample densities to perform LFA experiments on various density nano and micron composite samples. A minimum achievable density was observed due to the rigidity of the samples for handling (ie. if the sample was too soft it would crumble and break during handling and mounting). A maximum achievable density was observed due to sample quality (some high density samples would stratify and crack into thin layers) and failure

limitations of the die. As in Figure 3.1, the minimum and maximum achievable density is uniquely determined by the composite powder (and Al particle size). A density range from 1.07 to 1.79 g/cc (27.6 to 46% TMD) was generated for 50nm-Al+MoO<sub>3</sub> composite. A slightly overlapping density range of 1.54 to 2.52 g/cc (39.7 to 64.7% TMD) was generated for the 4.5-7 $\mu$ m-Al+MoO<sub>3</sub> composite.

Each sample was cycled through two heating programs from 25 to 300°C and the conductivity, specific heat and diffusivity were measured at 25°C increments. Data from the experiments is shown in Appendix A. Figures 3.8, 3.9, and 3.10 show the average specific heat, thermal conductivity and thermal diffusivity of the two heating rates at four temperature points.

Figure 3.8 shows that bulk specific heat is not a function of density or composite constituents. Note that the total Al<sub>2</sub>O<sub>3</sub> concentration is approximately 20% larger in the nanocomposite samples compared to the micron composite samples and the specific heat appears to be constant between particle size regimes.

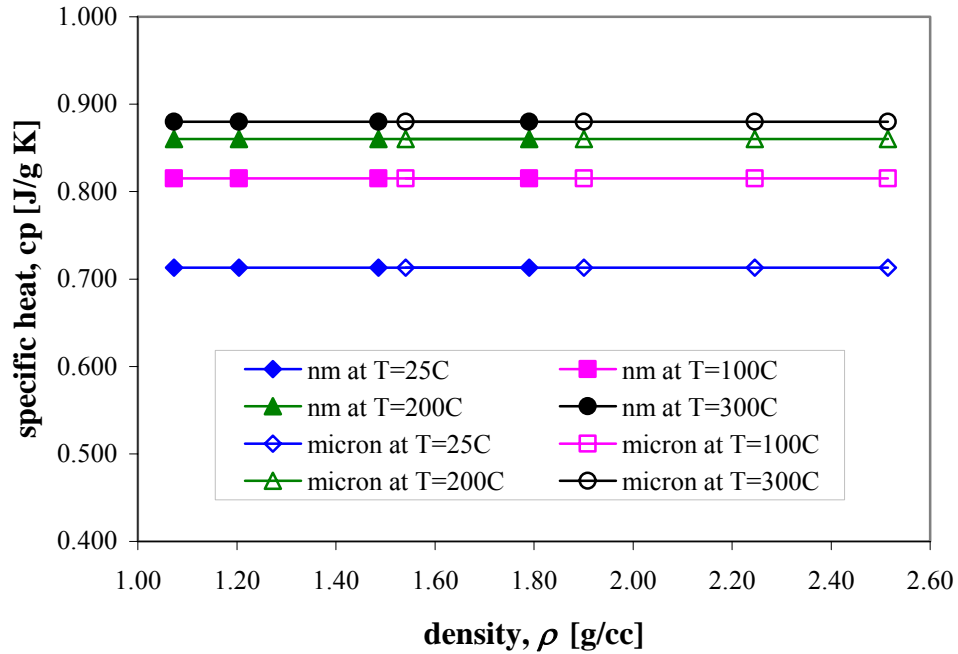


Figure 3.8: Composite specific heat as a function of bulk sample density

Figure 3.9 shows that the thermal diffusivity is a strong function of bulk sample density. The data suggests that the diffusivity is a strong function of bulk density but not a function of composite constituents. The overlap of the two high density nanocomposite samples and two low density micron composites suggests the same trend exists independent of Al particle size and  $\text{Al}_2\text{O}_3$  concentration.

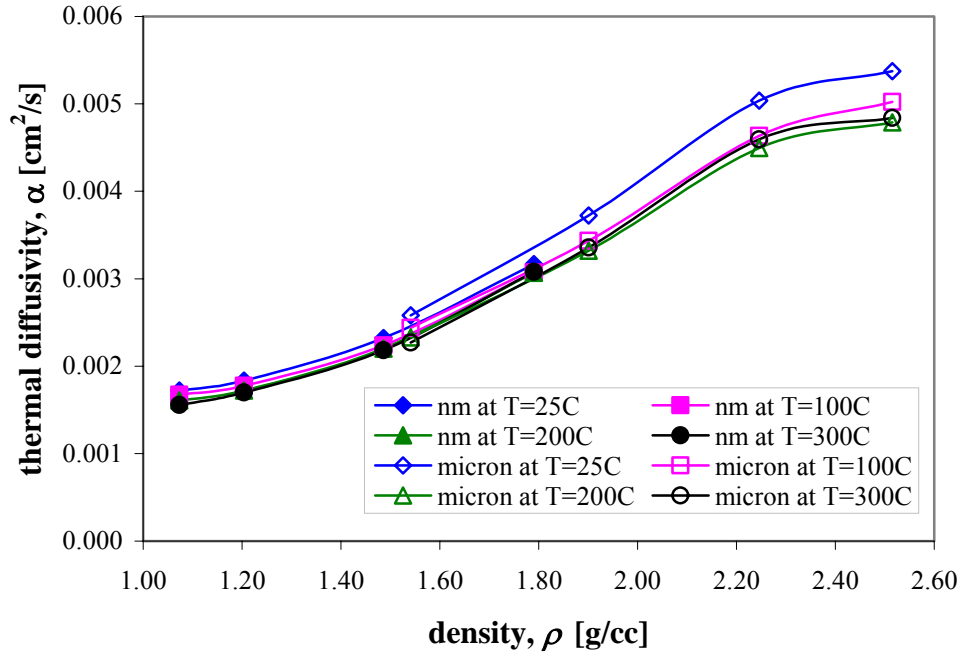


Figure 3.9: Composite thermal diffusivity as a function of bulk sample density

Figure 3.10 shows the thermal conductivity determined by Eq. (3.7) as a function of bulk composite sample density. Figures 3.9 and 3.10 have very similar trends because the sample density used is constant at 25°C and the specific heat is not a function of sample density as shown in Figure 3.8. The data in Figure 3.10 does show that the high density composite samples will provide better thermal transport than low density samples.



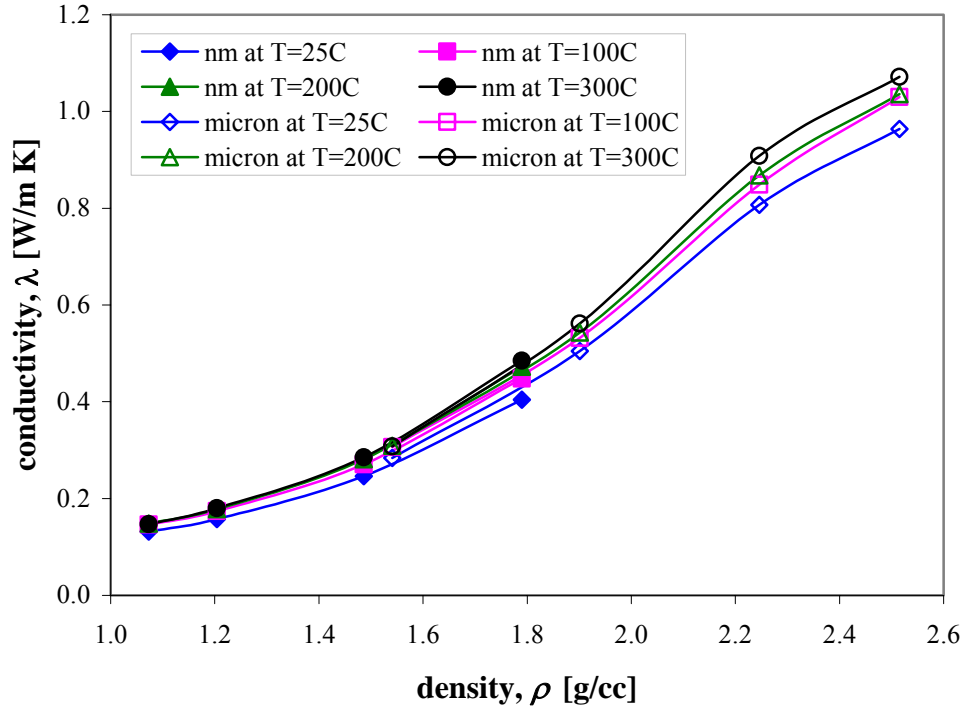


Figure 3.10: Composite thermal conductivity as a function of bulk sample density

The trend in Figure 3.10 can again be attributed to the porosity of the samples and the conductivity associated with the air voids. Though the thermal properties of individual Al and MoO<sub>3</sub> particles is unknown, it can be shown that the conductivity of air (9.34 W/mK at 100°C [31]) is much lower than the conductivity of bulk aluminum (237 W/mK at 27°C [31]), aluminum oxide (46 W/mK at 27°C [31]) and 50 W/mK for MoO<sub>3</sub> at 27°C). Thus as the porosity and air mass is reduced (density is increased) the conductivity transitions from a poor conduction medium (large air volume) to a more solid and better conduction medium.

This gradual transition in conductivity may explain the increase burn velocities in the micron composite samples in Figure 3.6. The higher density micron samples transport heat away from the flame zone better allowing faster heating of nearby reactants. As described earlier, flame propagation can be discretized into a sequence of local ignition points in linear progression. Faster heating of nearby reactants creates a faster propagation speed through a series of linear ignition locations.

## CHAPTER IV

### PRE-HEATING EFFECTS ON NANO-COMPOSITE THERMITE COMBUSTION

#### 3.1 Introduction

Past work has shown that reducing the reactant dimensions from micron to nano dimensions drastically alters the sensitivity and burn velocities of Al+MoO<sub>3</sub> thermite composites. Son et al. (2001) [56][5] showed increased burn velocities as large as 1000 m/s for nanocomposite loose powders. Granier and Pantoya (2003) [24] showed that ignition time reduced by two orders of magnitude for nano versus micron Al+MoO<sub>3</sub> compressed samples. But compressed micron samples showed much higher burn velocities than nanocomposite samples. It is thought that the nanocomposites are more sensitive to ignition due to the lower melting temperature of the nm-Al spheres [24] [65] and the affinity for gaseous O<sub>2</sub> reactions (Chapter VI). The increase burn rates presented in [56] and [5] are attributed to the increased homogeneity of nanocomposites. Granier and Pantoya [24] submitted the following table and graphs.

Table 4.1: Ignition time and burn rates for various Al particle diameters (Granier & Pantoya, 2003) [24]

<b>Al Particle Diameter</b> [nm]	<b>Ignition Time</b> avg [ms]	<b>Burn Rate</b> avg [m/s]
17.40	24.21	2.16
24.90	21.73	3.23
29.90	18.39	1.64
39.20	21.93	3.17
52.70	15.55	11.23
75.90	20.76	6.81
100.9	14.56	5.55
108	17.31	6.40
153.8	25.49	6.04
202	12.40	8.26
3-4 $\mu\text{m}$	89.43	1.20
10-14 $\mu\text{m}$	1384.13	29.92
20 $\mu\text{m}$	6039.43	22.91

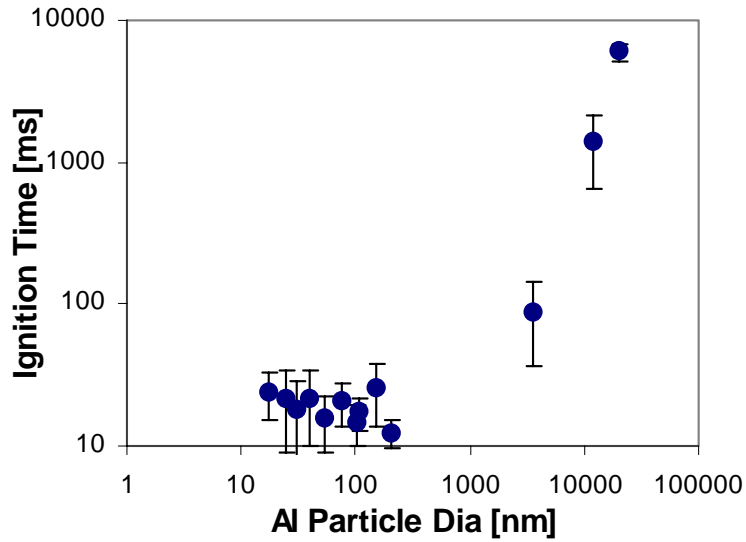


Figure 4.1: Ignition time as a function of Al particle diameter (Granier & Pantoya, 2003) [24]

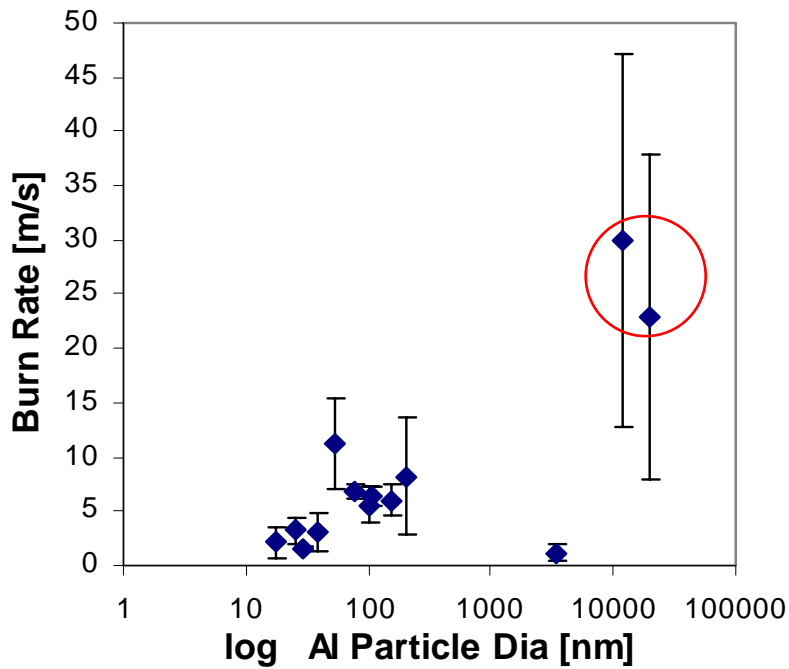


Figure 4.2: Burn rate (propagation velocity) as a function of Al particle diameter (Granier & Pantoya, 2003) [24]

It has been suggested that the higher burn rates seen in the 10 and 20 $\mu$ m-Al samples in Figure 4.2 are artificially elevated because of the large laser exposure time shown in

Figure 4.1. Based on the results of Son et al. [56], it was expected that the nanocomposite thermite velocities would be higher than the micron thermites (as shown with the 3-4.5  $\mu\text{m}$  sample burn rate shown in Figure 4.2). Table 4.1 shows that the 3-4.5  $\mu\text{m}$  data point was the only micron sample to have the same magnitude (compare to the nano samples) of preheating time prior to ignition and as expected the 3-4.5  $\mu\text{m}$  sample burned at a much slower rate than the nano samples. The 10 and 20  $\mu\text{m}$  data points in Figure 4.2 were allowed to preheat the entire sample for 1.38 and 6.0 s respectively. It is suggested that reactant preheating interval has a significant influence on the corresponding elevation in burn velocities.

Knowledge of hydrocarbon combustion (i.e. propane or methane burning in air) has been well explored through experimental and theoretical investigations. The effect of reactant temperature on hydrocarbon combustion behaviors such as adiabatic flame temperature and flame speed have been well researched [63]. Mechanisms of solid-solid combustion reactions have not been so thoroughly studied. To the authors knowledge there is little information on the influence of reactant temperature on solid-solid combustion behaviors.

The primary goal of this study was to examine flame propagation or burn velocities as a function of sample temperature (or reactant energy state) prior to ignition. The pre-ignition sample temperatures were varied by two methods: 1) volumetric preheating using a custom oven heated to a specified temperature and 2) varying laser power to allow more time for conductive heating prior to ignition.

### 3.2 Experimental Setup

Nano Al spheres are known to oxidize in an oxygen environment and manufactures purposely form a small  $\text{Al}_2\text{O}_3$  layer (4-8 nm thick) to decrease the pyrophoric sensitivity of the nano powders. The 40nm diameter Al powder was provided by Nanotechnologies (Austin, TX) at a stated Al concentration of 72% Al and 28%  $\text{Al}_2\text{O}_3$ . Technanogies (Santa Ana, CA) provided the  $\text{MoO}_3$ , which has a crystalline structure and is considered nano because at least one of the crystalline dimensions is less than 100 nm.

### 3.2.1 Sample Fabrication

Six batch mixtures of 1.5 grams were made at an equivalence ratio of 1.2 (slightly fuel rich using the true Al content). The mixed powders were suspended in Hexanes solution and sonicated for 25 minutes to break up any agglomerates and improve homogeneity. The hexanes liquid was then evaporated off on a hot plate at approximately 75°C leaving a homogeneous dry powder that was then collected. Because the powders were being compressed into pellets and not burned in a loose form, the powders were not sifted. The larger agglomerates formed during drying are considered to have the same Al-MoO<sub>3</sub> contact throughout and the larger agglomerates do improve pressing efficiency. Approximately thirty, 250 mg pellet samples were formed from the six powder batches. The samples were cold pressed using the steel die shown in Figure 2.6 and techniques outlined in Section 2.5 corresponding to Figure 2.7.

Each final pellet (seen in Figure 4.3) was approximately 220 mg (some mass is lost between the plunger and barrel wall), 6.52 mm diameter and 3.5 mm long resulting in a density of 2.02 g/cc or 52% TMD.

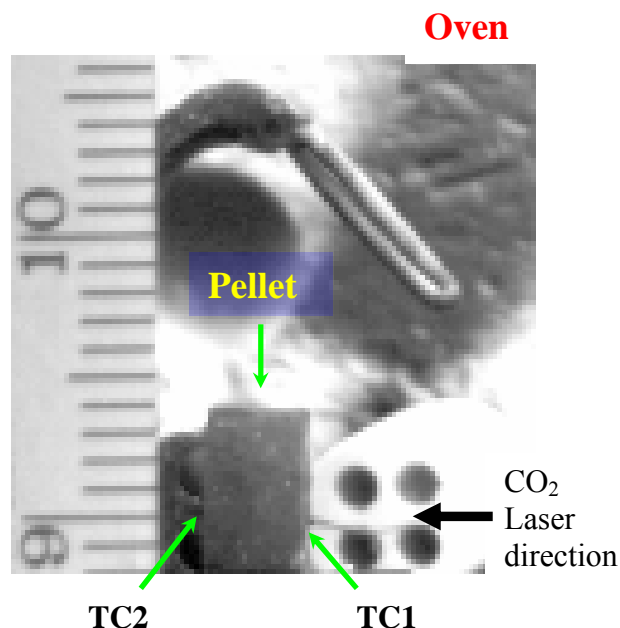


Figure 4.3: Cylindrical pellet on Stand with wedged between TC1 and TC2 in heated oven.

### 3.2.2 Equipment System

Each cylindrical sample was ignited on the vertical flat face perpendicular to the CO<sub>2</sub> laser (6.5 mm beam waist). The cylindrical pellet was placed on two thin copper bars parallel to the CO<sub>2</sub> laser beam path and carefully aligned such that the circular pellet face was centered with the beam waist. For the volumetric preheat variable, a firebrick oven was constructed around the pellet stand with a single glass window for camera imaging and two circular ports to insert the thermocouple insulators and another circular port for the CO<sub>2</sub> laser. The oven was allowed to stabilize at a specified temperature then the sample was placed on the stand and ignited by a 50 W laser power or 37.7 W/cm<sup>2</sup> laser flux. Prior to laser exposure the pellet was allowed to sit in the oven for approximately 8 min. to allow the oven heat to completely saturate the sample and to minimize any temperature gradients within the sample.

For the laser power variable, the pellets samples were still ignited inside oven to make any pressure contributions comparable between experimental variables, but the oven was turned off such that the inside was at ambient T (20°C.)

Two bare-wire C thermocouples (Omega - thickness of 0.005 in or 0.127 mm) were placed in spring tension on the front (laser side – TC1) and back (TC2) flat surfaces of the samples. The thermocouple voltages were recorded using an INET (model 100, Omega) data acquisition device in oscilloscope mode with a 10-bit 80mV range and 62kHz sample rate for each channel. A Phantom IV (Vision Research) high-speed digital camera was triggered by the laser shutter and recorded a 2 sec interval at 32000 frames per second with a resolution of 128x32 pixels. Camera light intensity was reduced to a manageable level by using a 32 f-stop and two ND filters in series resulting in a 2.5% light transmission.

### 3.2.3 Measuring Ignition

Ignition time was measure by the thermocouples and the high-speed imaging. TC1 could be used to roughly estimate the start of laser ablation ( $t_0$ ) and the point of ignition ( $t_{\text{ign.}}$ ) The difference between these two times can be used as an approximation of

ignition time considering the limiting factor to be the response time of TC1. In the same temperature acquisition, ignition temperatures can be estimated by TC1 and TC2 as the last reading prior to the vertical spike (shown in Figure 4.8).

The high-speed imaging can be used to determine ignition time based on a “first light” criteria considering the electromechanical delay in the shutter. The shutter and camera are triggered simultaneously using an electric relay switch, but the mechanical shutter servomotor has a consistent delay between the time of applied voltage and the time to completely open (clear laser path.) The shutter delay was measured by sending a visible red diode laser (used for aligning the CO<sub>2</sub> laser) through the same triggered shutter and recording the red dot’s first appearance with the high-speed camera at the same time resolution of 32kfps. The electro-mechanical delay was calculated as the time difference between time zero (actually triggering the shutter) and first view of the red diode laser.

#### *3.2.4 Measuring Flame Propagation*

Together the front and back thermocouples could be used to estimate two values of burn velocity. Knowing that each thermocouple is placed on two surfaces of a 3.5mm long pellet the burn velocity could be calculated based on the time difference between TC1 and TC2. The first thermocouple burn velocity estimate is based on the difference in time of ignition determined by an instantaneous positive slope change in the temperature history and second thermocouple burn velocity is determined by the time difference between TC1 and TC2 required to heat the thermocouple to an arbitrary temperature of 400°C (chosen significantly above the highest preheat oven temperature of 200°C).

The burn velocity is also estimated by the Phantom software using a given length reference (taken from a ruler at the focal length of the pellet) and time difference between sequential frames. For a planar burn the burn velocity could be easily measured as the flame advanced in small increments between frames.

### 3.3 Results

#### 3.3.1 Volumetric Preheating

The oven temperature was varied between ambient 20°C and 200°C and each sample was ignited with 50 W of laser power. For each data point three samples were burned corresponding measurements were averaged.

Figure 4.4 is the results of ignition time determined by the procedure outlined previously.

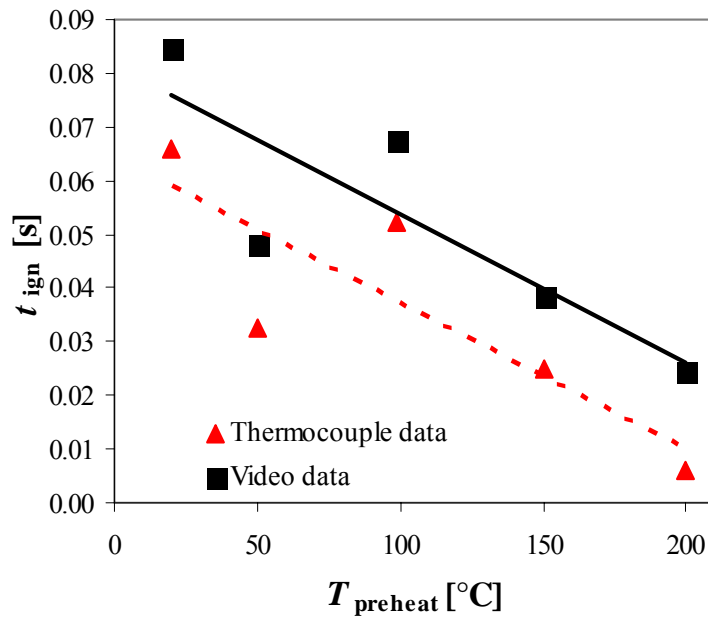


Figure 4.4: Ignition time as a function of preheat temperature  
40nm Al + MoO<sub>3</sub>

The ignition time shows a decreasing trend with preheat temperature because the sample will require less time of laser exposure (less laser energy) to raise the sample to a consistent ignition temperature (considered to be dependent only on sample constituents). The video estimates of ignition time drop from 0.085s to 0.024s for 20°C to 200°C preheat  $T$  respectively. The TC estimates of ignition time drop from 0.066s to 0.006s for 20°C to 200°C preheat  $T$  respectively.

Figure 4.5 displays the significant temperature magnitudes as a function of preheat temperature. The flame temperature is recorded as the maximum valid temperature



(some thermocouples broke during the experiment creating unrealistic magnitudes of noise oscillation) from the recorded temperature history (Figure 4.8). The lower two curves show the ignition temperatures ( $T_{\text{ign}}$ ) estimated by the front (TC1) and back (TC2) thermocouples.

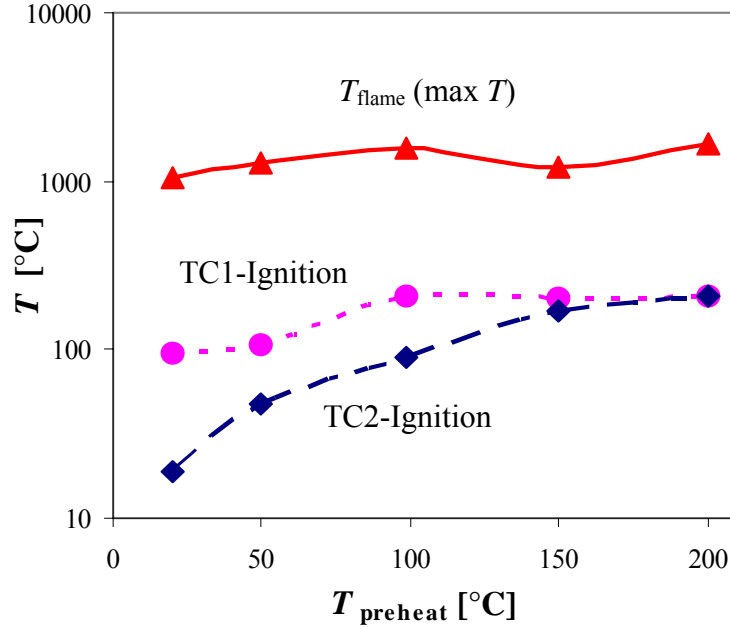


Figure 4.5: Temperature as a function of preheat temperature  
40nm Al + MoO<sub>3</sub>

The flame temperature ( $T_{\text{flame}}$ ) in Figure 4.5 varies from 1051°C to 1686°C for 20°C and 200°C preheat  $T$  respectively. The accuracy of  $T_{\text{ign}}$  is significantly affected by the response time of the thermocouple bead. Heating is rapid and transient event, with a 50W laser power. For longer ignition times ( $> 0.05\text{s}$ ) on the left side of Figure 4.5, TC1 does respond to the temperature change. On the right side of Figure 4.5, the ignition time is significantly reduced ( $< 0.05\text{s}$ ) and TC1 does not have the responsiveness needed to accurately estimate ignition temperature.  $T_{\text{ign}}$  from TC2 is basically equivalent to the preheat  $T$  because the 50W laser power ignites the sample before conduction can elevate the temperature of the back surface.  $T_{\text{ign}}$  is estimated to be closer to 450°C based on DSC/TG results shown in Chapter VII or 300°C at faster heating rates in Chapter VIII (Figure 8.5).

Figure 4.6 shows the propagation velocities estimated by the three methods discussed earlier. All three curves show a significant increase in burn velocity with increasing preheat  $T$ . Video estimates of burn velocity increase from 21.5m/s at 20°C preheat  $T$  to 61.6m/s at 200°C preheat  $T$ . Similarly the thermocouple slope criteria burn velocities increase from 0.965m/s to 11.0m/s and the thermocouple  $T_{400}$  criteria burn velocities increase from 189mm/s to 2.95m/s.

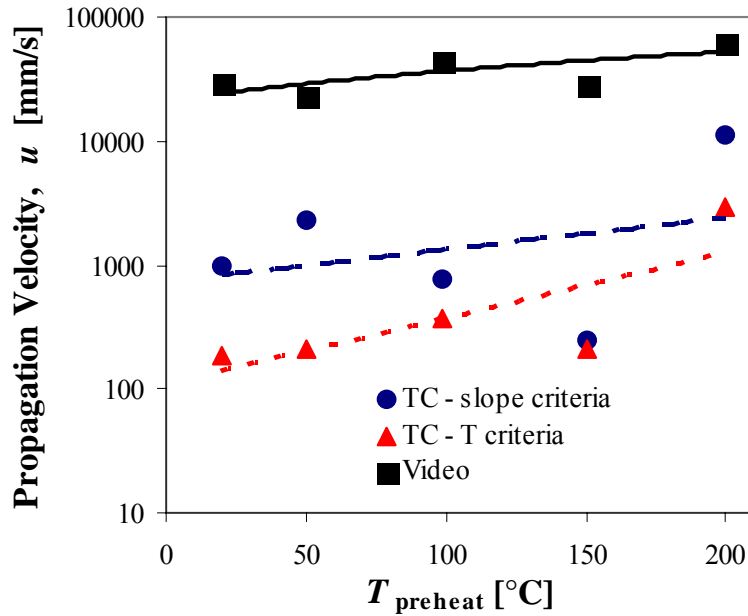


Figure 4.6: Propagation velocity as a function of preheat temperature  
40nm Al + MoO<sub>3</sub>

The data shown in Figure 4.2 was determined using high speed video only. Figure 4.7 shows the high speed video propagation velocity (or flame speed) recorded for volumetrically preheated samples (data from Figure 4.6) plotted with the original high-speed video data set (Figure 4.2). Figure 4.7 shows that the preheated nanocomposite pellet samples can in fact achieve flame speeds much higher than the micron samples with adjusted initial conditions. Note that the left video data point from Figure 4.6 corresponds to 40nm composite ignited at ambient temperature 22°C. The 40nm-Al is actual produced by Nanotechnologies and the bulk composite density is 52% TMD. The 39.2nm nanocomposite tested in the original data was at ambient initial temperature, the 39.2nm-Al is produced by Technanogies and the bulk composite density is only 38%

TMD. For the same initial conditions and laser power, the Al quality and morphology based on manufacturing processes and the bulk sample density may account for the dramatic differences in the nanocomposite burn rates.

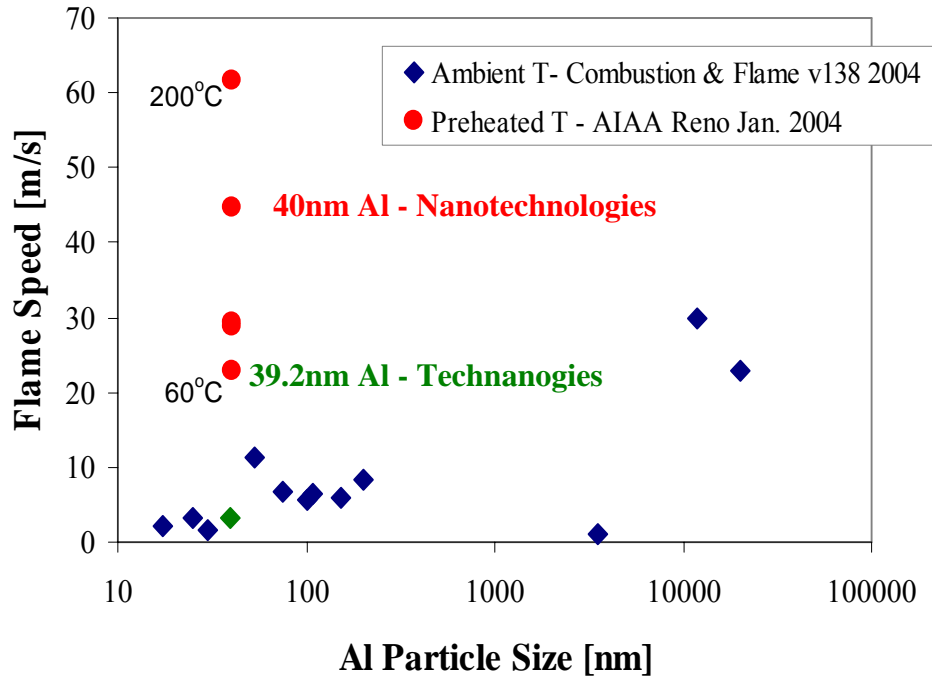


Figure 4.7: Volumetrically preheated nanocomposite flame speed plotted with ambient initial state nano and micron composite data

### 3.3.2 Variable Laser Power

Similar to the volumetric preheating, the pre-ignition energy state of the sample was altered using variable laser power. The goal is to slow down the front surface-heating rate such that heat can conduct axially through the pellet. For a higher laser power like 60 W, the front surface should rapidly rise to  $T_{\text{ign}}$  leaving the back plane at ambient temperature and the very large temperature gradient within the first few microns of pellet length. For a lower laser power like 10W, the front surface should slowly heat to or  $T_{\text{ign}}$  while also conducting heat axially towards the back of the pellet allowing a less drastic temperature gradient stretched over the entire pellet length.

Each sample was mounted identical to the procedure before. The pressed pellet was placed in spring tension between two small bead C thermocouples inside the brick oven (to allow comparative influences from any pressure build up inside the oven chamber). The oven was left off and the oven chamber was allowed to cool to ambient 20°C between sample burns (although unneeded because the sample energy release rate is so fast there is no lasting surrounding temperature effects.) Three samples were ignited with laser powers between 10W and 60W and the respective measurements were averaged for each data point.

Figure 4.8 illustrates the heat up and ignition of two recorded temperature histories for a 40W and 10W laser power. TC1 is the larger magnitude curve in both figures and it is obvious that TC1 has much more temperature response for the 10W laser power.

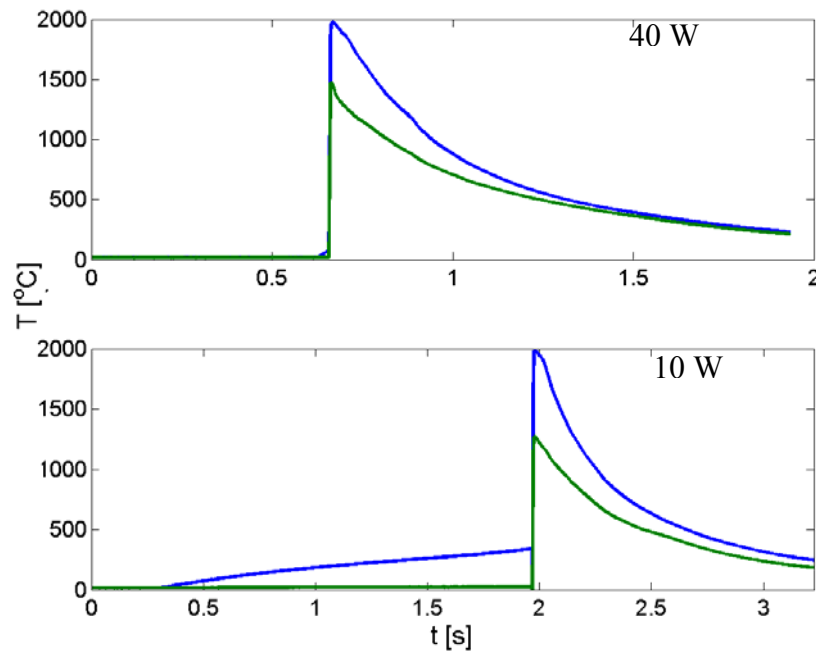


Figure 4.8: Temperature histories for 40 and 10W laser powers

Figure 4.9 is a zoomed in image of the ignition interval for the 40W laser power shown in Figure 4.8. Figure 4.9 shows the positive slope inflection point used for estimating ignition time and burn velocity and the  $T_{400}$  temperature criteria used for

estimating burn velocity. Figure 4.8 shows a sudden drop of 50°C in TC1 prior to the positive slope inflection. This temperature drop is due to the thermocouple being thrown from the pellet surface by the expanding gases from the reaction as witnessed in some high-speed videos. This fact would infer that ignition occurred at the negative slope inflection point. Since the thermocouple was not always thrown, a simple MATLAB program was written to detect the positive slope change for objectivity. For this discrepancy, the second burn velocity based on the time to reach 400°C was created to check the accuracy.

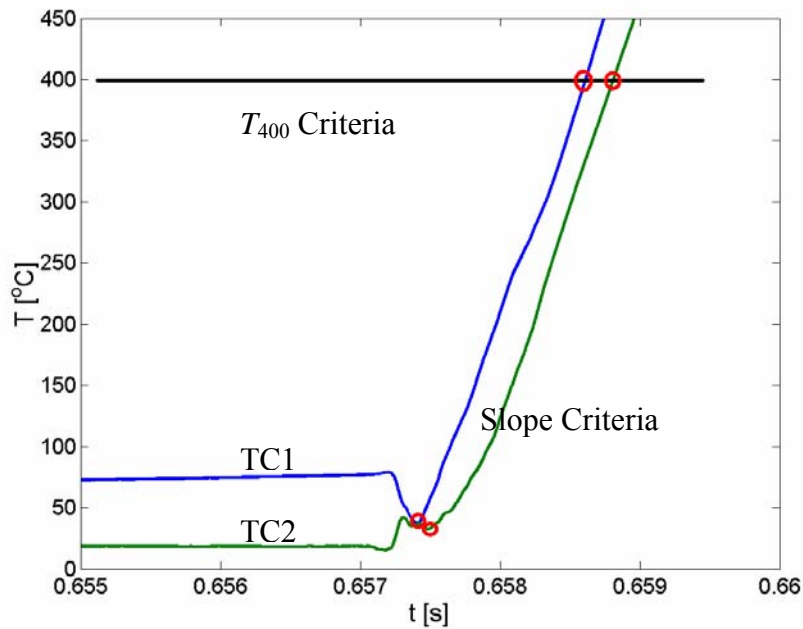


Figure 4.9: Magnified temperature history of 40W laser power *Ignition Zone*.

Figure 4.10 shows the ignition time delay results as a function of laser power. This is a much more exponentially increasing trend than Figure 4.4. Both video and TC measurements of ignition time closely matched varying from 1.54, 0.25, 0.06, and 0.03s for 10, 20, 30 and 60W respectively.

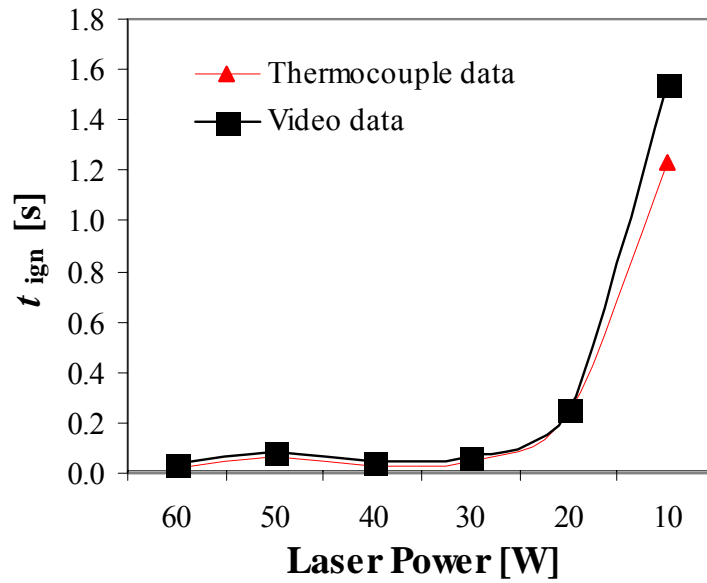


Figure 4.10: Ignition time as a function of laser power  
40nm Al + MoO<sub>3</sub>

Comparative to Figure 4.5, Figure 4.11 shows  $T_{\text{flame}}$  and  $T_{\text{ign}}$  for each laser power experiment. Flame temperatures vary from 1818°C to 1515°C for 10 to 60W respectively. Similar to Figure 4.5, the thermocouple ignition temperatures do not begin to vary until the ignition time interval becomes long enough for the thermocouples to respond. For instance, both TC1 and TC2 ignition temperatures (Figure 4.11) begin to increase once the ignition time in Figure 4.10 becomes larger than 0.06s at 30W.

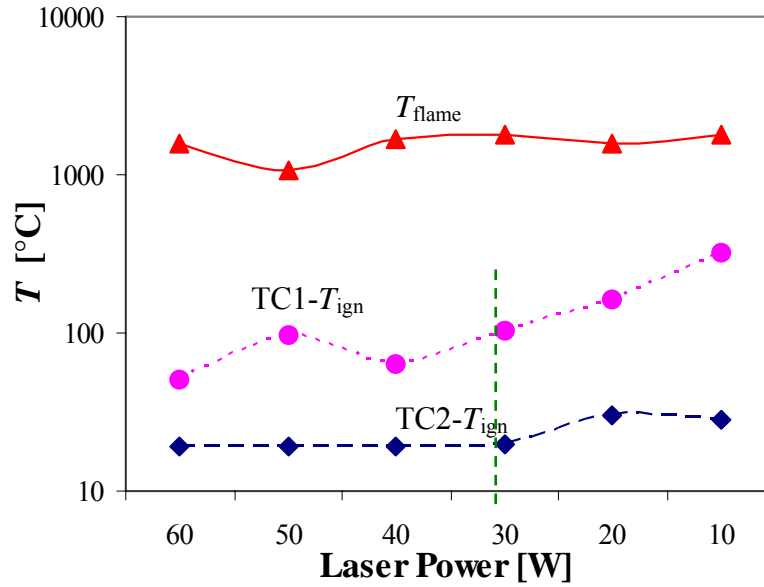


Figure 4.11: Flame and ignition temperatures as a function of laser power  
40nm Al + MoO<sub>3</sub>

Comparative to Figure 4.6, Figure 4.12 shows the propagation velocities estimated by the high-speed video and the thermocouples. The video burn velocities decrease from 44.9 to 20.1 m/s for 10 and 60W respectively. The thermocouple  $T_{400}$  criteria burn velocities decrease from 1808 to 634 mm/s for 10 and 60W respectively. The thermocouple slope criteria burn velocities inconsistently range from 3615 mm/s at 60W to 1809 mm/s at 10W with an average of 1676 mm/s across all laser powers.

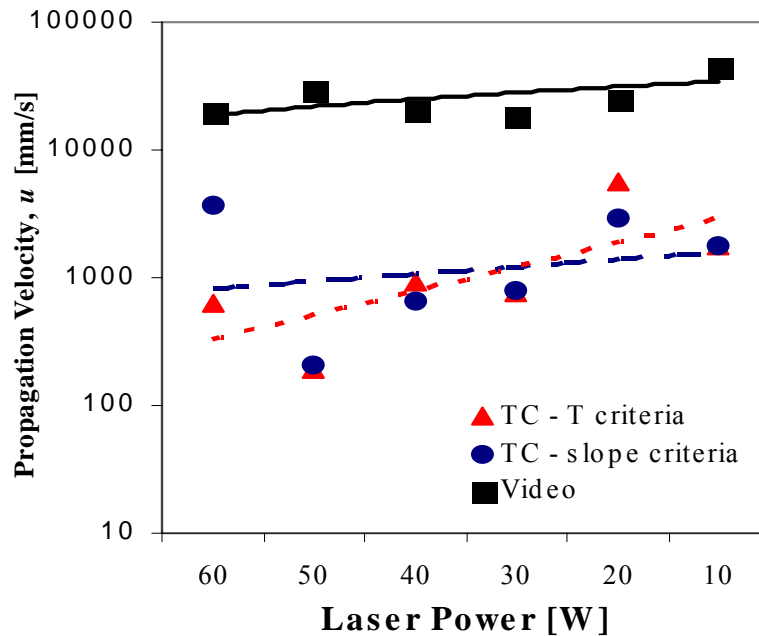


Figure 4.12: Propagation velocity as a function of laser power  
40nm Al + MoO<sub>3</sub>

The data shown in Figure 4.2 was determined using high speed video only. Figure 4.13 shows the high speed video propagation velocity (or flame speed) recorded for the laser preheated samples (data from Figure 4.12) plotted with the original high-speed video data set (Figure 4.2). Figure 4.13 shows that the laser preheated nanocomposite pellet samples can in fact achieve flame speeds with the same magnitude as the laser preheated micron samples. Note that the 50W video data point from Figure 4.12 corresponds to 40nm composite ignited at ambient temperature 22°C. The 40nm-Al is actual produced by Nanotechnologies and the bulk composite density is 52% TMD. The original 39.2nm nanocomposite tested at ambient initial temperature ignited by 50W laser power. The 39.2nm-Al is produced by Technanogies and the bulk composite density is only 38% TMD. For the same initial conditions and laser power, the Al quality and morphology based on manufacturing processes and the bulk sample density may account for the dramatic differences in the nanocomposite burn rates.



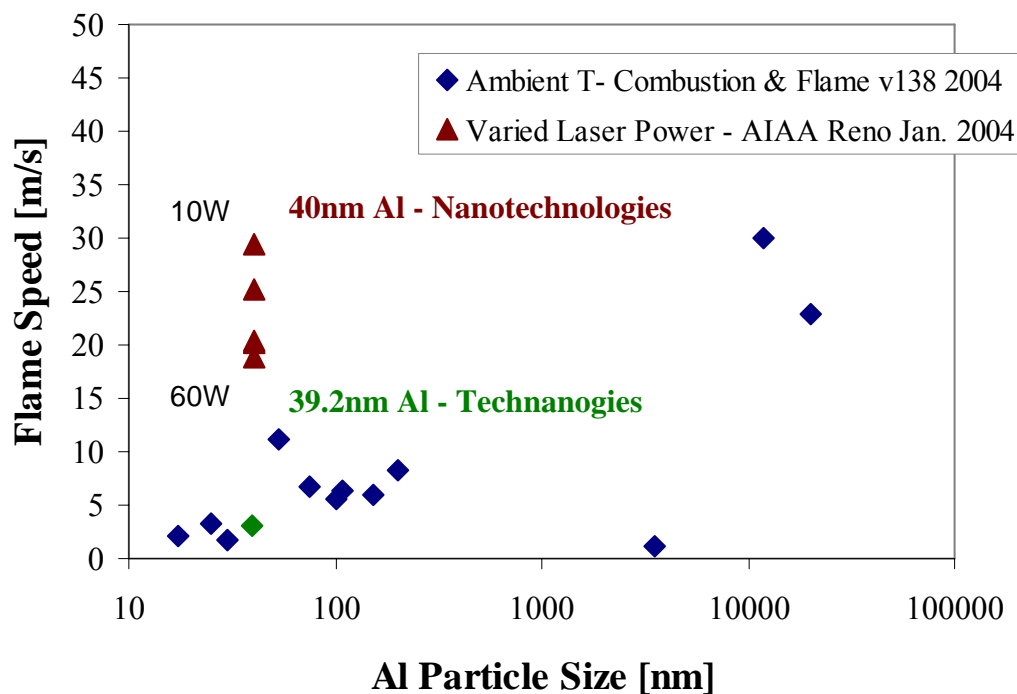


Figure 4.13: Laser preheated nanocomposite flame speed plotted with ambient initial state nano and micron composite data

### 3.4 Discussion

It has been shown that the ignition time delay decreases and the burn velocities increase with an elevated initial sample energy state. Whether the sample is volumetrically preheated to an elevated temperature or allowed to preheat itself through varied laser power, the flame propagates through the sample at a faster rate than previous experiments.

The  $T_{\text{ign}}$  of 317°C shown in Figure 4.11 for TC1 at 10W compares relatively well with the lower melting temperature of nm-Al shown by the Eq. 1.2 [65] and DSC results (see Chapter VII and VIII). Figure 4.6 shows that when the sample is already at an elevated energy state ( $E_o$ ), then less laser energy is required to elevate the sample to an ignition energy state ( $E_{\text{ign}}$ ). The flame propagation speed is determined by how fast the reaction energy ( $E_{\text{rxn}}$ ) can raise the energy of surrounding zones to  $E_{\text{ign}}$ . Thus, if the

difference between  $E_o$  and  $E_{ign}$  is small throughout the pellet then the  $E_{rxn}$  will compensate this difference faster and create a faster burn velocity.

After the 8min. of steady state oven preheating, it is assumed that the temperature gradients within the samples are insignificant in magnitude compared to the reaction temperatures. It can be shown that for each volumetric preheating TC1 and TC2 read within 4°C of each other prior to laser exposure. Other work with a thermocouple placed on top of the horizontal pellet (as to not be thrown off by horizontally flowing gases) has shown that the reaction temperatures can reach as high as 4000°C [23]. Adversely, Figure 4.11 shows that there are temperature gradients as large as 300°C at the lowest 10W laser power. This implies by the parabolic nature of Fourier conduction, that the initial temperature just prior to ignition is obviously not constant throughout the axial length of the sample. If the temperature steadily decreases as the reaction zone moves towards the back of the sample this provides an impedance to the flame propagation. This also suggests that the flame propagation is not constant along the axial length or that the flame should be decelerating. This deceleration is obviously not measured by either thermocouples but rather an average of the front pellet burn and the back pellet burn velocity. Even the high-speed video is limited in measuring this deceleration due to the magnitude of the velocities. At the 32kfps, only 8-12 clear images are taken before the view is obscured by the opaque *smoke plume* or condensing product dust trapped within the oven.

The averaging of the decelerating flame velocity is recognized by the lower velocity magnitudes (measured with the video) seen in the 200°C preheat (61.6 m/s) versus the 10W laser power (44.9 m/s). Also velocity measurements by the thermocouple slope, show a magnitude of 11 m/s at 200°C preheat and drops to 1.8 m/s with the 10W laser power.

It is noted that the 20°C 50W experimental burn velocities presented in this work are much larger in magnitude than results presented in similar work [24]. Previous work studying 39.2nm Al+MoO<sub>3</sub> (from Technanogy) compressed pellets at a 1.2 equivalence ratio showed a burn velocity of 3.17 m/s compared to 29.5 m/s shown in this work by 40nm-Al from Nanotechnology. As noted in the introduction, the preheated

nanocomposites in this work display burn velocities similar to the “laser preheated” 10 and 20 $\mu\text{m}$  samples presented in [24].

Another reason for this order of magnitude difference is the stated Al concentrations the slower mixture (Technanogy Al) was provided at a stated purity of 57.5% Al, while the faster mixture (Nanotechnology) was provided at a stated purity of 72% Al. Although the pure Al concentration is accounted for in the fuel/oxidizer masses to achieve 1.2 equivalence ratio, the higher 72% Al concentration implies that there is a thinner (less volume and mass) layer of  $\text{Al}_2\text{O}_3$  than the 57.5 % Al for the same particle size. A thinner oxide layer may increase sensitivity and burn velocity.

A second explanation for the difference in velocity for similar particle sizes is the difference in pressure influences. The faster burn velocities shown in this work are burned in a relatively confined environment of the oven whereas past work was done on a open stand with only a few shields to protect the equipment. The oven was loosely constructed of stacked firebricks with inside dimensions of 4 x 4 x 8 in. or a volume of approximately 128 in<sup>3</sup>. Though is a large volume compared to the pellet size (0.027 in<sup>3</sup>), the rapid expansion of heated air and vaporized products produced significant acoustic intensities and often knocked out the glass window. The oven was not completely rigid nor confined due to cracks between bricks and holes for thermocouples and the  $\text{CO}_2$  laser beam so pressure issues were not expected. No measurements were made to quantify the pressurization within the oven.

### 3.5 Summary

At least three important contributions have been shown by this study.

1. Flame speeds of micron and nanocomposite are dependent on the initial reactant temperature. Data suggests that the flame speeds of the large  $\mu\text{m}$ -Al+ $\text{MoO}_3$  samples presented by [24] were inadvertently elevated due to laser preheating. Data also suggests that the flame speed of the nm-Al+ $\text{MoO}_3$  samples shown in this study can be elevated to the same magnitude by tuning the initial reactant temperature or the laser heating rate.
2. A useful characteristic of thermites is the tunable combustion behaviors by altering composite properties. Many applications strive for tunable energy production to achieve

specific goals. There are many parameters in composite thermites (such as composite stoichiometry [24], constituent particle size [24] and particle size distribution [41], oxidizer choice, surfactant coatings, composite powder fabrication techniques, bulk density, initial reactant temperature, reactant heating rate and many others) that have shown significant influence and control over the final combustion behaviors.

3. The use of thermocouples is not well suited to make accurate transient temperature measurements for the time scales associated with composite thermite reactions. Figures 4.4 and 4.6 both show that the thermocouple data lags behind the high-speed video data by as much as 46% (similar for data in Figures 4.10 and 4.12). For this reason, it is believed that temperature measurements shown in Figures 4.5 and 4.11 may not be an accurate representation of the actual achieved sample temperature. The thermocouple data is beneficial by means of confirming the trendlines from the high-speed video data.

Figure 4.12 shows an increase in flame speed for decreasing laser power. The 10W laser power is heating the samples slower than the 60W laser power thus creating higher reactant temperatures due to ignition delayed conduction and elevated flame velocities. Chapter VIII discusses the effect of heating rates on similar reactions tested in DSC experiments. For argon atmosphere DSC experiments, higher heating rates ( $\beta=40\text{Kpm}$ ) produce more violent and faster reactions than slow DSC heating rates ( $\beta=5\text{Kpm}$ ). This is contradicting to the data shown (Figure 4.12) by the fast heating of the 60W laser and the slow heating of the 10W laser. Though the two experiments are unique and observation suggests that reaction mechanisms are completely different, compiling the data and observations may appear similar to Figure 4.14. The trends are opposing for the DSC and laser experiments indicating a maximum in flame speed dependent on heating rate to ignition. The DSC heating produces non-self-propagating reactions uniformly until the single 40Kpm reaction displayed rapid self-sustaining combustion reaction. The data in Figure 4.12 shows a steadily decreasing reaction speed with increasing heating rate. Basically a critical heating rate may exist that produces a maximum self-sustaining propagation speed. Note that Figure 4.14 is only a prediction and not an exact representation of actual data. As mentioned earlier, the heating rate ( $^{\circ}\text{C/min}$ ) of the laser experiments could not be accurately obtained. The true flame propagation speed cannot

be obtained for the 40Kpm DSC reaction shown in Figure 8.5. Also note the crucial involvement of air in the laser experiments, versus argon in the DSC experiments which may render the two studies uncomparable.

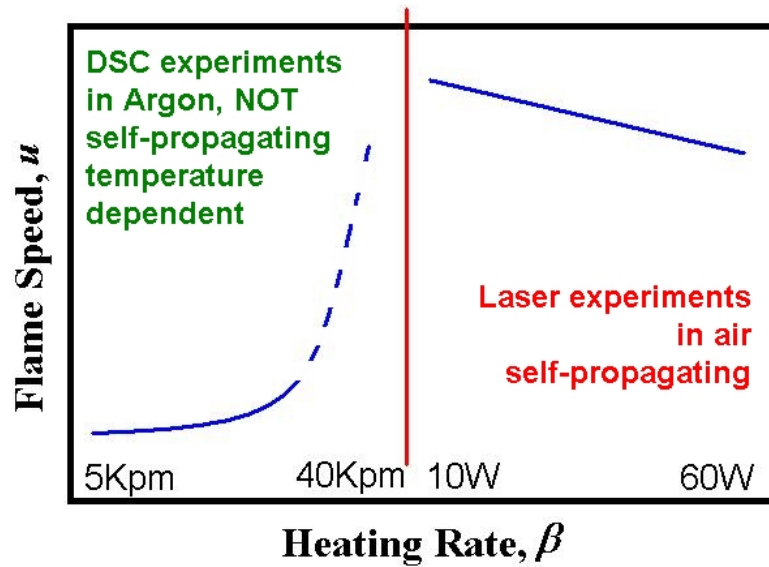


Figure 4.14: Estimated thermite propagation speeds for nanocomposite thermites tested by laser ignition and DSC heating

## CHAPTER V

### TG/DSC REACTION ANALYSIS

#### 5.1 Introduction

Every material is affected by temperature changes. Some changes are very slight such as thermal expansion or crystalline phase change and some changes are drastic such as melting and detonation. A TG/DSC device gives scientists the ability to precisely control the heating of a sample while measuring microgram mass changes and minute temperature changes which can be used to calculate energy absorption or production (alterations in enthalpy).

This chapter will describe the basic theory and application of a differential scanning calorimetry (DSC) and thermo-gravimetric (TG) device. Information will be presented on the basic design and thermodynamic concepts that allow a DSC to make accurate and calibrated enthalpy measurements. The reactions tested in this document are all solid powder samples; thus, techniques will be presented for setting up a TG/DSC experiment using a solid powder sample. All measurements are dependent on the gaseous environment inside the DSC/TG furnace and the crucible material.

Representative TG/DSC results will be present to outline a basic description of the data and the significant details used for analysis. Last, theory will be presented for chemical analysis using a first-order Arrhenius chemical kinetics equation. Two methods will be presented for calculating activation energies (defined in Chapter I) and pre-exponential factors based on DSC and TG data.

#### 5.2 Literature Review

Table 5.1 shows a brief list of studies using TGA, DSC and DTA devices for measuring various Al particle reactions. Table 5.2 shows a list authors theoretical and experimental determination of chemical kinetic parameters such as activation energy based on DSC data. All of the methods in Table 5.2 are designed for improved accuracy for specific types of chemical reactions. The Arrhenius analysis and Kissinger method are the most common and used for chemical analysis presented in this work.

Table 5.1.1: Literature Review of DSC/TG Thermal Analysis of Thermite/Al Oxidation Reactions

Author(s)/Date	Samples	Analysis	Results or Cited Data
Bulian, Kerr, & Puszynski (2004) [8]	nm Al + MoO <sub>3</sub> , WO <sub>3</sub> , CuO, Bi <sub>2</sub> O <sub>3</sub>	DSC (in air and argon)	Ignition temperatures for 4 metal oxides in both air and argon, affinity for reaction with air versus solid oxidizer
Eisenreich, Weiser, Fietzek, Juez-Lorenzo, Kolarik & Koleczko (2004) [17]	Al+Air	TGA	Two stage mass increments at temperatures 380-630°C and above 680°C. Kinetic reaction: $E_a = 23.9$ kJ/mol, $\log Z = 11.9$ , Diffusion reaction: $E_a = 24.2$ kJ/mol, $\log Z = 4.3$
Il'in, Popenko, Gromov, Shamina & Tikhonov (2003) [29][30]	Al (UFAP $\approx$ 0.1 $\mu$ m) + Air	DTA	Comparing agglomerated and un-agglomerated nano-Al, $T_{onset}$ of oxidation, maximum oxidation rate, degree of conversion of Al, and reduced thermal effect
Jones, R. Turcotte, Fouchard, Kwok, A.M. Turcotte & Qader (2003) [32]	Al (UFAP $\approx$ 0.1 $\mu$ m) + Air	DSC & TG/DTA	DSC $T_{onset}$ between 378 and 460°C and $\Delta H$ of reaction between 1.6 and 5.5 kJ/g
Jones, Turcotte, Kwok & Vachon (2003) [33]	Al (17-85nm) + Air/Ar/H <sub>2</sub> O	DSC & TG/DTA	$T_{onset}$ between 353 and 462°C, $\Delta H$ of reaction between 1.6 and 5.5 kJ/g, two stage mass gain with maximums of 39 and 37% respectively, pressure and atmosphere effects on oxidation mass
Revesz, Lendvai, & Ungar (2000) [50]	< 100 nm Al (ball milled)	DSC	Al melting point as a function of milling time ranging from 45 min to 32 days (grain sizes from 30-100nm), determination of determination of specific interface energies ( $\sigma_{s,i}$ ) from Wronski
Shevchenko, Kononenko, Latosh, Bulatov, Lukin, Saksonova, Dobrinskii, Malashin, & Gostyukov (1991) [55]	0.58 m <sup>2</sup> /g ASD-4 6.76 m <sup>2</sup> /g UDA	Programmed heating oxidation	Oxidation increase between 830-930K caused by cracking and reduction in protective properties of the oxide layer from volumetric expansion
Suvaci, Simkovich, & Messing (2000) [59]	1.2, 14.4, 20.2 m <sup>2</sup> /g (attrition milled) Al+Air	TGA	Critical temperature indicating transition between linear and parabolic oxide growth. Radial growth rates of $2.3$ to $9.2 \times 10^{-11}$ cm/s, $E_a$ for solid state oxidation between 112 and 152 kJ/mol

Author(s)/Date	Samples	Analysis	Results or Cited Data
Trunov, Schoentiz, & Dreizin (2003) [61]	Al+Mg	DTA/TG –filament ignition	TGA oxidation onset (750°C) determined $E_a$ of 215 kJ/mol by Kissinger method
Trunov, Schoentiz, Zhu, & Dreizin (2004) [62]	Al+O <sub>2</sub>	DTA/TGA	Oxidation below 550°C, $T_{\text{ign}}$ versus particle size literature review



Table .5.2: Literature Review of DSC Kinetic Parameter Studies

Author(s)/Date	Base Equation(s)	Analysis Description
Arrhenius (1889) [36]	$\frac{d\alpha}{dt} = k(T) \cdot f(\alpha)$ $k(T) = A \exp\left(\frac{-E_a}{RT}\right)$	General description of specific rate constant $k$ as a function of temperature [first introduction of Boltzmann factor] [Kuo]
Boswell (1980)	same as Kissinger ( $s=1, A=1$ ) [Starink [58]	
Flynn, Wall (1966) [20]	$\log \beta = \log \frac{AE_a}{g(\alpha)R} - 2.315 - \frac{0.457E_a}{RT}$	is the integral function of conversion. Equation does not require knowledge of reaction order ( $s$ ).
Freeman, Carroll (1958) [21]	$\frac{\Delta \ln d\alpha/dt}{\Delta \ln(1-\alpha)} = -\frac{E_a}{R} \cdot \frac{\frac{1}{T} - \frac{1}{T_0}}{\Delta \ln(1-\alpha)} + n$	
Friedman (1964) [22]		
Kissinger (1957) [34]	$\ln\left(\frac{\beta}{T_w^s}\right) = -A \frac{E_a}{RT} + f(Z)$	Equation based on peak DSC temperature corresponding to maximum species conversion rate. Parameters $s$ and $A$ are determined based on equating conversion rate equation to zero ( $s=2, A=1$ ).
Ozawa (1965) [46]	$\log \beta = -0.4567 \frac{E_a}{RT} + \left[ \log\left(\frac{AE_a}{RT}\right) - \log f(\alpha) - 2.315 \right]$	According to Starink [Ref] equation is same as Kissinger with ( $s=0, A=1.0518$ )
Starink (1996) [58]	same as Kissinger $s=1.8$ $A=1.0070-1.2 \times 10^{-5} \cdot E_a$ [ $E_a$ in kJ/mol]	Error analysis of Kissinger, Boswell and Ozawa isoconversion methods for determining $E_a$ . Derivation of new $s$ and $A$ constants based on

### 5.3 Theory of a Heat Flux DSC

Thermal analysis measurements were made using a simultaneous TG /DSC (thermo-gravimetric / differential scanning calorimetry) apparatus (Netzsch model STA 409PC/4/H/CO *Luxx*). Measurements were made in a flowing argon and oxygen atmospheres and the furnace provided a measuring temperature range between ambient (22°C) and 1450°C.

The goal of a TG device is to measure the mass (mass change) as a function of temperature. This simple measurement (in principle) can be used to trace the degradation of materials, determine reaction kinetics, study gaseous oxidation and reduction and many other applications. Many thermal changes in materials (i.e. phase transitions) do not involve a mass change and are not suitable for TG experiments. A DSC or DTA measures the temperature difference between an inert reference and a sample of interest as a function of temperature. Peak or valley enthalpy curves are determined from the DSC micro-voltage signal when the sample undergoes a chemical and/or physical change. The process is routinely applied in studies such as substance identification, phase diagrams, thermal stability, purity and reactivity.

DSC, differs fundamentally from DTA in that the sample and reference are both maintained at the temperature predetermined by the programmer even during a thermal event in the sample. Thus, if a change in temperature is detected between the sample and the reference, the input power to the sample is changed to equilibrate the temperature. In this way one can quantitatively determine the heat input (output) to (from) the sample during a reaction.

The rate of energy absorption by the sample (i.e. millicalories/sec) is proportional to the specific heat of the sample because the specific heat at any temperature determines the amount of energy necessary to change the sample temperature by a given amount. Any transition accompanied by a change in specific heat produces a discontinuity in the power signal, and exothermic or endothermic enthalpy changes display as peaks whose areas are proportional to the total enthalpy change. The basic principle is to compare the heat flow to the sample and inert reference which are heated at the same rate in the same environment. This is done by measuring the micro-volt difference in two thermocouples

placed in series in good thermal contact with the bottom of the sample and reference crucibles (Figure 5.1).

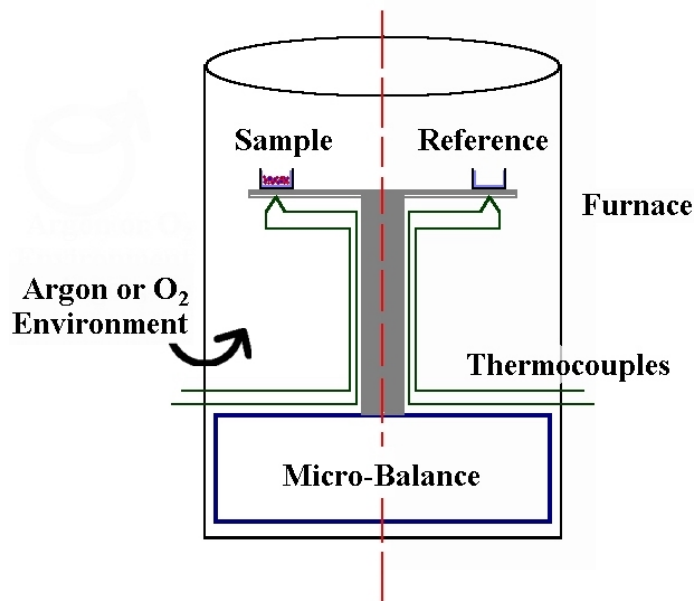


Figure 5.1 DTA/DSC thermocouple diagram

The accuracy of any DTA/DSC measurement is directly related to the sample-crucible-thermocouple thermal contact, stability and repeatability of the heating program, and the sensitivity of the temperature sensors. Many of these factors are addressed in the following section.

#### 5.4 Instrument and Sample Preparation

The balance, furnace and sample carrier of the DSC are shown in Figure 5.2 [44]. The system was first evacuated with a diaphragm pump (KNF model N 813.3 ANE) and then evacuated to  $< 2 \times 10^{-4}$  mbar with turbomolecular drag pump (Pfeiffer model TMU 071 P) both through port 4 shown in Figure 5.2 [44]. The system was filled with standard grade argon gas (99.9993% purity) or oxygen gas until reaching atmospheric pressure and the top valve (port 1) was opened to allow a constant flow of purge gas through the sample chamber. A 20 mL/min and 10 mL/min flow were set through ports 2 and 3 (Figure 5.2 [44]) for the balance protection and sample purge.

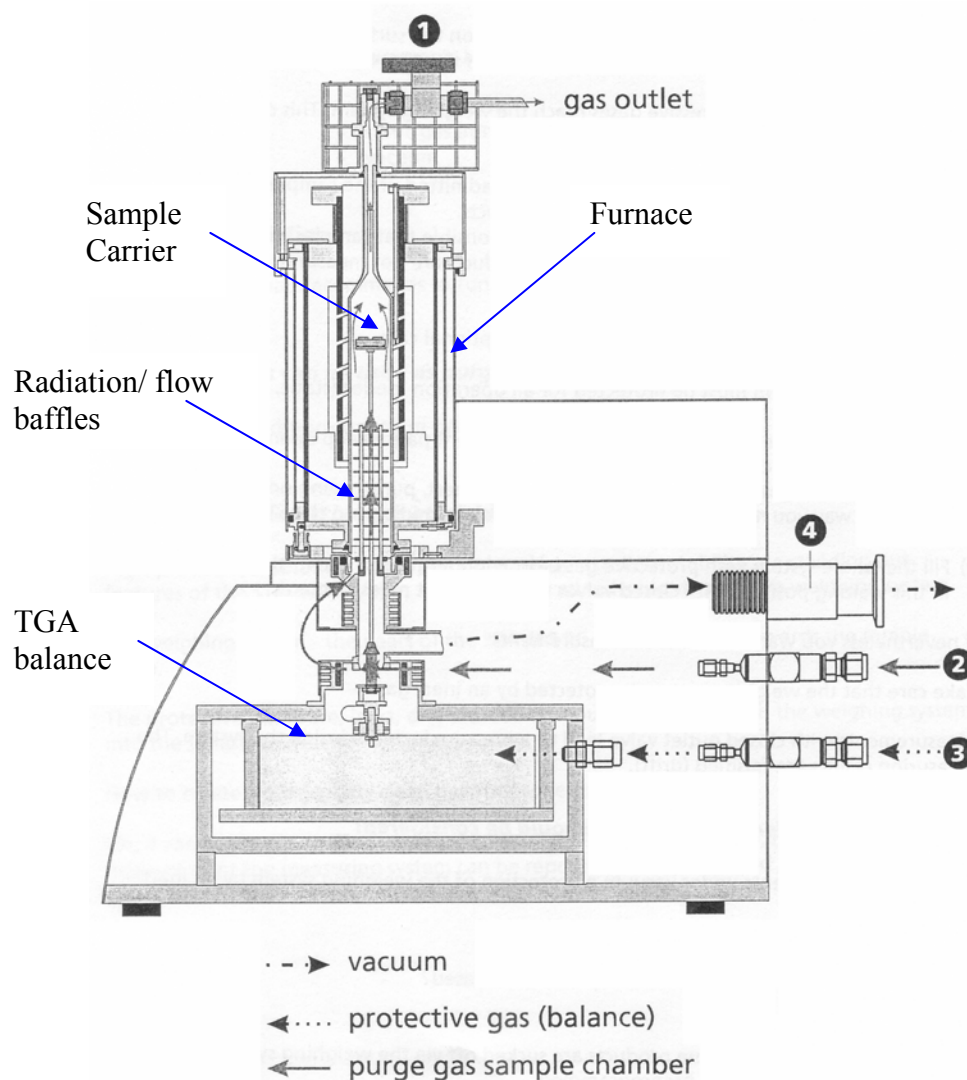


Figure 5.2: TG-DTA/DSC instrument diagram [44]

A series of aluminum-oxide (alumina) plates were inserted at the base of the sample carrier to prevent radiation effects on the balance and to create a homogeneous gas flow through the furnace (also shown in Figure 5.3 [44]). A platinum sample carrier and platinum crucibles were used to allow temperature measurements in the higher temperature range without radiation effects. Alumina carriers (typically used for lower financial expense) become semi-transparent at higher temperatures which effect the baseline calibrations. Four thermocouple wires are fed through the ceramic capillary tube and welded to a thin platinum plate beneath each crucible. A dual platinum ring was

firmly mounted at the top the carriers to ensure concentric alignment with the thermocouple junction and repetitive orientation within the furnace.

An alumina liner was inserted into the platinum crucibles since platinum is reactive with many metals at elevated temperatures. The liner and platinum crucible were custom made to tightly fit and provide better thermal contact with the thermocouple beneath the crucible. A thin platinum lid with a small hole to prevent gas pressure build up was used to improve heat containment.

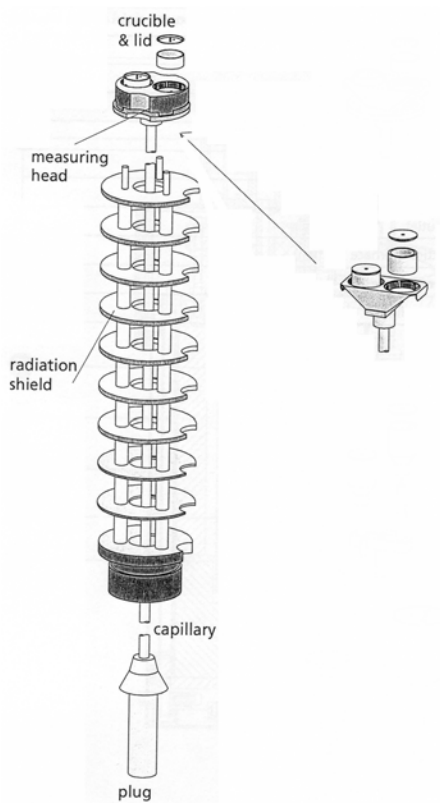


Figure 5.3: Sample carrier showing sample and reference crucibles [44]

A heating cycle is programmed into the operating computer and a control system monitors and adjusts the furnace power to control sample and reference temperatures. Three types of “calibration” were performed specific to each crucible and heating rate. The first is a baseline correction generated for each set of crucibles and heating rate. The baseline correction is generated by running a specific heating program with an empty sample and reference crucible. This curve value is subtracted from the true sample DSC

curve as electric noise and thermal drift in the instrument. The second is temperature calibration generated for each sample carrier (one carrier is typically used for hundreds of DSC experiments) which is specific to the thermocouples of the sample carrier. For this work, the temperature calibration was done using the onset melt temperature of a series of metal standards. The third is a sensitivity calibration generated for each crucible and heating rate. The sensitivity calculations calibrated the DSC voltages to enthalpy values using a standard sapphire sample with known specific heat as a function of temperature. The DSC instrument used in this work is not the typical DSC as discussed on page 73 in using a variable power input to the sample to determine enthalpy, but the enthalpy of the sample is calculated directly from calibration and thermocouple data. Further information on the calibration methods is provided in Appendices C and D.

#### *5.4.1 Sample Properties*

One goal is to analyze the effect of particle size on the reactivity of spherical Al particles and Al+MoO<sub>3</sub> thermite composites. Reactivity is a general term to describe unique ignition sensitivity, rate of reaction, exothermic energy production and many other combustion behaviors. Aluminum powder samples were prepared and reacted in O<sub>2</sub> for 50nm, 1-3μm, 4.5-7μm and 20μm Al (see Table 5.3) particle diameters. Composite thermite powder mixtures were made of spherical Al and nano-crystalline MoO<sub>3</sub>. Approximately one gram of thermite powder was prepared for eight average Al particle sizes listed in Table 5.3). In Table 5.3, the “Product Size” and “Purity” values are quantities provided by the manufacturer. The average product diameter of the nm-Al samples is a rounded classification of the “Calculated Diameter” determined from the experimental specific surface area (BET data) also provided by the manufacturer. The “Calculated Diameter” of the μm-Al samples is simply an average of the quoted particle size range. The “Calculated Oxide Thickness” was derived based on the average particle diameter and Al concentration.

Table 5.3: Thermite Composite Reactants used in DSC analysis

Material	Product Size		Manufacturer	Purity [%]	BET [m <sup>2</sup> /g]	Calculated Diameter		Calculated Oxide Thickness	
Aluminum									
	50	nm	Nanotechnologies	75.0	39.9	51	nm	1.69	nm
	80	nm	Nanotechnologies	84.0	25.3	83 +/- 4%	nm	1.63	nm
	120	nm	Nanotechnologies	81-82	17.4-18.4	120.00	nm	2.87	nm
	1-3	μm	Atlantic Equipment Engineers (AEE)	99.9		2	μm	0.23	nm
	3-4	μm	Alfa Aesar	98.5		3.5	μm	6.17	nm
	4.5-7	μm	Alfa Aesar	98.5		5.75	μm	10.13	nm
	10-14	μm	Alfa Aesar	98.5		12	μm	21.14	nm
	20	μm	Sigma Aldrich	99.9		20	μm	2.33	nm
Molybdenum Trioxide									
			Climax	99.9	64				

All of the thermite reactants were mixed at a slightly fuel rich stoichiometry ( $\phi=1.2$ ), sonicated in hexane solution and then the hexane evaporated for 15 minutes on a 60-70°C hotplate. The powders were not sieved after drying.

The platinum-alumina crucibles measured 6 mm internal diameter and 2.3 mm deep. This crucible volume allowed for approximately 16 mg of nanocomposite loose powder sample. For the series of experiments shown in Chapter VI, the sample mass for all of the Al powder (nano and micron) was kept between 4 and 6 mg. For the series of experiments shown in Chapters VII and VIII, the sample mass for all of the thermite mixtures (nano and micron) was kept between 13.2 and 15.3mg. Each specific mass was input prior to the experiment to allow a mass normalization of enthalpy calculations (this mass is also adjusted and tared by the TGA for enthalpies during mass loss or gain).

After each sample was tested, the crucible was removed from the sample carrier and cleaned. The solid products were scratched out of the alumina liner with a needle or metal probe and stored for SEM analysis. The platinum-alumina crucible was then placed in a 10% NaOH solution to generate bubble agitation by reacting with any remaining aluminum. After settling, the platinum-alumina crucible was rinsed with distilled water and placed in a sonic bath of distilled water for 3-5 minutes. The platinum-alumina crucible was loosely dried and placed on 200°C hotplate and the remaining water was baked off. The heating process would usually cause the alumina liner to unseat itself. The liner and platinum crucible were inspected for flaws and then

repeated. The alumina liners are very thin and fragile and would only survive approximately 8 to 10 sonication periods before cracking and being replaced. Many of the  $\mu\text{m-Al}+\text{O}_2$  reactions allowed the Al to melt into the crucible pores and the product  $\text{Al}_2\text{O}_3$  would be permanently bonded inside the crucible rendering the crucibles uncleanable and non-reusable.

### 5.5 Representative TG/DSC results

Figure 5.4 is TG/DSC data from the Al and  $\text{MoO}_3$  reactants tested separately. Figure 5.4 displays the endothermic melt (left solid line valley) of a 17 mg sample of 120 nm-Al. Figure 5.4 also displays the endothermic sublimation (right solid line valley) of a 12.2 mg sample of the nano-scale  $\text{MoO}_3$  with a subsequent mass loss from the sublimed gas leaving the crucible. Figure 5.4 shows how the endothermic (exothermic) valley (peak) onset temperatures are calculated based on intersection of tangential lines. As expected the 120 nm-Al shows an onset temperature of  $644.8^\circ\text{C}$  (compared to ASTM value of  $660.3^\circ\text{C}$  [39]), peaks at  $671^\circ\text{C}$  and then returns to the baseline with no mass change. The  $\text{MoO}_3$  shows an onset temperature of  $783.6^\circ\text{C}$ .  $\text{MoO}_3$  begins to sublime at  $700^\circ\text{C}$  and melts at  $795^\circ\text{C}$  [42]. This data is supported by Figure 5.4, by the DSC curve begin to fall beneath a flat baseline at  $700^\circ\text{C}$  as the sample is gradually sublimed and the mass is reduced, dropping the sample heat capacity and heat flow signal.



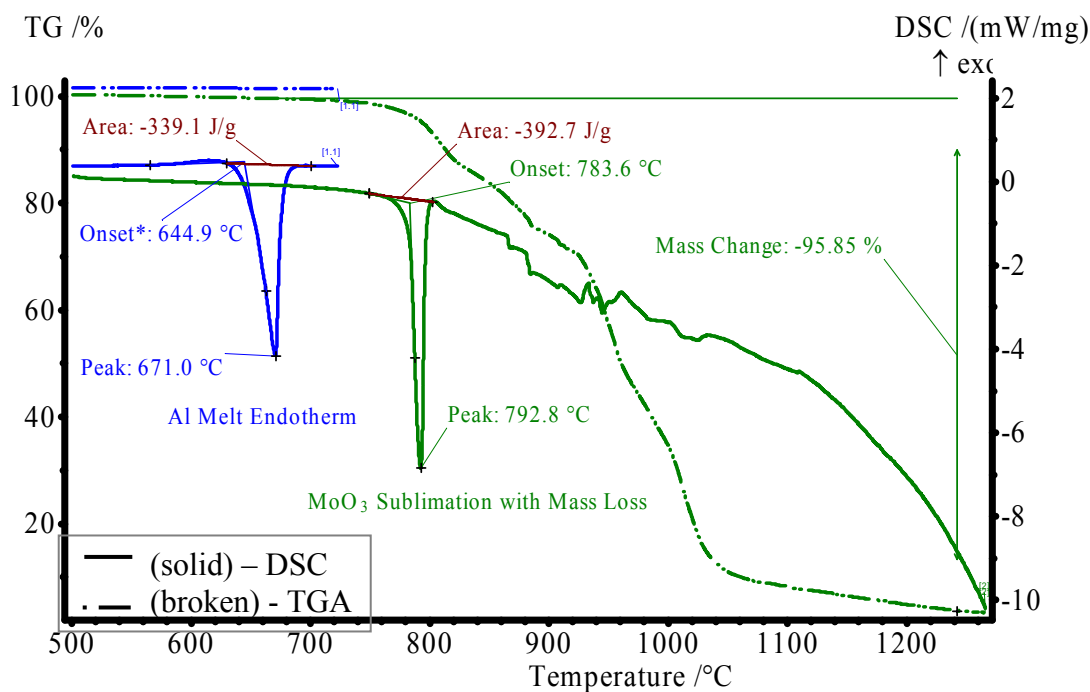
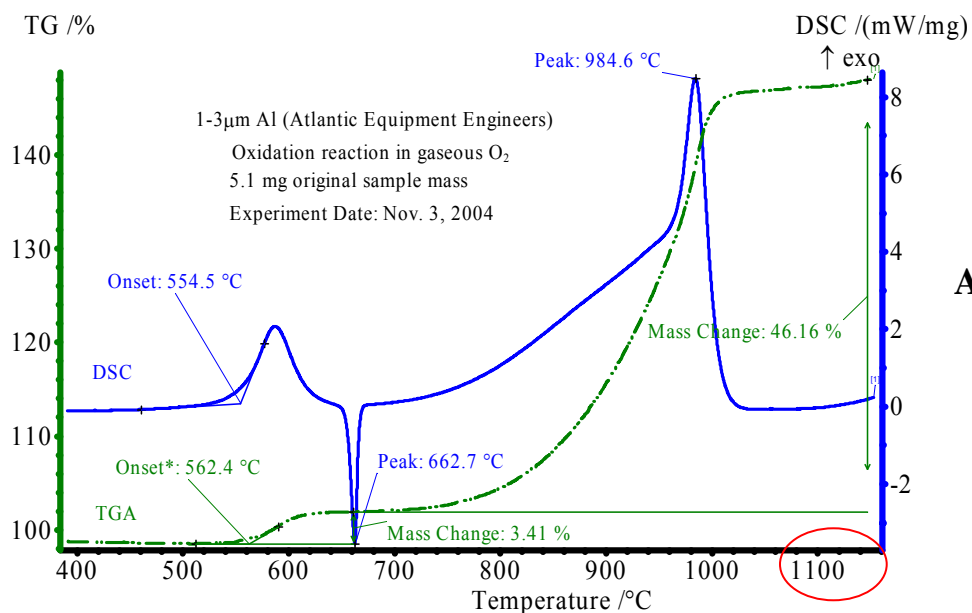
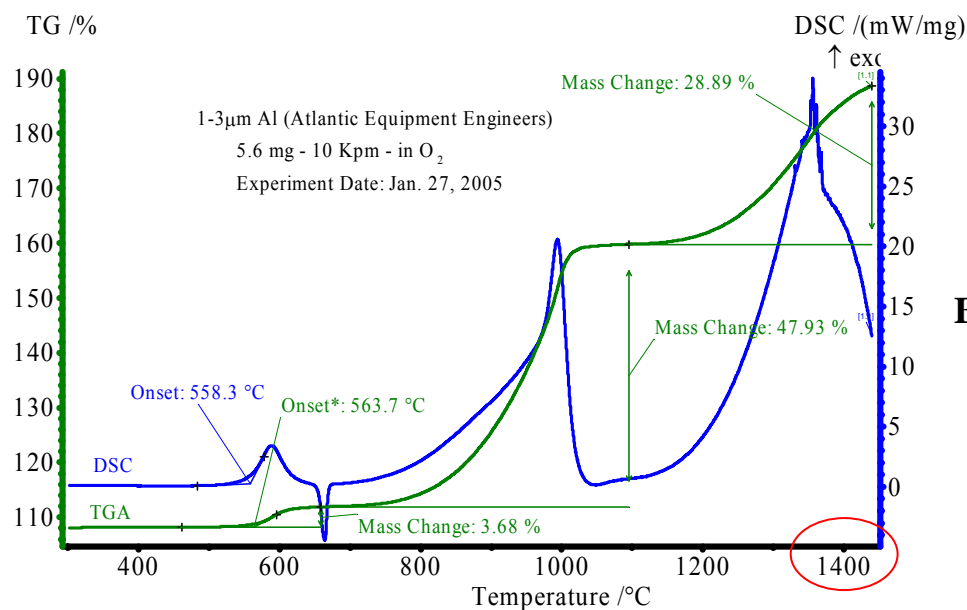


Figure 5.4: TG/DSC curves of 120 nm Al melt and MoO<sub>3</sub> Sublimation (both at 10 Kpm)

Figure 5.5 shows two TG/DSC data sets of Al oxidation in an O<sub>2</sub> environment during a heating program. Figure 5.5A shows a 1-3  $\mu\text{m}$ -Al+MoO<sub>3</sub> tested in November of 2004 and Figure 5.5B shows a 1-3  $\mu\text{m}$ -Al+MoO<sub>3</sub> tested in January of 2005. The DSC onset temperatures are fairly close as 554.5°C and 558.3°C for A and B respectively. The TGA onset temperatures are also similar as 562.4°C and 563.7°C for A and B respectively. The main difference to note is the user define equilibrium point for stopping the temperature program. Figure 5.5A shows a two-stage oxidation with a total mass change of 49.57% with the program stopped at 1150°C when the DSC returned to the baseline. This two-stage oxidation behavior of Al has been reported by many other authors [10][14][15][17][59][61][62]. The sample in Figure 5.5B is heated to 1450°C, allowing for a third oxidation stage and a total mass change of 80.5%. The three stage reaction is very repeatable for all  $\mu\text{m}$ -Al+O<sub>2</sub> TG/DSC reported in Chapter VI.



**A**



**B**

Figure 5.5: TG/DSC curves of 1-3  $\mu$ m-Al oxidation (10 K/min in O<sub>2</sub> environment)

Figures 5.6 through 5.8 illustrate representative curves from the TG/DSC experiments of the nano and micron composite mixtures. Figure 5.6 shows data from 40nm-Al+MoO<sub>3</sub> showing an exothermic reaction starting at 265.5°C (onset), peaking at 507.2°C with a enthalpy (area under the curve) of 2.441 kJ/g. Before the exothermic

reaction reaches completion, the remaining Al in the sample melts showing an overlapping endothermic melt peaking at 658.1°C.

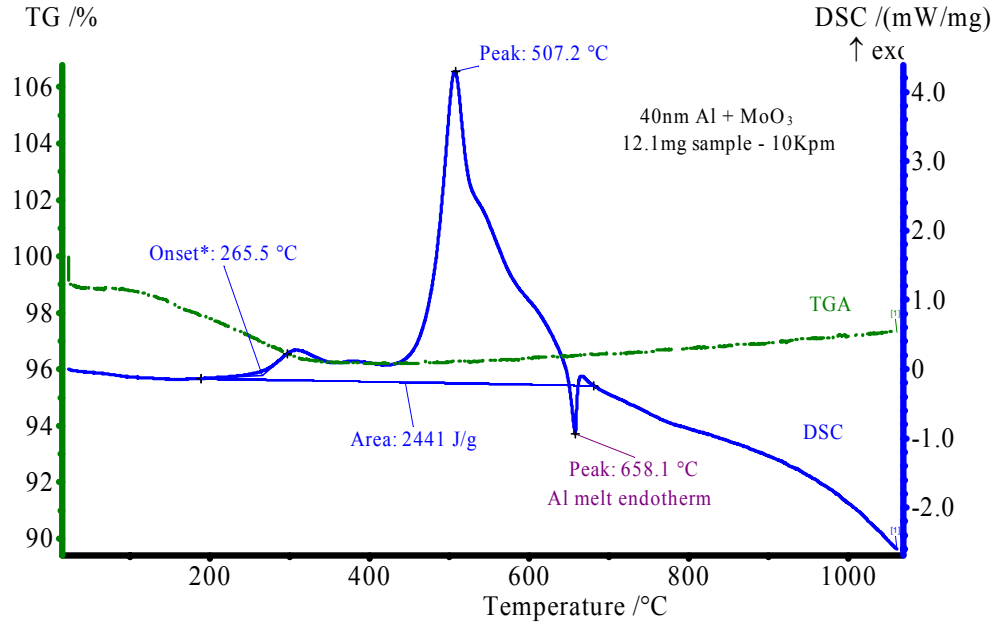


Figure 5.6: TG/DSC curves of 40nm-Al+MoO<sub>3</sub> reactions (10 K/min in argon)

Figure 5.7 shows data from 3-4.5  $\mu\text{m}$ -Al+MoO<sub>3</sub> showing an exothermic reaction starting at 522.2°C (onset), peaking at 889.6°C with a enthalpy (area under the curve) of 4.012 kJ/g. In this same temperature range (i.e. between the onset and end temperatures of the exothermic peak) the Al content of the sample shows endothermic melt and the MoO<sub>3</sub> content in the sample transitions by sublimation indicated by the TGA mass loss starting around 800°C. Figure 5.8 shows the DSC data for nine Al particle size composites of Al+MoO<sub>3</sub>. This figure shows that the main reaction for all of the nanocomposite samples occurs prior to the Al melt and in the solid state. Whereas the main exothermic reaction for all of micron composites may begin in the solid state but peaks well above phase transition temperatures of Al ( $T_{mp} = 660^\circ\text{C}$  [39]) and MoO<sub>3</sub> ( $T_{sublime} = 790^\circ\text{C}$  [39]).

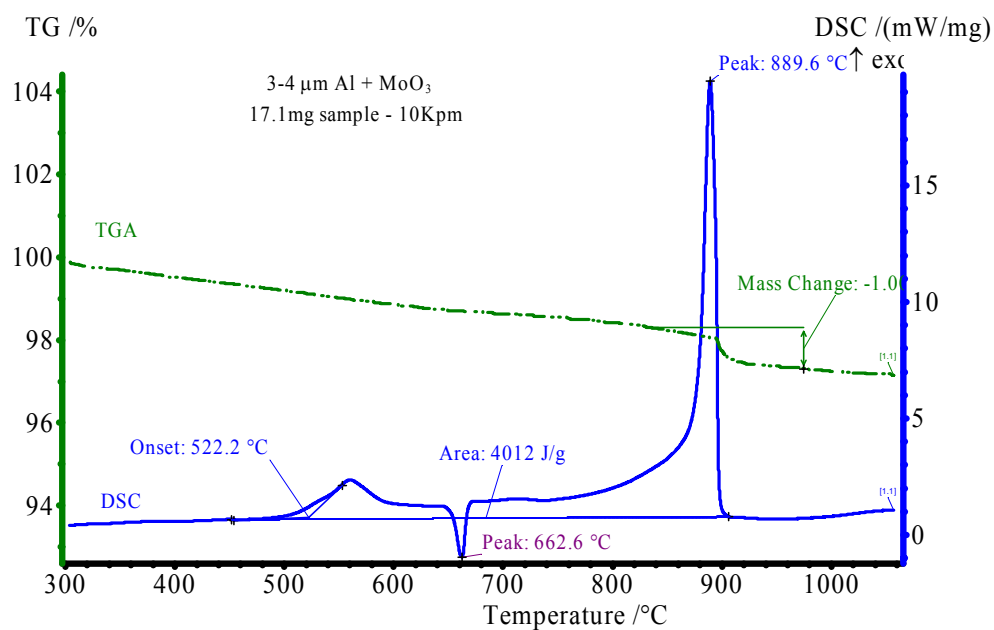


Figure 5.7: TG/DSC curves of 3-4.5  $\mu\text{m}$ -Al+ $\text{MoO}_3$  reactions (10 K/min in argon)

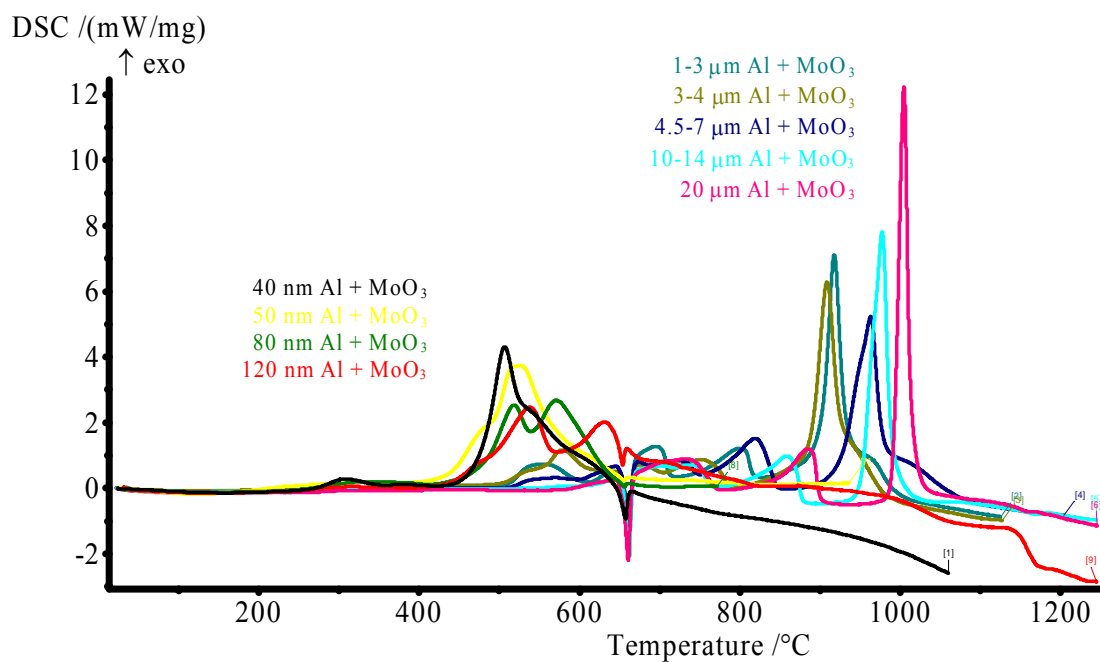


Figure 5.8: DSC curves of 40nm, 50nm, 80nm, 120nm, 1-3 $\mu\text{m}$ , 3-4.5  $\mu\text{m}$ , 4.5-7 $\mu\text{m}$ , 10-14 $\mu\text{m}$  and 20 $\mu\text{m}$ -Al+ $\text{MoO}_3$  reactions (10 K/min in argon)

TG/DSC experiments were done on four of the eight Al samples shown in Table 5.3 (50nm, 1-3 $\mu$ m, 4.5-7 $\mu$ m and 20 $\mu$ m) reacting in gaseous oxygen. Similar to the data shown in Figure 5.5, the four Al samples were tested in gaseous oxygen at a minimum of four heating rates (5, 10, 15 and 20 K/min). The DSC temperature data from each heating rate specific to a single sample will allow the calculation of reaction kinetic parameters (further discussion in sections 5.6 and 6.2). Results and observations from these experiments will be discussed in the following chapters. The DSC/TGA data from Al+O<sub>2</sub> gas experiments is shown in completion in Appendix E. Note that some of the onset temperature, area and mass change values are somewhat subjective based on cursor location to identify tangent slope intercepts. Thus data presented in Chapter VI may not be equal to data shown in the Appendix E figures.

TG/DSC experiments were done on all eight Al particle sizes shown in Table 5.3 mixed with MoO<sub>3</sub> for at least three heating rates (in argon): 5, 10, and 15 K/min. The DSC temperature data from each heating rate specific to a single sample will allow the calculation of reaction kinetic parameters (further discussion in sections 5.6 and 7.2). Attempts were made to obtain data from faster (20 and 40 K/min) and slower (2.5 K/min) heating rates to allow more data points in the thermal kinetics analysis. Results and observations from these experiments will be discussed in the following chapters. The DSC/TGA data from Al+MoO<sub>3</sub> composite experiments is shown in completion in Appendix G. As mentioned previously, some of the onset temperature, area and mass change values are somewhat subjective based on cursor location to identify tangent slope intercepts. Thus data presented in Chapter VII may not be equal to data shown in the Appendix G figures.

The onset temperatures are calculated by the intersection of tangential lines with curve locations defined by the operator. Similarly the enthalpy values (area under the curves) are defined by a start and end point corresponding to estimated divergence from and returning to a flat baseline curve. Most of the nanocomposite mixtures do not complete the exothermic reaction before reaching the melting temperature of Al (shown more definitively in the 5 Kpm and 2.5 Kpm nanocomposite curves in Appendix G). For this reason, the heat of reaction values are inaccurate due to the competing positive and

negative energy signals. An optimized DSC curve would show all reactions distinctly with each peak (or valley) returning to the baseline prior to a subsequent peak (or valley). The typical method of resolving the peaks is to slow the heating rate. The three nanocomposite samples were then tested at 2.5 Kpm with no success of resolving independent peaks. This result led to further testing to characterize the temperature dependent reactions (discussed in Chapter VIII).

### 5.6 Chemical Kinetic Analysis

All chemical reactions take place at a definite rate, dependent on reactant concentrations, temperature, pressure, presence of catalyst or inhibitors and radiative effects. For a generic bimolecular reaction between two molecules A and B, the reaction rate is proportional to the concentration of a reactant or the rate of consumption of that reactant.



$$RR \propto [A] \quad (5.2)$$

More specifically, the reaction rate can be expressed as

$$RR = k[A]^a[B]^b \quad (5.3)$$

where  $k$  is the proportionality constant called the specific reaction-rate constant and  $a$  is the order of reaction with respect to species A and  $b$  is the order of reaction with respect to species B. The  $RR$  term can be expressed in units of  $\{\text{mol}\cdot\text{L}^{-3}\text{s}^{-1}\}$ . For a given chemical reaction,  $k$  is independent of the species concentration  $[A]$  and depends only on the temperature.

$$k = BT^n \exp\left(-\frac{E_a}{R_u T}\right) \quad (5.4)$$

where  $BT^n$  represents the collision frequency and the exponential term is the Boltzmann factor, specifying the fraction of collisions that have an energy greater than the activation energy ( $E_a$ ). The values of  $B$ ,  $n$ , and  $E_a$  are based on the nature of the elementary reaction and are independent of concentration and temperature [63].

### 5.6.1 Arrhenius Equation

The Arrhenius law was defined in 1889, by Svante Arrhenius (1859-1927) as

$$k = Z \exp\left(-\frac{E_a}{R_u T}\right) \quad (5.5)$$

where  $Z$  is assumed to include the affect of the collision frequency and orientation ( $Z$  is also termed as the steric factor). The pre-exponential factor  $Z$  corresponds to  $BT^n$  in Eq. 5.4 where the exponent  $n$  lies between 0 and 1 to create less temperature dependence for small temperature ranges.

Assuming that DSC data has been calibrated correctly, the areas under the peaks are directly proportional to the enthalpy change. Assuming that a one directional bimolecular reaction is occurring, the rate of enthalpy change ( $dH/dt$ ) is directly proportional to the reaction or conversion rate ( $d\alpha/dt$ )

$$\frac{d\alpha}{dt} = \frac{1}{\Delta H} \left( \frac{dH}{dt} \right) \quad (5.6)$$

The total reaction heat is

$$\Delta H = \int \frac{dH}{dt} dt \quad (5.7)$$

and the partial reaction heat, which is generated from some moment  $t$ , is related to the conversion degree  $\alpha$ , as  $\alpha = H/\Delta H$ .

Based on the literature review, there are several methods for calculating kinetic parameters from DSC data: Kissinger [34], Freeman-Carroll [21], Ozawa [46], Flynn-Wall [20], Friedman [22] and others.

### 5.6.2 First-Order Arrhenius Reaction Kinetics Analysis

Reaction rates of many reactions can be modeled by the Arrhenius law. Assuming that the reaction rate constant  $k$  is independent of species concentration and depends on temperature only, the Arrhenius equation can be converted to

$$\ln k = \ln Z - \frac{E_a}{R_u} \left( \frac{1}{T} \right) \quad (5.8)$$

Traditionally the rate constant  $k$  is approximated by the DSC heating rate  $\beta$ . In correspondence with Eq. 5.8, the temperature and heating rate data from a DSC data can be plotted as  $\ln(\beta)$  versus  $1000/T$ . The kinetic parameters  $E_a$  and  $Z$  can be approximated by the slope and intercept of the linear curve fit, respectively. For a curve fit slope of  $M$  and y-intercept of  $B$

$$E_a = -R_u \cdot M \quad (5.9)$$

and

$$Z = \exp(B) \quad (5.10)$$

### 5.6.3 Kissinger Reaction Kinetics Analysis

The above analysis assumes a constant heating rate according to Eq. 5.11

$$T = T_0 + \beta \cdot t ; dT = \beta \cdot dt \quad (5.11)$$

and the reaction rate (or conversion rate of  $\alpha$ ) can be expressed as Eq. 5.12

$$RR = \frac{d\alpha}{dt} = \beta \frac{d\alpha}{dT} \quad (5.12)$$

Equation 5.5 can be rewritten as Eq. 5.13 or 5.14

$$\frac{d\alpha}{dt} = Z \cdot e^{-\frac{E_a}{RT}} (1-\alpha)^n \quad (5.13)$$

$$\frac{d\alpha}{dT} = \frac{Z}{\beta} \cdot e^{-\frac{E_a}{RT}} (1-\alpha)^n \quad (5.14)$$

Because the maximum rate takes place when  $dk/dt$  (or  $dk/dT$ ) is zero, differentiating Eq. 5.14 and equating to zero results in Eq. 5.15.

$$\beta \frac{E_a}{R \cdot T_m^2} = Zn(1-\alpha_m)^{n-1} e^{\left( \frac{-E_a}{RT_m} \right)} \quad (5.15)$$



where  $T_m$  is the min/max temperature of a DSC peak where the maximum reaction rate occurs. Eq. 5.15 can be expressed in the logarithmic form below

$$-\ln\left(\frac{\beta}{T_m^2}\right) = \ln\left(\frac{E}{R}\right) - \ln(Zn) - (n-1)\ln(1-\alpha_m) + \frac{E_a}{RT_m} \quad (5.16)$$

For this work a first-order Arrhenius equation is assumed ( $n=1$ ). The activation energy  $E_a$  and pre-exponential factor  $Z$  are determined by the slope and intercept of a linear curve fit on a  $-\ln(\beta/T_m^2)$  versus  $1000/T_m$  plot of DSC temperature data. For a curve fit slope of  $M$  and y-intercept of  $B$  ( $n=1$  in Eqn. 5.16)

$$E_a = -R \cdot M \quad (5.17)$$

and

$$Z = \exp(B) + \frac{E_a}{R} \quad (5.18)$$

Note that the strict definition of activation energy is dependent only on the reactant molecular properties and enthalpy states. Chapters VI and VII will discuss a series of experiments varying Al particle size and oxide layer thickness used to calculate  $E_a$  using the Arrhenius and Kissinger methods discussed above. The activation energies presented in the following chapters vary for the same elementary reactions indicatin that it is truly an *apparent activation energy*, which is dependent on other thermodynamic and material stress properties.

## CHAPTER VI

### Al OXIDATION TG/DSC ANALYSIS

#### 6.1 Literature Review

Table 6.1 presents a list of models derived based on experimental results of Al oxidation. All of the reactions listed in Table 6.1 are Al+O<sub>2</sub> gas (sometimes in the form of air). Cabrera and Mott [10] provide a fundamental model for basic metal oxidation that is described and applied specifically to Al. The other cited works study Al particles (spheres or flakes) with an aluminum oxide layer reacting in a gaseous O<sub>2</sub> environment. Experimental results have led to the development of a series of physical conditions and diffusion behaviors that control reaction behaviors.

Table .6.1: Literature Review of Al Oxidation Models and Theory

Author(s)/Date	Sample	Particle Description	Analysis Description
Cabrera and Mott (1948) [10]	Metals and Oxygen (ingeneral)		General theory of oxide film growth on metals discussing oxidation rates as first, logarithmic, then linear and finally parabolic (proportional to metal to oxygen gradient of $1/x$ through the oxide layer thickness). Statement that oxygen atoms are insoluble in $Al_2O_3$ bu $Al_2O_3$ will dissolve Al atoms (or metals).
Eisenrich, Wieser, Fietzek, Juez-Lorenzo, Kolarik & Koleczko (2004)[17]	Al+Air	Alex 0.01-25 $\mu$ m dia	Model: 1)oxidation governed by chemical reaction kinetics $\Delta T < 100K$ ; 2)diffusion of oxygen to the metal core and oxidationreaction $\Delta T > 300K$
Shimizu, Furneaux, Thompson, Wood, Gotoch, & Kobayashi (1990) [54]	Electro-polished Al+air Held at 515°C for specified time intervals		T<425°C air-form oxide film thickness to 20nm; T<300°C migration of Al ions through the oxide filem under the influence of high electric field created by oxygen ions at the outer amorphous oxide surface; 300-425°C parabolic growth rate controlled by outward diffusion of $Al^{3+}$ ions; T>450°C displays $\gamma$ -alumina growth at amorphous oxide-metal interface; cracking in amorphous oxide layer due to tensile stresses
Suvaci, Simkovich, & Messing (2000) [59]	Al+Air	Attrition milled, SSA=1.2, 14.4 and 20.2 m <sup>2</sup> /g	Model: 1) Initial oxidationby outward diffusion of $Al^{3+}$ forming amorphous alumina; 2) formation of channels in amorphous oxide layer and nucleation of $\gamma$ -alumina, rapid diffusion of $O_2$ through channels; 3) controlled oxygen transport through the $\gamma$ -alumina grain structure
Trunov, Schoentiz, Xiaoying & Dreizin (2004) [62]	Al+O <sub>2</sub>	3-4.5 $\mu$ m, 10-14 $\mu$ m, +325mesh and flake Al	Model: 1)T<500°C, slow growth of amorphous oxide layer by Al ion diffusion; 2)550<T<650°C exceeding critical thickness of amorphous oxide then generating crystalline alumina polymorph ( $\gamma$ -alumina). Rapid rate increase due to exposed Al surface in alumina transition; 3)650<T<1100°C closing/completion of $\gamma$ -alumina layer – slow oxidation again.

## 6.1 TG/DSC Results

TG/DSC experiments were performed for four Al particle sizes (50 nm from Nanotechnologies, Inc., 1-3  $\mu\text{m}$  Atlantic Equipment Engineers, 4.5-7  $\mu\text{m}$  from Alfa Aesar and 20  $\mu\text{m}$  from Sigma Aldrich) oxidizing in a gaseous  $\text{O}_2$  environment. Each of the four Al samples were tested at four heating rates (5, 10, 15, and 20 Kpm) to allow calculations of the activation energy and pre-exponential factors. Each sample was weighed to a mass of 4 to 6 mg and placed loosely into the alumina crucible liner. The powder samples were not compressed as mentioned in the previous chapter to allow more surface area exposure to gas. The DSC furnace was evacuated to  $P < 2 \times 10^{-4}$  mbar prior to testing such that the powder samples may have settled during removal of the air voids.

There were distinct reaction differences as shown in Figures 6.1 and 6.2 for the nm and  $\mu\text{m}$ -Al samples respectively.

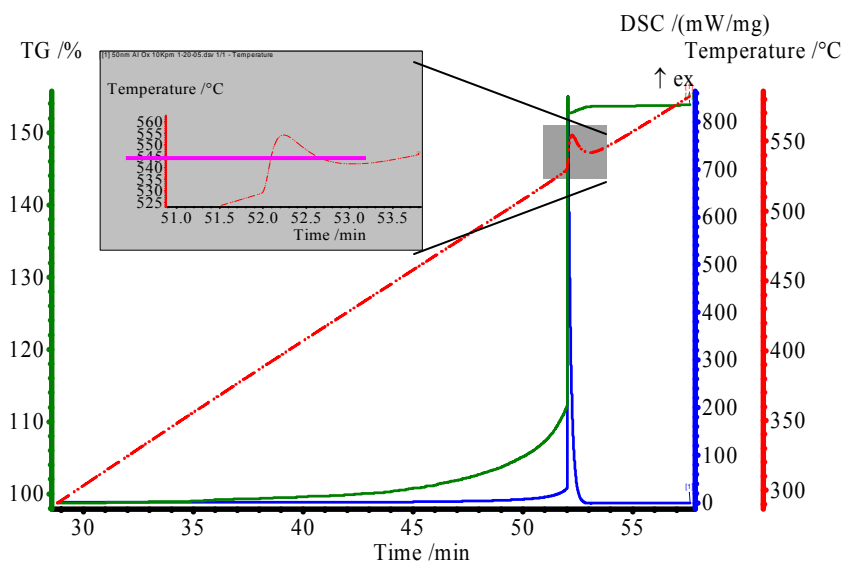


Figure 6.1:a TGA, DSC and reference temperature curves of 50nm-Al in  $\text{O}_2$  ( $\beta=10\text{Kpm}$ ) indicating reference crucible heating from exothermic reaction. Data displays a single oxidation stage of reaction.

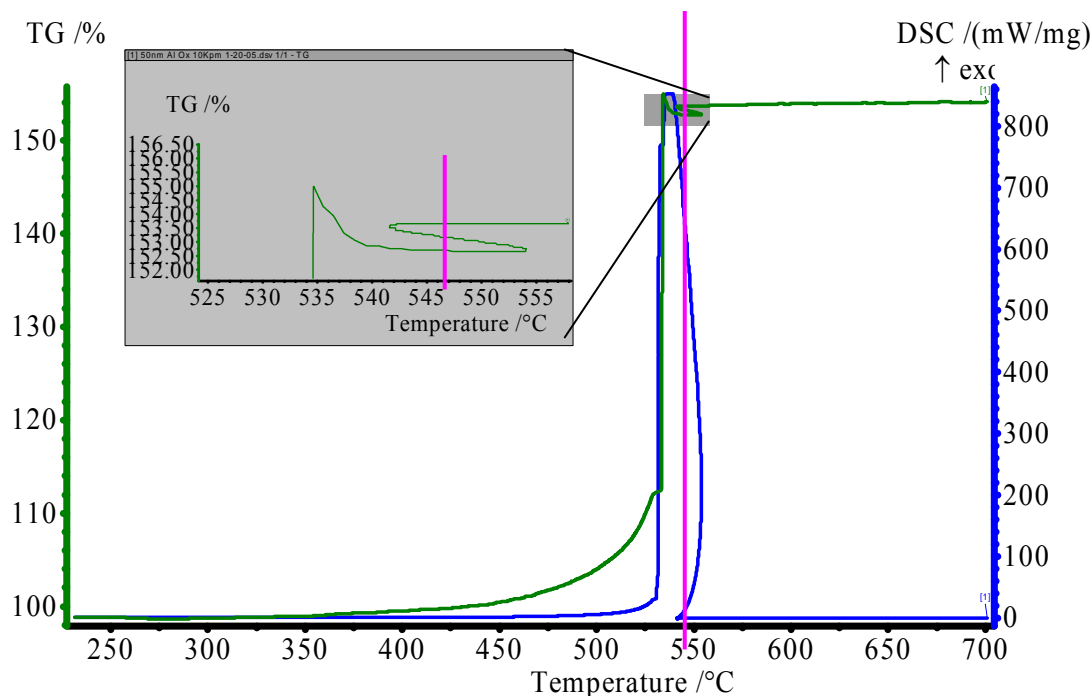


Figure 6.1:b TGA and DSC curves of 50nm Al 50nm Al in O<sub>2</sub> ( $\beta=10\text{Kpm}$ ) indicating DSC and TG curves are not a true function of x-axis temperature

Note the color notation of the three curves shown in Figures 6.1 and 6.2.

- Reference temperature – red (broken dashed line) with matching y-axis
- DSC – blue (solid line) with matching y-axis
- TGA – green (solid line) with matching y-axis

This color notation will be used for most TG/DSC plots shown in the document. The complete series of TG/DSC data plots for the Al in O<sub>2</sub> (gas) are shown in Appendix E with similar plot color designation. Appendix E also shows some plots that include isothermic temperature segments as purple curves and TGA derivatives (axis indicated as DTG) as red broken dash-dot (— · —) curves.

The 50nm-Al sample in Figure 6.1 shows a very rapid and high magnitude exothermic oxidation. The nm-Al oxidizes in a single stage starting in a solid phase ( $T_{\text{onset}} = 529.4^{\circ}\text{C}$ ) and reaching steady-state baseline again in the solid phase (approximately  $550^{\circ}\text{C}$  in Figure 6.1b). Figure 6.1b also shows that all of the nm-Al does

convert to alumina ( $\text{Al}_2\text{O}_3$ ) by not displaying an endothermic Al melt around  $660^\circ\text{C}$  (as shown in Figure 5.4 on page 80).

Note that the nm-Al oxidation is very exothermic with a peak magnitude of nearly 800mW/mg as compared to the  $\mu\text{m}$ -Al sample (peak exothermic magnitude of approximately 4.5 mW/mg) in Figure 6.2. The intensity of the nm-Al crucible caused a non-uniform heating of the reference crucible as indicated by the reference temperature spike occurring simultaneous to the DSC exotherm and TGA mass gain. The reference temperature spike is automatically used in the Netzsch Proteus software in plotting the TGA and DSC data as function of temperature as shown in Figure 6.1b. If one were to draw a horizontal line through the temperature curve of Figure 6.1a at the spike location, the horizontal line would intersect the temperature curve twice for a single DSC and TGA data point. This same horizontal line can then be rotated to form a vertical line in Figure 6.1b indicating two DSC points or two TGA points for a single temperature (x-axis).

This nonfunctional form of the DSC curves generates inaccurate integrals making heat of reaction values impossible to calculate. Contrary to this occurrence the 50nm-Al tested at 5Kpm did not have the same exothermic intensity ( $h_{\text{peak}} = 10.32 \text{ mW/mg}$ ), therefore not altering the reference temperature data and making an integral area and heat of reaction calculation possible ( $\Delta h_{\text{rxn}} = 7220 \text{ J/g}$  see Figure E.1a in Appendix E).

Figure 6.2 shows a representative data set for the three different micron samples tested. All  $\mu\text{m}$ -Al samples tested in gaseous oxygen show a three-stage oxidation reaction as indicated by the three plateaus in the TGA mass gain curve and the three exothermic spikes in the DSC curve. Figure 6.2 shows that the oxidation reaction started in the solid phase ( $T_{\text{onset}}=553.1^\circ\text{C}$  from Table 6.2 determined more precisely based on plotting the TGA and DSC data as function of temperature rather than time as shown in Figure 6.2) and does not complete prior to the endothermic aluminum melt. Onset of the Al melt also signifies the end of the first oxidation stage coinciding with stagnant TGA curve (horizontal plateau). Once the melting endotherm has completed, the DSC and TGA slopes indicate that the second stage of oxidation begins. Figure 6.2 shows the second stage oxidation peaks and ends at approximately  $967.8^\circ\text{C}$  as indicating by the drop in DSC magnitude and TGA plateau. The reaction stops for a finite time interval of

approximately 15 min from 206.9 to 221.9 min as indicated by a zero derivative of the TGA curve. This starts the beginning of the third oxidation stage, which continues into the isothermic (temperature constant with time) peak temperature of the furnace.

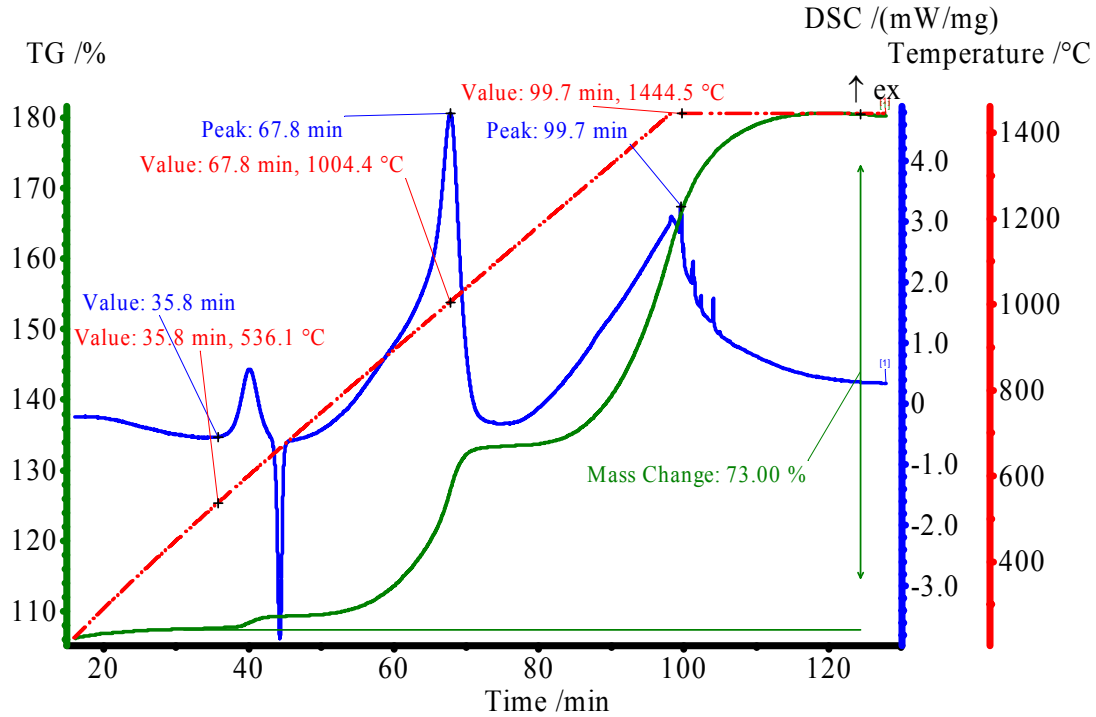


Figure 6.2: TGA, DSC and reference temperature curves of 1-3µm-Al in  $O_2$  ( $\beta=5Kpm$ ) displaying three basic oxidation stages

The maximum programmable temperature allowed by our DSC and furnace system is 1500°C which allows a steady-state sample and reference temperature of approximately 1435-1445°C. Figure 6.2 shows a 1-3µm-Al sample that is still reacting (as indicated by the positive slopes of the exothermic DSC curve and TGA curves) when the system reached 1444.5°C. Most of the µm-Al samples did not complete the oxidation reaction below 1445°C independent of larger time intervals allowed by slower heating rates. For this reason, data was recorded for a programmed isothermic temperature at the maximum allowable system temperature. The isothermic time interval in Figure 6.2 is indicated by the horizontal shift in the reference temperature curve at approximately 99 min and continuing for 30 min. Multiple isotherm intervals ranging from 30 to 90 minutes were programmed into the DSC heating system to obtain a complete oxidation of

the three different  $\mu\text{m-Al}$  samples. A complete reaction and an accurate total mass gain was not acquired for any of the  $20\mu\text{m-Al}$  samples tested (shown in Appendix E). It is believed that the peak temperatures of the some of the second and third oxidation stages are falsely generated based on the maximum steady-state temperature of the DSC furnace.

The specific points taken from the TGA, DSC and DTG curves shown in Appendix E are listed in Table 6.2. Table 6.2 includes four columns for the four different Al sample sizes, and nine data points including  $T_{\text{onset}}$  from the DSC and TGA curves,  $T_{\text{peak}}$  for the first and second oxidation stages from the DSC curve, the original sample mass, the total mass gain from the TGA curve and the peak mass rate of change ( $dm/dt$ ) from the DTG (TGA derivative) curve. The data from Table 6.2 is plotted as function of Al particle size in Figures 6.3 through 6.7. The data from Table 6.2 is also plotted as function of DSC heating rate ( $\beta$ ) in Appendix F starting on page 193.

Figures 6.3 and 6.4 display  $T_{\text{onset}}$  as a function of particle size for each heating rate and the average of the four different heating rates as determined by the DSC and TGA data respectively. As shown in Figures 5.6 and 5.7,  $T_{\text{onset}}$  is determined by the intersection of two tangents at the beginning of the DSC exothermic peak or TGA mass gain. Figures 6.3 and 6.4 both show a similar logarithmic increasing trend of the average  $T_{\text{onset}}$  with respect to Al particle size  $d$ .

Figures F.1 and F.2 show the  $T_{\text{onset}}$  data plotted as a function of heating rate,  $\beta$  which is the relationship that will be used in the calculations of activation energy ( $E_a$ ) and pre-exponential factor. Figure F.2 shows that the onset temperature is much more consistent in a linearly increasing relationship to  $\beta$  for each of the four different Al particle sizes. Figure F.1 and Table 6.2 show an anomaly point in  $T_{\text{onset}}$  as determined by the DSC data for the  $20\mu\text{m-Al}$  tested at  $20\text{Kpm}$ . Figure F.2 (TGA data) shows better linear trends for each of the four Al particle sizes as compared to the DSC data in Figure F.1.



Table 6.2: DSC data from Al and O<sub>2</sub> gas reactions

Material	Nanotechnology 50 nm	AEE 1-3µm	Alfa Aesar 4.5-7µm	Sigma Aldrich 20µm
<b>Test/DSC run</b>				
<b>5 kpm</b>				
DSC T <sub>onset</sub> [°C]	499.8	541	553.1	572.3
TGA T <sub>onset</sub> [°C]	504.2	548.5	559.8	584.5
DSC T <sub>peak</sub> [°C] 1	527	967.6	944.5	994.4
DSC T <sub>peak</sub> [°C] 2	n/a	1308.2	1408.4	1446.7
Original Mass (mg)	4.9	5.2	4.6	4.5
Total Δm [%]	56.08	81.23	70.78	47.82
Total Δm [mg]	2.75	4.22	3.26	2.15
dTG dm/dt max [%/min]	3.75	2.52	1.96	0.64
dm/dt max [mg/min]	0.184	0.131	0.090	0.029
<b>10 kpm</b>				
DSC T <sub>onset</sub> [°C]	529.4	558.6	564.1	582.3
TGA T <sub>onset</sub> [°C]	529.4	560.7	570.7	587.6
DSC T <sub>peak</sub> [°C] 1	539.5	994.4	993.3	1051.7
DSC T <sub>peak</sub> [°C] 2	n/a	1356.5	1431	1445.5
Original Mass (mg)	4	5.6	5	5.3
Total Δm [%]	55.00	80.93	78.24	61.74
Total Δm [mg]	2.20	4.53	3.91	3.27
dTG dm/dt max [%/min]	1569.94	4.53	2.97	1.13
dm/dt max [mg/min]	34.54	0.21	0.12	0.04
<b>15 kpm</b>				
DSC T <sub>onset</sub> [°C]	540.3	563	568.9	593
TGA T <sub>onset</sub> [°C]	530	575.6	587.3	605.4
DSC T <sub>peak</sub> [°C] 1	540.7	1010.8	1005.1	1079.3
DSC T <sub>peak</sub> [°C] 2	n/a	1379	1444.5	1444.8
Original Mass (mg)	4.4	5.5	4.6	4.4
Total Δm [%]	48.59	72.96	73	57.14
Total Δm [mg]	2.14	4.01	3.36	2.51
dTG dm/dt max [%/min]	445.76	5.42	4.36	1.48
dm/dt max [mg/min]	9.53	0.22	0.15	0.04
<b>20 kpm</b>				
DSC T <sub>onset</sub> [°C]	536.4	563.2	570.9	557.8
TGA T <sub>onset</sub> [°C]	536.4	579	589.3	608.3
DSC T <sub>peak</sub> [°C] 1	541.3	1035.6	994.7	1075.4
DSC T <sub>peak</sub> [°C] 2	n/a	1414.6	1433	1443.6
Original Mass (mg)	4.2	5.2	5.2	5.2
Total Δm [%]	44.67	80.73	77.88	42.83
Total Δm [mg]	1.88	4.20	4.05	2.23
dTG dm/dt max [%/min]	550.75	8.96	7.25	1.73
dm/dt max [mg/min]	10.33	0.38	0.29	0.04
<b>Average of Heating Rates</b>				
TGA T <sub>onset</sub> [°C]	525.0	566.0	576.8	596.5
DSC T <sub>peak</sub> [°C] 1	537.1	1002.1	984.4	1050.2
TGA Total Δm [%]	51.1	79.0	75.0	52.4
dTG dm/dt max [%/min]	642.55	5.36	4.14	1.25
<b>Standard Deviation of Heating Rates</b>				
TGA T <sub>onset</sub> [°C]	14.2	14.1	14.1	12.1
DSC T <sub>peak</sub> [°C] 1	n/a	n/a	n/a	n/a
TGA Total Δm [%]	5.4	4.0	3.7	8.6
dTG dm/dt max [%/min]	662.1	2.7	2.3	0.5

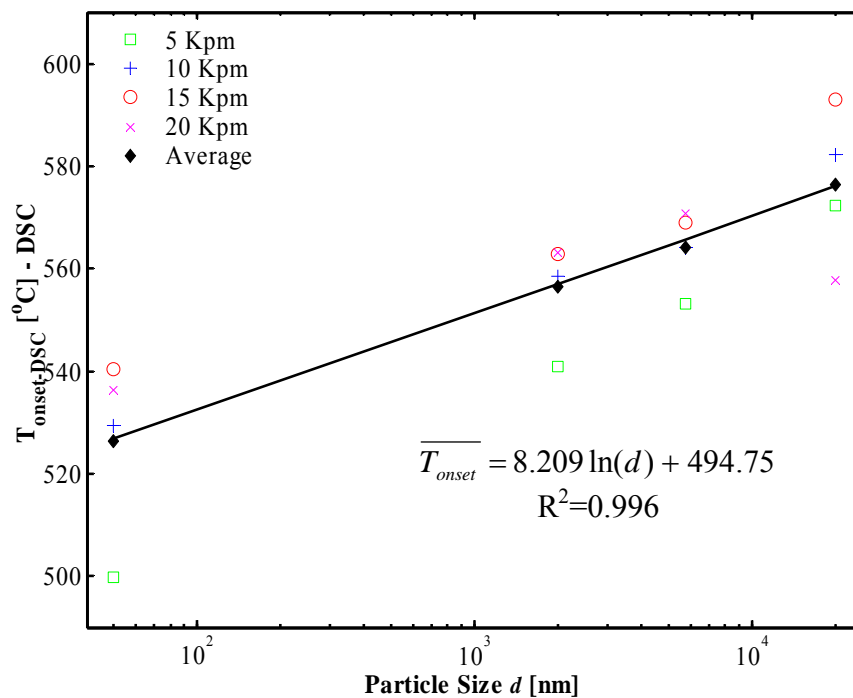


Figure 6.3: DSC Onset temperature as a function of Al particle size

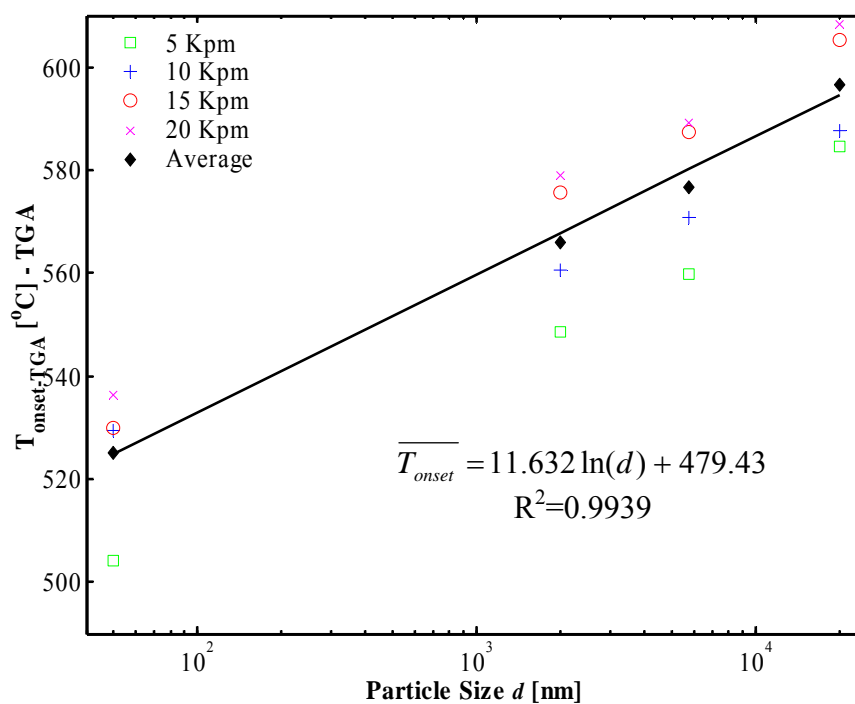


Figure 6.4: TGA Onset temperature as a function of Al particle size

Figure 6.5 is a plot of  $T_{\text{peak}}$  as a function of Al particle size  $d$ . Note that all of the nm-Al samples display a peak DSC exotherm prior to melt and the reaction completes in a single oxidation stage. Note that the micron DSC curves suggest that the exotherm prior to the Al melt and after the Al melt would connect into a single exothermic Al melt peak if not for the overlapping and contradicting endothermic peak. The data suggests that the reaction interval for the micron samples from the first DSC  $T_{\text{onset}}$  to the second DSC  $T_{\text{peak}}$  is representative of the single reaction stage in the nanometer sample. Basically, the first true DSC peak for the micron samples is artificially created by the energy absorption of the melting Al. Thus, the data in Table 6.2 and Figure 6.5 is based on the single  $T_{\text{peak}}$  for the 50nm-Al and the second  $T_{\text{peak}}$  for the micron samples.

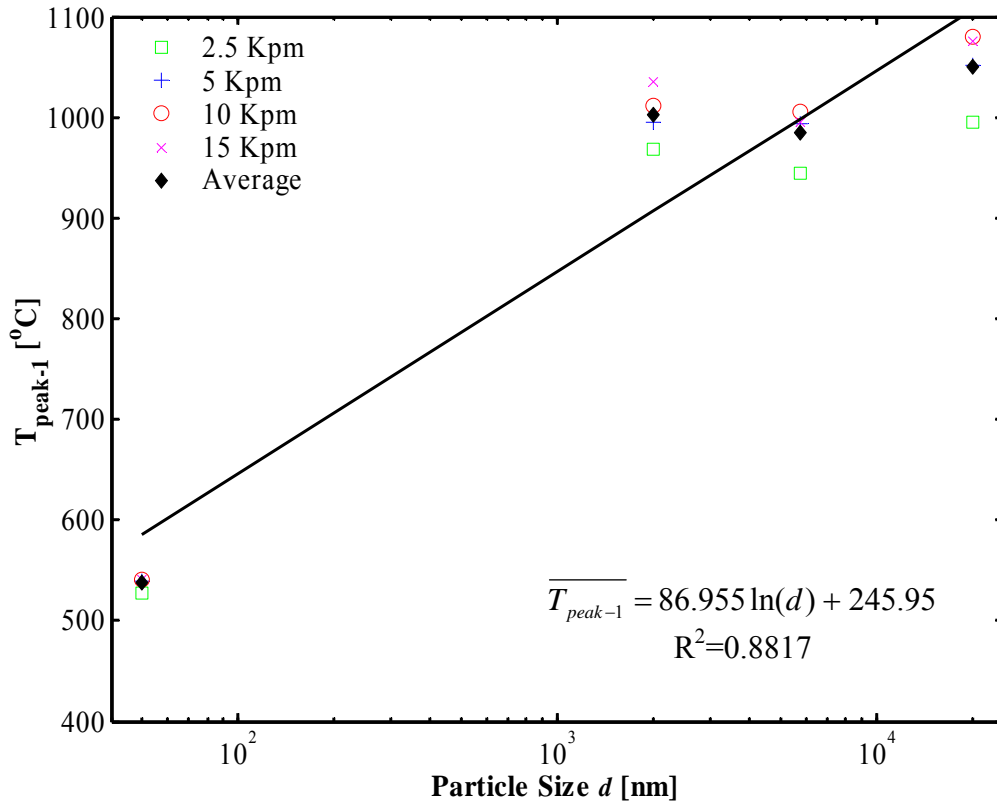


Figure 6.5: Peak-1 DSC temperature as a function of Al particle size

Figure 6.6 shows the total percent change in sample mass over the entire experiment. Theoretically this value could be used to determine the present Al

concentration in the sample, which is an important concern in nano-Al manufacturing and applications. As mention in previous chapters, the ratio of pure Al to  $\text{Al}_2\text{O}_3$  becomes significant in nano-Al samples and this ratio may be continually changing based on aging of the materials. Note that the  $20\mu\text{m}$ -Al data point in Figure 6.6 is not accurate because none of the four reactions displayed complete reaction prior to the end of the experiment (even with the programming of time interval isotherms discussed earlier). Because the reactions seem to be unique for nm and  $\mu\text{m}$ -Al there is no apparent trend between the two particle regimes total mass gain, but the  $\mu\text{m}$ -Al do show an exponential decay in total mass gain as a function of particle size  $d$ .

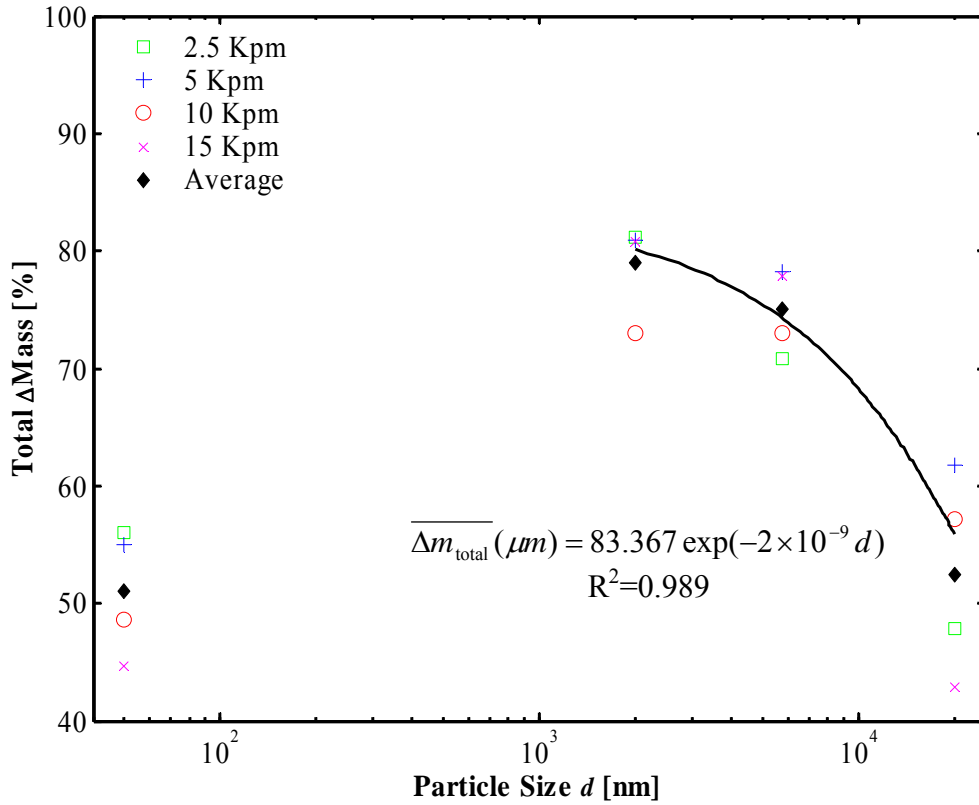


Figure 6.6: Total mass gain as a function of Al particle size

Figure 6.7 shows the peak mass rate of change [%/min] as a function of Al particle size  $d$ . As shown in Figures 6.1 and 6.2, the nm-Al oxidizes at a much faster rate than the  $\mu\text{m}$ -Al. The 50nm-Al exhibits an average  $\text{dm}/\text{dt}_{\text{peak}}$  two orders of magnitude larger than

the  $\mu\text{m}$ -Al samples (Table 6.2: 50nm-Al  $dm/dt_{\text{peak}} = 642.55 \text{ \%/min}$  compared to the  $\mu\text{m}$ -Al samples  $dm/dt_{\text{peak}} < 6 \text{ \%/min}$ ). The average  $dm/dt_{\text{peak}}$  values are proportional to a  $1/d$  relationship.

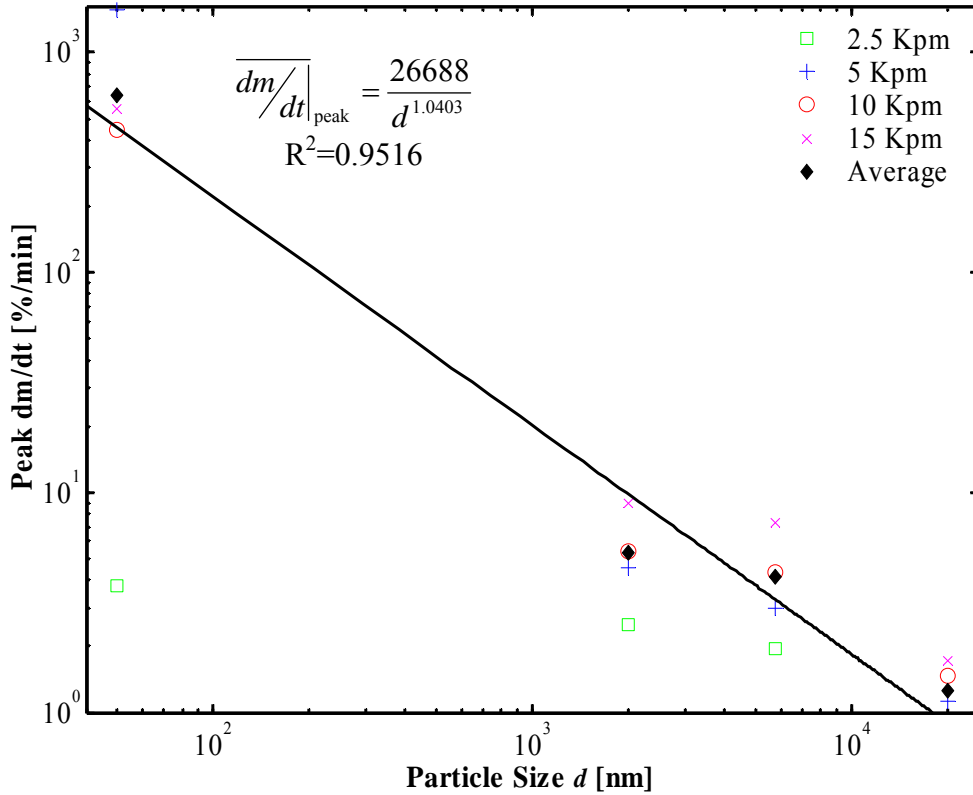


Figure 6.7: Peak mass rate of change as a function of Al particle size

## 6.2 Kinetic Parameter Approximation

### 6.2.1 Reaction Parameters Calculated by Peak Temperatures

Figures 6.8 and 6.9 show the plots of reaction temperatures and DSC heating rates according to the Arrhenius parameter approximation (Eq. 5.8) and the Kissinger parameter approximation (Eq. 5.16) as calculated using the peak exotherm temperatures from the Al oxidation DSC data. The actual  $T_{\text{peak}}$  values used are shown in Table 6.2 and Figure 6.5.

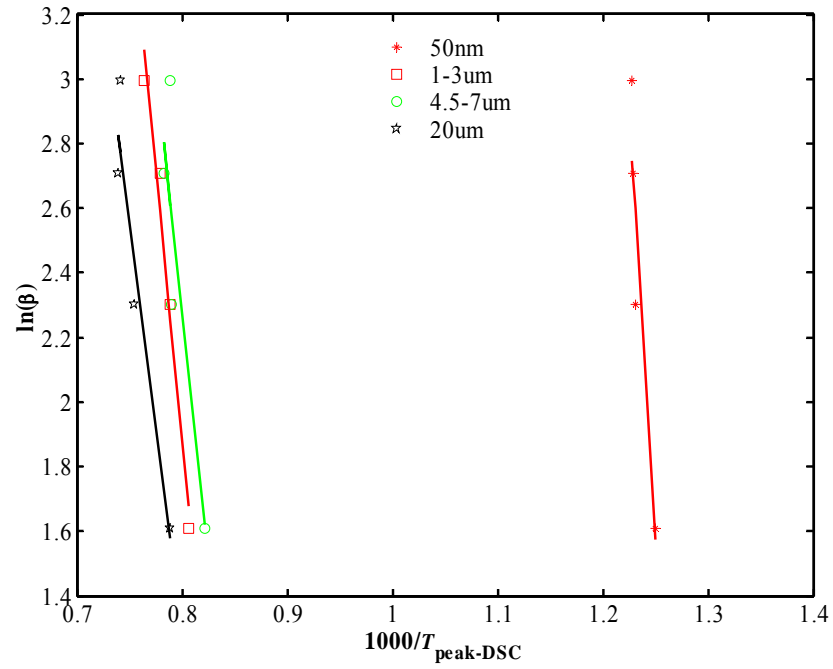


Figure 6.8: Slope plot to determine activation energy based on  $T_{\text{peak-1}}$  using Arrhenius method (see Section 5.6.2)

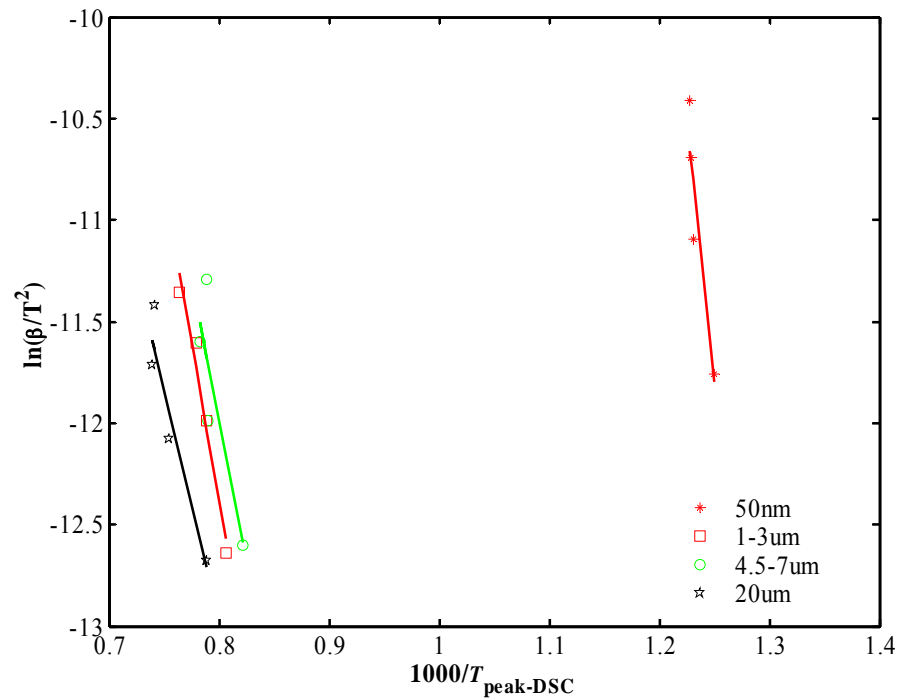


Figure 6.9: Slope plot to determine activation energy based on  $T_{\text{peak-1}}$  using Kissinger method (see Section 5.6.3)

Figure 6.10 shows that the  $E_a$  (calculated from slopes in Figure 6.8 and 6.9) logarithmically increases with particle size. Note that  $T_{\text{peak}}$  was objectively selected as the first and only DSC exothermic peak for the 50nm-Al. The  $\mu\text{m}$ -Al samples were more subjectively chosen as the second peak based on the theory that the first peak is artificially generated by the Al melt endotherm.

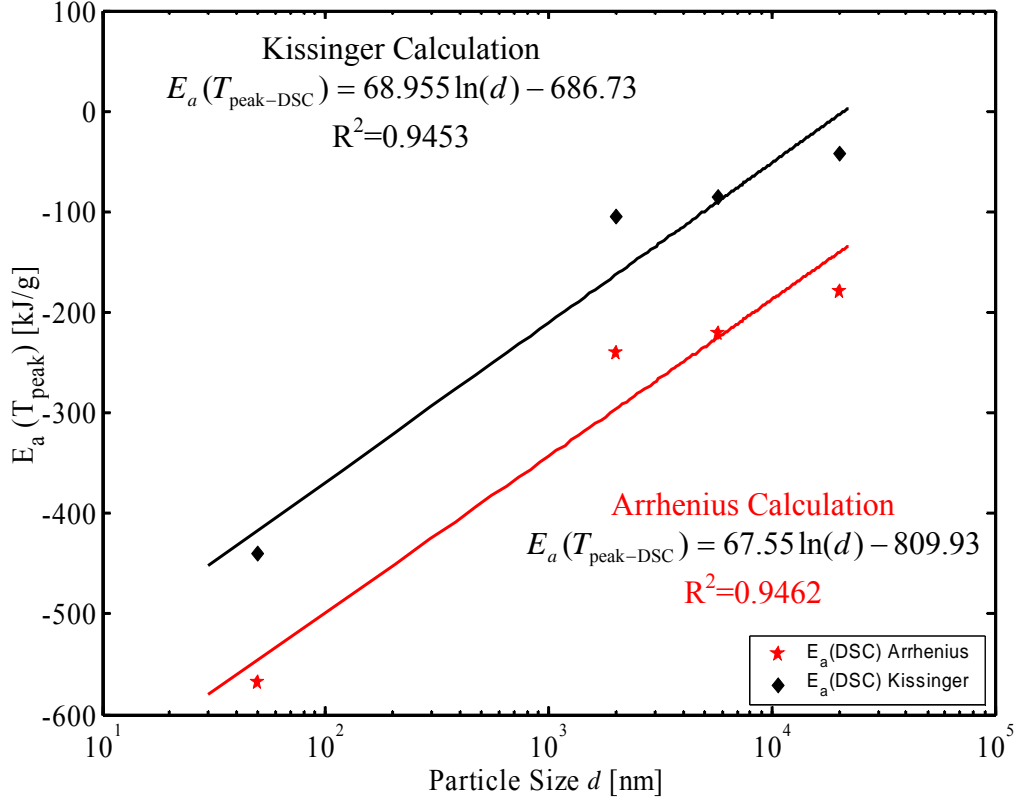


Figure 6.10: Activation energy ( $E_a$ ) calculated by  $T_{\text{peak-1}}$  as a function of particle diameter

The negative notation of the  $E_a$  values shown in Figure 6.10 are correct indicating an exothermic reaction. Typically chemical energy generation is modeled in an Arrhenius equation form (Eqn 5.5) as shown in Eqn. 6.1 [45]. According to Eqn. 6.1, a negative  $E_a$  quantity would generate a positive exponential in the form of  $C * (e^y)$  versus a positive  $E_a$  quantity would generating  $C * (1/e^y)$ .

$$q_{\text{chem}} = Qx_{\text{fuel}}\rho K \left[ \exp\left(-\frac{E_a}{RT}\right) \right] \quad (6.1)$$

Clearly the negative  $E_a$  quantity will produce exponential runaway with increasing temperature. The event of chemical reaction ignition is commonly referred to as *thermal runaway*, which is a characteristic corresponding to the exothermic chemical energy generation.

The data points and trend shown in Figure 6.10 do not support the laser experiment results shown in Figure 4.1. Activation energy basically quantifies ignition sensitivity. Granier and Pantoya [24] showed that nanocomposites were much more igniton sensitive than similar micron composites suggesting that the activation energy of nanocomposites is a lower magnitude (absolute value). As shown in Table 6.3 and represented in Figure 1.1, the  $\mu\text{m-Al}$  data in Figure 6.10 indicates a smaller enthalpy wave to crest. In short, the  $E_a$  magnitudes in Figure 6.10 indicate that less energy is required to stimulate the  $\mu\text{m-Al}$  oxidation versus the  $\text{nm-Al}$  oxidation.

### 6.2.2 Reaction Parameters Calculated by Onset Temperatures

The Kissinger method or peak-displacement method ([7]) is based on peak temperature of a DSC exotherm or endotherm. The Kissinger method proposed that for specific single thermally activated reactions, the fraction of a given chemical species  $x_m$  transformed at a specific temperature  $T_m$  is independent of heating rate. Typically the Kissinger method is performed using the maximum rate of reaction  $T_{peak}=T_m$ . This reasoning is part of the justification for using the second  $\mu\text{m-Al}$  DSC peaks as these temperatures typically correspond to the peak TGA mass gain (Section 6.2.1).

Data from the  $\text{Al+MoO}_3$  thermite reactions indicates that the reaction rates and reaction paths are definitely temperature dependent (Chapter VIII). The goal of the Kissinger analysis is to obtain at consistent reaction stage for manipulation of the Arrhenius equation. In similar studies of Al oxidation, Eisenrich et al. [17] and Trunov et al. [61][62] used the onset temperature ( $T_{onset}$ ) from DTA and TGA data as the heating rate independent stage  $T_m$ . Figures 6.11 through 6.14 show the slope plots using the Arrhenius equation and Kissinger method in conjunction with DSC and TGA onset temperatures to enable calculation of  $E_a$ .



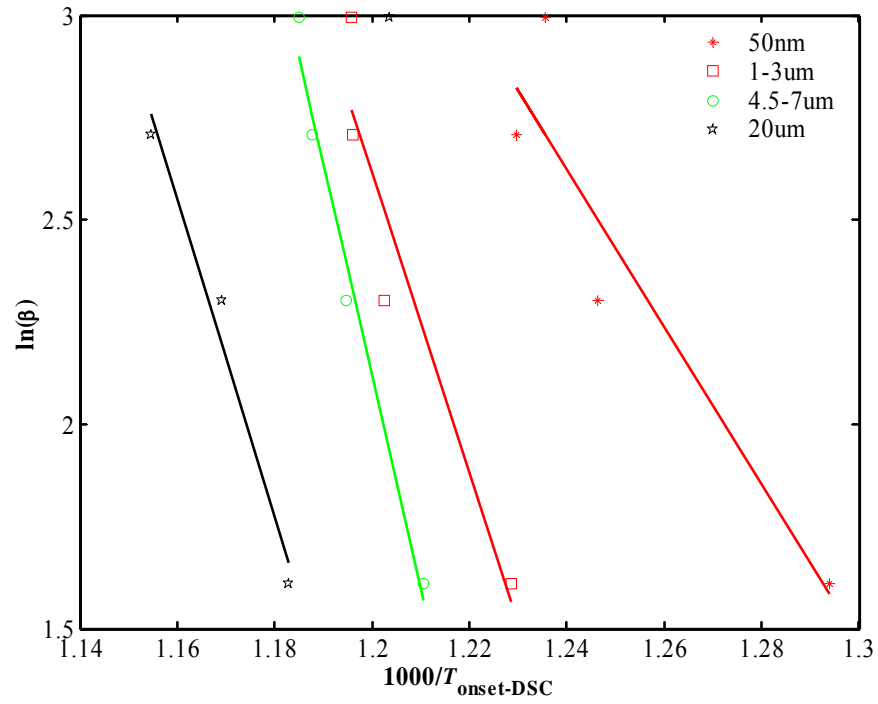


Figure 6.11: Slope plot to determine activation energy based on  $T_{\text{onset-DSC}}$  using Arrhenius method (see Section 5.6.2)

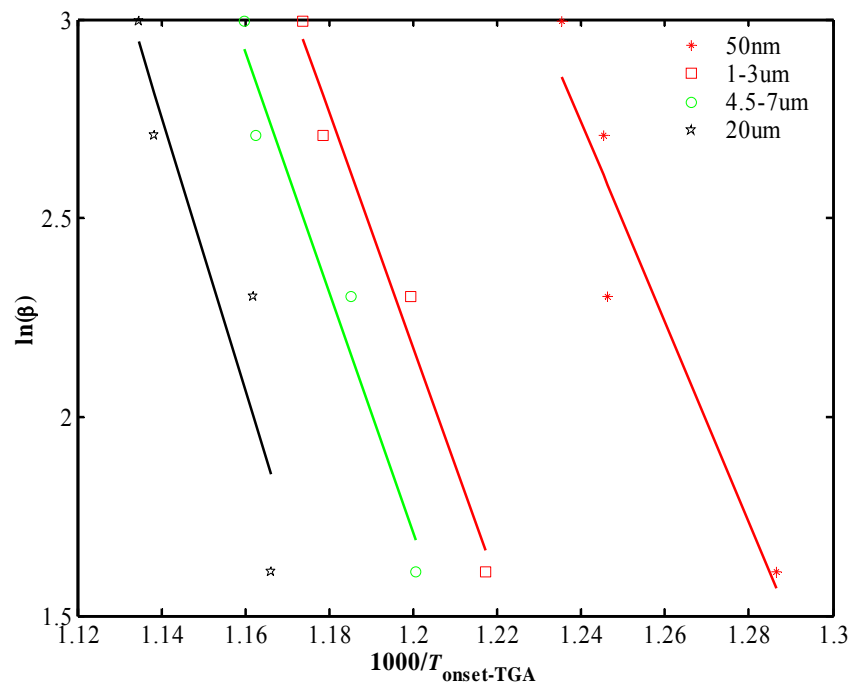


Figure 6.12: Slope plot to determine activation energy based on  $T_{\text{onset-TGA}}$  using Arrhenius method (see Section 5.6.2)

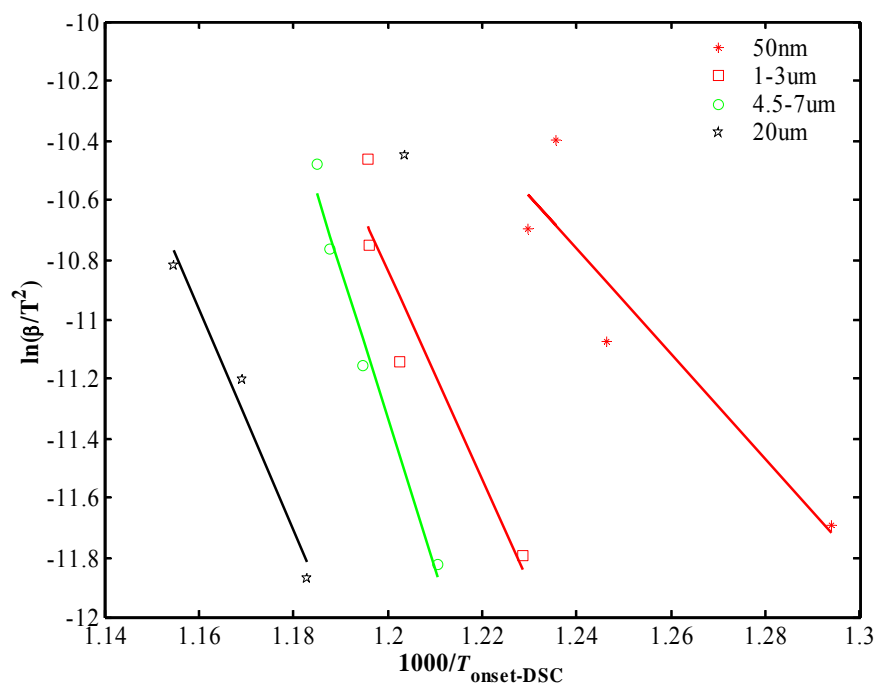


Figure 6.13: Slope plot to determine activation energy based on  $T_{\text{onset-DSC}}$  using Kissinger method (see Section 5.6.3)

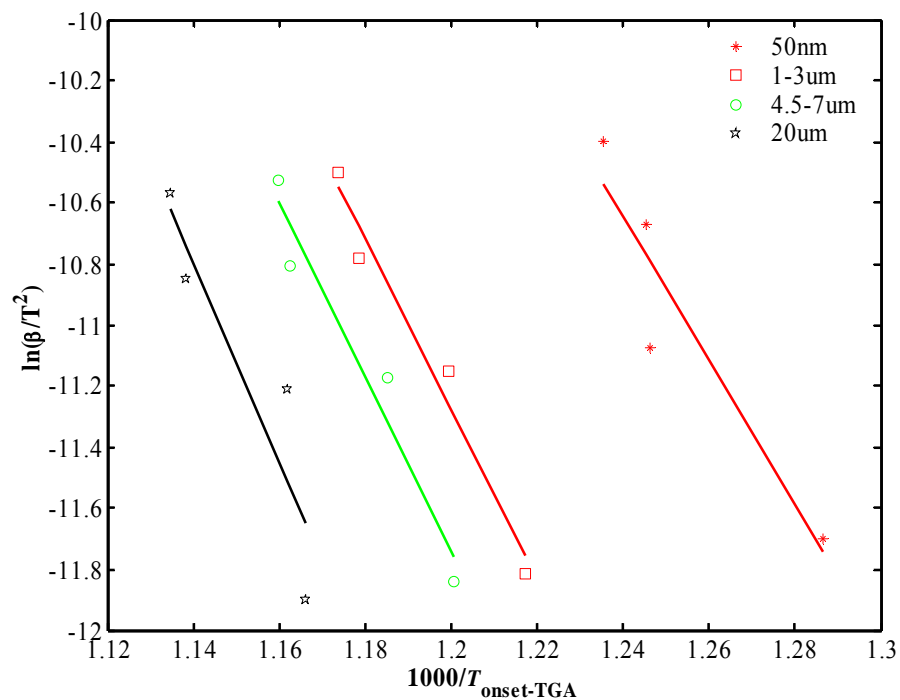


Figure 6.14: Slope plot to determine activation energy based on  $T_{\text{onset-TGA}}$  using Kissinger method (see Section 5.6.3)

The slope and y-intercept were determined for the linear curve fit lines shown in Figures 6.11 through 6.14. These values were used to calculate  $E_a$  and  $Z$  in Tables 6.3 and 6.4. Figure 6.15 shows a plot of  $E_a$  determined by  $T_{onset}$  as a function of Al particle size.

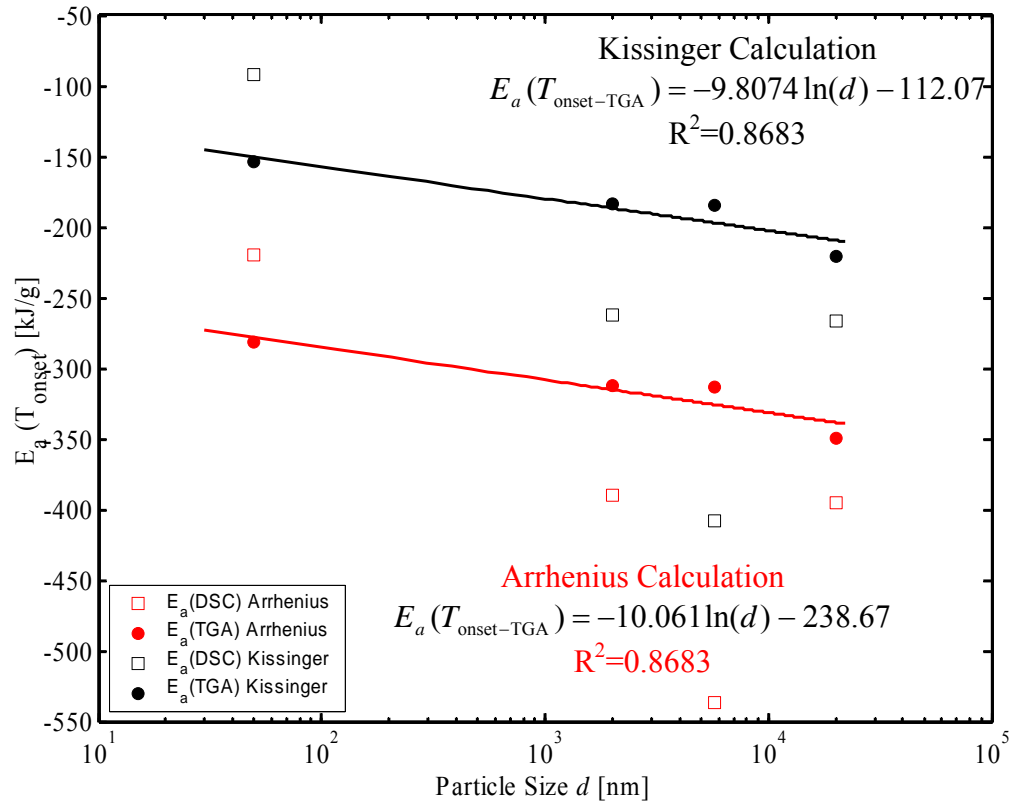


Figure 6.15: Activation energy ( $E_a$ ) calculated by  $T_{onset}$  as a function of particle diameter

Table 6.3: Activation energy for Al+O<sub>2</sub> reactions calculated from DSC and TGA data

Al Particle Size	Activation Energy, $E_a$ [kJ/g]					
	Onset Arrhenius		Onset Kissinger		Peak Arrhenius	Peak Kissinger
	DSC	TGA	DSC	TGA	DSC	DSC
50 nm	-219.80	-281.64	-92.19	-154.03	-568.17	-440.25
1-3 $\mu$ m	-390.35	-312.27	-262.06	-183.74	-239.73	-104.22
4.5-7 $\mu$ m	-536.94	-313.73	-408.45	-184.98	-220.91	-85.77
20 $\mu$ m	-395.16	-349.62	-266.26	-220.46	-178.92	-42.96

Table 6.4: Pre-exponential factor for Al+O<sub>2</sub> reactions calculated from DSC and TGA data

Al Particle Size	Pre-Exponential Factor Z					
	Onset Arrhenius		Onset Kissinger		Peak Arrhenius	Peak Kissinger
	DSC	TGA	DSC	TGA	DSC	DSC
50 nm	4.56E-09	1.25E-11	-11.09	-18.53	6.35E-24	-52.95
1-3 μm	9.02E-17	1.56E-13	-31.52	-22.10	2.34E-15	-12.54
4.5-7 μm	2.47E-23	9.20E-14	-49.13	-22.25	6.42E-14	-10.32
20 μm	1.45E-17	1.07E-15	-32.03	-26.52	1.05E-11	-5.17

The data from Table 6.3 is plotted as a function of Al particle size in Figures 6.15 and 6.10. There is no apparent trend in  $E_a$  calculated from the DSC  $T_{\text{onset}}$  data as predicted by the poor  $T_{\text{onset-DSC}}$  to  $\beta$  relationship shown in Appendix F (Figure F.1). Figure 6.15 does display a decreasing logarithmic curve fit of  $E_a$  calculated from the TGA  $T_{\text{onset}}$  data as a function of Al particle size. Note that it has been shown that nm-Al+MoO<sub>3</sub> samples are two-orders of magnitude more ignition sensitive than μm-Al+MoO<sub>3</sub> samples when ignited in laser experiments [24]. It can also be shown in a simple lab experiment that nm-Al is easily ignitable and sustains a self-propagating flame when burned in air. The μm-Al samples tested in this work will not ignite or self-propagate in air alone. Data in Figure 6.15 supports this phenomenon. The nm-Al samples display 11-24% less magnitude  $E_a$  compared to the μm-Al samples. The Kissinger method approximation of  $E_a(T_{\text{onset-TGA}})$  produces magnitudes 36-45% (absolute magnitude) less than similar Arrhenius  $E_a(T_{\text{onset-TGA}})$  values.

#### 6.4 Summary

Results from Al+O<sub>2</sub> reactions at DSC heating rates ranging from 5 to 20 Kpm have shown at least three significant trends:

1. Nano and micron Al particle sizes (nano and micron) begin to oxidize in the solid state as shown by  $T_{\text{onset}} < T_{mp}(\text{Al})$  in Figures 6.3 and 6.4. Confirmed by data from [17] [54] [59] and [62].
2. Nano-Al samples show a rapid single stage reaction while micron-Al samples show two and three stage reactions with slow mass gain and strong resistance for completing

the oxidation reaction. Nano-Al samples have shown average mass gain rates as large as 662.1 %/min compared to micron-Al samples oxidizing at < 3 %/min.

3. Nano-Al particles display at least 11% lower activation energy magnitude than micron-Al particles (based on the more reliable and objective onset temperature data).

All of the models in Table 6.1 describe multiple stage reactions that can be classified by specific temperature intervals. Like Cabrera and Mott [10], Suvaci et al. [59] and Trunov et al. [62] the DSC/TGA micron-Al experiments in this work do show a three-stage reaction. None of the models in Table 6.1 accurately describe the nm-Al+O<sub>2</sub> reaction.

Note the aluminum particle size distributions in Figures 1.3 and 1.4. Moore et al. [41] presented SEM images of the 3-4.5µm-Al manufactured by Alfa Aesar and tested in this work (shown in Figure 6.16). The images below show that the 3-4.5µm-Al has a true particle diameters ranging from 500 nm to 10 µm. It is believed that most of the micron Al samples were manufactured by ball-milling and sieving. Seiving allows no control of the minimum particle size and the 3-4.5µm-Al manufacturer classification is assumed to be just an average particle representation. This large particle size distribution may exist for the other µm-Al samples presented in this chapter and account for the multiple stage reactions. For example the particles <1µm in Figure 6.16 may be reacting in the first exotherm of Figure 6.2 (similar to the 50nm-Al in Figure 6.1) and the second and third exotherms may be caused by two larger micron-diameter particle regimes. Note that Trunov et al. [62] identified three reaction stages for 3-4.5µm-Al also manufactured by Alfa Aesar (shown in Figure 6.16) with a similar expected particle size distribution.

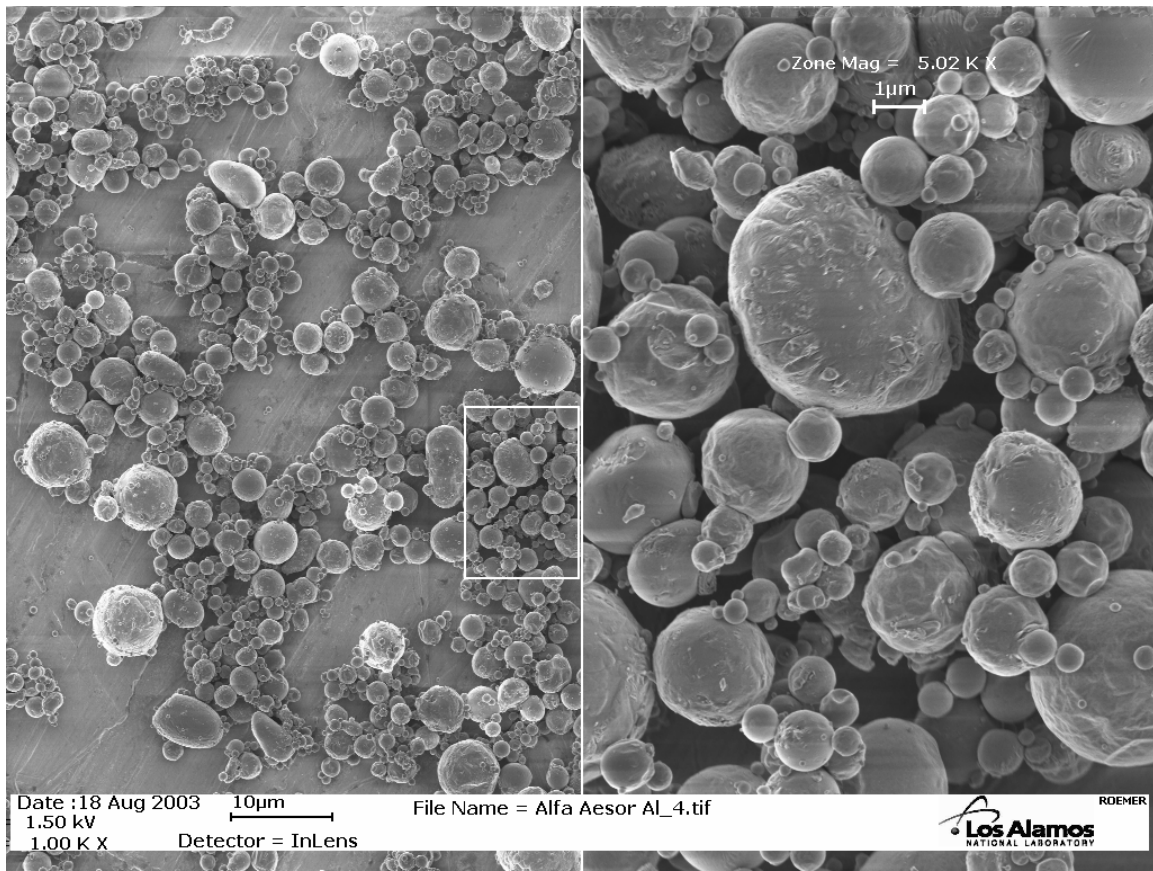


Figure 6.16: SEM Image of 3-4.5 $\mu$ m-Al manufactured by Alfa Aesar

Taken by Ed Romer under the direction of Dr. Steve Son LANL [41]

It has also been suggested [47] that crystalline structure of the Al core may influence the oxidation behavior. The 50nm-Al produced by Nanotechnologies is fabricated by the nucleation of a single Al crystal that is grown to specified diameter. Fabrication by ball-milling and attrition-milling does not allow control of the Al core crystalline organization. Thus the  $\mu$ m-Al samples may have multiple Al crystals within a single  $\mu$ m-Al core. The unorganized Al core structure combined with diffusion effects of multiple crystals may vary from one micron particle to the next in the same sample. This unmeasured variation in the  $\mu$ m-Al samples may also account for the multiple phase reaction mechanisms.

Other researchers [14][15][17][19][54][59][61][62] (see Table 6.1) have put much emphasis on the role of the  $\text{Al}_2\text{O}_3$  coating on Al combustion. Obviously the aluminum oxide coating is a physical barrier resisting atomic diffusion. Eisenrich et al. [17] believe

that oxygen atoms (or ions) diffuse through the oxide layer to react with the Al core inside the oxide shell. Cabrera and Mott [10] have discussed that it is more likely that Al ions diffuse through the oxide layer to react on the exterior surface of the oxide shell. Dreizen et al. [62] and Suvaci et al. [59] have expanded this theory further to introduce a model of physical gaps or diffusion channels forming in the oxide layer to allow faster diffusional movement. Dreizen has [14][15] predicted that there are temperature dependent phase changes in the aluminum-oxide layer that may generate deteriorating stresses within the oxide layer. Once the phase transitions occur, differential expansion can cause regions (channels) of exposed Al core allowing uninhibited diffusion paths.

Data from this work has shown that the oxide layer effects nano and micron-sized Al particles uniquely. Data confirms that the oxide layer thickness and composition contribute to the Al particle combustion mechanisms. Oxide layer thickness can be analyzed based on the overall strength as a diffusion barrier. Developing Dreizen et al. [62] and Suvaci et al. [59] models further, one can surmise that oxide layer of the 50nm-Al is quickly broken and ineffective as a diffusion barrier whereas the  $\mu\text{m}$ -Al samples' oxide layer plays a significant role as a partial barrier throughout the experiment.

The high surface area of the nm-Al sample promotes rapid chemical energy generation simultaneously at multiple locations on the surface of a single particle and other surrounding particles. The rapid elevation in energy (Figure 6.1) and local temperatures will induce large thermal stress that can physically break the thin oxide coating. This condition may not occur in the  $\mu\text{m}$ -Al reactions. First the reduced surface area does not produce the magnified transient temperature changes, thus reducing spatial thermal gradients and reducing the thermal expansion effects. Second the true  $\mu\text{m}$ -Al particles will have thicker  $\text{Al}_2\text{O}_3$  layers (1-4 $\mu\text{m}$  thick based Al purity, average particle diameter and mass balance calculation). A thicker  $\text{Al}_2\text{O}_3$  layer will have improved stress toleration and better resistance to thermal deformation.

In summary, it is believed that the nm-Al particles quickly obliterate any oxide layer by rapid thermal expansion and subsequent rapid reaction of the exposed Al core. The huge number of simultaneous surface oxidation sites produces so much energy that the initially formed "diffusion channels" are uncontrollably expanded creating exponentially

increasing exposed Al surface area. The nm-Al reaction quickly travels to completion in a single step of bypassing the  $\text{Al}_2\text{O}_3$  layer. This also explains the influence of heating rate on reaction behavior. Slower heating rates to ignition will create a controlled volume of simultaneously diffusing ions, thus limiting the simultaneous reactions and exponential energy growth.

The  $\mu\text{m}$ -Al samples are better described by the controlled models in Table 6.1: 1) slow oxide layer growth formed by Al ion diffusion, 2) formation of diffusion channels in the oxide layer creating faster diffusion rates (high  $\text{dm}/\text{dt}_{\text{peak}}$  at second exotherm) and finally 3) closure of the diffusion channels allowing slow diffusion through oxide grain structure. Fast or slow heating rates to the ignition temperature do not provide the exponential growth in diffusing particles (because of insufficient surface area) and exponential growth in chemical energy production.



# CHAPTER VII

## Al/MoO<sub>3</sub> THERMITE TG/DSC ANALYSIS

### 7.1 TG/DSC Results

Table 7.1 shows the temperature and enthalpy values measured from the DSC curves corresponding to the reactions of Al+MoO<sub>3</sub> shown in Appendix G. The results shown are for the main exothermic reaction. For exothermic curves with multiple peaks (see the 80 and 120nm-Al+MoO<sub>3</sub> curves in Appendix G) in the same exotherm, T<sub>peak</sub> was recorded as the first of the sequential peaks. The results shown in Table 7.1 are plotted as a function of Al particle size in Figures 7.1 through 7.3.

Table 7.1: DSC data from Al/MoO<sub>3</sub> thermite reactions

Material	Nanotechnology			AEE 1-3μm	Afla Aesar			Sigma Aldrich 20μm	
	50 nm	80nm	120nm		3-4μm	4.5-7μm	10-14μm		
Test/DSC run									
2.5 kpm	T <sub>onset</sub> [°C]	414.1	450.5	468.8					
	T <sub>peak</sub> [°C]	511.5	500.8	519.7					
	Dh [J/g]	3357	3430	4000					
5 kpm	T <sub>onset</sub> [°C]	425.1	460.4	457.1	808	818	861	943.2	987.3
	T <sub>peak</sub> [°C]	522.3	507.9	528.1	900.3	901.6	906.6	961.7	996.6
	Dh [J/g]	2377	1604	2428	1469	1500	1306	1208	1112
10 kpm	T <sub>onset</sub> [°C]	435.1	475.9	466.2	901.7	888.5	923	950.5	991.9
	T <sub>peak</sub> [°C]	527.1	518.9	538.4	918.2	909.1	963.5	978	1005
	Dh [J/g]	2039	1659	2386	1567	1898	1860	1296	1246
15 kpm	T <sub>onset</sub> [°C]	443.1	483.9	488	914.2	921.4	930.9	975.7	1004.3
	T <sub>peak</sub> [°C]	525.5	524.2	547.9	929.7	939.3	957.2	1004.2	1018.7
	Dh [J/g]	1885	2192	1808	1752	1898	2117	1693	1270
Average of Heating Rates									
T <sub>onset</sub> [°C]	429.4	467.7	470.0	874.6	876.0	905.0	956.5	994.5	
T <sub>peak</sub> [°C]	521.6	513.0	533.5	916.1	916.7	942.4	981.3	1006.8	
Dh [J/g]	2415	2221	2655.5	1596	1765	1761	1399	1209.3	
Standard Deviation of Heating Rates									
T <sub>onset</sub> [°C]	12.6	15.0	13.0	58.0	52.8	38.3	17.1	8.8	
T <sub>peak</sub> [°C]	7.0	10.6	12.3	14.8	20.0	31.2	21.4	11.2	
Dh [J/g]	661.1	848.3	939.9	143.7	229.8	414.5	258.4	85.1	

Figure 7.1 shows the onset temperatures for the main exothermic reaction shown in each DSC experiment. The solid diamonds and trendline represent the average value of the 3 or 4 heating rates for a specific particle size. The figure shows a logarithmically increasing trend in  $T_{\text{onset}}$  as a function Al particle size. The average  $T_{\text{onset}}$  ranges from  $429.4 \pm 12.6$  to  $994.5 \pm 8.8$  °C for 50 nm and 20  $\mu\text{m}$ -Al/MoO<sub>3</sub> composites respectively.

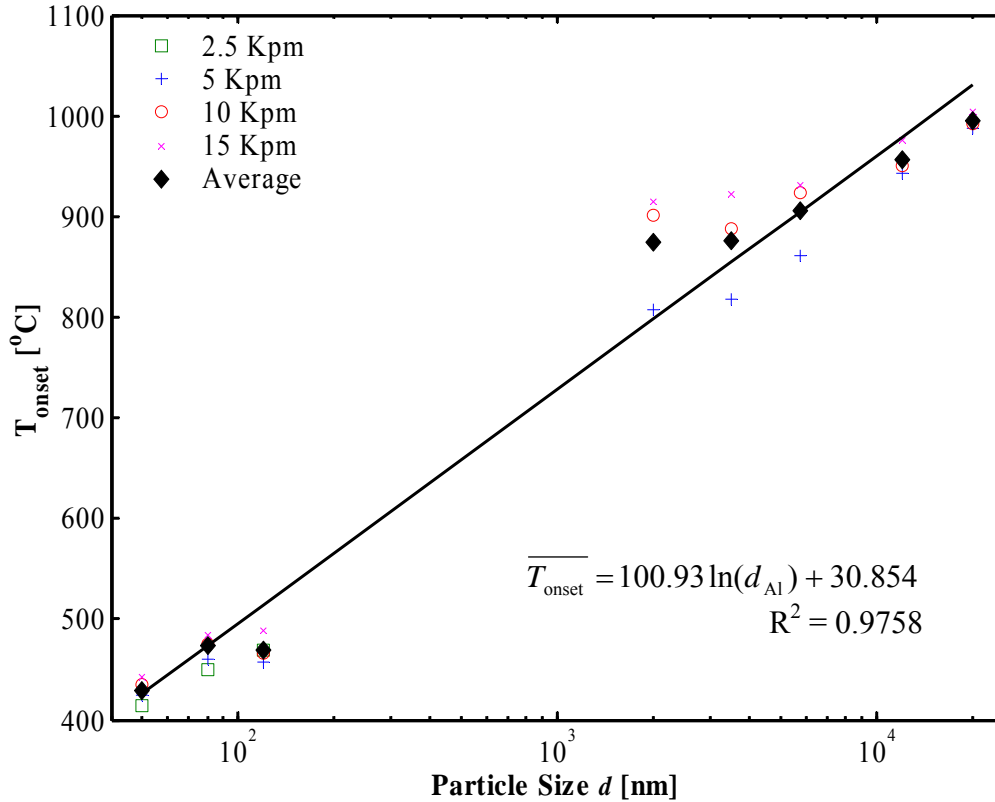


Figure 7.1: Onset temperature as a function of Al particle size for various heating rates

Figure 7.2 shows the peak temperatures for the main exothermic reaction shown in each DSC experiment. The solid diamonds and trendline represent the average value of the 3 or 4 heating rates for a specific particle size. The figure shows a logarithmically increasing trend in  $T_{\text{peak}}$  as a function Al particle size. The average  $T_{\text{peak}}$  ranges from  $521.6 \pm 7.0$  to  $1006.8 \pm 11.2$  °C for 50 nm and 20  $\mu\text{m}$ -Al/MoO<sub>3</sub> composites respectively.

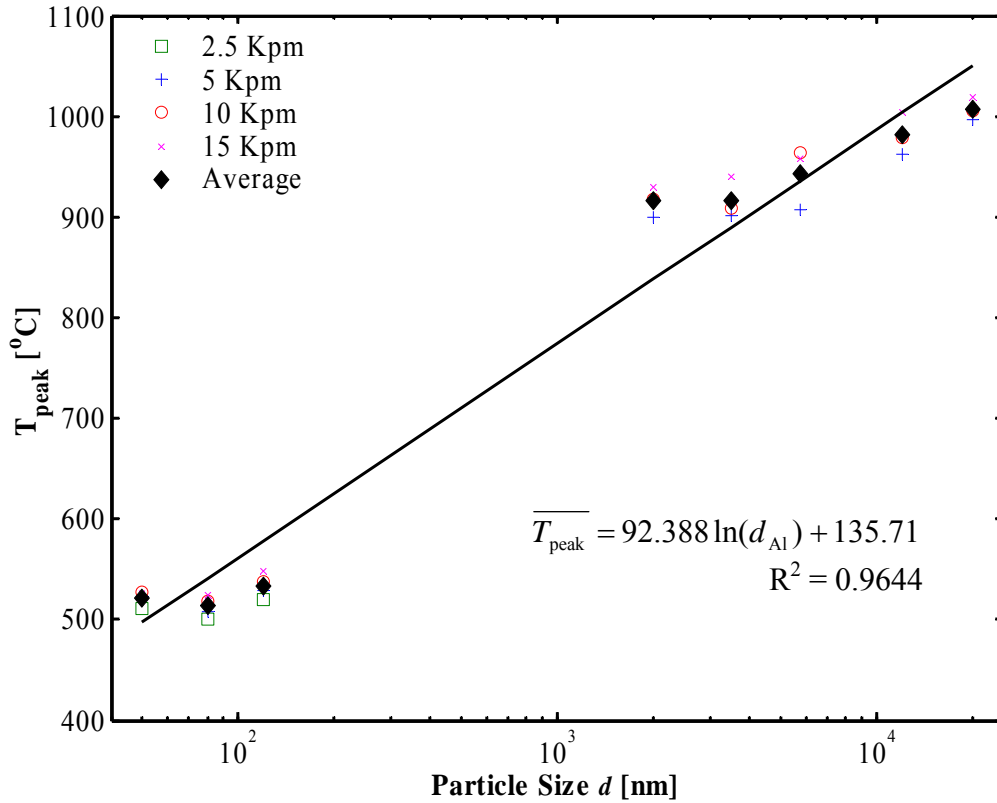


Figure 7.2: Peak temperature as a function of Al particle size for various heating rates

Figure 7.3 shows the change in enthalpy or heat of reaction for the main exothermic peak shown in each DSC experiment. The heat of reaction  $\Delta h_{rxn}$  is measured as the area under the DSC curve from  $T_{onset}$  to the temperature where the curve returns to a flat baseline. The solid diamonds and trendline represent the average value of the 3 or 4 heating rates for a specific particle size. The figure shows a logarithmically decreasing trend in reaction energy as a function Al particle size. The average  $\Delta h_{rxn}$  ranges from  $2415 \pm 661.1$  to  $1209.3 \pm 85.1$  J/g for 50 nm and 20  $\mu\text{m}$  Al/MoO<sub>3</sub> composites respectively. Fischer [19] reported a theoretical heat of reaction of 4705 J/g for an Al+MoO<sub>3</sub> reaction (Discussed in Chapter IX).

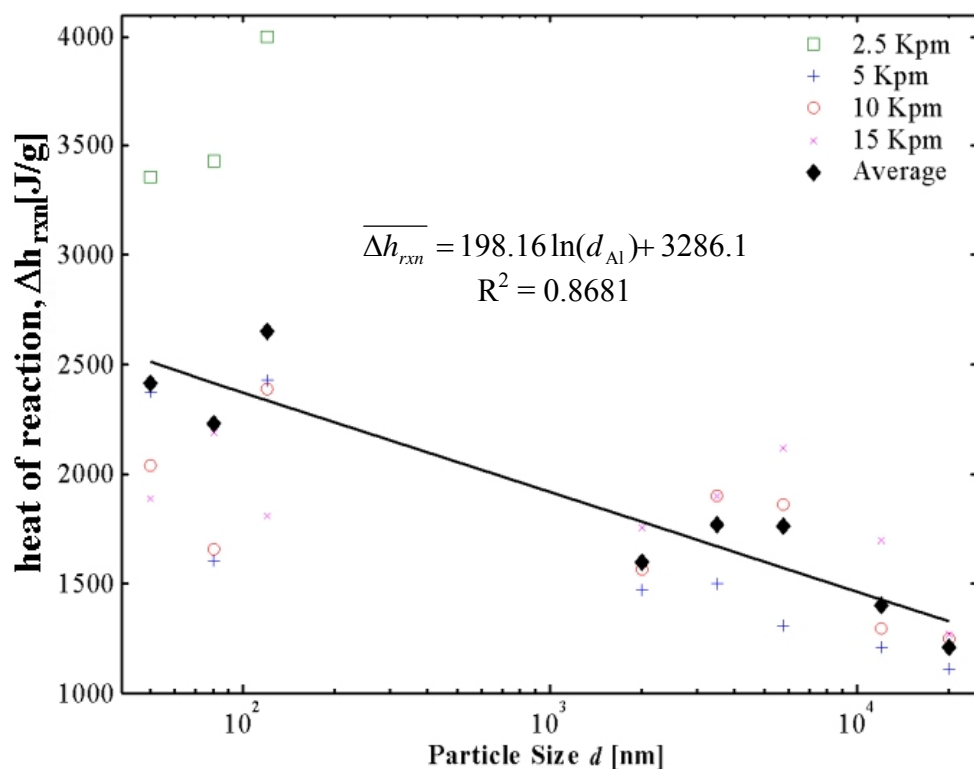


Figure 7.3: DSC Heat of reaction as a function of Al particle size for various heating rates

The large variability of the nm-Al+MoO<sub>3</sub> data points in Figure 7.3, are due to the temperature dependence of the exothermic peak and the overlapping of endo/exothermic peaks. Section 6.3 discusses the observed behavior that the nm-Al+MoO<sub>3</sub> reactions are not self-propagating. This behavior affects the accuracy and applicability of reaction energies shown in Figure 7.3. The short (fast  $\beta$ ) and extended (slow  $\beta$ ) reaction times are used to integrate the DSC measurement of mW/mg to J/mg (shown in Figure 7.3). Figure 7.3 shows that the area under the DSC curve (the reaction energy) consistently increases with decreasing heating rate ( $\beta$ ).

## 7.2 Kinetic Parameter Approximation

The chemical kinetic parameters  $E_a$  and  $Z$  were estimated using the Arrhenius equation (Section 5.6.2) and the Kissinger method (Section 5.6.3). It is noted that many

other similar methods exist as listed in the literature review (see Table 5.2). The main assumption in the Kissinger method is that at an endo/exothermic peak in a DSC curve, the reaction has reached a maximum conversion rate  $(d\alpha/dT|_{\max})$  as described by equating the derivative of Eq. 5.12 to zero to derive Eq. 5.13. It has been suggested that  $T_m$  in Eq. 5.13 can be the temperature at any fixed state of transformation [60]. Thus, the Kissinger method has also been applied using onset temperatures from DSC or TGA data [60]. In some experiments (such as Al oxidation in a gaseous environment) the  $T_{\text{onset}}$  is more consistent than  $T_{\text{peak}}$ . For this reason, the activation energy and pre-exponential factors were determined by applying the Arrhenius equation (Eq. 5.8) and the Kissinger method (Eq. 5.14) to the onset and peak temperature data from the Al+MoO<sub>3</sub> DSC data (TGA measurements are negligible in the Al+MoO<sub>3</sub> solid-solid reaction).

### 7.2.1 Reaction Parameters Calculated by Onset Temperatures

Figures 7.4 and 7.5 show the slope plots using the Arrhenius equation analysis Kissinger method calculated by  $T_{\text{onset}}$ .

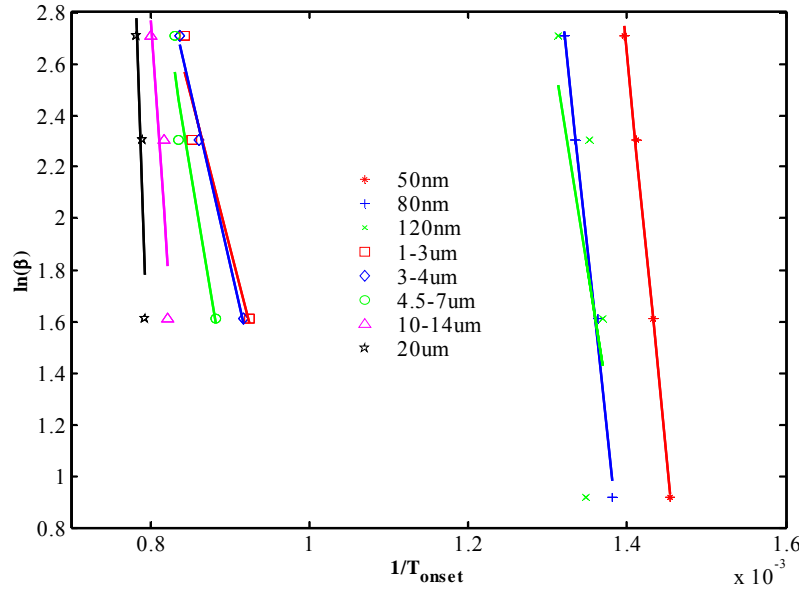


Figure 7.4: Slope plot to determine activation energy based on  $T_{\text{onset}}$  based on Arrhenius equation analysis Kissinger method (see Section 5.6.2)

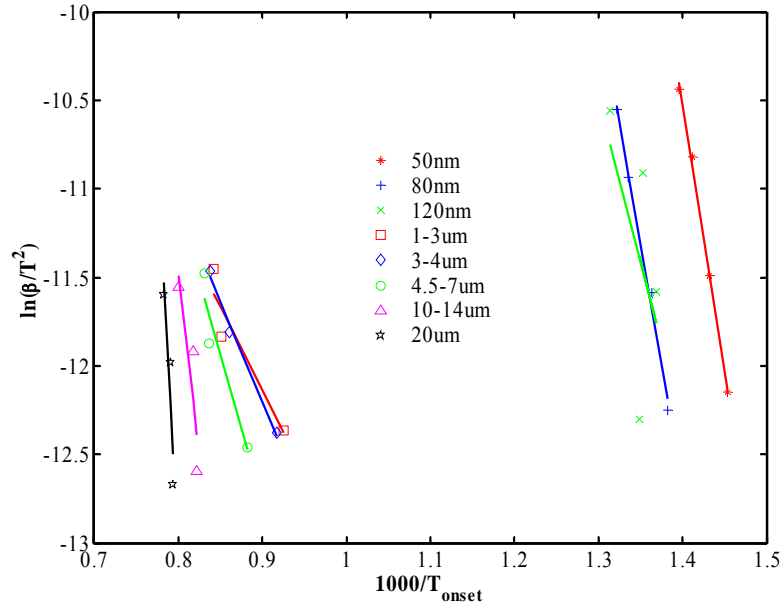


Figure 7.5: Slope plot to determine activation energy based on  $T_{\text{onset}}$  based on Kissinger method (see Section 5.6.3)

Figure 7.6 shows the values  $E_a(T_{\text{onset}})$  approximated for each Al particle size tested determined by the slope values in Figures 7.4 and 7.5. The values in Figure 7.6 are listed in Table 7.2.

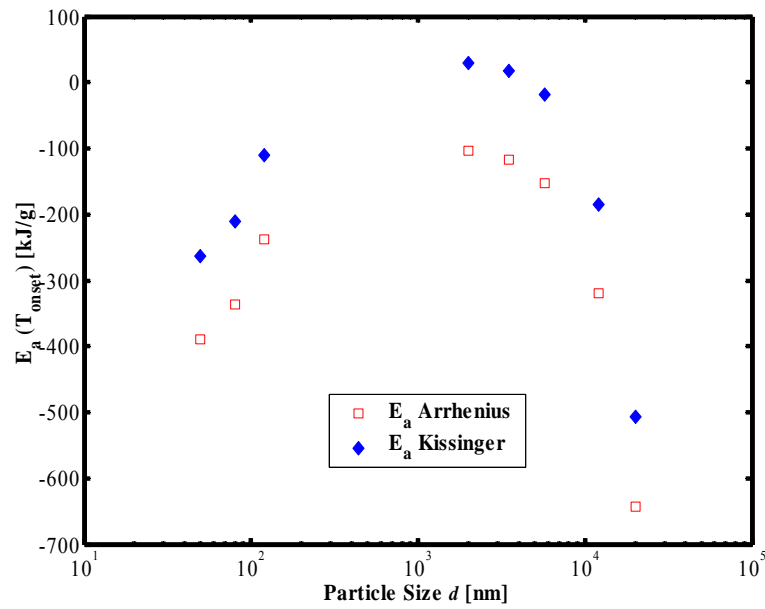


Figure 7.6: Activation energy ( $E_a$ ) calculated by  $T_{\text{onset}}$  as a function of particle diameter

### 7.2.2 Reaction Parameters Calculated by Peak Temperatures

Figures 7.7 and 7.8 show the slope plots using the Arrhenius equation analysis Kissinger method calculated by  $T_{\text{peak}}$ .

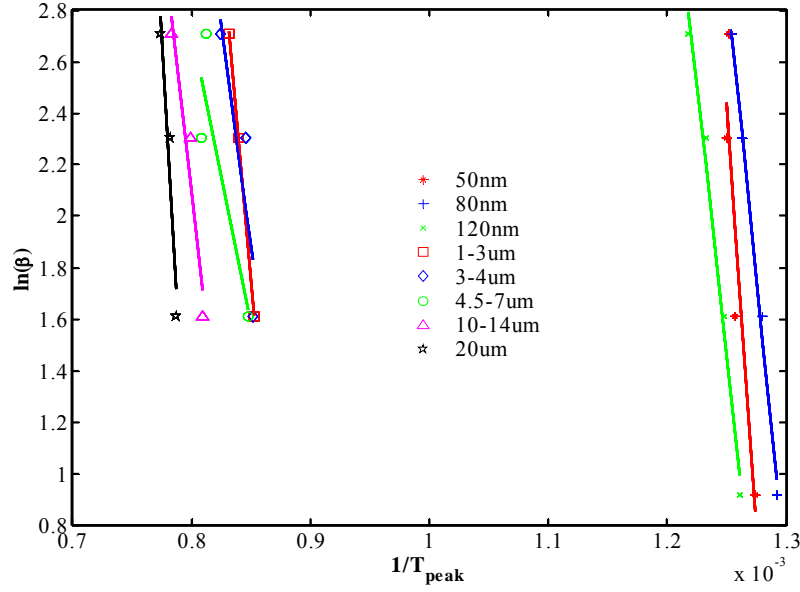


Figure 7.7: Slope plot to determine activation energy based on  $T_{\text{peak}}$  based on Arrhenius equation analysis Kissinger method (see Section 5.6.2)

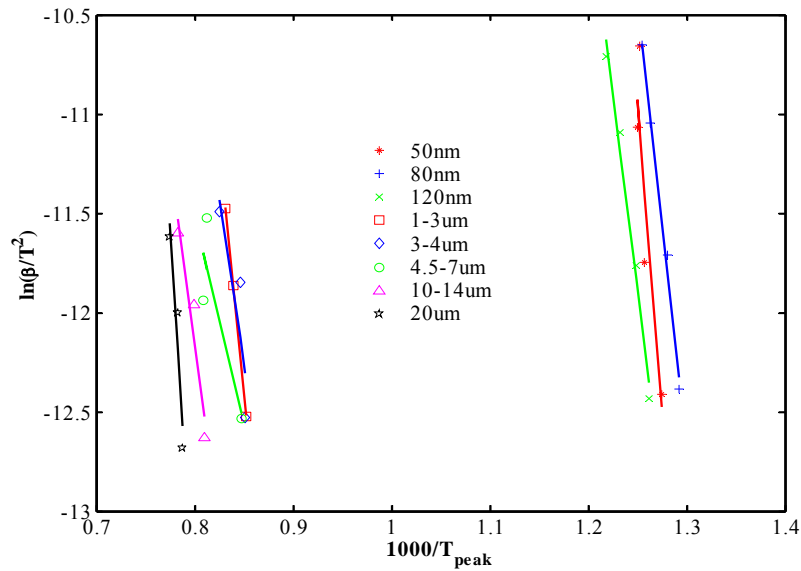


Figure 7.8: Slope plot to determine activation energy based on  $T_{\text{peak}}$  based on Kissinger method (see Section 5.6.3)

Figure 7.9 shows the values  $E_a(T_{\text{peak}})$  approximated for each Al particle size tested determined by the slope values in Figures 7.7 and 7.8. The values in Figure 7.9 are listed in Table 7.2.

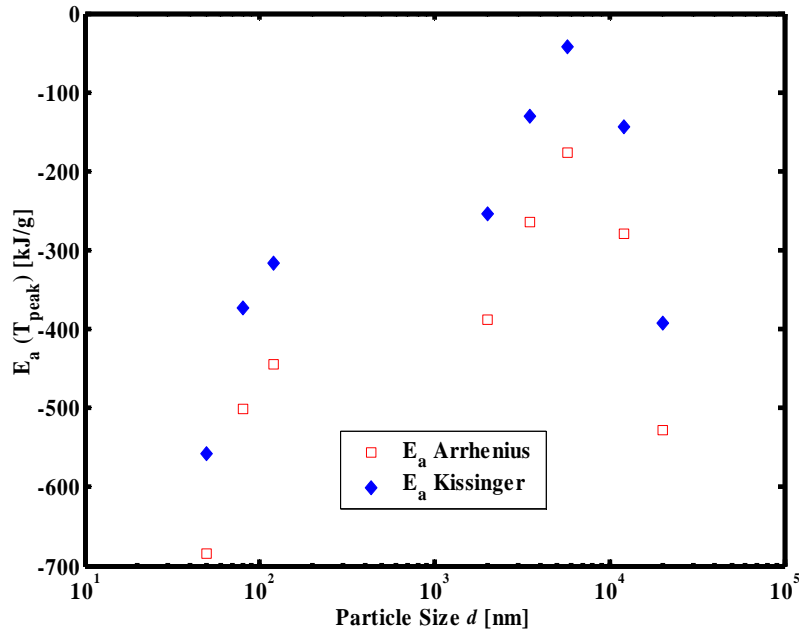


Figure 7.9: Activation energy ( $E_a$ ) calculated by  $T_{\text{peak}}$  as a function of particle diameter

Comparing the two methods of calculation, the Kissinger method produced  $E_a$  values with a 131.3 and 132.2 kJ/mol (average) magnitude increase above the Arrhenius equation results for  $T_{\text{onset}}$  and  $T_{\text{peak}}$  respectively.

Table 7.2: Activation energy for Al+MoO<sub>3</sub> reactions calculated from DSC data

Al Particle Size	Activation Energy ( $E_a$ ) [kJ/mol] Calculated by			
	Arrhenius		Kissinger	
	$T_{\text{onset}}$	$T_{\text{peak}}$	$T_{\text{onset}}$	$T_{\text{peak}}$
50 nm	-388.6	-684.7	-263.0	-557.0
80 nm	-336.9	-501.0	-210.4	-373.5
120 nm	-237.5	-444.0	-110.9	-316.1
1-3 $\mu\text{m}$	-103.8	-388.0	29.7	-253.6
3-4 $\mu\text{m}$	-116.9	-264.6	16.8	-130.2
4.5-7 $\mu\text{m}$	-152.7	-176.5	-18.6	-41.9
10-14 $\mu\text{m}$	-319.7	-279.4	-184.7	-144.1
20 $\mu\text{m}$	-643.1	-528.2	-507.6	-392.5



Calculations of  $E_a$  based on  $T_{\text{onset}}$  and  $T_{\text{peak}}$  show a similar trend: The magnitude of  $E_a$  values steadily decrease for the nano-Al samples (50-80nm), showing the lowest magnitude  $E_a$  values are between 1-7 $\mu\text{m}$ -Al samples, and then the magnitude sharply increasing again for the 10-20 $\mu\text{m}$ -Al samples. Comparing the max and min Al particle sizes, based on  $T_{\text{onset}}$  shows that the 50nm-Al+MoO<sub>3</sub> has a lower magnitude  $E_a$  than the 20 $\mu\text{m}$ -Al/MoO<sub>3</sub> (-388 and -643 kJ/mol respectively – Arrhenius calculations). Alternatively, calculations based on  $T_{\text{peak}}$  show that the 50nm-Al+MoO<sub>3</sub> has a higher magnitude  $E_a$  than the 20 $\mu\text{m}$ -Al+MoO<sub>3</sub> (-685 and -528 kJ/mol respectively – Arrhenius calculations). Again the  $E_a$  calculated by  $T_{\text{onset}}$  seems to present the more accurate data that is support by other experiments. It has been clearly shown by Granier and Pantoya [24] (Figure 4.1) that the 20 $\mu\text{m}$ -Al+MoO<sub>3</sub> samples are far less igniton sensitive than the nanocomposites in laser ignition experiments. The onset temperature  $E_a$  supports the data presented by Granier and Pantoya [24] suggesting that the nanocomposite thermites have a lower magnitude  $E_a$  than similar micron composites.

### 7.3 Reaction Product Analysis

Unlike traditional Al+MoO<sub>3</sub> testing, the controlled heating of the DSC allowed the Al+MoO<sub>3</sub> samples to react relatively slow (as portrayed by the temperature dependent reactions, Chapter VIII) and calm (most reactions left a solid product in the crucible after reacting with the exception of the 40 K/min 80nm-Al+MoO<sub>3</sub> shown in Figure 8.5). Because of the violence of the reaction and the dispersion of products, the Al+MoO<sub>3</sub> products have not been thoroughly studied.

Visual observation of the reactant and products were made by comparing SEM images. Figure 7.10 shows SEM images of A. 20μm-Al+MoO<sub>3</sub> reactants and B. 20μm-Al+MoO<sub>3</sub> products reacted during a 15 K/min DSC heating. The images in the left column show single 20μm (approximate) Al particles coated in nm-MoO<sub>3</sub> crystals (with a few anomaly large MoO<sub>3</sub> sheets). The images in the right column show a more continuous structure (absent of the large void between micron size particles) with a few distinct crystalline structures. It is suggested that the crystalline structures in the product images are condensed molybdenum (larger crystals and more defined in images B 2 and 3).

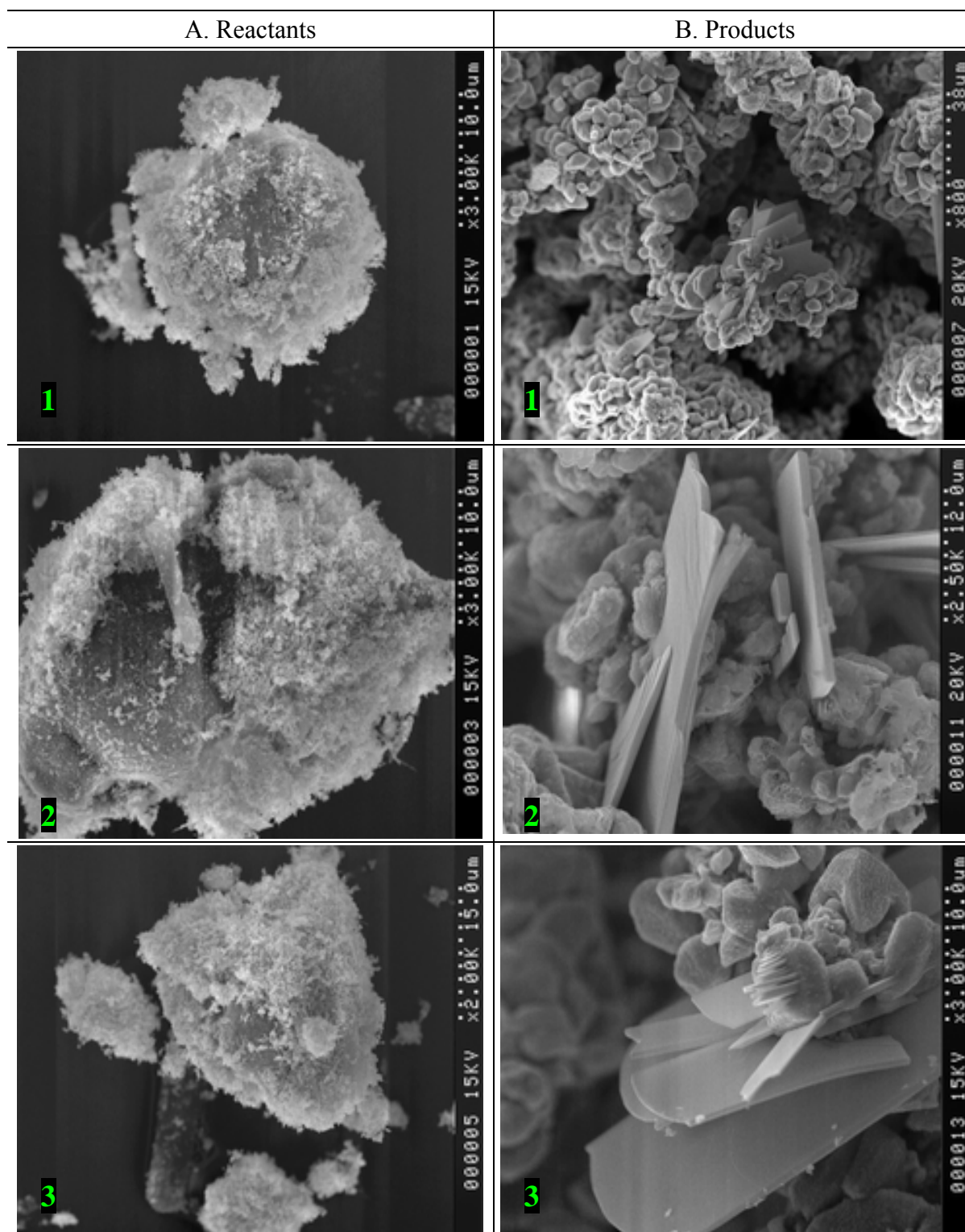


Figure 7.10: SEM Images of 20 $\mu$ m-Al+MoO<sub>3</sub> before (A) and after (B) combustion

Figure 7.11 shows the microscopic images of the reactants and products of 10-14 $\mu\text{m}$ -Al+MoO<sub>3</sub> reacted in the DSC at 15 K/min heating. Figure 7.11 A1 shows several individual micron size Al particles coated in the nm-MoO<sub>3</sub> crystals. As shown in this image the particles do range in diameter around 10-14 $\mu\text{m}$ , but some of particles are not spherical as stated. Figure 7.11 A2 shows what appears to be at least two micron size Al particles coated in MoO<sub>3</sub> with spherical shape and diameters of approximately 18 and 7.5  $\mu\text{m}$ .

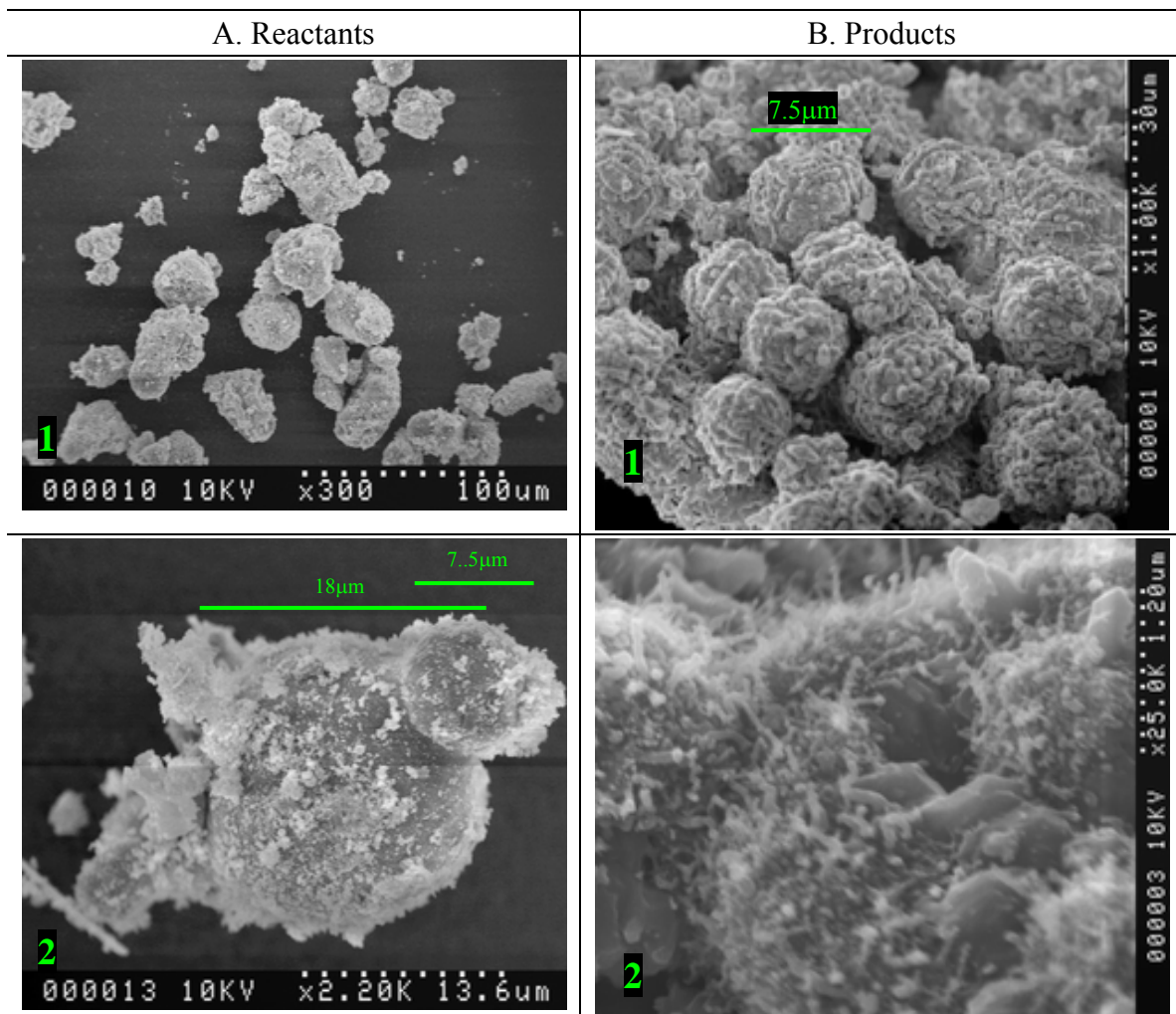


Figure 7.11: SEM Images of 10-14 $\mu\text{m}$ -Al+MoO<sub>3</sub> before (A) and after (B) combustion

Unlike the 20 $\mu\text{m}$ -Al+MoO<sub>3</sub> products, Figure 7.11 B1 does not appear to be as homogeneous and continuous. The product in Figure 7.11 B1 still shows the spherical

shape of the micron Al particles that were apparently agglomerated or sintered during the reaction.

The 10-14 $\mu$ m products also showed many images of fibrous whiskers (Figure 7.11 B2). It has been suggested that whisker formation during an Al oxidation reaction is the rapid deposition (or solidification) of vaporized Al<sub>2</sub>O<sub>3</sub> products [18][25] and [39]

#### 7.4 Summary

At least three significant observations can be formed based on the DSC analysis of Al+MoO<sub>3</sub> thermites.

1. Nanocomposite thermites do ignite at lower temperatures than micron-composites. The three nanocomposites thermite samples show an average  $T_{\text{onset}}$  of 455.7°C, which is lower than the Al melting temperature or MoO<sub>3</sub> sublimation indicating that it is a solid-solid reaction. Based on the largest exothermic peak in DSC experimental data, the micron thermites show an average  $T_{\text{onset}}$  between 874.6 and 994.5°C for 1-3 and 20 $\mu$ m respectively which is above the phase transition temperature of both reactants indicating a liquid Al and gaseous MoO<sub>3</sub> reactant state. The increasing trend in  $T_{\text{onset}}$  versus particle size (Figure 7.1) supports the laser ignition time data presented by Granier and Pantoya [24].
2. DSC experiments may confirm incomplete reactions caused by heating rates and Al particle size. Figure 7.3 shows that the nanocomposite heat of reaction ( $\Delta h_{\text{rxn}}$ ) values dramatically decrease with increasing heating rate. Theory suggests that  $\Delta h_{\text{rxn}}$  should be constant and dependent only on molecular properties for the same Al+MoO<sub>3</sub> reaction, with the same stoichiometry [19].

In a comparison of heating rate effects, the three nanocomposite samples suggest that the Al+MoO<sub>3</sub> reaction is path dependent displaying variable  $\Delta h_{\text{rxn}}$  depending on the DSC heating rate. The nanocomposite samples heated at 2.5 Kpm display an average (of the three nanoparticle sizes)  $\Delta h_{\text{rxn}}$  of 3596 J/g, which is reduced to an average  $\Delta h_{\text{rxn}}$  of 1962 J/g for the 15 Kpm experiments. This suggests that the reaction is proceeding

differently based on heating rate and that the process is preventing complete reaction of all of the reactants (preventing the maximum energy production).

In a comparison of  $\Delta h_{\text{rxn}}$  versus Al particle size, Figure 7.3 shows that the micron composite samples consistently produce lower heat of reaction than the nanocomposite samples. Models of Al oxidation [54][59][62] combined with experimental results in this work (Chapters VI and IX) suggest that the opposing processes of  $\text{Al}_2\text{O}_3$  growth versus the formation of  $\text{Al}_2\text{O}_3$  diffusion barriers prevents the micron samples from completely reacting. In summary, as the micron reaction proceeds each Al particle forms thicker organized  $\text{Al}_2\text{O}_3$  layers. This oxide layer eventually prevents any diffusion before the total Al core mass is consumed. Thus the micron composite  $\Delta h_{\text{rxn}}$  values shown Figure 7.3 are representative of even more incomplete reactions than the nanocomposites discussed earlier. Note that the micron-Al+ $\text{MoO}_3$  DSC  $\Delta h_{\text{rxn}}$  values are only for the main exotherm and do not include area calculations of the other smaller exotherms.

3. Activation energy values based on thermite DSC experiments, suggest an optimum sensitivity (based on a minimum  $E_a$  magnitude) for composites containing Al particles between 120nm and 1 $\mu\text{m}$  diameter. Activation energy values determined by  $T_{\text{onset}}$  and  $T_{\text{peak}}$  (Figures 7.6 and 7.9 respectively) show decreasing  $E_a$  magnitude for increasing nano-regime Al particle sizes and decreasing  $E_a$  with increasing micron-regime Al particle sizes. Similar to the Al+ $\text{O}_2$  DSC experiments in Chapter VI, the  $E_a(T_{\text{onset}})$  data appears to be the most accurate based on consistent trends and support of sensitivity data presented by [24]. This may be true due variations in  $T_{\text{peak}}$  caused by reaction path variations.

## CHAPTER VIII

### TEMPERATURE DEPENDENT AL+MOO<sub>3</sub> REACTION MECHANISMS

#### 8.1 Introduction

Figure 5.6 shows an overlapping exothermic reaction (starting around 265.5°C) and endothermic Al melt (starting around 650°C) of 40nm-Al+MoO<sub>3</sub>. This overlapping data was shown in all three nm-Al samples (see Appendix G). As discussed earlier, the overlapping of opposing peaks prevents an accurate measurement of reaction enthalpy. Further DSC experiments were performed to resolve the exothermic reaction and endothermic Al melt by slowing the DSC heating rate. Experiments were performed for DSC heating rates as low as 2.5Kpm and as high as 40Kpm. Results show that the three different nm-Al+MoO<sub>3</sub> DSC reactions proceed only by increasing temperatures. Thus the reaction duration and reaction rates are dependent on the DSC heating rate and the exothermic and endothermic peaks could not be resolved.

Experiments were performed on nano and micron-Al+MoO<sub>3</sub> reactions by applying various DSC heating rates and also applying transient isotherms. DSC heating was intentionally stopped at different temperatures during the main exothermic reactions. The isothermic temperature was systematically varied to evaluate the existence of a threshold temperature that would allow the reaction to go to completion (or return to the baseline in the same manner as the constant heating rate experiments).

#### 8.2 nm-Al+MoO<sub>3</sub> Reactions

Figure 8.1 shows DSC curves of 80nm-Al+MoO<sub>3</sub> at heating rates varying from 2.5 to 20Kpm. Figures 8.1 A and B are the same data plotted versus time and temperature, respectively. Figure 8.1 B shows the dual peak exotherms occurring similarly for each heating rate (with the signal amplitude reduction for decreasing heating rates).

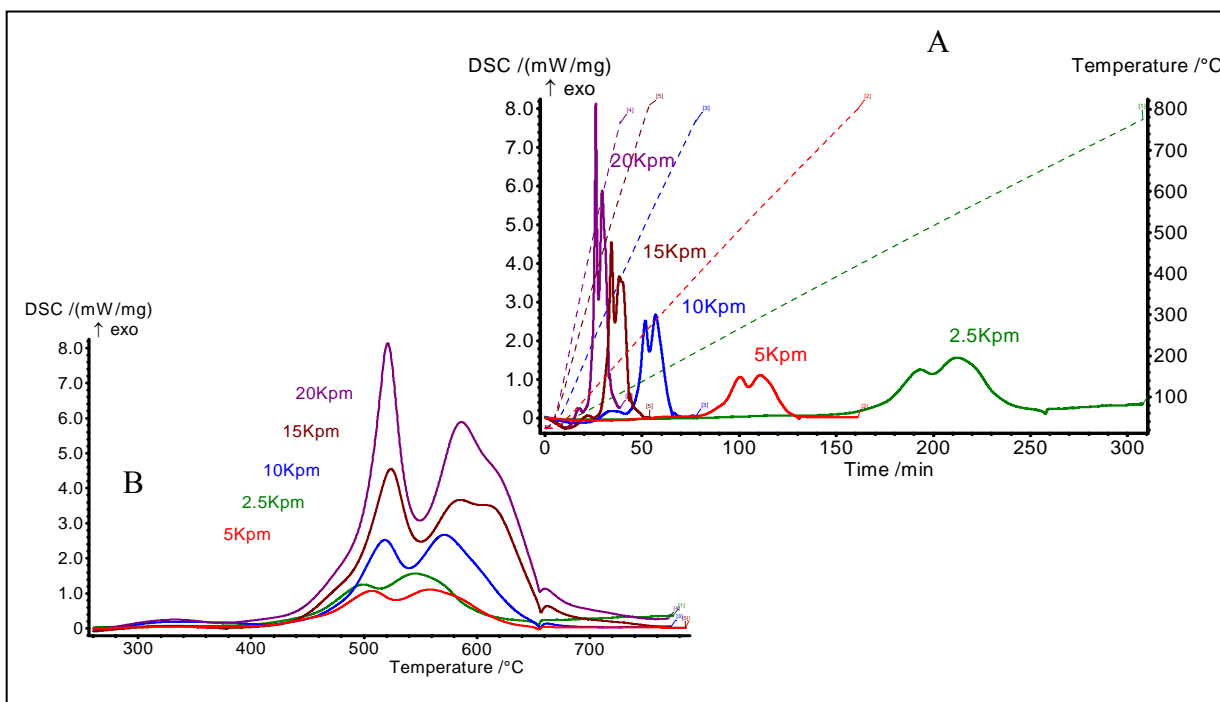


Figure 8.1: 80nm Al+MoO<sub>3</sub> DSC results plotted versus Time (A) and Temperature (B)

Figure 8.1 shows that even at slower heating rates, the 80nm Al/MoO<sub>3</sub> still reacts over the same temperature interval indicating that the reaction is temperature dependent.

Figure 8.2 shows the inverse relationship between the reaction duration and applied heating rate. Reaction duration is measured as the time interval between the exothermic peak deviating from the baseline at onset and returning to the baseline at the reaction end. Figure 8.2 also shows the relationship between reaction energy (heat of reaction) and DSC heating rate. The heat of reaction is measured as the integrated area under the exothermic DSC curve. As mentioned earlier, data suggests that the slower heat rates promote improved reaction mechanisms and more organized diffusion processes allowing a closer to optimal energy production. Figure 8.2 indicates that the nm-Al+MoO<sub>3</sub> reactions are heating rate dependent.



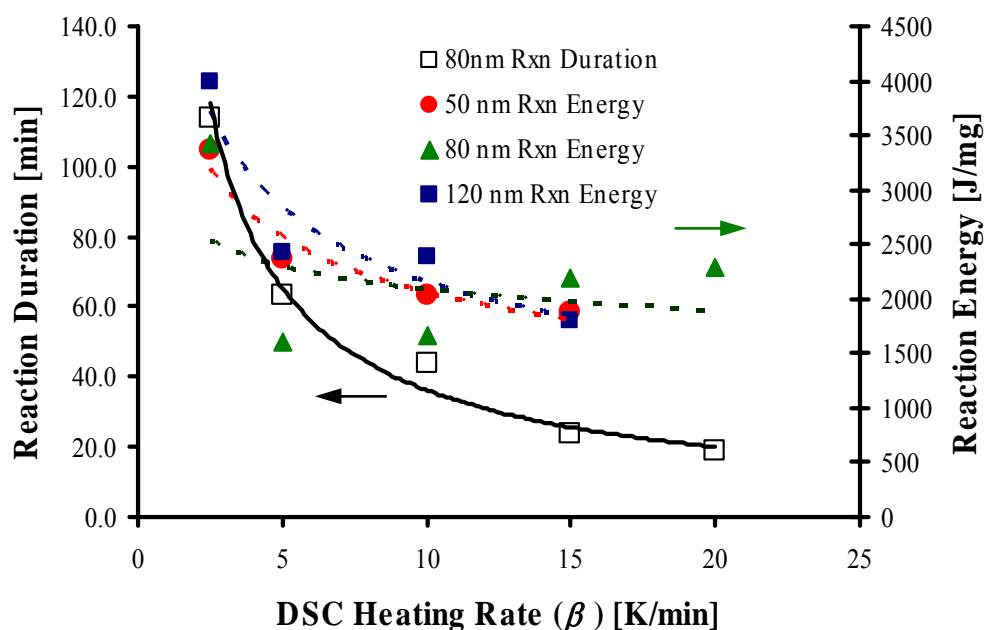


Figure 8.2: Reaction time duration and energy (area under DSC curve) versus heating rate for 80nm-Al+MoO<sub>3</sub>

Further tests were performed on nm-Al+MoO<sub>3</sub> using more elaborate heating programs to confirm and evaluate the severity of temperature dependence. Figure 8.3 shows a DSC curve of 80nm-Al+MoO<sub>3</sub> with a programmed isotherm inside the reaction temperature interval. The solid line is the DSC curve and the broken line is the applied heating program (heating from 30 to 535°C at 10Kpm, isotherm at 535°C for 25min, then heating from 535 to 1000°C at 10Kpm). Figure 8.3 shows that the exothermic reaction started around 410°C and then abruptly stopped when the heating stopped. The moment heat is applied again at 78min, the 80nm-Al+MoO<sub>3</sub> sample begins its exothermic reaction again and continues into the Al melt similar to Figure 8.1.

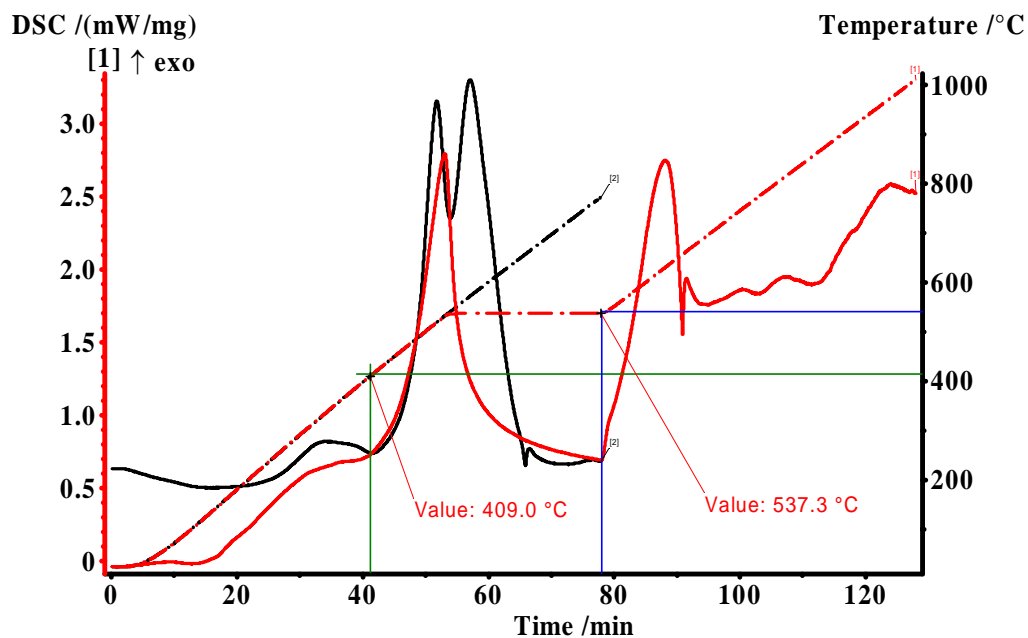


Figure 8.3: Temperature dependence DSC testing for 80nm-Al+MoO<sub>3</sub>

Figure 8.4 shows four DSC experiments of 120nm-Al+MoO<sub>3</sub>: 1) constant heating rate of 15Kpm to 1000°C, 2) 15Kpm heating to 634°C, 3) 15Kpm heating to 523°C, and 15Kpm heating to 430°C. This set of experiments was designed to evaluate if a minimum threshold temperature exists to allow the reaction to continue to completion.

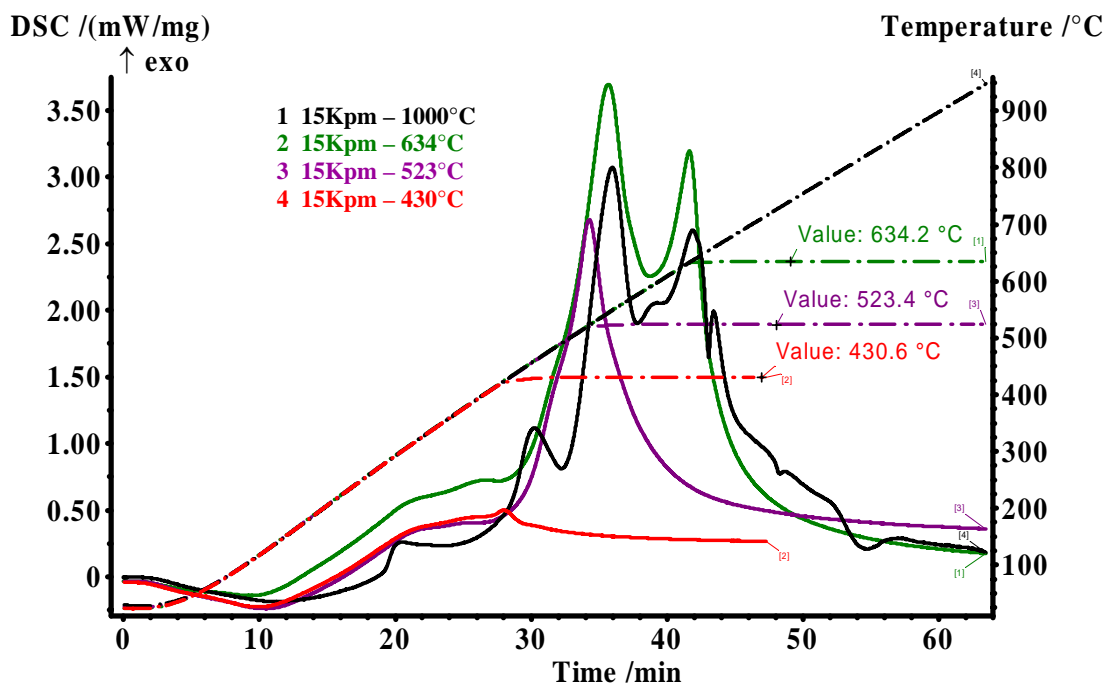


Figure 8.4: Partial reaction threshold testing for 120nm-Al+MoO<sub>3</sub>

Solid lines 2, 3 and 4 show partial reactions ending at the beginning of the specified temperature isotherms. Solid line 4 shows a very small exothermic peak just before the sample reached the 430°C isotherm and then the exothermic reaction stopped and returned to the baseline for the remaining time at 430°C. Similar incomplete reactions occurred for lines 2 and 3 at temperatures of 634 and 523°C respectively indicating that “thermal runaway” was not initiated. Basically, the nm-Al+MoO<sub>3</sub> samples display certain reactions between the Al and MoO<sub>3</sub> that only occurring because an entire range of incremental temperatures (400-700°C) is applied to stimulate the reaction. Unlike traditional experiments of Al+MoO<sub>3</sub> powder and pellets, the exothermic reaction is not self-sustaining (local reactions are not providing enough energy to stimulate neighboring reactions).

The temperature dependence of the nm-Al+MoO<sub>3</sub> reactions is not universally true for all DSC tests. In attempt to evaluate more data points for the activation energy calculations, higher heating rates (>20Kpm) were applied and rapid violent reactions

occurred. Figure 8.5 shows the DSC/TG data from an experiment of 80nm-Al+MoO<sub>3</sub> at 40Kpm. The figure shows a sharp DSC peak compared to the broad peaks shown in Figure 8.3 and a distinct TG mass loss (no mass loss occurred in any of previous nm-Al+MoO<sub>3</sub> TG results).

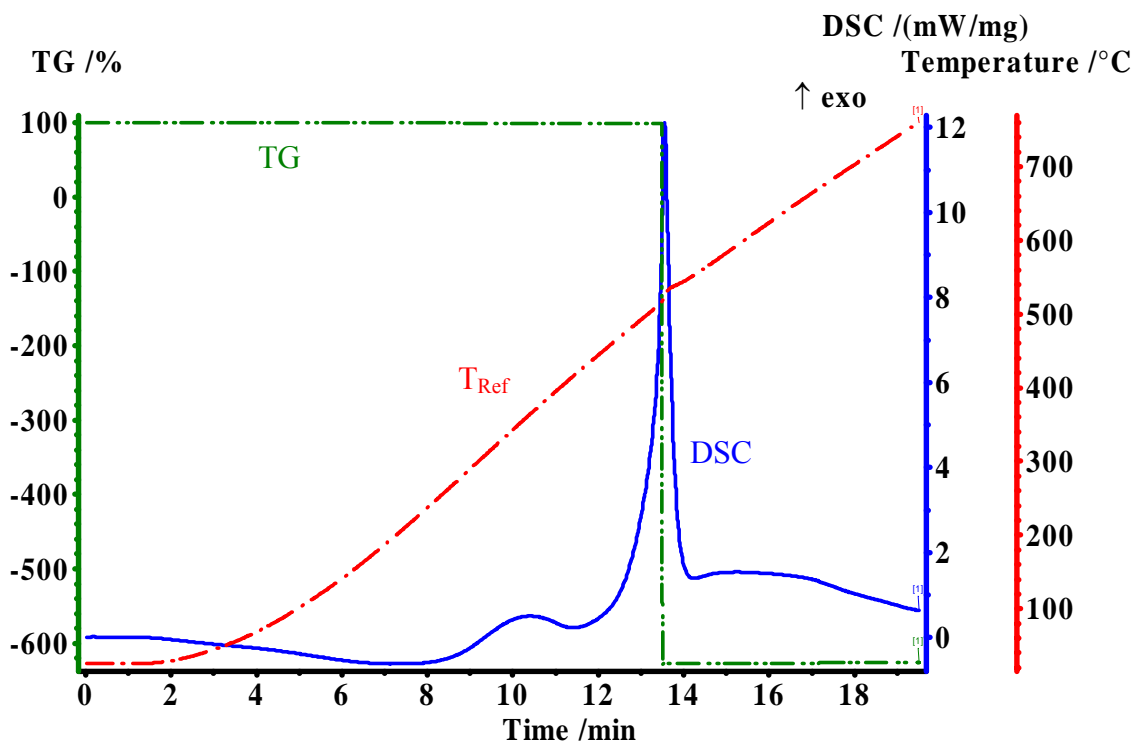


Figure 8.5: 40Kpm violent reaction of 80nm-Al+MoO<sub>3</sub>

The reference temperature line (showing the heating cycle which should be a straight line with a slope of 40Kpm) shows a small spike at the DSC exotherm. All three curves shown in Figure 8.5 indicate a rapid and violent Al+MoO<sub>3</sub> reaction. Once the DSC furnace was opened, it was apparent that the crucible and lid were had been thrown from the sample carrier (represented by the large TG mass loss and the loss of signal by the thermocouple). Even for a small mass (13.7mg), the reaction was hot enough to elevate the temperature of the reference crucible (making any enthalpy calculations past the reference disturbance point incorrect). The crucible was also empty of any sample products because the products were ejected from the crucible, solidified and dispersed as powder inside the furnace. All of these observations are more consistent with Al+MoO<sub>3</sub>

experiments performed in powder or pellet form with nichrome wire [4][56][57] or laser ignition [24].

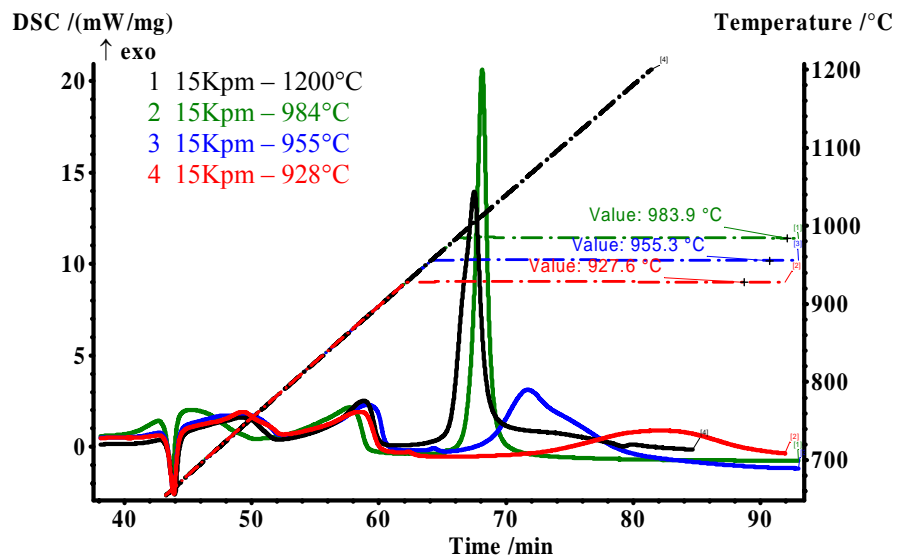
### 8.3 $\mu\text{m-Al+MoO}_3$ Reactions

A similar set of experiments was performed on the 10-14 $\mu\text{m-Al+MoO}_3$  sample to evaluate the temperature dependence of the reaction and a temperature threshold to stimulate thermal runaway. Figure 8.6 shows four DSC experiments of 10-14 $\mu\text{m-Al+MoO}_3$ : 1) constant heating rate of 15Kpm to 1200°C, 2) 15Kpm heating to 984°C, 3) 15Kpm heating to 955°C, and 15Kpm heating to 928°C. Unlike the nm-Al+MoO<sub>3</sub>, stopping the heating cycle did not prevent the reaction but it did alter the reaction onset time and reaction rate (noted by the time to exothermic peak and duration of the exotherm).

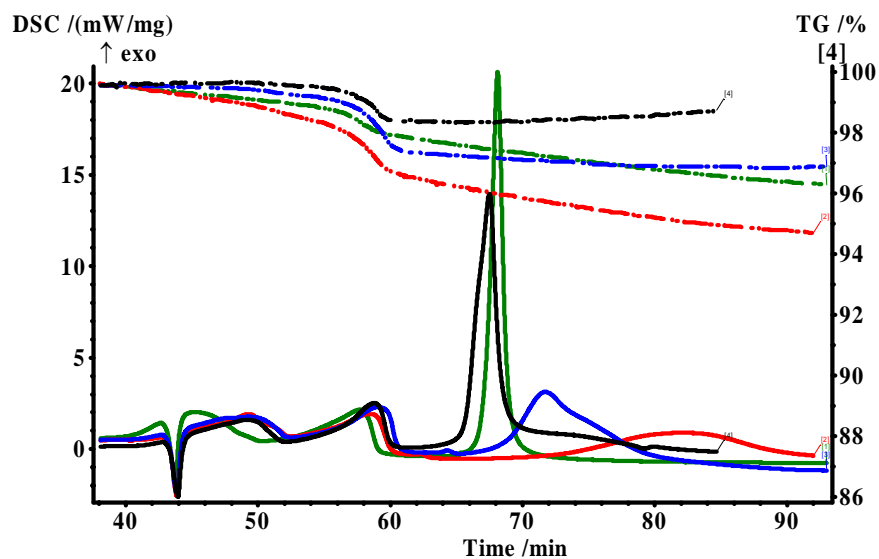
Figure 8.6 A shows curve 1 (constant heating, no isotherm) beginning to react around 940.3°C or 63.1min (derived by the first point of exothermic deviation from the baseline – not  $T_{\text{onset}}$  as defined by intersecting tangent lines). Curves 2, 3 and 4 seem to start reacting later but actually subjective arguments could be made that all four curves never return to the baseline after the 60 min (MoO<sub>3</sub> sublimation) exotherm. It is certain that reaction rate is reduced by reducing the sample temperature (reducing the applied isotherm temperature). Assuming all four curves start exothermically reacting at the end of the 60min exothermic peak, curve 1 reaches its maximum exotherm first at 67.5min followed by curves 2, 3 and 4 at 68.2, 71.7 and 82.3min respectively (shown in Figure 8.8 and Table 8.1). This suggests that the sample corresponding to curve 1 reacts the fastest because the constantly increasing temperature promotes more simultaneous reactions in the bulk sample; whereas the lower sample temperatures encourage fewer simultaneous reaction and slower reaction rates.

Figure 8.6 B shows the DSC energy curves (solid lines) and the TGA (broken lines). The observation to note from this plot is the mass loss starting around 53min for all four curves corresponding to approximate temperature of 800°C or the sublimation temperature of MoO<sub>3</sub>. Notice in Figure 8.6 B, that curve 4 (928°C isotherm) continually losses mass through a longer time duration corresponding to the time delayed reaction.

For example, curve 1 has a relatively sharp mass loss at 53min and then the exothermic reaction quickly starts and the TG curve stays constant. This can be explained by theory that once the sublimed  $\text{MoO}_3$  begins reacting with the Al, then solid  $\text{Al}_2\text{O}_3$  and Mo products are formed and stay in the same crucible with a constant mass and a new molecular structure. For a delayed onset time ( $t_{\text{onset}}$ ), as shown in curves 2,3,and 4, the  $\text{MoO}_3$  has more time to sublime, escape the crucible and avoiding reaction with the Al. The escaping  $\text{MoO}_3$  gas changes the stoichiometry of the remaining sample and may be the phenomenon responsible for the decreased reaction enthalpy magnitudes ( $h_{\text{peak}}$ ).



A



B

Figure 8.6: Partial reaction threshold testing for 10-14 $\mu$ m-Al+MoO<sub>3</sub>

Figure 8.7 shows the exponential relationships of the exothermic peak times and original sample mass with peak enthalpy values. As discussed earlier,  $t_{\text{peak}}$  affects the quantity of MoO<sub>3</sub> sublimed; thus effecting the reaction stoichiometry by making the sample more fuel rich (shown by decreasing enthalpy magnitude,  $h_{\text{peak}}$ ).

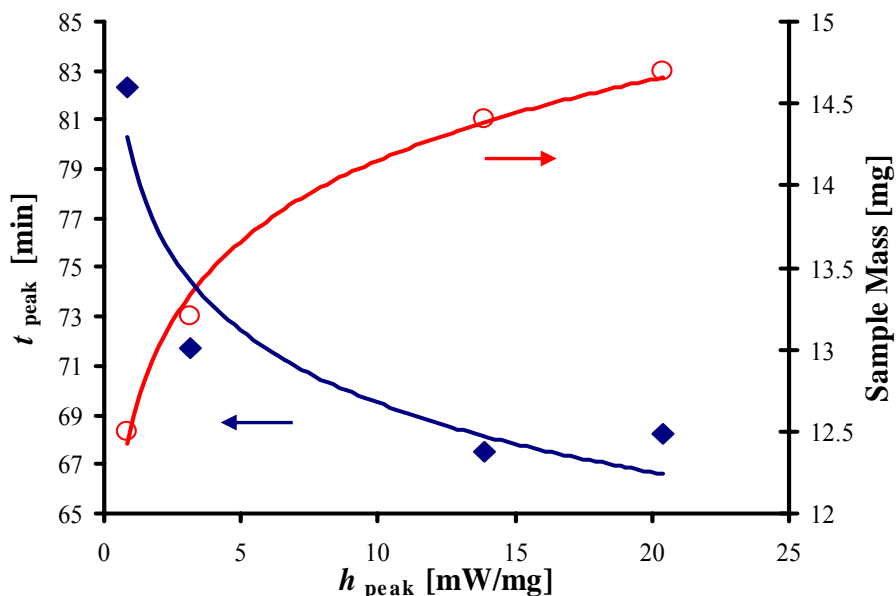


Figure 8.7: Decrease reactivity based on  $\text{MoO}_3$  sublimation and sample stoichiometry for 10-14 $\mu\text{m}$ -Al+ $\text{MoO}_3$

Figure 8.7 also shows an increasing relationship between  $h_{\text{peak}}$  and the original sample mass. Note that enthalpy measurements are normalized by the original sample mass. The trend in Figure 8.7 suggests that the larger sample mass promotes more efficient energy production and more complete reactions for  $\mu\text{m}$ -Al+ $\text{MoO}_3$  samples.

Figure 8.8 and Table 8.1 show the trends of the specific data from Figure 8.6. Theory suggests that the heat of reaction (area under peak) is constant and independent of sample mass (since it is a mass normalized specific enthalpy) and heating rate. The theory of independence of heating rate was disproved for the nm-Al+ $\text{MoO}_3$  samples by Figure 8.2. Figure 8.7 disproves the theory of sample mass independence for  $\mu\text{m}$ -Al+ $\text{MoO}_3$  samples. Note the difference in exothermic peak magnitude from the same 10-14 $\mu\text{m}$ -Al+ $\text{MoO}_3$  sample in the four curves of Figure 8.6. Figure 8.7 shows that the magnitude of the peaks ( $h_{\text{peak}}$ ) in Figure 8.6 are exponentially related to the original sample mass even though the DSC enthalpy values are mass normalized. Note that a discussion of area ( $\Delta h$ ) under an exothermic peak has no relevance using isothermal data.



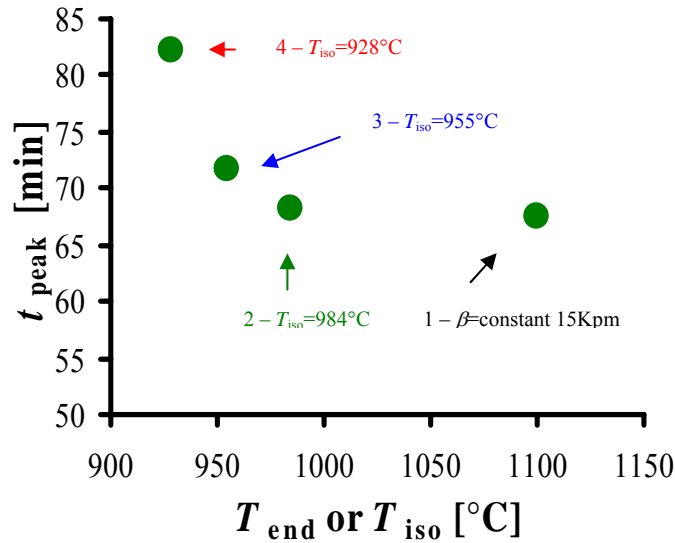


Figure 8.8: Isothermal reaction data for 10-14 $\mu\text{m}$ -Al+MoO<sub>3</sub>

This relationship may be more a function of instrumentation and sample preparation than actual reaction mechanisms. A larger sample mass may have better thermal contact in the sample crucible to produce a larger voltage signal.

Table 8.1: Isothermal reaction data for 10-14 $\mu\text{m}$ -Al+MoO<sub>3</sub> (from Figures 8.6 and 8.8)

$T_{\text{end}} / T_{\text{iso}}$ [ $^{\circ}\text{C}$ ]	Sample Mass [mg]	$t_{\text{peak}}$ [min]	$h_{\text{peak}}$ [mW/mg]
1100	14.4	67.5	13.91
984	14.7	68.2	20.42
955	13.2	71.7	3.106
928	12.5	82.3	0.8762

#### 8.4 Summary

This chapter provides some important clues to characterize the diffusion mechanisms of nano and micron-Al+MoO<sub>3</sub> reactions. It is well known that diffusion models are strong exponential functions of temperature. Thus the temperature dependent behavior is not surprising for the bimolecular composite thermite that is diffusion dependent. DSC experiments suggest that the nanocomposite samples are not providing there own energy source and heating source to self-sustain the diffusion reaction is

surprising. Many other studies have shown that nano-Al reactions are self-propagating [5][6][8][18][23][24][29][30][41][52][53][56][57] indicating that based on certain experimental conditions, the diffusion movement can be sustained the chemical reaction energy generation.

A comparison of Figures 8.1 and 8.4 indicate that the ability for the 80nm-Al+MoO<sub>3</sub> reaction to be self-sustaining is dependent on the heating rate to reaction onset. As discussed in previous chapters, heating rate may influence the volume of simultaneous reactions, which then influences the rate of energy production. An elevated number of simultaneous reactions will display a short reaction duration (as shown in Figure 8.4), which theoretically will produce a given energy magnitude (Watts) in a short time interval. This rapid energy release (caused by the volume of simultaneous reactions) will provide the bulk heating necessary to sustain subsequent diffusional movement and allow the global reaction to proceed to completion.

A comparison of isothermal experiments performed on micron and nanocomposite thermites suggests that micron-Al composites have better chemical reaction momentum than nano-Al composites. Figure 8.4 shows that the nm-Al+MoO<sub>3</sub> reactions stopped completely based on the halting of external heating. Figure 8.8 showed that the  $\mu$ m-Al+MoO<sub>3</sub> reactions did not stop, but simply slowed down and still proceeded to completion. This behavior supports the models describing the slower methodical reactions of  $\mu$ m-Al spheres.

A large difference in the reaction behaviors of nano and micron Al particles is the *unorganized* versus *organized* Al<sub>2</sub>O<sub>3</sub> product formation. For all particle sizes, the product formation is its own deterrent to future reactions. Based on heating rate, which has been shown to alter reaction rates as well (noted by reaction duration of exothermic peaks) the Al<sub>2</sub>O<sub>3</sub> product can be formed rapidly or slowly. Fast or slow Al<sub>2</sub>O<sub>3</sub> product formation, may display drastic difference in molecular density because of differences in lattice structure and alumina phases. Tighter lattice structures with larger densities will inevitably deter intermediate grain diffusion and potentially alter or prevent complete consumption of the Al core.

## CHAPTER IX

### TWO-DROP CALORIMETER THERMITE EXPERIMENTS

#### 9.1 Introduction

Calorimetry experiments were designed and conducted to measure heat of reaction values for Al + MoO<sub>3</sub> thermites. The goal is to measure enthalpy change due to the chemical reaction between the fuel particles (Al) and oxidizer particles (MoO<sub>3</sub>). These results are compared to heat of reaction results from the DSC experiments presented earlier and theoretical calculations from Fischer and Grubelich (1998) [19].

Initial experiments were conducted using a Parr Bomb Calorimeter designed for liquid hydrocarbon fuels. The Parr Bomb Calorimeter used a large water volume heat sink to measure enthalpy changes. Energy output from Al + MoO<sub>3</sub> thermite samples was too rapid and low magnitude to significantly alter the water transient temperature making any measurements inaccurate.

A second series of experiments was designed using a 2-drop calorimeter (or titration calorimeter) in collaboration with Calorimetry Sciences Corporation (CSC) ([www.calscorp.com](http://www.calscorp.com)). A 2-drop calorimeter is an isothermal heat conduction calorimeter originally designed by Lars Wadsö (University of Lund, Lund Sweden) and Dr. Thomas Hofelich (Dow Chemical Co., Midland, MI) [43]. Researchers at CSC have produced a 2-drop calorimeter designed so that only microliters of reagents (reactants) are necessary to measure chemical heat release. The application of a 2-drop calorimeter to measure the reaction heat release from the thermite samples is possible due to the thermal sensitivity of the instrument.

#### 9.2 Experimental Design

Similar to the DSC design, the 2-drop calorimeter measures a voltage potential across a series of thermocouples thermally bonded to a sample and reference container. Figure 9.1 shows a simplified diagram of a 2-drop calorimeter used for these experiments. As deemed by the “2-drop”, a small volume of liquid reactants would be extruded by the syringe into the sample vial initiating the chemical heat release.

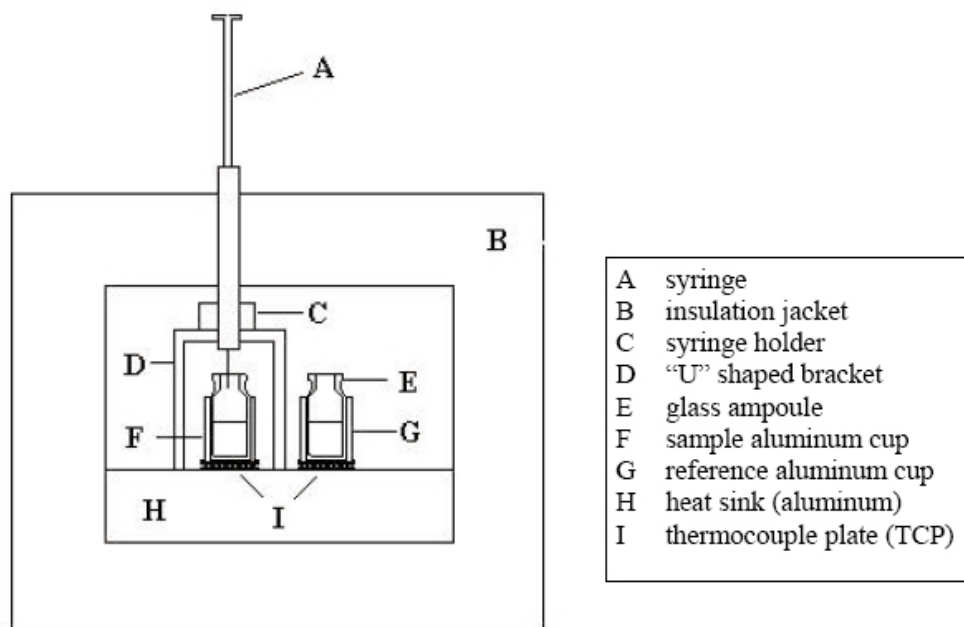


Figure 9.1: Two-drop calorimeter system schematic [43]

In a typical experiment using a 2-drop calorimeter, a calibration is done before and after an experiment to account for any heat production and loss not measured by the thermocouples (i.e. absorbed by the sample vessel). Typically, the calibration is performed electric joule heating by applying a known voltage ( $V$ ) across a electric resistor of resistance  $R$  attached to the side of the aluminum cup shown in Figure 9.1. This electrical circuit provides a known thermal power to the sample thermocouple junction.

$$P = V^2/R \quad (9.1)$$

When a steady state output voltage is obtained, the calibration coefficient may be found.

$$\varepsilon = P/U \quad (9.2)$$

where  $U$  is the total measured voltage output. Typical values of  $\varepsilon$  range from 2.4-2.5 W/V [43].

For the experiments presented in this chapter, the solid reaction of the thermite composite is ignited by a nichrome wire ignition apparatus (similar to ignition source used by the Parr water-bomb calorimeter discussed earlier). Similar to the syringe needle

penetrating the sample vial cap septum, a series of electrical wires was inserted through the septum to ignite the thermite powder.

The ignition apparatus consisted on a 15VAC voltage source that allowed 1.8 amps of current for a maximum power (input into the sample vessel) of 27 Watts. The power supply was connected to a 2.5 cm segment of nichrome wire to provide a joule heating ignition source. Two segments of bare copper wire (approximately 5 cm in length) were inserted through the sample vial cap septum. About 3 mm of each end of the nichrome wire was crimped into a small pin connector and the pin connectors were attached to the end of the bare copper wire leads. The nichrome filament was bent into a loose “W” shape and folded perpendicular to the plane of the copper leads.

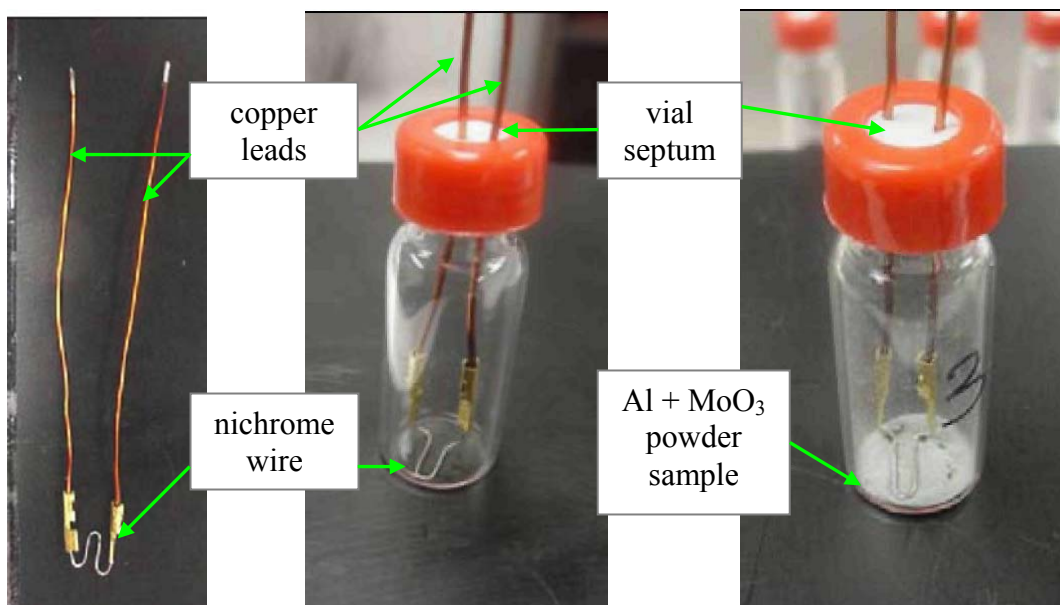


Figure 9.2: Sample vial with nichrome wire igniter

A small mass of Al + MoO<sub>3</sub> composite powder was measured and placed at the bottom of the sample vial. The screw cap was attached ensuring that the nichrome wire was in contact with the sample powder.

The sample vial was placed in the CSC 2-drop calorimeter sample holder and an empty vial was placed in the reference holder. The exposed copper leads were attached to pin connectors at the end of insulated wires from the external firing box. The insulated

wires were taped to the calorimeter body to prevent movement. The instrument door was closed over the insulated ignition wires and the system was equilibrated to 25°C.

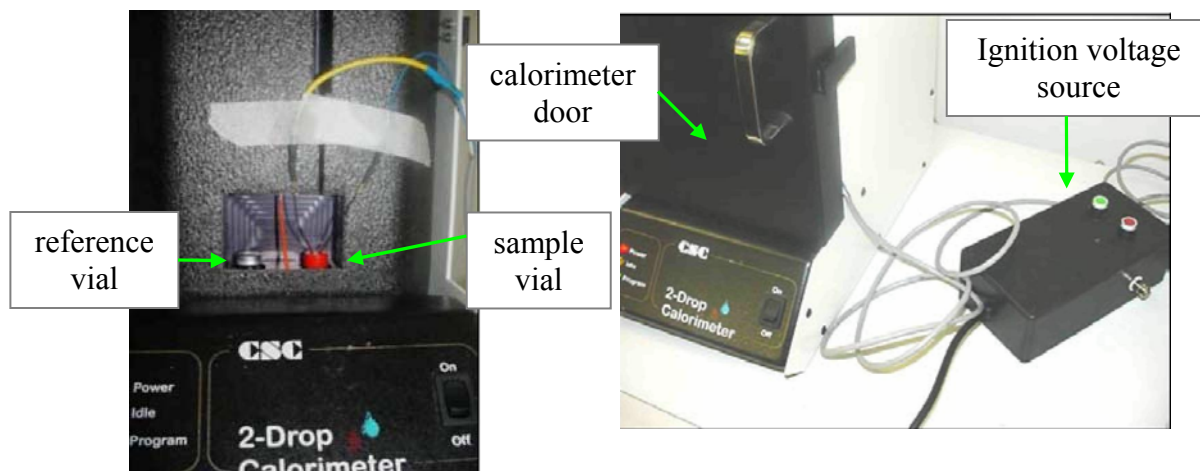


Figure 9.3: Sample vial, ignition system and calorimeter orientation

During each experiment, the voltage source was triggered causing the nichrome filament to burn briefly (1-2 seconds until the wire broke). The sample ignited and the heat was measured. Calibration heater pulses (as discussed earlier) were performed before and after the sample ignition to verify accuracy within the approximate range of the sample peak.

Three different samples of Al (40nm Al, 3-4 $\mu$ m Al and 10-14 $\mu$ m Al) and nanocrystalline MoO<sub>3</sub> were tested. The Al and MoO<sub>3</sub> powders were mixed to slightly fuel rich (1.2 equivalence ratio) based on the pure Al content and neglecting any Al reactions with air. A total composite mass of 200 mg was fabricated for each Al particle size by suspending the solid particles in hexane and sonciating to break up agglomerates. The hexane was then evaporated off for 12 minutes and the dried powder was brushed out of the steel drying pan. Approximately 6 to 28 mg of loose powder composite was used for each experiment. Each composite sample was tested three times as shown in Table 9.2.

Blanks were also tested to determine the energy input from the nichrome wire. Tests labeled as blanks were done with a similar setup without the thermite sample. The average heat of the wire ignition was subtracted from the thermite sample results.

### 9.3 Results

The heating rate histories for the three blanks are overlaid in Figure 9.4. The 1 and 5 cal. calibration pulse are performed before and after each blank. Results from the three tests in Figure 9.4 are shown in Table 9.1.

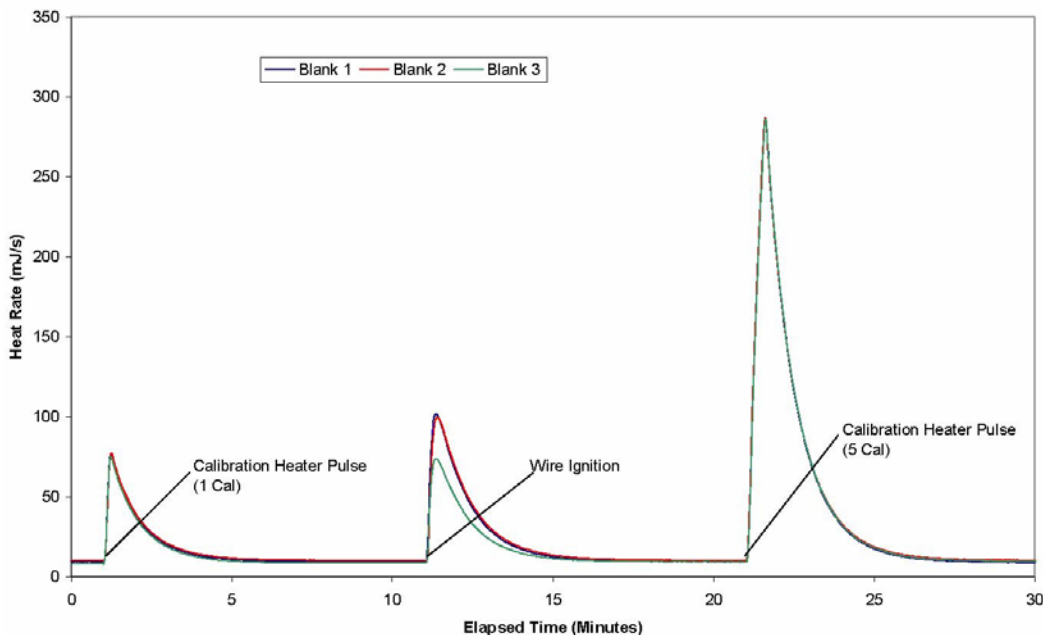


Figure 9.4: Experimental data for the 3 nichrome wire blanks tested

Table 9.1: Nichrome wire blank heat adjustment values

Sample Name	Peak Area [Cal]	Average Blank [Cal]	Blank Std. Dev. [Cal]
Nichrome Blank 1	1.761	1.583	0.285
Nichrome Blank 2	1.733		
Nichrome Blank 3	1.254		

Figure 9.5 shows the heating rate history data for the first three Al + MoO<sub>3</sub> composite samples tested. Table 9.2 shows the area calculations from all of the thermite experiments. Table 9.2 also shows the area values corrected by the subtraction of average nichrome wire heat input. Note that the two micron samples are not nearly as ignition sensitive and require much higher thermal stimuli than nanocomposite thermites. Experiments showed that some of the 10-14 $\mu$ m samples did not ignite and the nichrome

wire was the only heat input into the system resulting in a negative blank-corrected area (column 5, Table 9.2).

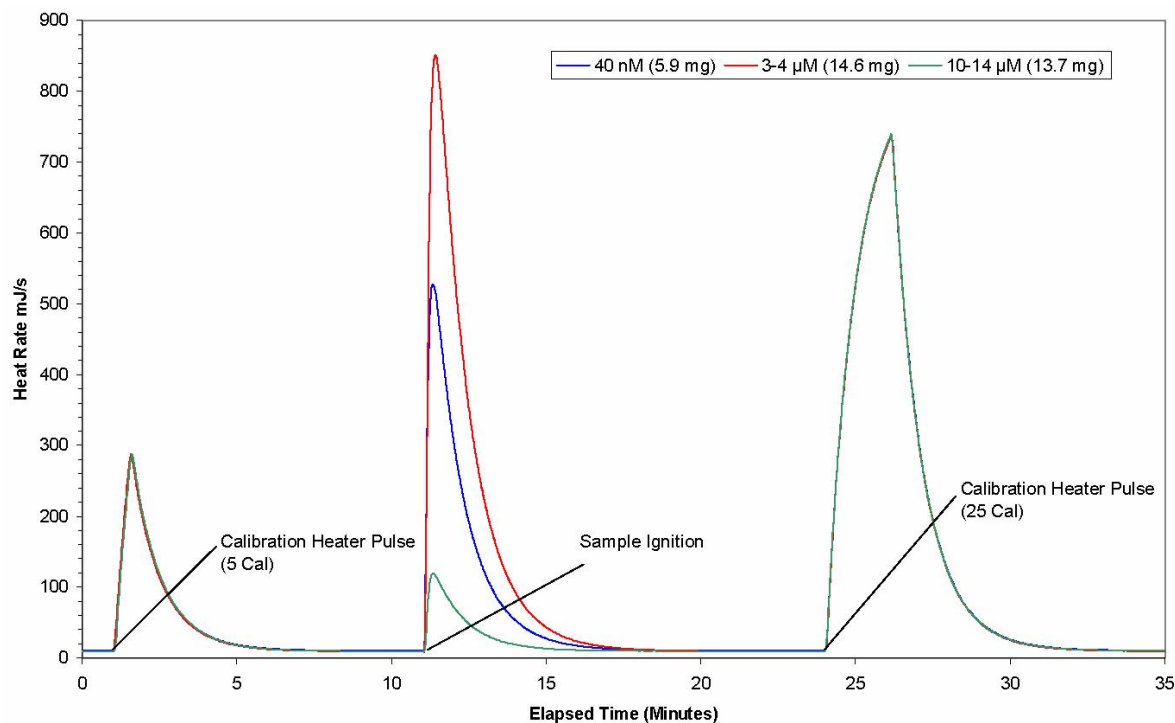


Figure 9.5: Experimental data for Samples 1-3

Data on the calibration pulses used in determining the calibration coefficients are shown in Appendix I.

Table 9.2: Al+MoO<sub>3</sub> Calorimeter peak integration areas

Sample Number	Al Powder	Weight [mg]	Peak Area [Cal]	Avg. Blank-Corrected Peak	Min. Blank-Corrected Peak Area [Cal]	Max. Blank-Corrected Peak Area [Cal]
1	40 nm	5.9	9.748	8.165	7.88	8.45
2	3-4 μm	14.6	17.314	15.732	15.447	16.017
3	10-14 μm	13.7	2.02	0.437	0.152	0.722
4	40 nm	7.9	12.55	10.967	10.682	11.252
5	3-4 μm	12.1	11.977	10.395	10.11	10.68
6	10-14 μm	10.9	2.135	0.552	0.267	0.837
7	40 nm	11.3	11.943	10.361	10.076	10.646
8	3-4 μm	22.1	21.471	19.889	19.604	20.174
9	10-14 μm	28.1	1.419	0*	0*	0.121

\* A value of zero is assigned for calculated quantities which yield a negative result.

Data from Table 9.2 was then normalized by the original sample mass, converted to SI units (Joule/milligram) and averaged (shown in Table 9.3).



Table 9.3: Two-drop calorimeter Al+MoO<sub>3</sub> heat of reaction results

	40 nm Al + MoO <sub>3</sub>			3-4 μm Al + MoO <sub>3</sub>			10-14 μm Al + MoO <sub>3</sub>		
	$\Delta h_{\text{rxn}}$ [J/g]			$\Delta h_{\text{rxn}}$ [J/g]			$\Delta h_{\text{rxn}}$ [J/g]		
Rep	Avg	Min	Max	Avg	Min	Max	Avg	Min	Max
1	5794.5	5593.6	5995.5	4513.4	4429.6	4592.9	134.0	46.1	221.9
2	5811.3	5660.6	5962.0	3596.5	3500.2	3696.9	213.5	104.7	322.4
3	3839.3	3734.6	3944.0	3734.6	3713.7	3822.5	0*	0*	16.7
Average	5148.4	4996.2	5300.5	3948.2	3881.2	4037.5	173.8	75.4	187.0
Std Dev	1133.7	1093.1	1174.9	494.3	486.8	485.1	56.2	41.4	155.8

The data from Table 9.3 is plotted as a function of Al particle diameter in Figure 9.6. The figure shows that  $\Delta h_{\text{rxn}}$  measured by the calorimeter decreases linearly with increasing Al particle size.

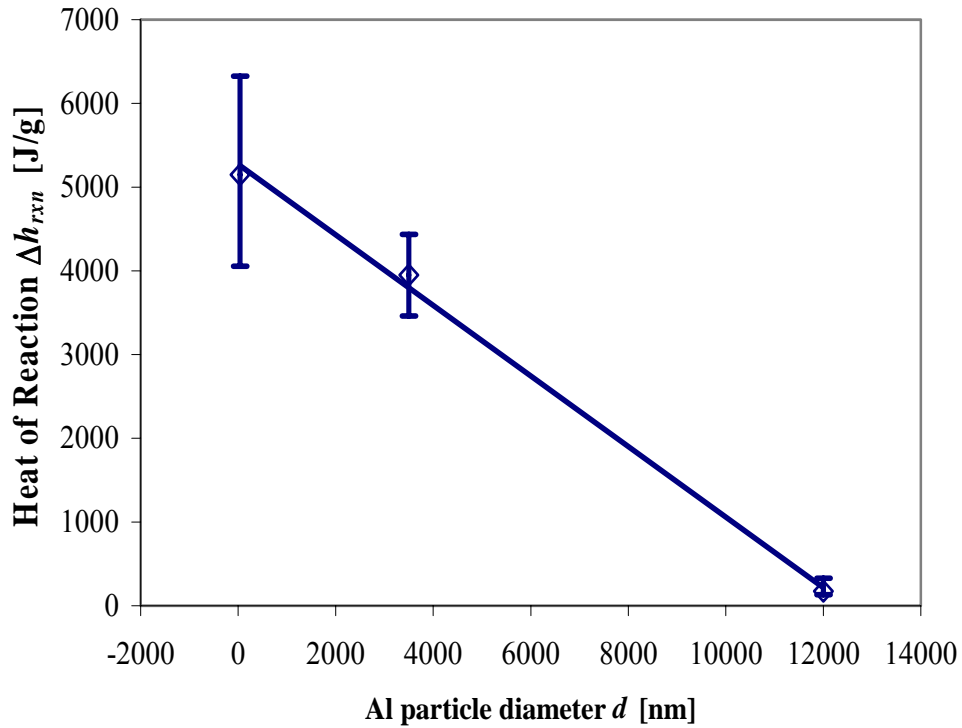


Figure 9.6: Two-drop calorimeter Al+MoO<sub>3</sub> heat of reaction results

Figure 9.6 also shows that the standard deviation in data sets consistently decreases with increasing Al particle size. The samples used in Figure 9.6 were fabricated at the same fuel to oxidizer ratios based on the true Al content. The  $\Delta h_{\text{rxn}}$  values were mass

normalized based on the total composite mass including Al, Al<sub>2</sub>O<sub>3</sub> and MoO<sub>3</sub>. The slight mass difference of Al<sub>2</sub>O<sub>3</sub> in the nanocomposite versus micron composite does not account for the three orders of magnitude difference in  $\Delta h_{\text{rxn}}$ . Thus the data trend in Figure 9.6 may be best explained as an incomplete reaction.

When comparing the mass normalized data in Table 9.3 and the original composite sample mass in Table 9.2, one can note that for all three Al particle sizes the presence of more material may suppress the reaction. Observe that the third 40nm sample was the largest nanocomposite sample mass and yet it produced the lowest  $\Delta h_{\text{rxn}}$  value of the three tests. Similarly, the third 10-14 $\mu\text{m}$  sample was the largest mass and it did not even react.

#### 9.4 Summary

Figure 9.7 shows three DSC exotherms for thermite samples similar to the samples tested with the 2-drop calorimeter. Integration of the area under the DSC exotherm provides estimates of the mass normalized heat of reaction. Figure 9.7 also shows the endothermic energy absorption near 660°C corresponding to the melting of the Al in the composite mixture. As shown, the 50nm-Al+MoO<sub>3</sub> curve is a single exothermic spike that is easily integrated (except for the overlap with the Al melt endotherm discussed in previous chapters) and the two micron thermite samples are more complex with several peaks and valleys over a broad temperature range. Area integrals were determined for three to four samples ranging from 50nm to 20mm-Al at different heating rates and averaged (data presented in Table 7.1).

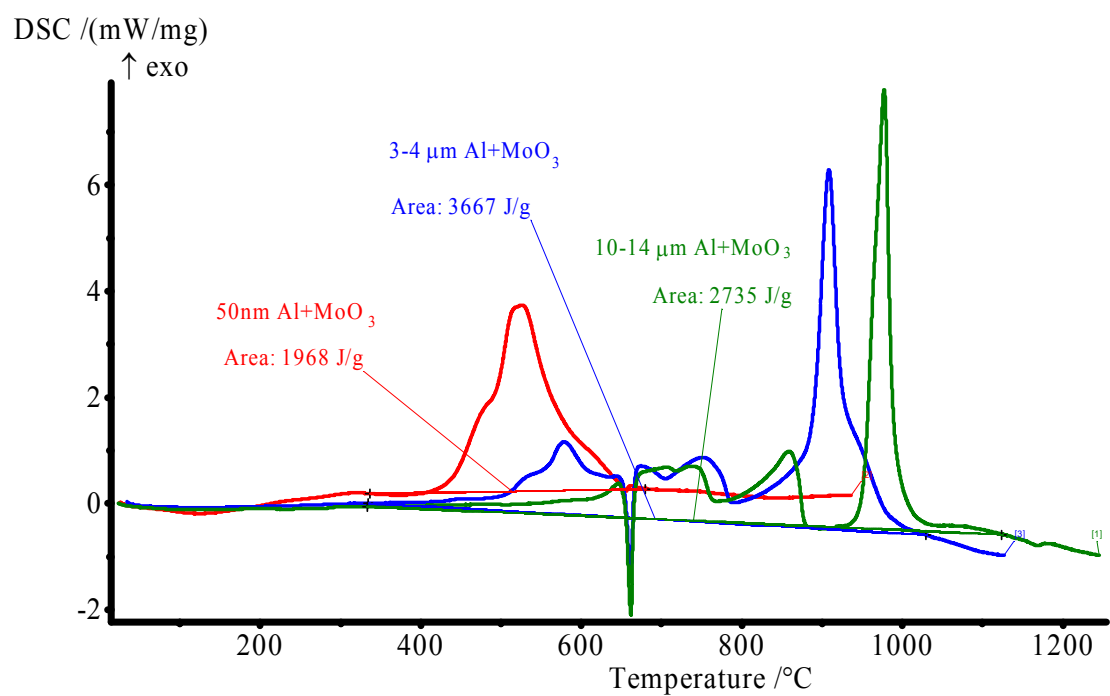


Figure 9.7: Heat of Reaction determined by DSC Al+MoO<sub>3</sub> experiments

Figure 9.8 shows the 2-drop calorimeter data compared to DSC data and the theoretical  $\Delta h_{\text{rxn}}$  calculated by Fischer and Grubelich [19].

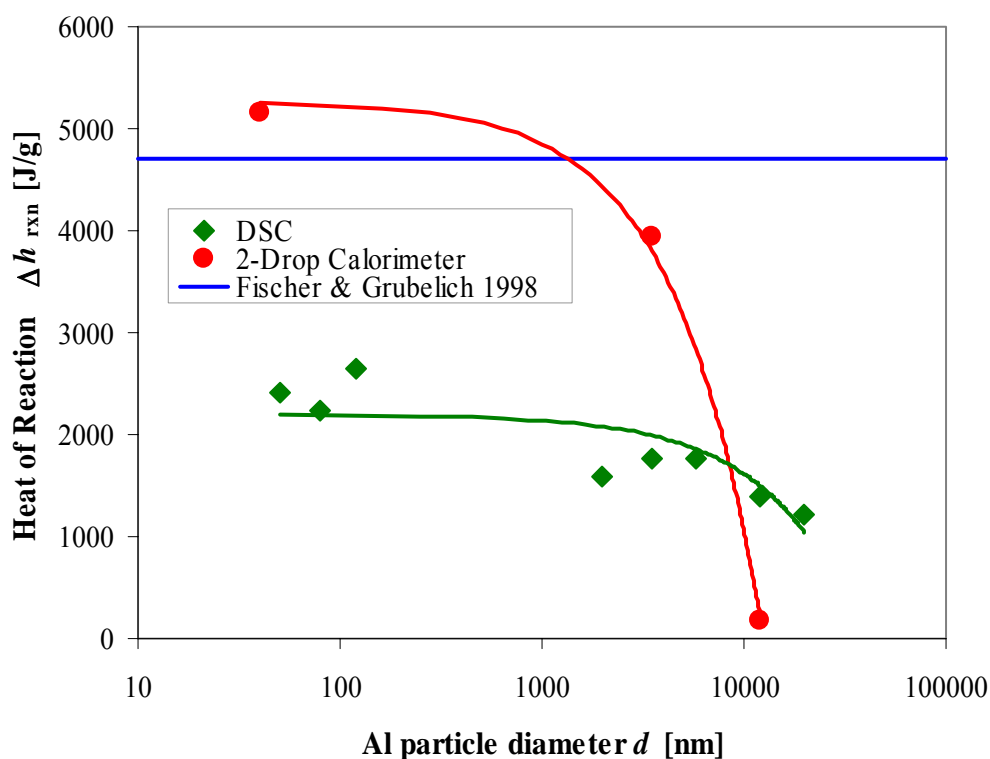


Figure 9.8: Heat of reaction comparison between instruments and cited source

Note: Error bars are not indicated because the 2-Drop Calorimeter data is the average of three identical experiments; whereas the DSC data is an average of varied heating rates (ie. 5, 10 and 15Kpm), thus different experiments

Both the DSC and calorimeter data show a linear decreasing trend (shown more clearly in Figures 7.3 and 9.6 respectively) of  $\Delta h_{\text{rxn}}$  with increasing Al particle size. Theoretically for the same fuel to oxidizer content and ratio, the energy production should be constant and only a property of molecular bond energy and reactant and product enthalpy states. This is not the case, and the data in Figure 9.8 suggests that the micron thermite reactions are incomplete. Recall that experiments in Chapter VI showed that  $\mu\text{-Al}$  reactions were still reacting after hours of exposure to elevated DSC furnace temperatures and adequate gaseous  $\text{O}_2$ . The observed long time intervals of micron Al reactions cannot occur using the point source nichrome wire or laser ignition.

Figure 9.8 also suggests that the Al+MoO<sub>3</sub> reaction is path dependent. For example, similar to the laser experiments, the 2-drop calorimeter experiments are ignited rapidly with a nichrome wire. This rapid heating and subsequent ignition results in a violent reaction with energy levels near 5000 J/g for nm-Al samples. On the other hand, the slowly heated DSC samples were not violently reacted (evident by the unmoved powder product still in the crucible after the experiment) and displayed a maximum reaction energy around 2600 J/g for similar nm-Al samples. This suggests that the rate of heating to stimulate ignition of a diffusion based reaction dramatically effects the reaction path.

One can speculate that the slow reactions in the DSC may generate highly organized oxide layer growth around the Al cores that inhibit the Al and oxygen diffusion. Slow heating rates allow elongated oxide growth intervals that may deter future reactions. Whereas rapid reactions do not allow organized oxide growth. The rapid thermal expansion of the Al particles and gases around reaction zones may prevent the formation of oxide barriers between unreacted Al and oxygen molecules. Instead, the thermal gas expansion may propel reacting particles to new locations generating separated and dispersed Al<sub>2</sub>O<sub>3</sub> that have less effect subsequent molecular diffusion and reactions. The heat of reaction measured by DSC experiments cannot achieve the same magnitudes as the 2-drop calorimetry tests due to a combination of the reaction path dependence and overall reaction duration.

## CHAPTER X

### CONCLUSIONS

Several experimental works have been presented outlining the unique combustion characteristics of micron and nano-Al particles. Reactions of Al+O<sub>2</sub> gas and Al+MoO<sub>3</sub>, display evidence that separate diffusion mechanisms exist that control the reaction characteristics. Experimental results have shown unique combustion behaviors of micron and nano-Al reactions listed in Table 10.1.

Discussion has been presented describing numerous physical models of the diffusion reaction of a single Al particle (see Chapter VI and Table 6.1). Data suggests that the mechanism controlling the diffusion process is different in the nano versus micron-Al particles due to the geometric and dimensional differences alone. These differences can be quantitatively compared by specific surface area (SSA) and oxide layer thickness. For example, a 50nm Al particle has a SSA of approximately 39.9m<sup>2</sup>/g, while Suvaci et. al [59] presented data for a 2-5μm Al powder with a SSA of 1.24m<sup>2</sup>/g. Calculations have shown that nm-Al oxide layer thicknesses are 2-4 nm, while μm-Al oxide layer thicknesses can be as large as 22 nm (Chapter V). The experimental results in this work can be attributed to the differences in surface area, oxide thickness, or a combination of both. Both factors contribute to the volume (or number) of simultaneously occurring reactions.

Eisenrich et al. [17] and Trunov et al. [61][62] describe the diffusion process as a flow of molecules through channels or fissures in the oxide layer. One can envision that if the number of channels is even slightly dependent on surface area (describing a consistent spatial area between channels for micron and nano particles), then the 3000% increase in surface area as the particle diameter decreases to the nano regime increasing the total number of diffusion channels. Increasing the number of diffusion channels will inevitably increase the number of simultaneous ignition and reaction sites; thus increasing the reaction rate (noted by the increase in oxidation mass gain rate in Chapter VI), heat production and reactivity.

Table 10.1: Comparison remarks for micron and nano-Al reactions

	$\mu\text{m-Al}$	nm-Al
Density Effects on Al+MoO <sub>3</sub> Composite Flame Velocity		
Porosity effects on combustion flame velocity	Improved thermal properties resulting in increased velocities 0.6 to 42 m/s	Decreased interstitial air volumes resulting in decreasing burn velocity 500 to 0.5 m/s
Laser Ignition of Compressed Al+MoO <sub>3</sub> Composites		
Ignition Sensitivity [24]	Insensitive to low thermal stimuli and electric spark, 50W laser ignition times between 90 ms and 6 sec	Two orders of magnitude more ignition sensitive, 50W laser ignition times less than 25 ms
Burn Velocity	Larger than nanocomposites due to laser preheating prior to ignition	Can be artificially elevated above micron composites based on similar laser pre-heating experiments
DSC/TG Al+O <sub>2</sub> (gas) experiments		
DSC/TG reaction rates based rate of mass gain	Two or three stage reaction with maximum mass gain of 3 %/min	Single stage reactions with peak mass gain of 642 %/min
Activation Energy based on $T_{\text{onset}}$	Increasing $E_a$ (-312 to -350 kJ/g) for increasing particle sizes	Decrease in $E_a$ magnitude (-281 kJ/g) supporting improved ignition sensitivity
DSC Al+MoO <sub>3</sub> Composite experiments		
DSC reaction temperature regimes	Onset after phase transition of both Al and Al <sub>2</sub> O <sub>3</sub> with rapid main exotherm ( $T_{\text{onset}}$ = 808 to 1004°C)	Onset in solid phase of both constituents, with overlapping exothermic peaks ( $T_{\text{onset}}$ = 410 to 488°C)
Heat of Reaction	Relatively independent of heating rate and constant between 1200 and 2100 J/g	Increasing for decreasing heating rate, maximum of 4000 J/g, double all micron reactions
Heating rate	Consistent onset with delayed peak temperatures for main exotherm	Sooner onset with exponential change in reaction rate
Two-drop Calorimeter Al+MoO <sub>3</sub> Composite experiments		
Heat of reaction	Exponential decrease in $\Delta h_{\text{rxn}}$ ( $\Delta h_{\text{rxn}}$ = 3948 to 174J/g), some samples would not ignite with nichrome wire	$\Delta h_{\text{rxn}}$ = 5148 J/g which is larger than theoretical optimum

The number and spatial density of diffusion channels can also be linked to the oxide thickness. Dreizin [14][15] presents a model of Al combustion describing that the diffusion paths are created by unequal thermal expansion of the Al core versus oxide layer and alumina-oxide phase transitions. A thicker oxide layer may have larger stress (thermal or dynamic) tolerances and more organized crystalline organization. Both of these factors will contribute to a decreased Al core exposure area and a reduced number of diffusion channels in the micron-Al samples and decreased reactivity.

Results showing that the reaction characteristics are heavily dependent on heating rate to ignition support the notion that nano-Al reactions can be modeled as a combination of both surface area and oxide layer thickness effects. Results have shown that laser ignited nm-Al+MoO<sub>3</sub> samples react violently at burn velocities as large as 500 m/s. DSC experiments testing nm-Al+MoO<sub>3</sub> at controlled heating rates between 2.5 and 20°C/min have shown a calm methodical reaction behavior (leaving the powder products in the same general shape within the crucible). A single DSC experiment testing nm-Al+MoO<sub>3</sub> at 40°C/min showed a violent and uncontrollable reaction similar to the near explosive reactions seen with laser experiments. This suggests the heating rate has a dramatic influence on diffusion rates and thus reaction rates. The elevated heating rate of the laser and DSC experiments may be described by the following sequence of events leading to thermal runaway

- 1) Formation of diffusion channels proportional to the surface area of the nano-Al particles due to thermal expansion (or density variations) (described by Dreizin [14][15] and Eisenrich [17])
- 2) Rapid diffusion of Al ions producing more heat
- 3) Increased diffusional movement of molecules due to external thermal energy and thermal energy produce from local reactions
- 4) Further destruction of the thin oxide layer, presenting exponential Al core surface area exposure
- 5) Nearly uninhibited diffusion of Al and O atoms until complete conversion to Al<sub>2</sub>O<sub>3</sub>



The key to understanding the thermal explosion of the nm-Al+MoO<sub>3</sub> reactions, is in describing the near full destruction or at least insignificant role of the oxide layer once a critical reaction moment has been achieved. Once the external energy source (DSC or laser) achieves a specific volume of simultaneous reactions, the reaction itself becomes self-sustaining (produces its own thermal energy), which makes the oxide layer ineffective in controlling the diffusion rate and promotes self-propagating thermal runaway.

A similar explanation can be made to describe the difference in reaction onset temperatures for nano and micron-Al samples. It can be assumed, that the molecular velocities of identical molecules is only dependent on temperature and independent of the bulk particles. Basically, stating that Al ions and O<sub>2</sub> molecules will move at the same speed based on temperature excitation alone. Thus, the main difference between nano and micron-Al reactions is the volume of molecules moving at that speed for a given temperature. For instance, describing a micron-Al sample (of a finite mass) at a single instant at 400°C, which has total volume of Al ions ( $G$ ) moving at a finite velocity ( $u$ ) through the diffusion channels. Where  $G$  is dependent on the number of channels or the SSA. A nano-Al sample (of the same mass) at the same temperature will have a volume of  $30 \cdot G$  (3000% increase based on the increase in SSA) Al ions moving at the same velocity  $u$ . Thus the mass flow rate or volumetric flow rate of the nano-Al sample is drastically larger than the micron-Al sample. Increased mass flow rate will produce increased levels of exothermic energy for the same sample temperature, which is presented as a lower DSC onset temperature for the nano-Al samples. This description suggests that the micron-Al samples will still be reacting at the lower temperatures with decreased exothermic magnitudes (which is supported by some of the DSC results in Appendices E and G). Another condition must be considered also for the composite reactions: the heat produced by the nm-Al mass flow rate may generate enough energy to locally decompose the MoO<sub>3</sub> where the  $\mu$ m-Al reactions may not have a constant oxygen supply necessary to react (which is supported by the Al+O<sub>2</sub> gas experiments showing similar  $T_{\text{onset}}$  for nano and micron-Al particles).

The five stages presented above can be used to understand the heat of reaction measurements recorded by the DSC and Two-drop calorimeter experiments (Figures 7.3 and 9.7 respectively). Slower heating rates of the nm and  $\mu\text{m}$ -Al samples (with  $\text{O}_2$  or composite reaction with  $\text{MoO}_3$ ) will allow more controlled channel formation. Controlling the number of diffusion paths will inevitably control the diffusion rate and  $\text{Al}_2\text{O}_3$  product formation. Dreizin's model [14][15] suggests that eventually the diffusion channels will clog themselves with reaction products and then diffusion will occur by molecular movement between the  $\text{Al}_2\text{O}_3$  crystal grains. Because the heat of reaction values are linearly dependent on heating rate, it can be assumed that different quantities of reactants are being consumed based on diffusion mechanisms. Slower DSC heating rates allow a more organized diffusion migration, which may contribute to more organized  $\text{Al}_2\text{O}_3$  grain formation promoting diffusion once the channels are clogged. Data suggests that the slower heating rates allow more of the Al to react presenting  $\Delta h_{\text{rxn}}$  values closer to optimum (see Figure 9.8). Similarly for the micron-Al reactions, as the reaction proceeds more  $\text{Al}_2\text{O}_3$  oxide is formed, which becomes a more significant diffusion barrier (displayed by the  $\mu\text{m}$ -Al+ $\text{O}_2$  gas reactions not reaching completion, Chapter VI).

## CHAPTER XI

### FUTURE WORK

#### 11.1 Fabrication

Mixing of composite components and fabrication of compressed pellets has typically been done all by manual labor. In this process, as discussed in Chapter II, there is much room for human subjectivity and lack of consistency. There are many industries that specialize in powder manufacturing and handling that could provide needed knowledge of automated systems to avoid human error. It should be possible to creating a single automated system to measure Al and oxidizer powder ratios in a controlled atmosphere, then suspend the powder mixture in a solvent, sonicate and dry off the solvent. This would prevent human errors in measurement, time lag between sonication and evaporation that allows settling, variability in liquid solution volume, time of evaporation (which generates various agglomeration).

#### 11.2 Nanocomposite Al/MoO<sub>3</sub> Reaction Characteristics

Because the Al+MoO<sub>3</sub> and similar nanocomposite thermites have potential as ordinance and military energetic materials, there seems to be great interest in obtain pressure data from these nanocomposite materials. It is has be shown by this work and other by the DSC experiments that the Al+MoO<sub>3</sub> reaction is a solid-solid reaction with zero or negligible gas generation. This being noted, the pressurization of this specific reaction can be attributed to thermal gas expansion. Work has been done to measure peak pressure output and pressurization rates by Moore [41] and Sanders [52]. Sanders showed that the peak pressure and pressurization rate of Al+MoO<sub>3</sub> alone is inapplicable even as a small artillery primer. The solution was to add small amounts of high-explosives in the composite mixture to provide an applicable pressure generator.

There are still many tests to perform to characterize the pressure output and pressurization rates of nanocomposite thermites and similar mixture energetic materials. It is known that nanocomposite mixtures of Al+Bi<sub>2</sub>O<sub>3</sub> (bismuth oxide) is a better gas generate and peak pressure performer. There is a little quantitative experimental data on

critical reaction temperatures (i.e. onset and peak), heat of reaction, and pressure output for many of the other nanocomposite thermites (Al + metal oxides) available (listed by Fischer [19]).

Using additives like high-explosives (HE) seems to be overpowering the advantages of nanocomposite energetic materials. The one advantage of such a mixture (nanothermite + HE) is the ignition sensitivity and large exothermic energy release of nanomaterials. Traditionally HE are hard to thermally ignite to detonation. The small amount of ignition stimuli require for nanocomposite thermites could provide more consistency in ignition and then the reaction is exothermic enough to stimulate the detonation of the intermixed HE (much of this idea is presented by [52]).

Another application of nanocomposites thermites is use as incendiary devices which take advantage of their large energy density properties (see Figure 1.2 on page 3). This property has not been properly explored (evident by the difficulty of measuring true flame temperature in Chapter IV and difficulty in obtaining accurate heat of reaction quantities shown in Chapters VII, VIII and IX) nor exploited. The speed of the heat release in traditional nanocomposite experiments makes accurate temperatures very hard to obtain. Moore and Pantoya [41] have suggested that the ideal gas law can properly model the temperature and pressure state around a nanocomposite thermite reaction based on a finite mass. Calculations have been made to approximate the ideal peak pressure output based on the adiabatic flame temperature presented by Fischer [19]. This model can be taken a step further. If it can be shown that a pressure sensor is more dynamically accurate than a micro-thermocouple in the minute time interval of the reaction, then one should be able to approximate the flame temperature and heating rate from experimental pressure data (peak pressure and pressurization rate respectively). From this same method of calculation, since the ideal gas law is thermodynamically simplified, more complex models and relationships between pressure and temperature may be more accurate based on a thermodynamic equation of state.

Note that the 2-drop calorimeter in Chapter IX, was originally designed as a “homemade” instrument and was not always commercially available by CSC. This fact indicates that one could design a calorimeter specifically for measuring the heat of

reaction nanocomposite thermites. It seems that a few minor adjustments to the current design and theory of existing calorimeters would make measurements of rapid and violent reactions possible.

1. Miniaturization: A differential heat conduction calorimeter could be made very similar to the 2-drop calorimeter with smaller sample vessels. A smaller sample vessel should allow the rapid heat release to be absorbed quicker and the vessel itself would have less thermal mass to induce heat loss (producing smaller overall calibration effects). One disadvantage of miniaturizing the sample vessel is the containment of a rapid thermal expansion.

2. Robustness: A very small sample vessel could be a copper crucible similar to the DSC platinum crucibles. A copper crucible would allow easy fabrication with a simple stamping press and relatively inexpensive individual cost. The copper crucible would have a more durable wall with improved transient heat flow compared to the glass sample vials used in the 2-drop calorimeter.

To address the issue of the composite mixture (specifically the Al) reacting with the copper or copper-oxide, the copper crucible could be dipped in Neolube (a solution of graphite and isopropanol commercially available from Huron Industries, PO Box 610104, Port Huron, MI 48061-0104 810-984-4213). Letting sit for a few minutes would allow the isopropanol to evaporate, leaving a thin and semi-homogeneous coating of graphite (carbon) between the reactants and the copper. SHS research at Texas Tech University has shown that it is difficult or impossible to react carbon with micron or nano-Al. If unsuccessful, a second protection coating could be created by a similar approach of making a powder  $\text{Al}_2\text{O}_3$  (alumina) and isopropanol solution. The platinum DSC crucibles are protected by a solid alumina liner that is very brittle and would not withstand the reaction. Again the copper crucibles could be coated in a powder alumina layer. Obviously, the carbon or alumina protection layers would inhibit heat flow but the hope is that the protection layers would be so thin that they would be negligible and easily accounted for in calibration.

The copper crucible could be constructed to allow 5–10mg of nanocomposite powder with minimal void space. The copper crucible could then be tightly fit into an

insulating solid (this material will have to be tested) similar to the 2-drop calorimeter. Then micro-thermocouples could be attaché to the bottom of the copper crucible using thermal epoxy.

3. Ignition: The goal of the ignition source is to provide a constant energy input without creating a significant heat loss window. One suggestion, would be to use a YAG, copper-vapor or an other visible wavelength laser that could pass through a glass microscope slide. There could be two designs for the ignition source: 1) a very small hole through an insulating solid with a glass slide backing and a focused laser beam or 2) several glass slides to provide a conductive heat loss barrier still allowing efficient radiant energy transmission. The advantages of the radiant energy source are that the laser pulse can be tuned and finitely controlled making very consistent energy input and the radiant transmission through the sample vessel wall without allowing significant conductive or convective heat loss. As noted by the DSC experiments, there are various reaction behaviors of the Al+MoO<sub>3</sub> composite and a laser energy pulse would also allow for different heating rates prior to ignition generating different reaction behaviors.

The combination of these three ideas specific to thermite reaction calorimetry could also be applied to an adiabatic calorimeter design. Perhaps, the combination of a heat conduction calorimeter and adiabatic calorimeter experiments would allow for more accurate heat of reaction comparisons.

### 11.3 DSC experiments

Oxidizer is a crucial factor in the Al reaction

1. Nm and micron Al reaction behaviors and activation energies in artificial air (0 humidity) and true air (with control humidity levels).
2. DSC Testing different solid oxidizers
  - a. Bismuth oxide Bi<sub>2</sub>O<sub>3</sub>+
  - b. Copper oxide
  - c. Palladium oxide
  - d. Iron oxide
  - e. Etc.

Unique oxidizers may reveal a stronger significance on the oxidizer decomposition mechanisms in applications striving for more consistent energy output, faster reaction rates from phase transitions

## REFERENCES

- [1] Andrievski, R. A. "Compaction and Sintering of Ultrafine Powders." *International Powder Metallurgy*, V. 30 pp.59-66 (1994).
- [2] Ashish, R., Lee, D., Park, K., and Zachariah, M.R. "Importance of Phase Change of Aluminum in Oxidation of Aluminum Nanoparticles." *Journal of Physical Chemistry B* V.108, pp. 14793-14795 (2004).
- [3] Balakir, E.A., Bushuev, Y.G., Bareskov, N.A., Kosyakin, A.E., Kudryavtsev, Y.V. and Fedorova, O.N. "Rate of Combustion of Exothermic Mixtures." *Combustion, Explosion, and Shock Waves* V.11 No.1 pp.43-46 (Jan. 1974).
- [4] Blackman, M. and Curzon, A.E. Structure and Properties of Thin Films, John Wiley, London: New York, pp.217-222 (1959).
- [5] Bockmon, B.S., Pantoya, M.L., Son, S.F. and Asay, B.W., "Burn Rate Measurements in Nanocomposite Thermites." *Proceedings of the American Institute of Aeronautics and Astronautics Aerospace Sciences Meeting*, Paper No. AIAA-2003-0241 (2003).
- [6] Bockmon, B., Son, S.F., Asay, B.W., Busse, J.R., Mang, J.T., Peterson, P.D., and Pantoya, M. "Combustion Performance of Metastable Intermolecular Composites (MIC)." *38<sup>th</sup> JANNAF Combustion Subcommittee*, Destin, FL, (April 2002).
- [7] Boswell, P.G. "On the Calculation of Activation Energies Using a Modified Kissinger Method." *Journal of Thermal Analysis* V.18 pg.353-358 (1980).
- [8] Bulian, C.J., Kerr, T.T., and Puszynski, J.A. "Ignition studies of Aluminum and Metal Oxide Nanopowders." *Proceedings of the 31<sup>st</sup> International Pyrotechnic Seminar (IPS)*, Ft. Collins, CO, (July 2004).
- [9] Campbell, T., Kalia, R.K., Nakano, A., Vashishta, P., Ogata, S., and Rogers, S. "Dynamics of oxidation of aluminum nanoclusters using variable charge molecular-dynamics simulations on parallel computers." *Physics Review Letters*, V. 82 No. 24 pp. 4866, (1999).
- [10] Cabrera, N. and Mott, N.F. "Theory of the Oxidation of Metals." *Repts. Prog. Phys.* V.12 pp.163-181 (1948-49).
- [11] Carver, Inc. 1569 Morris St. PO Box 544 Wabash, IN 46992-0544. Phone (260)563-7577, Internet [www.carverpress.com](http://www.carverpress.com) .



- [12] Chen, W., and Malghan, S. G., "Investigations of Compaction Equations for Powders." *Powder Technology*, V81 pg.75-81 (1994).
- [13] Degussa AG Internet "The Railway Pioneer: Hans Goldschmidt Chemist and Entraperner." website [http://www.degussa-history.com/geschichte/en/personalities/hans\\_goldschmidt.html](http://www.degussa-history.com/geschichte/en/personalities/hans_goldschmidt.html) retrieved 11/3/2004.
- [14] Dreizin, E.L. "Experimental Study of Stages in Aluminum Combustion in Air." *Combustion and Flame* V.105 pp.541-556 (1996).
- [15] Dreizin, E.L., "Ignition of Al powders under different experimental conditions." presentation at the 1<sup>st</sup> Workshop on Pyrotechnic Combustion (preceeding the 31<sup>st</sup> *International Pyrotechnic Seminar (IPS)*, Ft. Collins, CO, (July 2004).
- [16] Eckert, J., Holzer, J.C., Ahn, C.C., Fu, Z. and Johnson, W.L. "Melting behavior of nanocrystalline aluminum powders." *Nanostructured Materials* V.2 Iss.4 pp.407-413 (July-Aug. 1993).
- [17] Eisenrich, N., Weiser, V., Fietzek, H., Juez-Lorenzo, M., Kolarik, V., and Koleczko, A. "Mechanisms of Low Temperature Oxidation for Metal Particles Down to the Nano-Scale and their influence to Propellant Combustion." *Proceedings of the 31<sup>st</sup> International Pyrotechnic Seminar (IPS)*, Ft. Collins, CO, (July 2004).
- [18] Feng, H.J., Moore, J.J., and Wirth, D.G. "The Combustion synthesis of TiB<sub>2</sub>-Al<sub>2</sub>O<sub>3</sub>-Al Composite Materials." *Proceedings of the Symposium on Developments in Ceramic and Metal Matrix Composites, TMS Annual Meeting*, TMS, San Diego, CA p.219 (1992).
- [19] Fischer, S.H., Grubelich, M.C. "Theoretical Energy Release of Thermites, Intermetallics, and Combustible Metals." *Proceedings of the 24<sup>th</sup> International Pyrotechnics Seminar* (1998).
- [20] Flynn, J.H., and Wall, L.A. "A Direct Method for determination of Activation Energy from Thermogravimetric Data." *Polymer Letters* V.4 pp. 323-328 (1966).
- [21] Freeman, B. and Carroll, B. "The application of thermoanalytical techniques to reaction kinetics. The thermogravimetric evaluation of the kinetic of the decomposition of calicium oxalate monohydrate." *Journal of Physical Chemistry* V.62 pp. 394-397 (1958).
- [22] Friedman, H.L. "Kinetics of thermal degradation of char forming plastics from thermogravimetry. Application to phenolic plastic." *Journal of Polymer Science* V.6 Part C pp.183-195 (1964).

- [23] Granier, J.J. and Pantoya, M.L. "Combustion Behaviors of Nanocomposite Thermites as a Function of Bulk Density." *JANNAF 39<sup>th</sup> Combustion Symposium Joint Meeting*, Colorado Springs, CO (Dec. 1-5, 2003).
- [24] Granier, J.J., and Pantoya, M.L. "Laser Ignition of Nanocomposite Thermites." *Combustion and Flame* V.138 pp.373-383 (2004).
- [25] Granier, J.J., Plantier, K.B., and Pantoya, M.L. "The role of Al<sub>2</sub>O<sub>3</sub> passivation shell surrounding nano-Al particles in the combustion synthesis of NiAl." *Journal of Materials Science* V.39 pp.6421-6431 (2004).
- [26] Goodman, J. "The Thermite Reaction, A Chemistry Honors Project." Chipola Junior College, website  
[www.chipola.edu/instruct/science/Breivogel/HonorsChemistry/The%20Thermite%20Reaction.doc](http://www.chipola.edu/instruct/science/Breivogel/HonorsChemistry/The%20Thermite%20Reaction.doc) retrieved 11/1/2004.
- [27] Harrick Scientific Products, Inc. 88 Broadway Box 1288 Ossining, NY 10562. Phone (914) 762-0020. Internet <http://www.harricksci.com> ;  
[http://www.harricksci.com/accessories/H\\_pelletpresses.cfm](http://www.harricksci.com/accessories/H_pelletpresses.cfm) .
- [28] Ichinose, N. *Superfine Particle Technology*, Springer London; New York (1992).
- [29] Il'in, A.P., Gromov, A.A., Vereshchagin, V.I., Popenko, E.M., Surgin, V.A., and Lehn, H. "Combustion of Ultrafine Aluminum in Air." *Combustion, Explosion, and Shock Waves* V.37 No.6 pp.664-668 (Dec. 2001).
- [30] Il'in, A.P., Popenko, E.M., Gromov, A.A., Shamina, Y.Y., and Tikhonov, D.V. "Combustion of Agglomerated Ultrafine Aluminum Powders in Air." *Combustion, Explosion, and Shock Waves* V.38 No.6 pp.665-669 (2002).
- [31] Incropera, F.P. and DeWitt, D.P. *Fundamentals of Heat and Mass Transfer, Fifth Edition* John Wiley and Sons; Hoboken, NJ (2002).
- [32] Jones, D.E.G., Turcotte, R., Fouchard, R.C., Kwok, Q.S.M., Turcotte, A.M., and Qader, Z.A. "Haqard Characterization of Aluminum Nanopowder Compositions." *Propellants, Explosives and Pyrotechnics* V.28 No.3 pp.120-131 (2003).
- [33] Jones, D.E.G., Turcotte, R., Kwok, Q.S.M., and Vachon, M. "Comparative Studies of the Thermal Hazards of Aluminum Nanopowders." *Proceedings of the 34<sup>th</sup> International Annual Conference of Institut Chemische Technologie (ICT)*, Karlsruhe, Federal Republic of Germany (June 2003).
- [34] Kissinger, H.E. "Reaction Kinetics in Differential Thermal Analysis." *Analytical Chemistry* V.29 pp. 1702-1706 (1957).

- [35] Koch, C. C., Nanostructured Materials, (Processing, Properties and Potential Applications), Noyes Publications / William Andrew Publishing, Norwich NY (2002).
- [36] Kuo, K.K. Principles of Combustion, John Wiley and Sons, Inc. New York (1986)
- [37] Kwok, Q.S., Fouchard, R.C., Turcotte, A.-M., Lightfoot, P.D., Bowes, R., and Jones, D.E.G., "Characterization of Aluminum Nanopowder Compositions." *Propellants, Explosives and Pyrotechnics* V.27 pp. 229-240 (2002).
- [38] Kwon, Y.S., Gromov, A.A., Ilyin, A.P., Popenko, E.M., and Rim, G.H. "The mechanism of combustion of superfine aluminum powders." *Combustion and Flame* V.133 pp.385-391 (2003).
- [39] Lide, David R., CRC Handbook of Chemistry and Physics, 79<sup>th</sup> Edition, CRC Press Inc. (1998-1999).
- [40] Moore, J.J., Readey, D.W., Feng, H.J., Perkins, N., and Wirth, D.G. "Combustion Synthesis of Composites, Powders and Whiskers." *Advanced Powder Metallurgy* V.9 Particulate Materials and Processes p.381-393 (1992).
- [41] Moore, K., Pantoya, M.L. and Son. S.F. "Thermite Combustion Enhancement due to Bimodal Aluminum Distribution." *Proceedings of the 31<sup>st</sup> International Pyrotechnic Seminar (IPS)*, Ft. Collins, CO, (July 2004).
- [42] Mallinckrodt Chemicals, J.T. Baker Molybdenum Trioxide MSDS, Mallinckrodt Baker, Inc. website <http://www.jtbaker.com/msds/englishhtml/m7829.htm> retrieved on 1/21/03.
- [43] Mulligan, R. B., "Studies in Isothermal Heat Conduction Calorimetry." Thesis submitted to Drexel University, Philadelphia, PA. (Dec. 2002). Available online at <http://dspace.library.drexel.edu/handle/1860/72> retrieved on 1/10/2005.
- [44] Netszch Operating Manuals
- [45] Ostmark, H. and Roman, N. "Laser Ignition of Pyrotechnic Mixtures: Ignition Mechanisms." *Journal of Applied Physics* V.73 No.4 pp.1993-2003 (Feb. 1993)
- [46] Ozawa, T. "A New Method of Analyzing Thermogravimetric Data." *Bulletin of the Chemical Society of Japan* V.38 pp. 1881-1886 (1965).
- [47] "Personal communication with Technanogy, Inc. (Santa Anna, CA) and Nanotechnologies, Inc. (Austin, TX)." Dr. Kurt Schroder.
- [48] Popenko, E.M., Il'in, A.P., Gromov, A.M., Kondratyuk, S.K., Surgin, V.A., and Gromov, A.A. "Combustion of Mixtures of Commercial Aluminum Powders and

Ultrafine Aluminum Powders and Aluminum Oxide.” *Combustion, Explosion, and Shock Waves* V.38 No.2 pp.157-162 (2002).

- [49] Puszynski, J.A. “Reactivity of Nanosize Aluminum with Metal Oxides and Water Vapor.” *Materials Research Society Symposium Proceedings* V.800 (2004).
- [50] Revesz, A., Lendvai, J., and Ungar, T. “Melting Point Depression and Microstructure in Ball-Milled Nanocrystalline Aluminum Powders.” *Journal of Metastable and Nanocrystalline Materials* V.8 pp.326-331 (2000).
- [51] Rogers, R.N. and Rogers, J.L. “Explosive Science.” website <http://home.att.net/~rnrogers/> retrieved 9/2/2004.
- [52] Sanders, V.E., Busse, J.R., and Son, S.F. “Environmentally Responsible Percussion Primers for Small and Medium Caliber Ammunition.” *Proceedings of the 39<sup>th</sup> JANNAF Conference*, Colorado Springs, CO (Dec. 2003).
- [53] Sandstrom, M.M., Oschwald, D.M., and Son, S.F. “Laser Ignition of Aluminum Nanoparticles in Air.” *Proceedings of the 31<sup>st</sup> International Pyrotechnic Seminar (IPS)*, Ft. Collins, CO, (July 2004).
- [54] Shimizu, K., Furneaux, R.C., Thompson, G.E., Wood, G.C., Gotoh, A., and Kobayashi, K. “On the Nature of ‘Easy Paths’ for the Diffusion of Oxygen in the Thermal Oxide Films on Aluminum.” *Oxidation of Metals* V.35 Nos.5/6 pp.427-439 (1991).
- [55] Shevchenko, V.G., Kononenko, V.I., Latosh, I.N., Bulatov, M.A., Lukin, N.V., Saksonova, L.R., Dobrinskii, E.K., Malashin, S.I., and Gostyukov, E.A. “Influence of the Degree of Dispersion on the Kinetics of Oxidation of Aluminum.” Translated from *Poroshkovaya Metallurgiya* No.5(341) pp.80-82 (1991).
- [56] Son, S.F., Asay, B., Busse, J.R., Jorgensen, B.S., Bockmon, B., and Pantoya, M. “Reaction Propagation Physics of Al/MoO<sub>3</sub> Nanocomposite Thermites.” *Proceedings of the 28<sup>st</sup> International Pyrotechnic Seminar (IPS)*, Adelaide, Australia, (Nov. 2001).
- [57] Son, S.F., Dye, R.C., Busse, J.R., Sandstrom, M.M., Oschwald, D.M., and Janicke, M.T. “Combustion of Nanoaluminum in Air.” *39<sup>th</sup> JANNAF Combustion Subcommittee*, Colorado Springs, CO (Dec. 2003).
- [58] Starink, M.J. “A new method for the derivation of activation energies from experiments performed at constant heating rates.” *Thermochimica* V.288 pp.97-104 (1996).
- [59] Suvaci, E., Simkovich, G., and Messing, G.L. “The Reaction-Bonded Aluminum Oxide Process: I, The effect of Attrition Milling on the Solid-State Oxidation of

Aluminum Powder.” *Journal of the American Ceramic Society* V.83 No.2 pp. 299-305 (2000).

- [60] Takagi, M. *Journal of the Physical Society of Japan* V.9 pp.359-363 (1954).
- [61] Trunov, M.A., Schoenitz, M., and Dreizin, E.L. “Ignition of Al-Mg Mechanical Alloys.” *9<sup>th</sup> International Workshop on Combustion and Propulsion, Novel Energetic Materials and Applications*, Lerici, La Spezia, Italy (Sept. 2003).
- [62] Trunov, M.A., Schoenitz, M., Xiaoying, Z., and Dreizin, E.L. “Effect of Polymorphic Phase Transformations in Al<sub>2</sub>O<sub>3</sub> Film on Oxidation Kinetics of Aluminum Powders.” *Submitted to Combustion and Flame* (June 2004).
- [63] Turns, S.R. *An Introduction to Combustion*, The McGraw Hill Companies Boston (2000).
- [64] Wikimedia Foundation, Inc. “Thermite – Definition of Thermite by Webster’s Online Dictionary.” website <http://www.webster-dictionary.org/definition/Thermite> retrieved 10/1/2004.
- [65] Wronski, C.R.M. “The size dependence of the melting point of small particles of tin.” *British Journal Applied Physics*, 1967, 1731-1737.
- [66] Zhang, Z., Lu, X.X., and Jiang, Q. *Physica B* V.270 pp.249-254 (1999).

## APPENDIX

### A. Compressed Composite LFA 447 data

#### A.1 50nm-Al+MoO<sub>3</sub> Thermal Properties

bulk thickness density temperature @ 25°C ρ @ 25°C			(1st heating)			@ 25°C ρ @ 25°C		(2nd heating)			Average of heating rates			
			c <sub>p</sub>	α	λ			c <sub>p</sub>	α	λ	λ % incr (1st to 2nd)	λ	c <sub>p</sub>	α
(mm)	(g/cm <sup>3</sup> )	(°C)	(J/g-K)	(cm <sup>2</sup> /s)	(W/m-K)	(mm)	(g/cm <sup>3</sup> )	(J/g-K)	(cm <sup>2</sup> /s)	(W/m-K)		(W/m-K)	(J/g-K)	(cm <sup>2</sup> /s)
1.88 TMD	1.07 27.61%	25	0.713	0.00163	0.125	1.88	1.07	0.713	0.00181	0.138	11.0%	0.132	0.713	0.00172
		50	0.763	0.00163	0.133			0.763	0.00182	0.149	11.7%	0.141	0.763	0.00172
		75	0.796	0.00160	0.137			0.796	0.00180	0.154	12.3%	0.145	0.796	0.00170
		100	0.815	0.00158	0.138			0.815	0.00176	0.154	11.4%	0.146	0.815	0.00167
		125	0.829	0.00157	0.139			0.829	0.00173	0.154	10.4%	0.147	0.829	0.00165
		150	0.840	0.00156	0.141			0.840	0.00171	0.154	9.4%	0.147	0.840	0.00164
		175	0.851	0.00157	0.143			0.851	0.00168	0.153	6.8%	0.148	0.851	0.00162
		200	0.860	0.00157	0.145			0.860	0.00165	0.152	5.2%	0.148	0.860	0.00161
		225	0.867	0.00156	0.145			0.867	0.00163	0.152	4.7%	0.148	0.867	0.00159
		250	0.872	0.00155	0.145			0.872	0.00160	0.150	3.0%	0.148	0.872	0.00158
		275	0.876	0.00154	0.145			0.876	0.00158	0.148	2.4%	0.147	0.876	0.00156
		300	0.880	0.00155	0.146			0.880	0.00157	0.148	1.1%	0.147	0.880	0.00156
1.89 TMD	1.20 30.98%	25	0.713	0.00176	0.151	1.89	1.20	0.713	0.00191	0.164	8.7%	0.158	0.713	0.00184
		50	0.763	0.00171	0.157			0.763	0.00192	0.177	12.1%	0.167	0.763	0.00182
		75	0.796	0.00169	0.162			0.796	0.00190	0.182	12.7%	0.172	0.796	0.00180
		100	0.815	0.00167	0.164			0.815	0.00188	0.184	12.2%	0.174	0.815	0.00177
		125	0.829	0.00166	0.166			0.829	0.00186	0.185	11.6%	0.176	0.829	0.00176
		150	0.840	0.00166	0.168			0.840	0.00183	0.185	10.3%	0.177	0.840	0.00175
		175	0.851	0.00166	0.171			0.851	0.00180	0.184	7.9%	0.177	0.851	0.00173
		200	0.860	0.00167	0.173			0.860	0.00177	0.184	6.3%	0.178	0.860	0.00172
		225	0.867	0.00168	0.175			0.867	0.00176	0.183	4.8%	0.179	0.867	0.00172
		250	0.872	0.00166	0.174			0.872	0.00174	0.183	4.6%	0.178	0.872	0.00170
		275	0.876	0.00167	0.176			0.876	0.00172	0.182	3.1%	0.179	0.876	0.00170
		300	0.880	0.00169	0.179			0.880	0.00171	0.181	0.8%	0.180	0.880	0.00170
1.92 TMD	1.49 38.24%	25	0.713	0.00220	0.233	1.92	1.49	0.713	0.00245	0.259	11.3%	0.246	0.713	0.00232
		50	0.763	0.00215	0.244			0.763	0.00244	0.277	13.7%	0.260	0.763	0.00230
		75	0.796	0.00213	0.252			0.796	0.00240	0.284	12.6%	0.268	0.796	0.00227
		100	0.815	0.00209	0.253			0.815	0.00238	0.288	13.8%	0.271	0.815	0.00224
		125	0.829	0.00207	0.255			0.829	0.00234	0.288	13.0%	0.271	0.829	0.00220
		150	0.840	0.00208	0.260			0.840	0.00233	0.291	11.7%	0.275	0.840	0.00221
		175	0.851	0.00210	0.266			0.851	0.00231	0.292	9.9%	0.279	0.851	0.00220
		200	0.860	0.00212	0.271			0.860	0.00228	0.292	7.6%	0.281	0.860	0.00220
		225	0.867	0.00214	0.276			0.867	0.00225	0.290	5.1%	0.283	0.867	0.00220
		250	0.872	0.00216	0.280			0.872	0.00224	0.290	3.6%	0.285	0.872	0.00220
		275	0.876	0.00216	0.281			0.876	0.00221	0.287	2.3%	0.284	0.876	0.00218
		300	0.880	0.00217	0.284			0.880	0.00220	0.287	1.3%	0.285	0.880	0.00218
1.99 TMD	1.79 46.06%	25	0.713	0.00299	0.381	1.99	1.79	0.713	0.00335	0.427	12.0%	0.404	0.713	0.00317
		50	0.763	0.00295	0.404			0.763	0.00333	0.455	12.8%	0.429	0.763	0.00314
		75	0.796	0.00292	0.416			0.796	0.00329	0.468	12.7%	0.442	0.796	0.00310
		100	0.815	0.00288	0.420			0.815	0.00326	0.476	13.4%	0.448	0.815	0.00307
		125	0.829	0.00286	0.425			0.829	0.00323	0.479	12.9%	0.452	0.829	0.00305
		150	0.840	0.00289	0.434			0.840	0.00321	0.483	11.2%	0.459	0.840	0.00305
		175	0.851	0.00295	0.449			0.851	0.00319	0.486	8.1%	0.468	0.851	0.00307
		200	0.860	0.00297	0.456			0.860	0.00317	0.488	7.0%	0.472	0.860	0.00307
		225	0.867	0.00299	0.464			0.867	0.00315	0.489	5.4%	0.476	0.867	0.00307
		250	0.872	0.00302	0.471			0.872	0.00312	0.488	3.6%	0.479	0.872	0.00307
		275	0.876	0.00302	0.473			0.876	0.00311	0.488	3.1%	0.480	0.876	0.00306
		300	0.880	0.00305	0.481			0.880	0.00311	0.490	1.8%	0.485	0.880	0.00308

## A.2 4.5-7 $\mu$ m-Al+MoO<sub>3</sub> Thermal Properties

thickness @ 25°C (mm)	bulk density ρ @ 25°C (g/cm³)	temperature (°C)	(1st heating)			@ 25°C   ρ @ 25°C		(2nd heating)			Average of heating rates			
			c <sub>p</sub>	α	λ			c <sub>p</sub>	α	λ	λ % incr (1st to 2nd)	λ (W/m-K)	c <sub>p</sub> (J/g-K)	α (cm²/s)
			(J/g-K)	(cm²/s)	(W/m-K)	(mm)	(g/cm³)	(J/g-K)	(cm²/s)	(W/m-K)				
2.02	1.54	25	0.713	0.00249	0.274	2.02	1.54	0.713	0.00267	0.293	6.9%	0.284	0.713	0.00258
TMD	39.66%	50	0.763	0.00245	0.289			0.763	0.00263	0.309	7.2%	0.299	0.763	0.00254
		75	0.796	0.00239	0.293			0.796	0.00256	0.314	7.2%	0.304	0.796	0.00248
		100	0.815	0.00235	0.295			0.815	0.00253	0.318	7.8%	0.306	0.815	0.00244
		125	0.829	0.00230	0.294			0.829	0.00246	0.315	7.1%	0.304	0.829	0.00238
		150	0.840	0.00231	0.298			0.840	0.00242	0.314	5.1%	0.306	0.840	0.00236
		175	0.851	0.00230	0.302			0.851	0.00239	0.313	3.5%	0.308	0.851	0.00235
		200	0.860	0.00230	0.305			0.860	0.00236	0.312	2.4%	0.309	0.860	0.00233
		225	0.867	0.00230	0.307			0.867	0.00234	0.312	1.6%	0.310	0.867	0.00232
		250	0.872	0.00227	0.305			0.872	0.00232	0.311	1.9%	0.308	0.872	0.00229
		275	0.876	0.00224	0.303			0.876	0.00230	0.311	2.7%	0.307	0.876	0.00227
		300	0.880	0.00224	0.304			0.880	0.00229	0.311	2.2%	0.308	0.880	0.00227
2.02	1.90	25	0.713	0.00359	0.487	2.02	1.90	0.713	0.00386	0.523	7.3%	0.505	0.713	0.00372
TMD	48.92%	50	0.763	0.00348	0.505			0.763	0.00377	0.547	8.2%	0.526	0.763	0.00363
		75	0.796	0.00337	0.509			0.796	0.00365	0.553	8.5%	0.531	0.796	0.00351
		100	0.815	0.00330	0.511			0.815	0.00357	0.554	8.4%	0.532	0.815	0.00343
		125	0.829	0.00325	0.512			0.829	0.00349	0.550	7.5%	0.531	0.829	0.00337
		150	0.840	0.00326	0.521			0.840	0.00345	0.550	5.7%	0.535	0.840	0.00335
		175	0.851	0.00327	0.528			0.851	0.00339	0.549	3.9%	0.539	0.851	0.00333
		200	0.860	0.00326	0.534			0.860	0.00338	0.552	3.5%	0.543	0.860	0.00332
		225	0.867	0.00328	0.541			0.867	0.00337	0.556	2.7%	0.549	0.867	0.00333
		250	0.872	0.00327	0.541			0.872	0.00338	0.560	3.4%	0.550	0.872	0.00332
		275	0.876	0.00326	0.543			0.876	0.00337	0.561	3.2%	0.552	0.876	0.00331
		300	0.880	0.00335	0.561			0.880	0.00336	0.562	0.2%	0.561	0.880	0.00336
2.02	2.25	25	0.713	0.00482	0.773	2.02	2.25	0.713	0.00525	0.841	8.8%	0.807	0.713	0.00504
TMD	57.80%	50	0.763	0.00466	0.799			0.763	0.00509	0.873	9.3%	0.836	0.763	0.00488
		75	0.796	0.00452	0.808			0.796	0.00502	0.897	11.0%	0.853	0.796	0.00477
		100	0.815	0.00439	0.804			0.815	0.00487	0.892	10.9%	0.848	0.815	0.00463
		125	0.829	0.00434	0.808			0.829	0.00478	0.889	10.0%	0.849	0.829	0.00456
		150	0.840	0.00433	0.818			0.840	0.00470	0.887	8.4%	0.852	0.840	0.00452
		175	0.851	0.00435	0.831			0.851	0.00465	0.889	7.0%	0.860	0.851	0.00450
		200	0.860	0.00435	0.840			0.860	0.00464	0.896	6.6%	0.868	0.860	0.00449
		225	0.867	0.00437	0.850			0.867	0.00463	0.901	6.0%	0.876	0.867	0.00450
		250	0.872	0.00435	0.852			0.872	0.00463	0.907	6.4%	0.880	0.872	0.00449
		275	0.876	0.00441	0.867			0.876	0.00461	0.907	4.6%	0.887	0.876	0.00451
		300	0.880	0.00457	0.902			0.880	0.00462	0.914	1.3%	0.908	0.880	0.00459
2.05	2.52	25	0.713	0.00511	0.917	2.05	2.52	0.713	0.00564	1.011	10.2%	0.964	0.713	0.00537
TMD	64.72%	50	0.763	0.00500	0.960			0.763	0.00554	1.063	10.8%	1.012	0.763	0.00527
		75	0.796	0.00488	0.977			0.796	0.00538	1.077	10.2%	1.027	0.796	0.00513
		100	0.815	0.00477	0.978			0.815	0.00528	1.082	10.6%	1.030	0.815	0.00502
		125	0.829	0.00467	0.973			0.829	0.00516	1.076	10.5%	1.025	0.829	0.00492
		150	0.840	0.00463	0.978			0.840	0.00509	1.075	9.9%	1.027	0.840	0.00486
		175	0.851	0.00461	0.986			0.851	0.00503	1.076	9.1%	1.031	0.851	0.00482
		200	0.860	0.00460	0.995			0.860	0.00498	1.077	8.2%	1.036	0.860	0.00479
		225	0.867	0.00456	0.993			0.867	0.00495	1.079	8.6%	1.036	0.867	0.00475
		250	0.872	0.00455	0.998			0.872	0.00490	1.075	7.7%	1.037	0.872	0.00473
		275	0.876	0.00457	1.008			0.876	0.00484	1.067	5.9%	1.038	0.876	0.00471
		300	0.880	0.00476	1.053			0.880	0.00492	1.090	3.5%	1.071	0.880	0.00484

B. DSC System Diagram

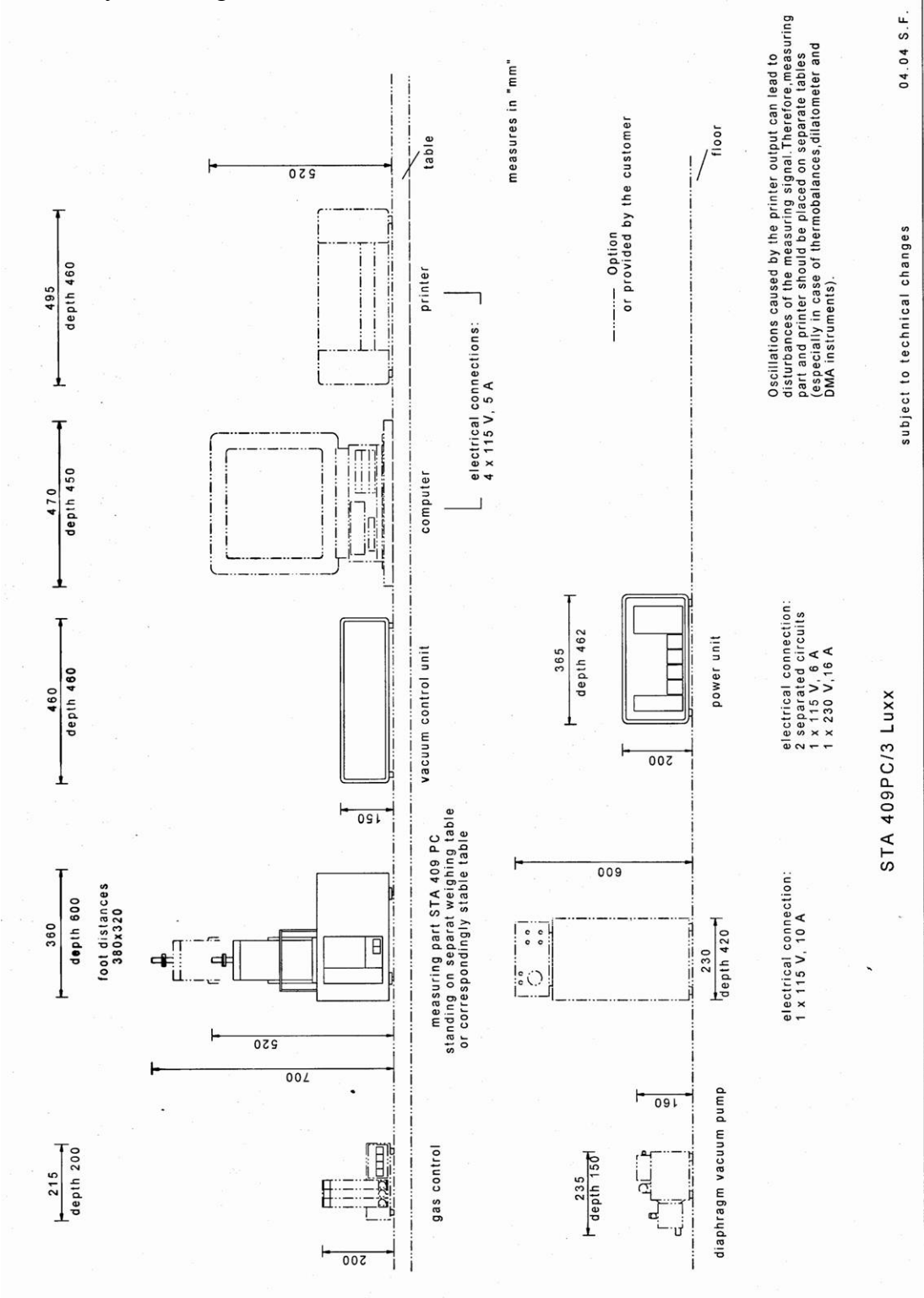


Figure A.1 – DSC/TGA Instrument Schematic with External Peripheral systems [43]



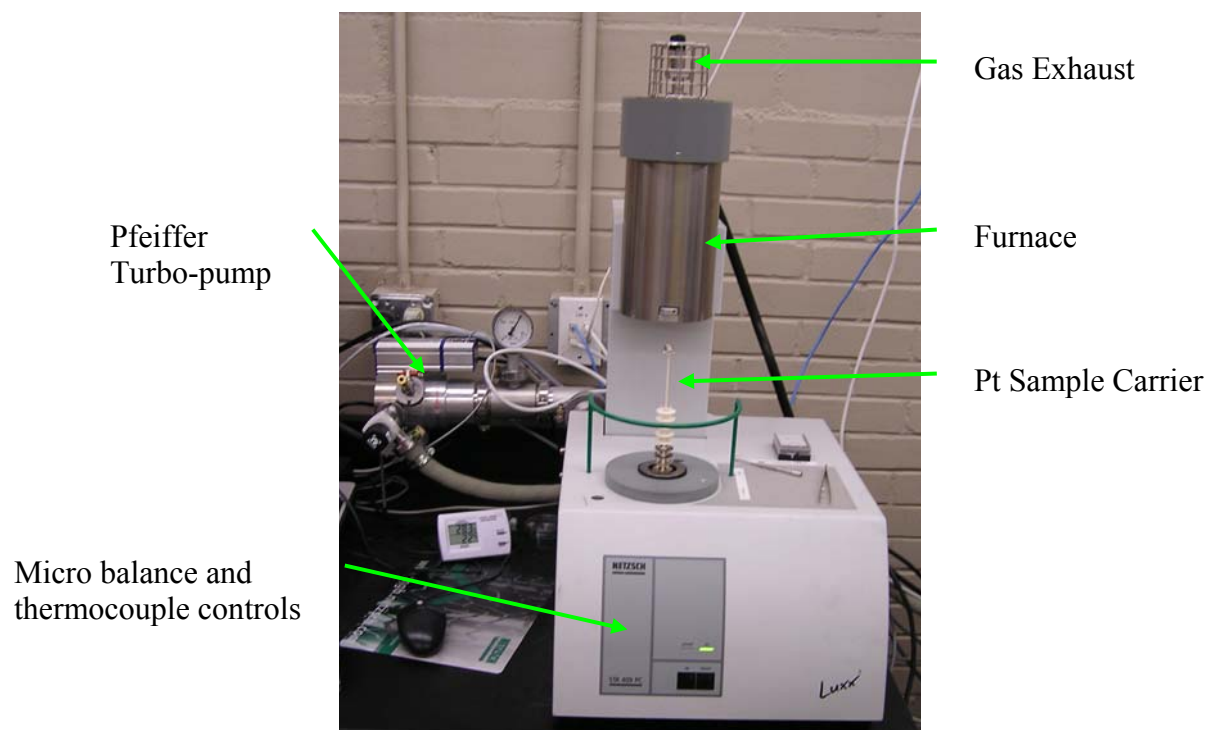


Figure A.2 – DSC/TGA Instrument Digital Photograph (Front View)

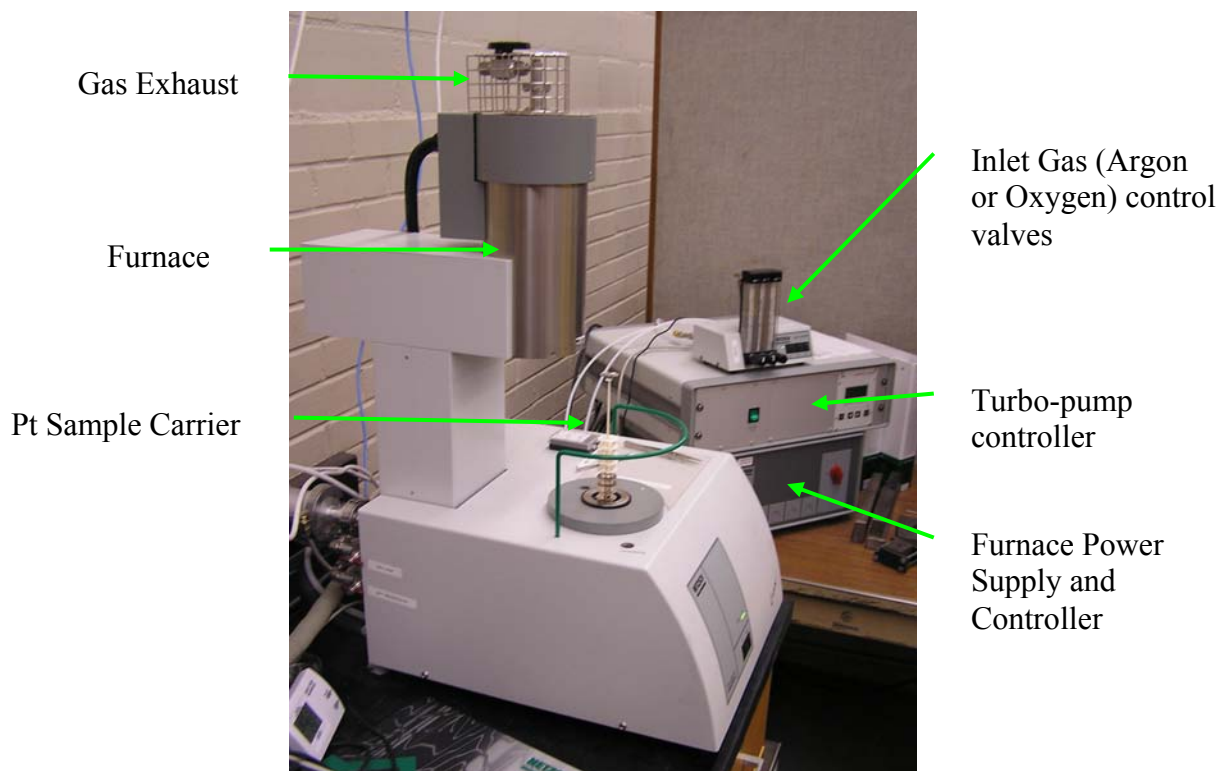


Figure A.3 – DSC/TGA Instrument Digital Photograph (Side View)

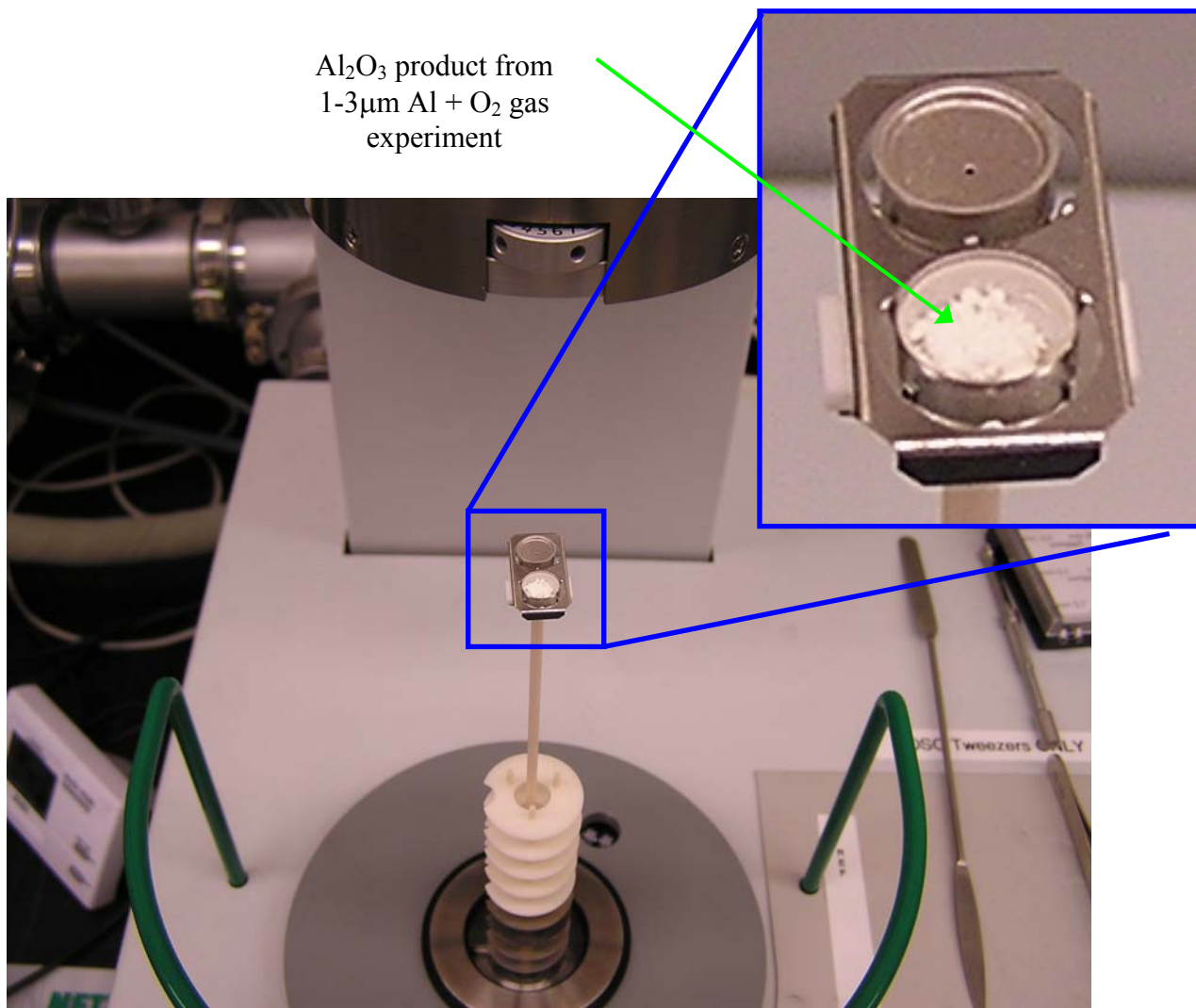


Figure A.4 – DSC/TGA Sample Carrier Photograph

C.

### DSC Temperature Calibration

DSC curves were generated for five pure metal standard samples: indium (In), tin (Sn), Zinc (Zn), aluminum (Al) and gold (Au). The range of metals was used to calibrate the sample carrier thermocouples for a temperature range between 150 and 1100°C. The figure below shows the DSC curves of the metal standards with the measured onset temperatures.

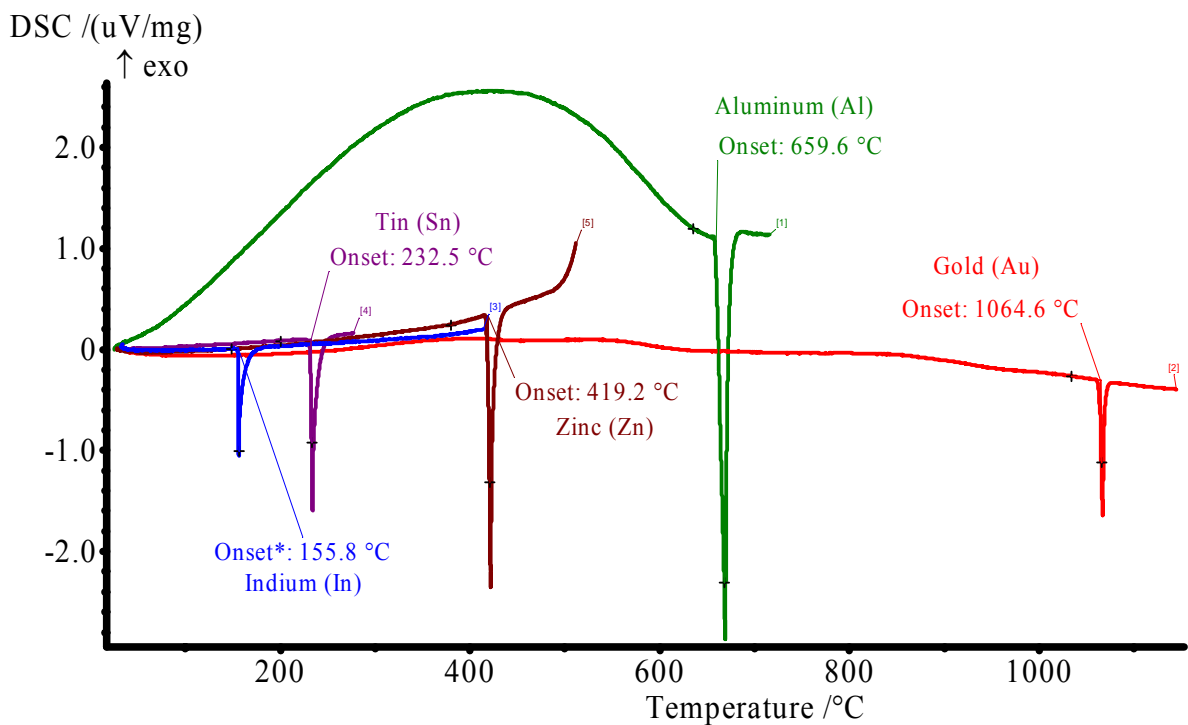


Figure C.1 DSC Endothermic Curves of ASTM Metal Standards used for Instrument Temperature Calibration

The figure and table below show the temperature calibration data as calculated by the NETZSCH Proteus software. The image shows a series of nominal temperatures ( $T_{\text{nom}}$  – data from ASTM standards) and experimental temperatures ( $T_{\text{exp}}$  – data taken from DSC curve). For the extracted polynomial curve fit, a mathematical weighting of 10 was given to the Al sample since majority of the experiments should produce critical data around the Al onset temperature.

NETZSCH Temperature Calibration - DSC/(TG) HIGH RG 2

File name: 06-22-2004  
 Heating rate: 20.0  
 Crucible: DSC/TG pan Al<sub>2</sub>O<sub>3</sub>  
 Atmosphere: Argon  
 Date: 6/22/2004 7:59:44 AM

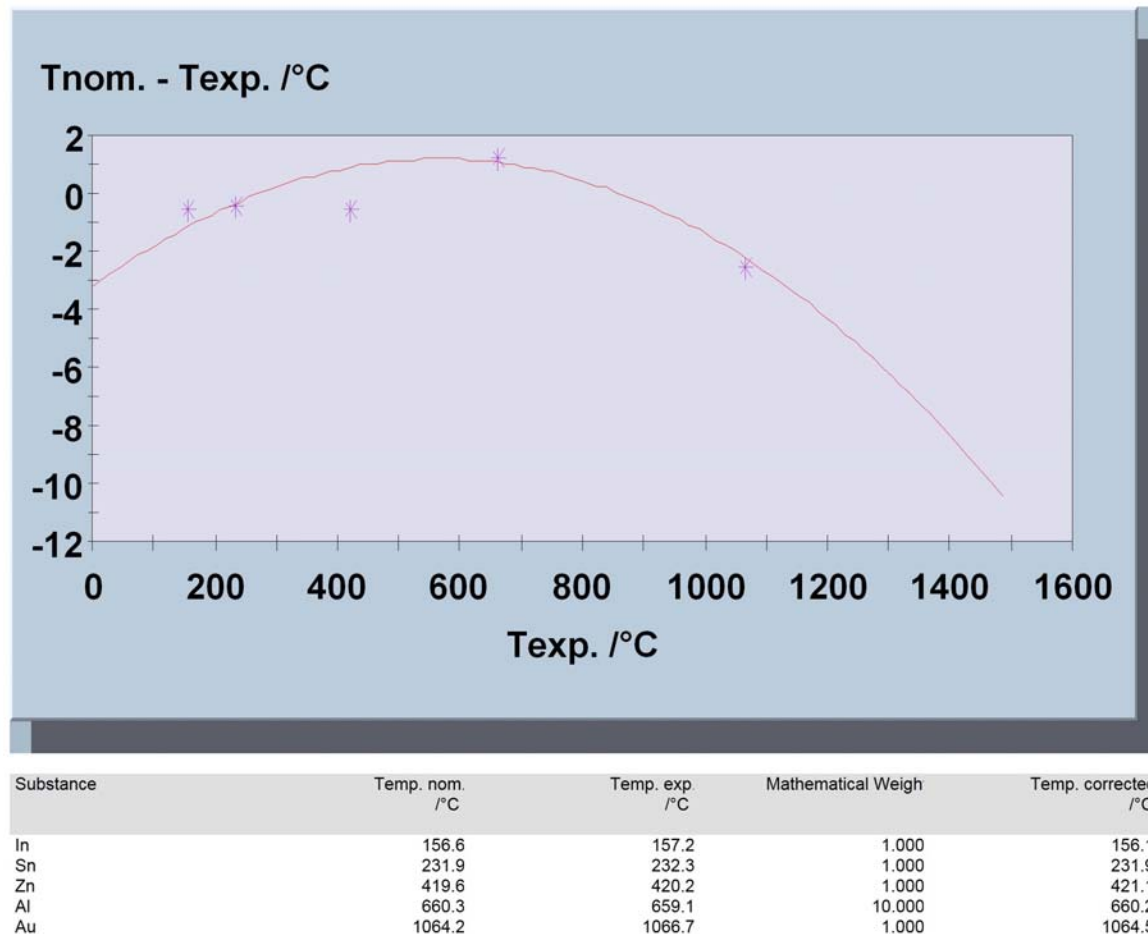


Figure C.2 – Temperature Calibration Polynomial Curve Fit Applied to Al+MoO<sub>3</sub> DSC Experimental Curves

D. DSC Sensitivity Calibration

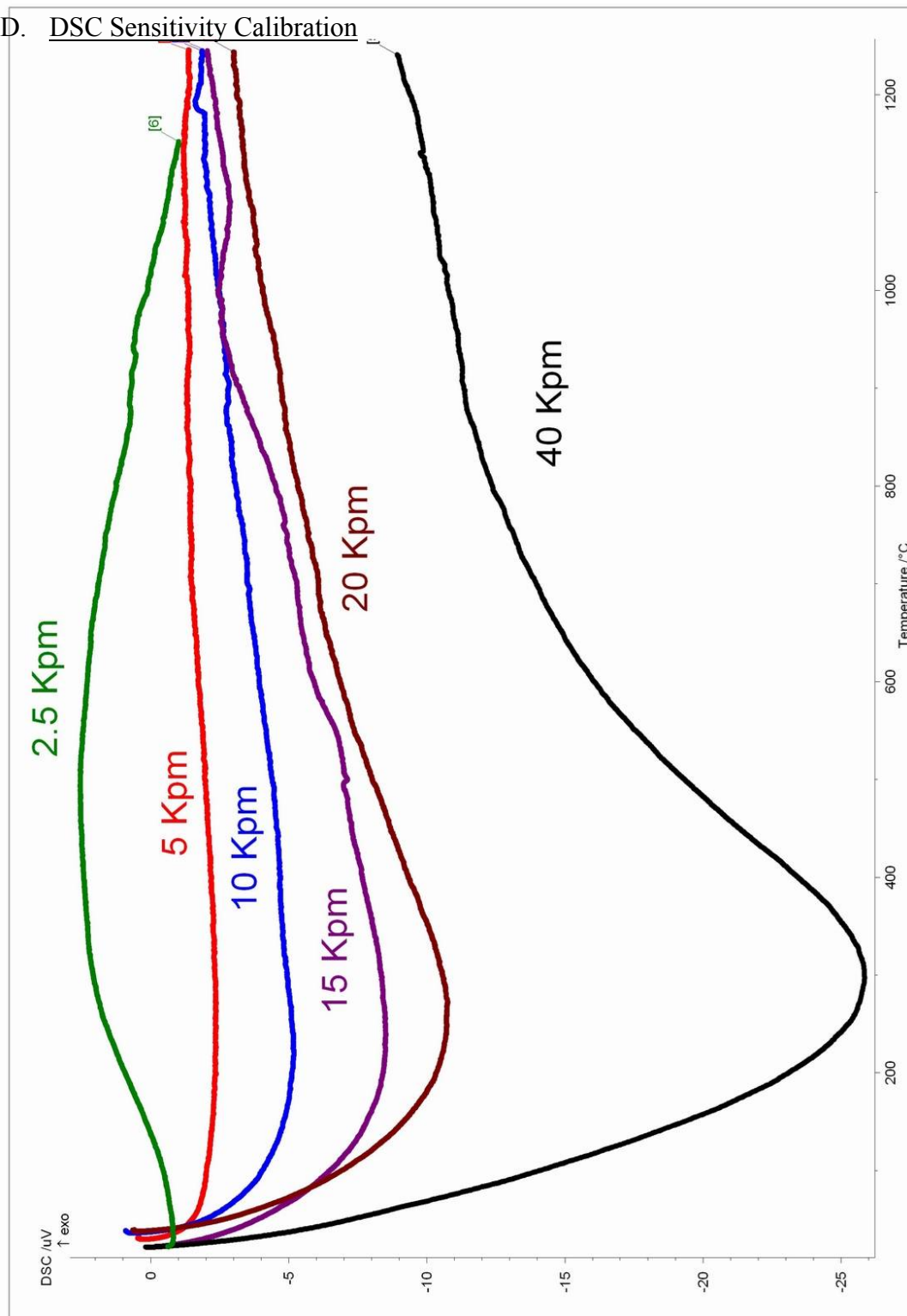


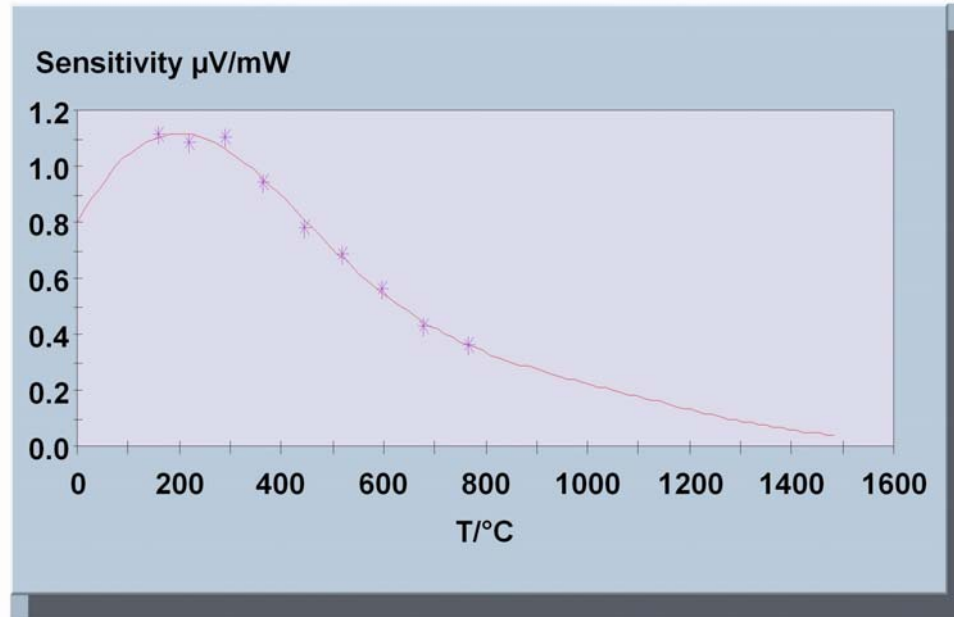
Figure D.1 – Sapphire Standard Calibration (0.25mm thick wafer, 21.2mg mass)

DSC Sensitivity Calibration by Specific Heat Method

The figure and table below shows the specific heat polynomial curve fit generated specifically based on the data from crucible C1 at a heating rate of 2.5 Kpm. As shown, the enthalpy (or  $\mu\text{V}/\text{mW}$ ) values are taken at 8 temperatures values generating a 7<sup>th</sup> degree polynomial curve fit. Similar sensitivity calibrations were conducted for all crucibles and heating rates.

NETZSCH Sensitivity - DSC/(TG) HIGH RG 2

File name: 2\_5 kpm SapphireSensitivity 8-18-04.esv  
 Calibration file: 2.5 Kpm Sapphire Sens 8-18-04.dsv  
 Heating rate: 2.5  
 Crucible: DSC/(TG) HIGH RG 2  
 Atmosphere:  
 Date: 8/19/2004 2:54:54 AM



Substance	Temp. /°C	-----	Cp sensitivity	Sensit.Exp uV/mW	Mathem. Weighting	Sensit. Calc. uV/mW
Value 4	159.1	1.000	1.113	1.113	1.000	1.106
Value 5	217.7	1.000	1.085	1.085	1.000	1.115
Value 6	290.9	1.000	1.105	1.105	1.000	1.061
Value 7	364.1	1.000	0.942	0.942	1.000	0.955
Value 8	444.6	1.000	0.783	0.783	1.000	0.810
Value 9	517.8	1.000	0.688	0.688	1.000	0.676
Value 10	598.3	1.000	0.564	0.564	1.000	0.546
Value 11	678.8	1.000	0.427	0.427	1.000	0.443
Value 12	766.7	1.000	0.362	0.362	1.000	0.360

Figure D.2 – Sapphire Sensitivity Calibration (7<sup>th</sup> order polynomial curve fit)

## E. Aluminum Oxidation DSC/TGA Curves

### E.1 50nm Al + O<sub>2</sub> Gas

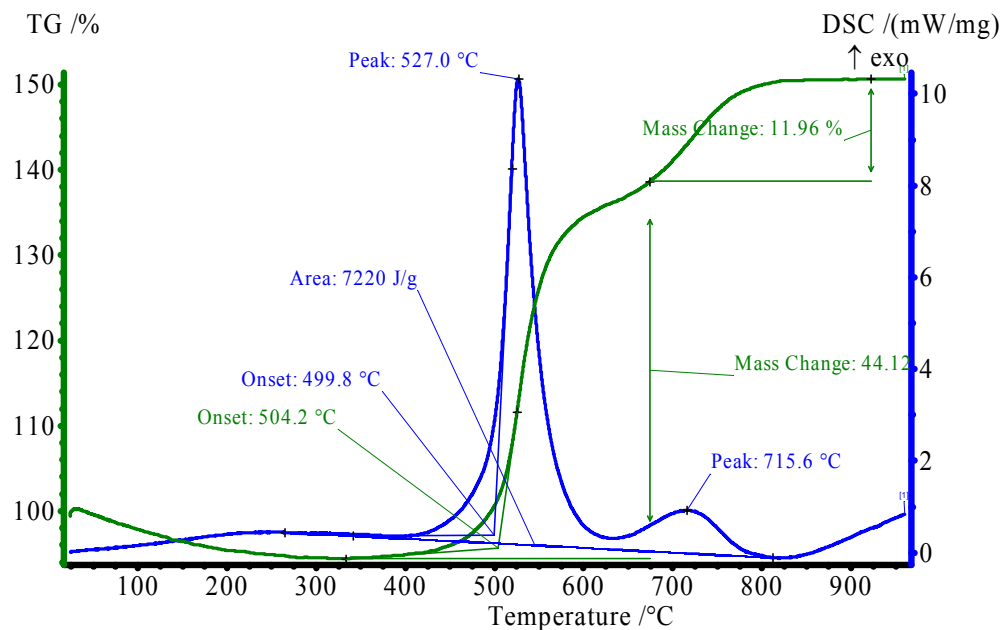


Figure E.1a – 50nm Al + O<sub>2</sub> DSC/TGA Curves (5Kpm)

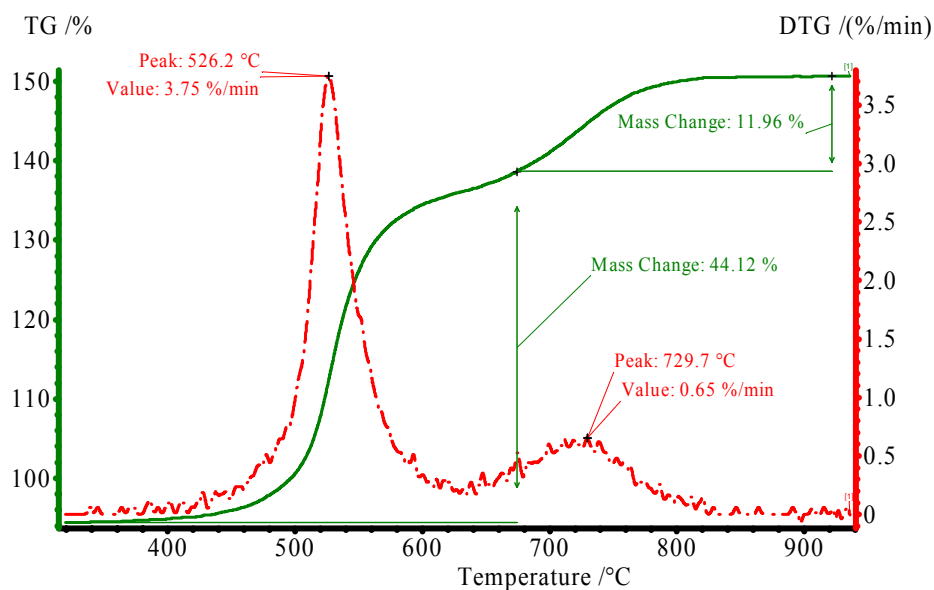


Figure E.1b – 50nm Al + O<sub>2</sub> TGA and DTG Curves (5Kpm)

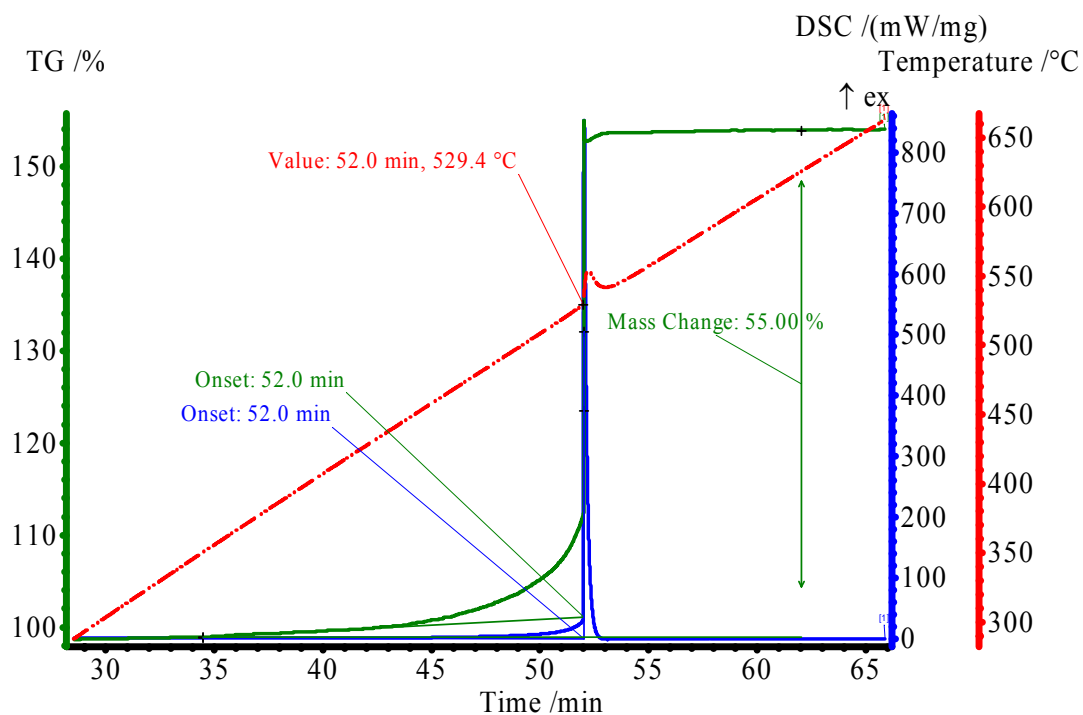


Figure D.1c – 50nm Al + O<sub>2</sub> DSC/TGA Curves (10Kpm)

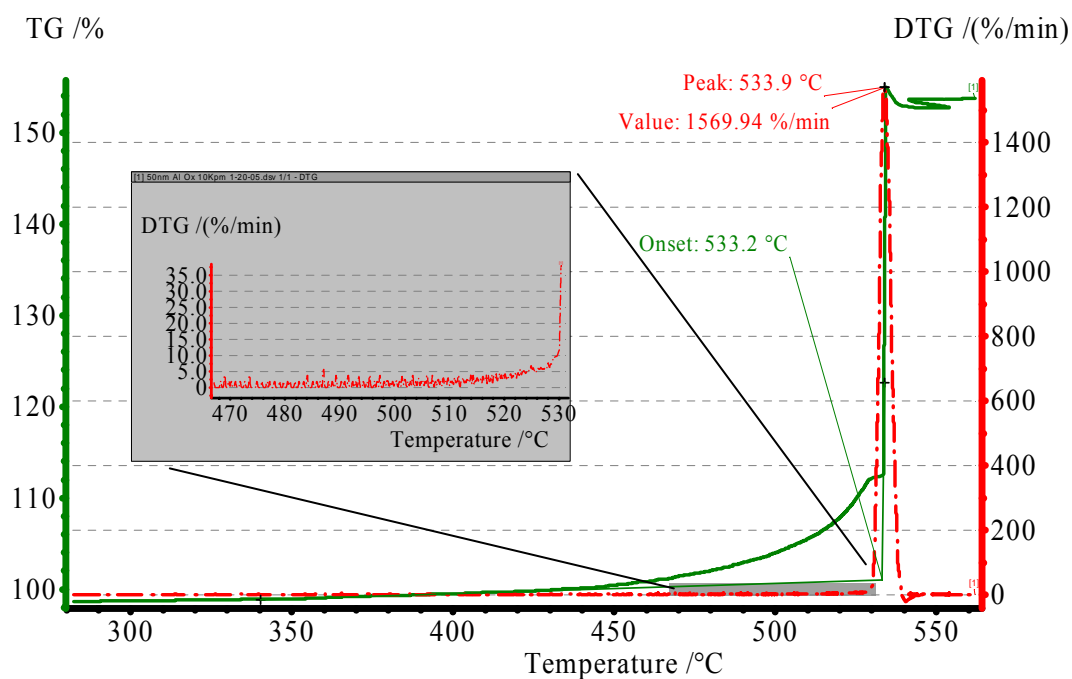


Figure E.1d – 50nm Al + O<sub>2</sub> TGA and DTG Curves (10Kpm)



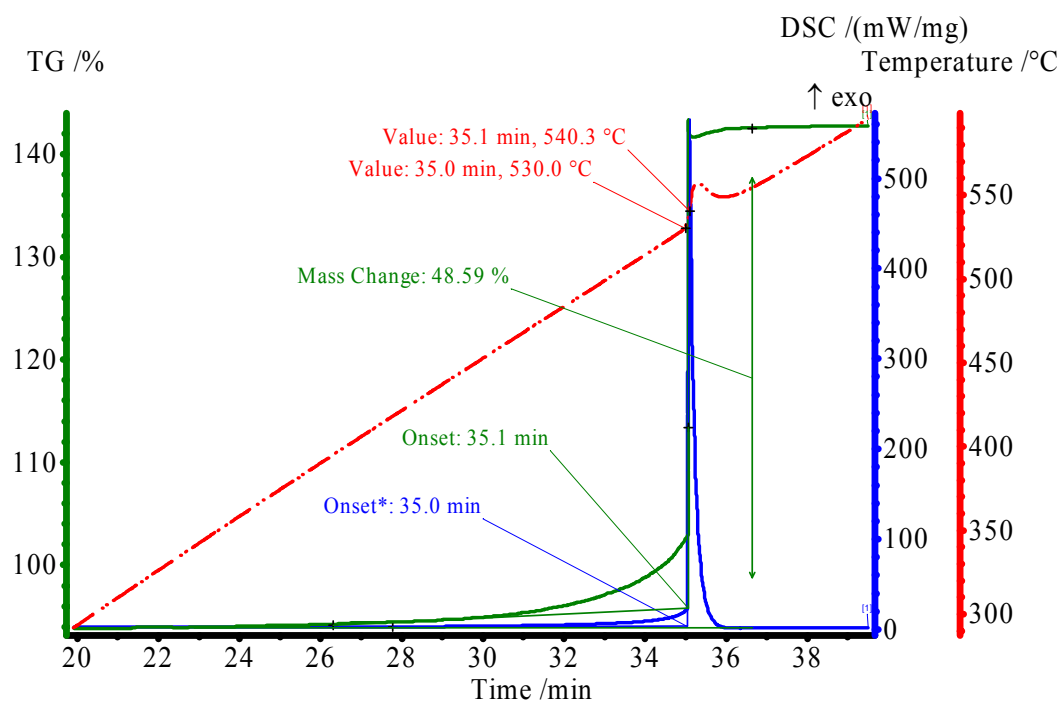


Figure E.1e – 50nm Al + O<sub>2</sub> DSC/TGA Curves (15Kpm)

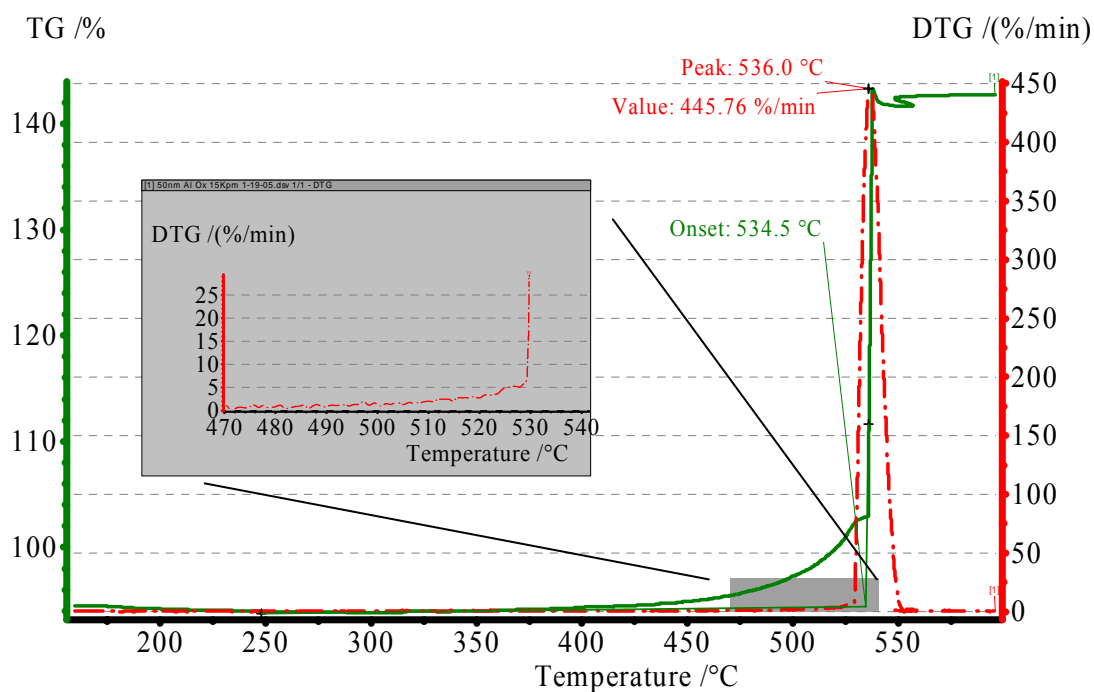


Figure E.1f – 50nm Al + O<sub>2</sub> TGA and DTG Curves (15Kpm)

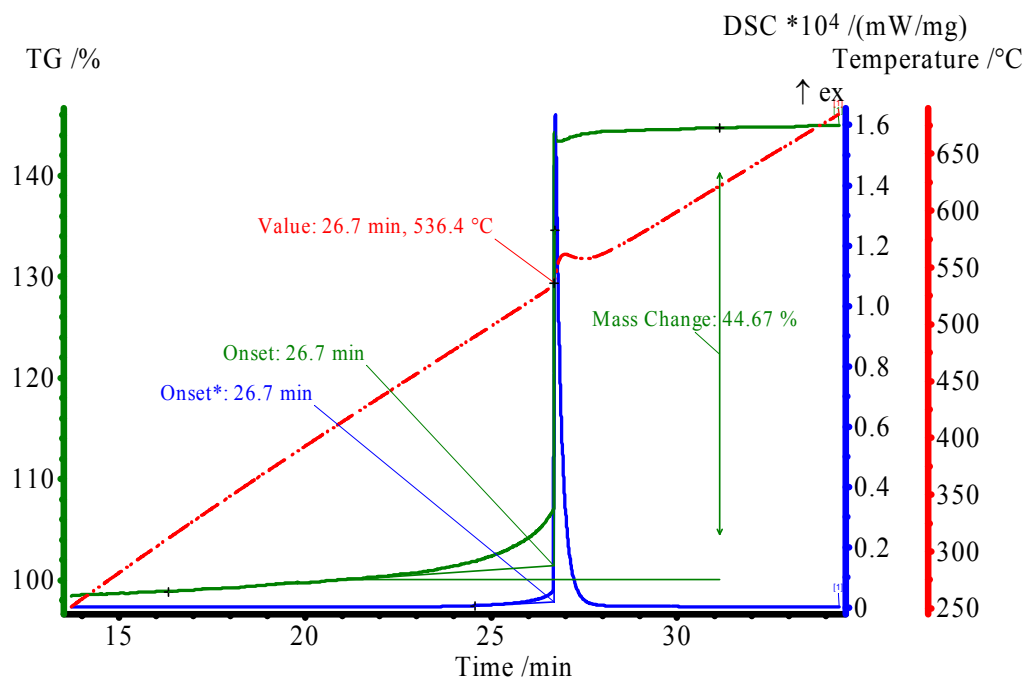


Figure E.1g – 50nm Al + O<sub>2</sub> DSC/TGA Curves (20Kpm)

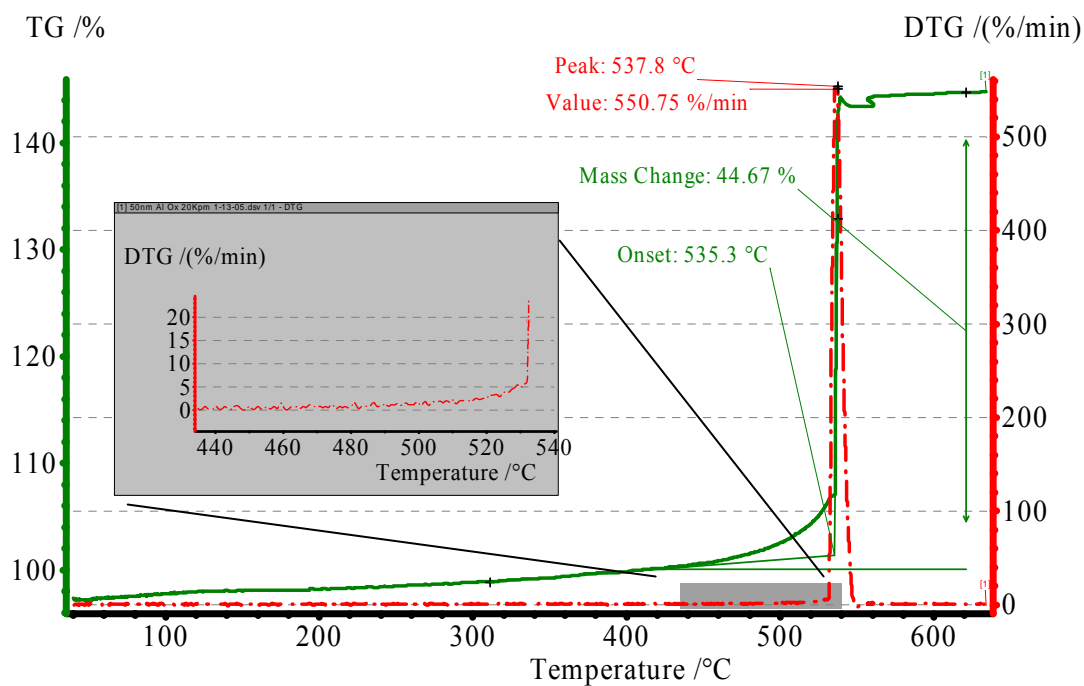


Figure E.1h – 50nm Al + O<sub>2</sub> TGA and DTG Curves (20Kpm)

## E.2 1-3 $\mu$ m Al + O<sub>2</sub> Gas

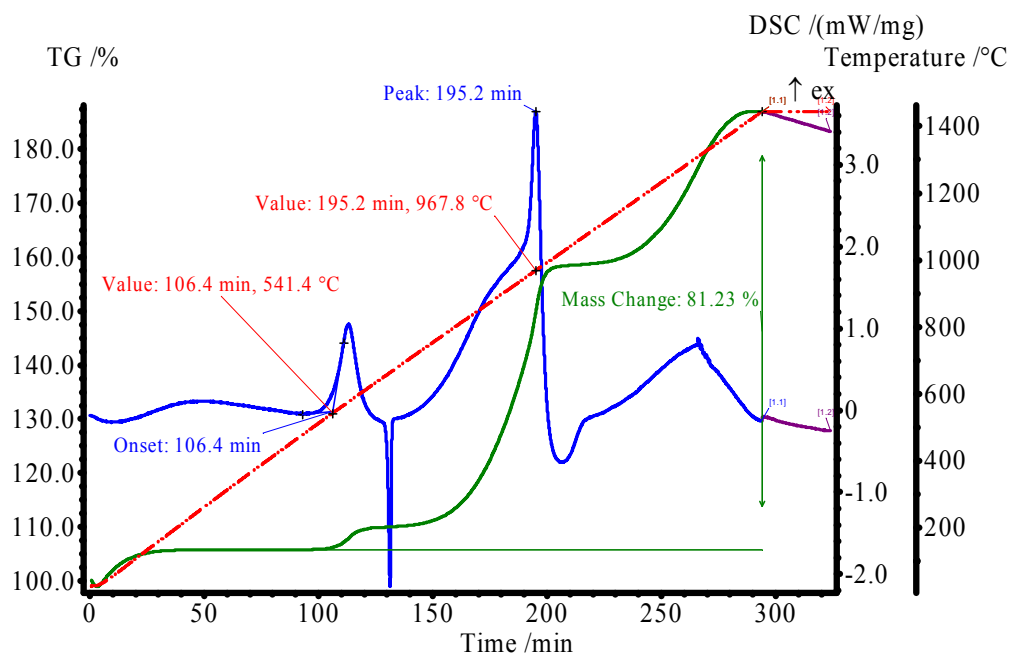


Figure E.2a – 1-3 $\mu$ m Al + O<sub>2</sub> DSC/TGA Curves (5Kpm)

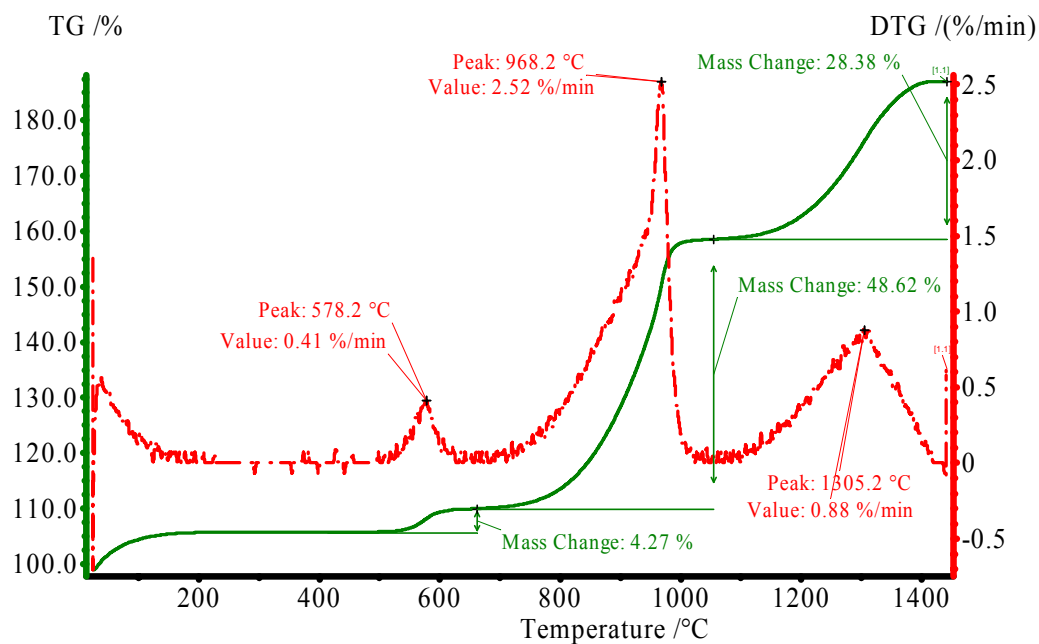


Figure E.2b – 1-3 $\mu$ m Al + O<sub>2</sub> TGA and DTG Curves (5Kpm)

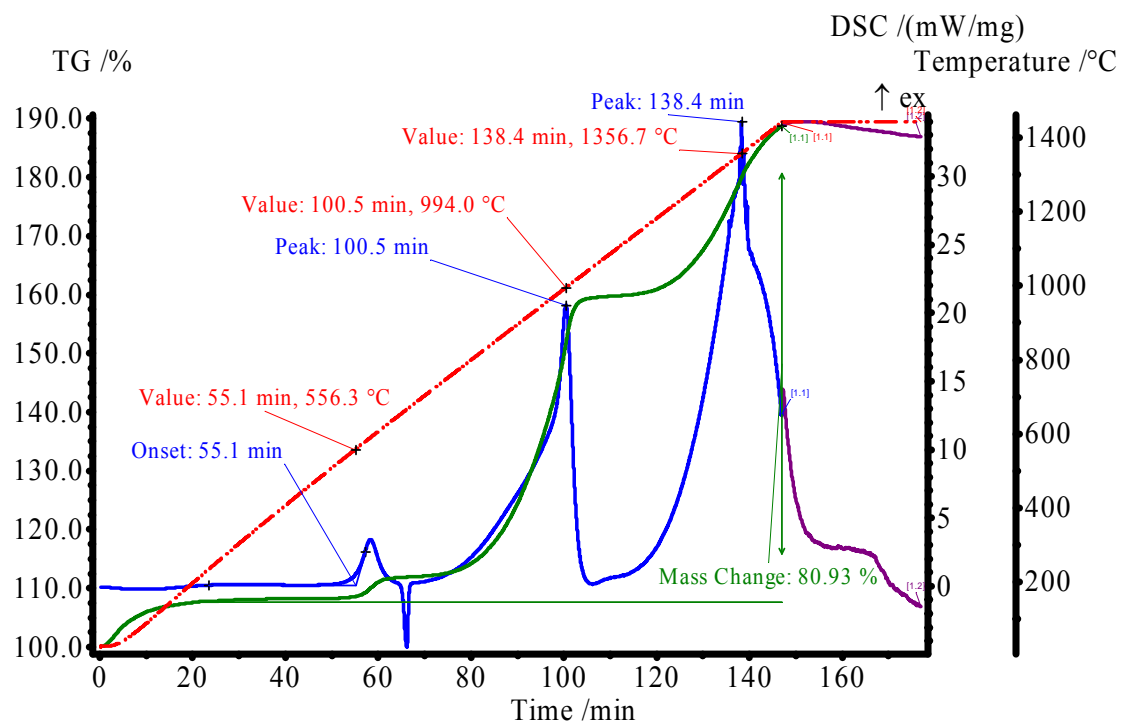


Figure E.2c – 1-3 $\mu$ m Al + O<sub>2</sub> DSC/TGA Curves (10Kpm)

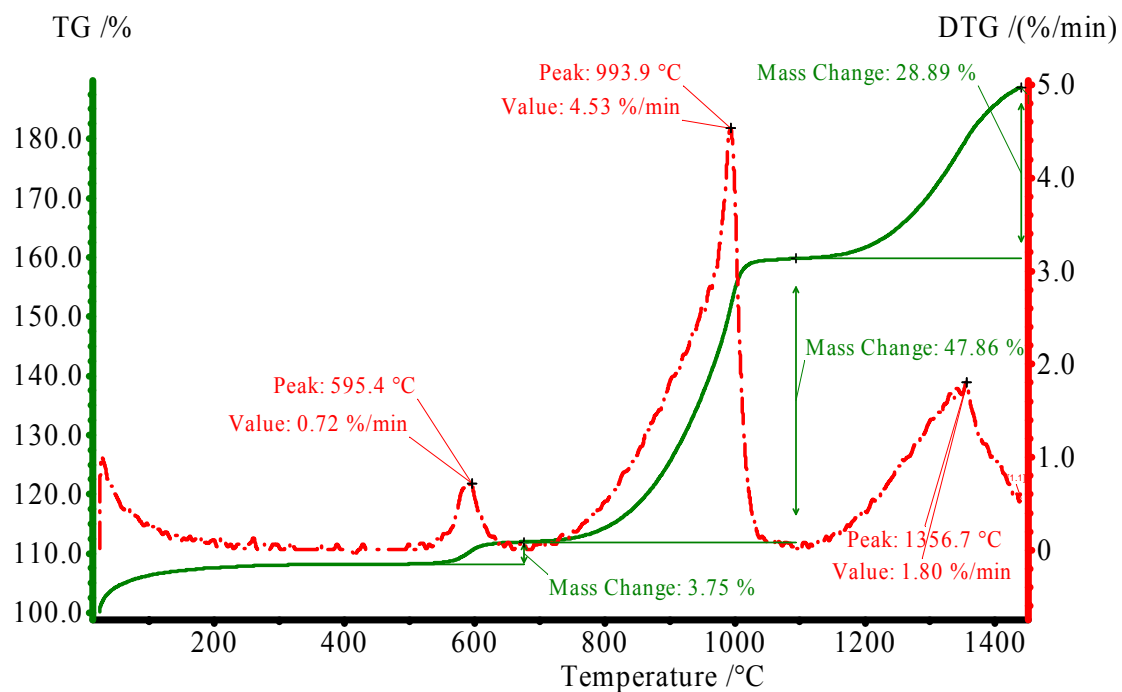


Figure E.2d – 1-3 $\mu$ m Al + O<sub>2</sub> TGA and DTG Curves (10Kpm)

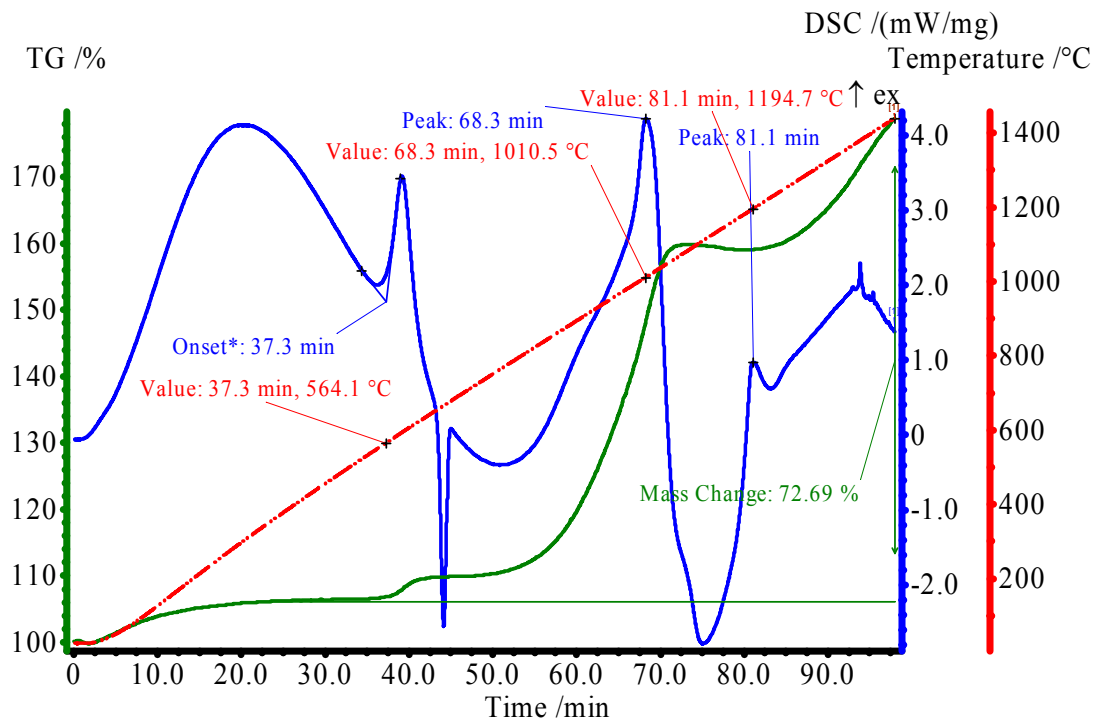


Figure E.2e – 1-3 $\mu$ m Al + O<sub>2</sub> DSC/TGA Curves (15Kpm)

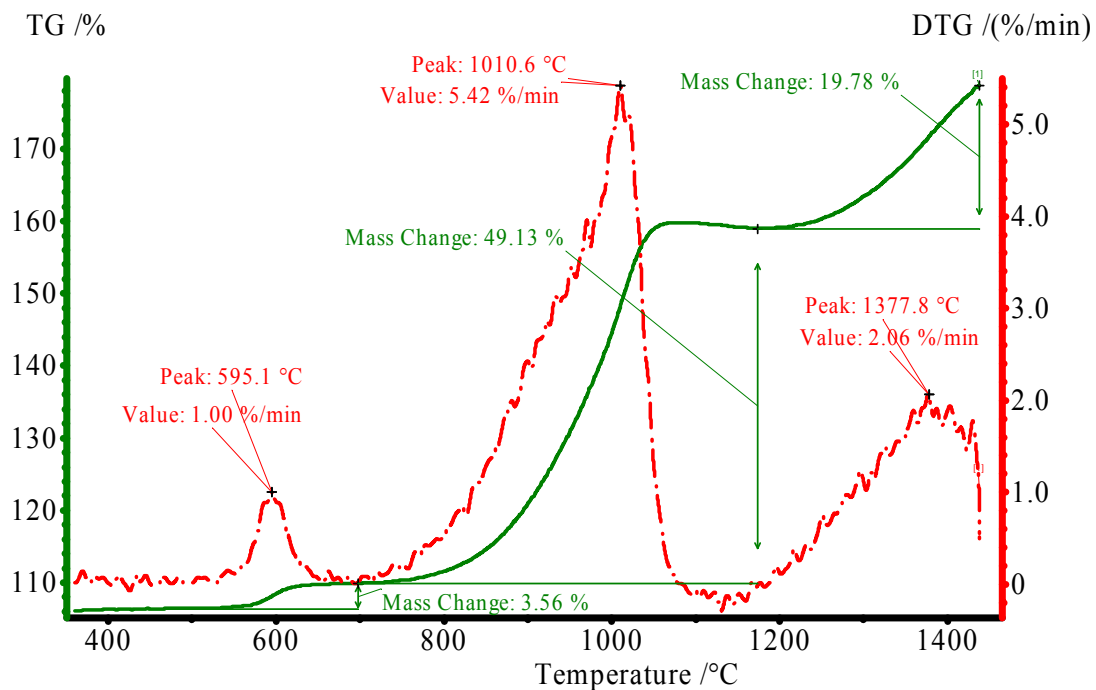


Figure E.2f – 1-3 $\mu$ m Al + O<sub>2</sub> TGA and DTG Curves (15Kpm)

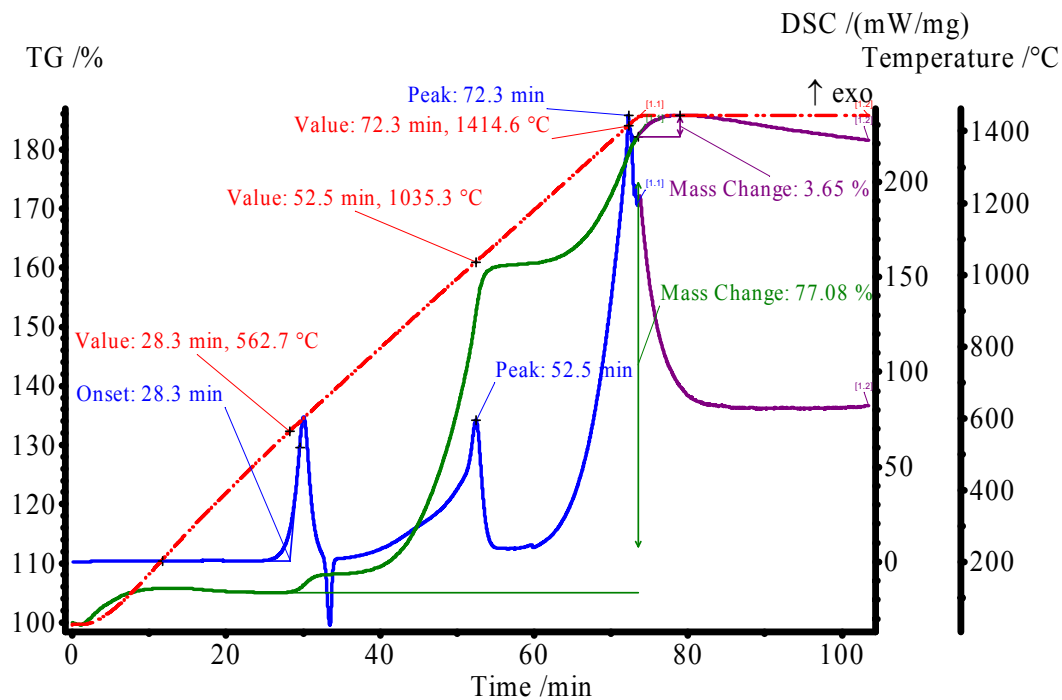


Figure E.2g – 1-3 $\mu$ m Al + O<sub>2</sub> DSC/TGA Curves (20Kpm)

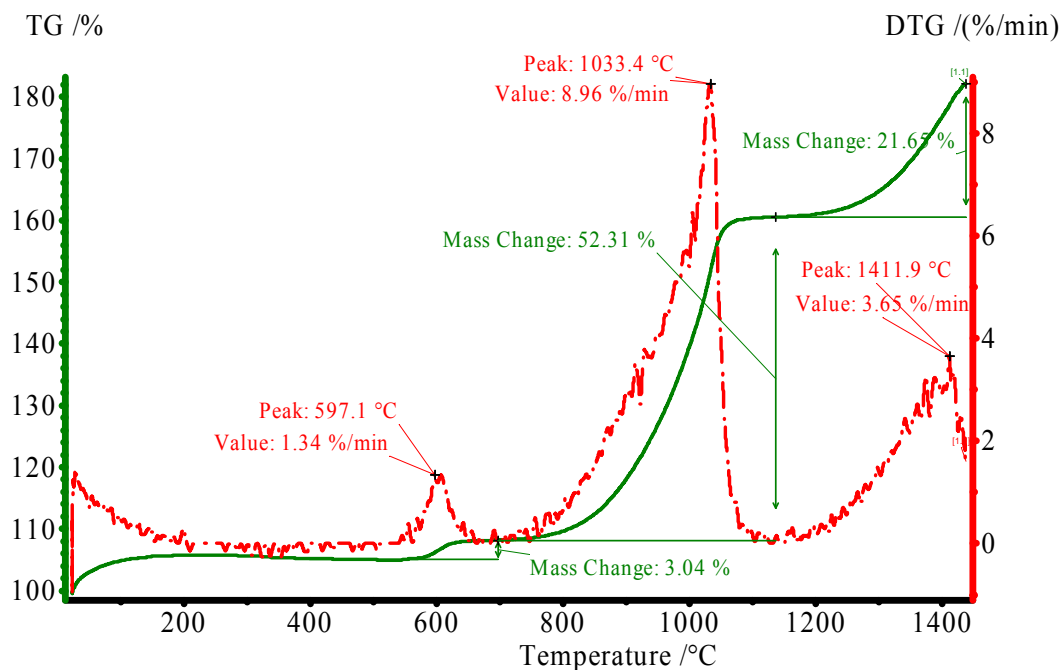


Figure E.2h – 1-3 $\mu$ m Al + O<sub>2</sub> TGA and DTG Curves (20Kpm)

*E.3 4.5-7 $\mu$ m Al + O<sub>2</sub> Gas*

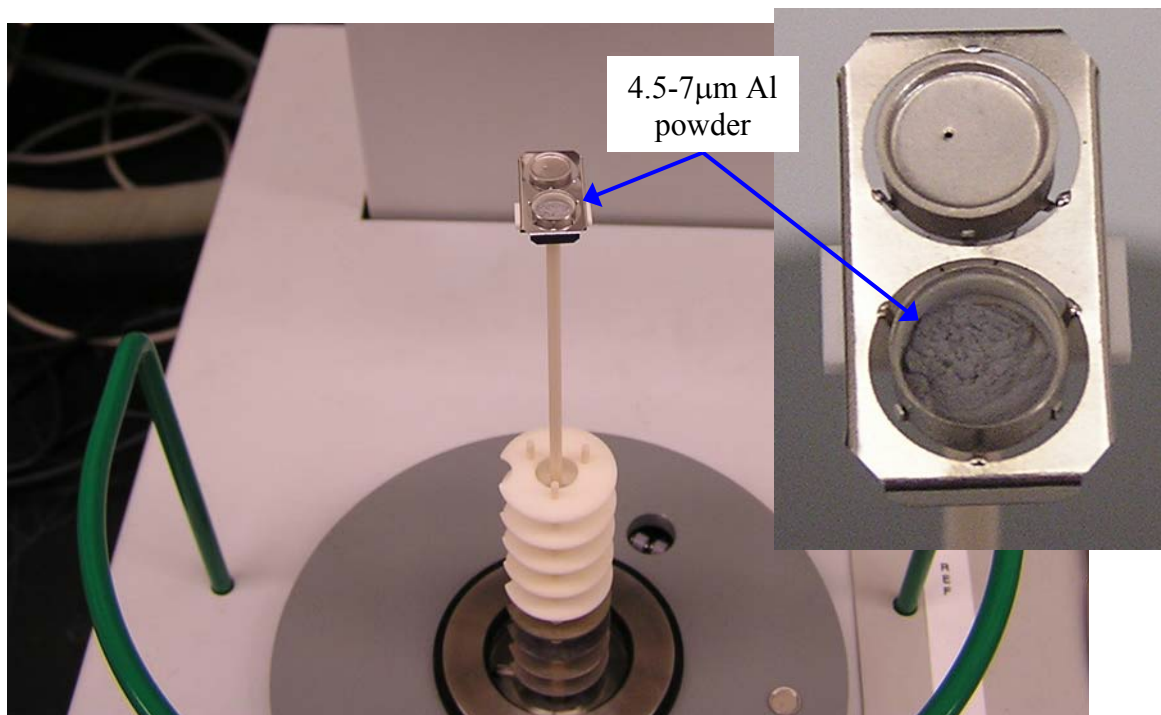


Figure XXX - 5.2mg of 4.5-7 $\mu$ m Aluminum powder in DSC crucible prior to oxidation

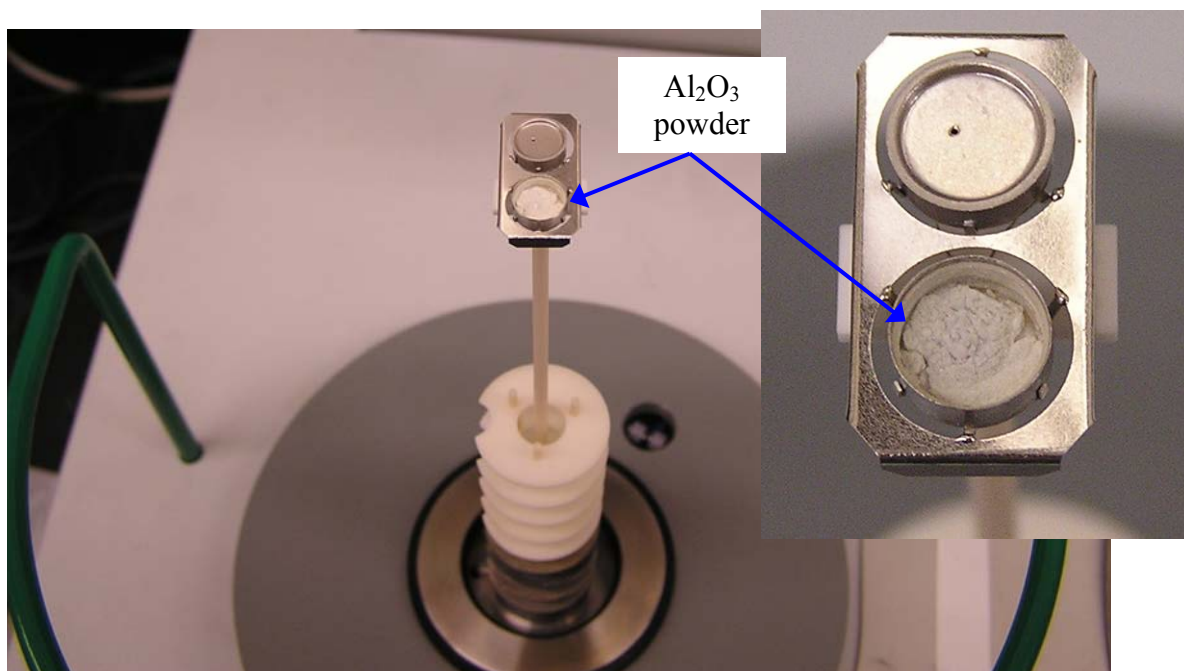


Figure XXX – 9.24mg Al<sub>2</sub>O<sub>3</sub> from 4.5-7 $\mu$ m Al (originally 5.2mg above) oxidation

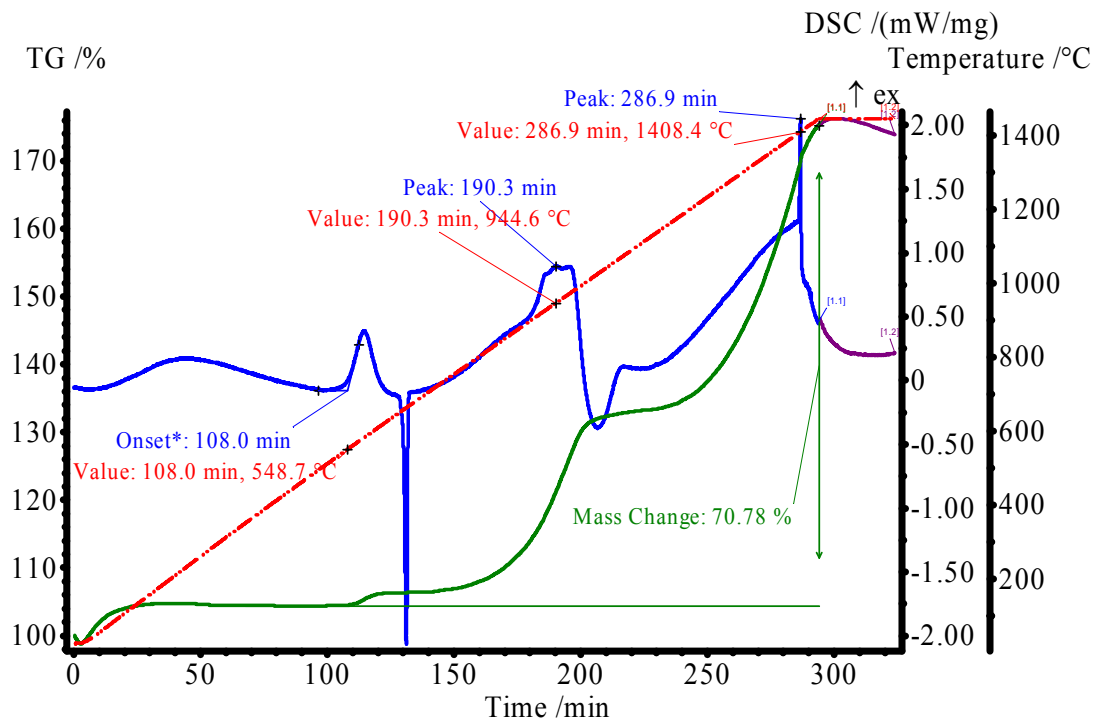


Figure E.3a – 4.5-7 $\mu$ m Al + O<sub>2</sub> DSC/TGA Curves (5Kpm)

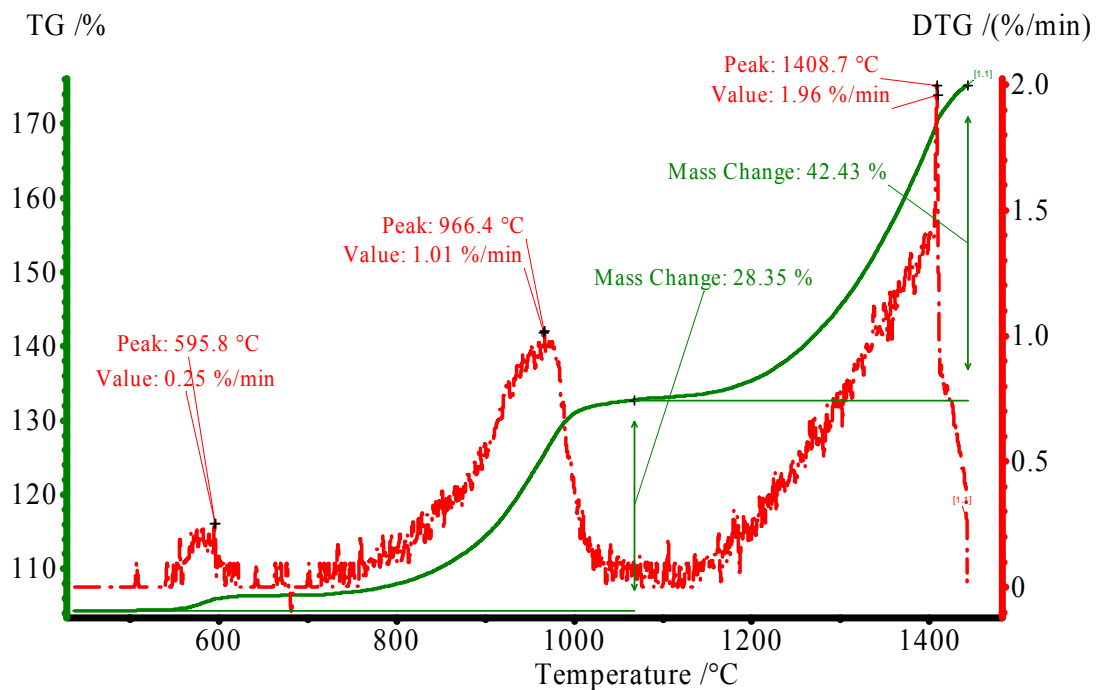


Figure E.3b – 4.5-7 $\mu$ m Al + O<sub>2</sub> TGA and DTG Curves (5Kpm)



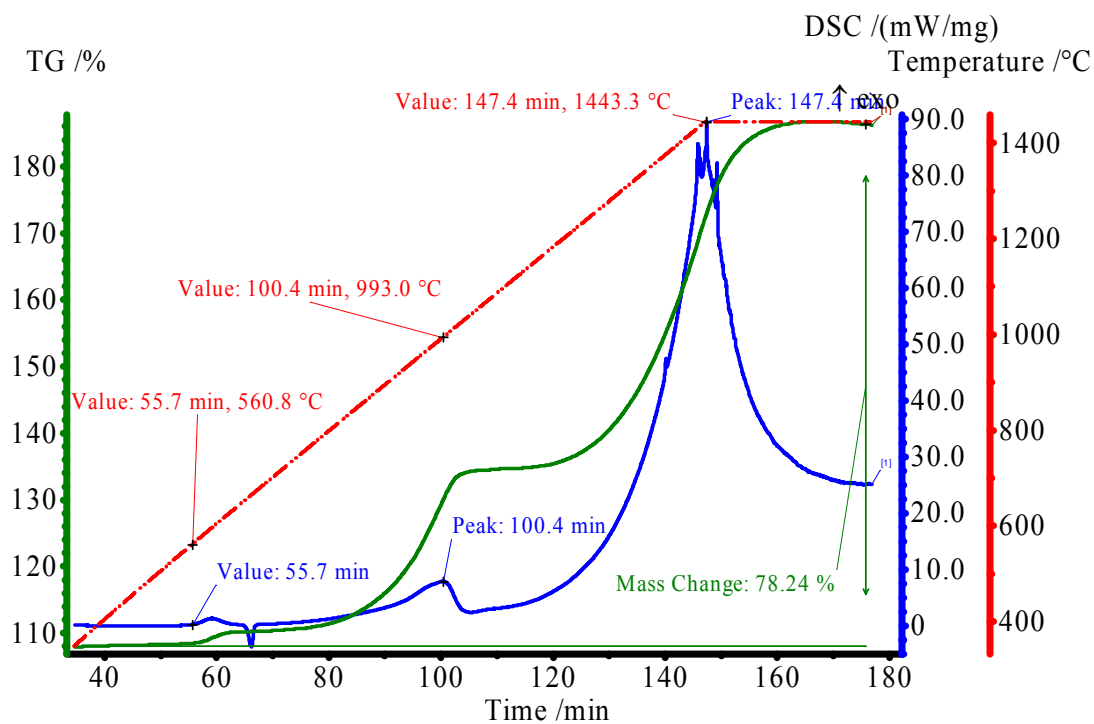


Figure E.3c – 4.5-7 $\mu$ m Al + O<sub>2</sub> DSC/TGA Curves (10Kpm)

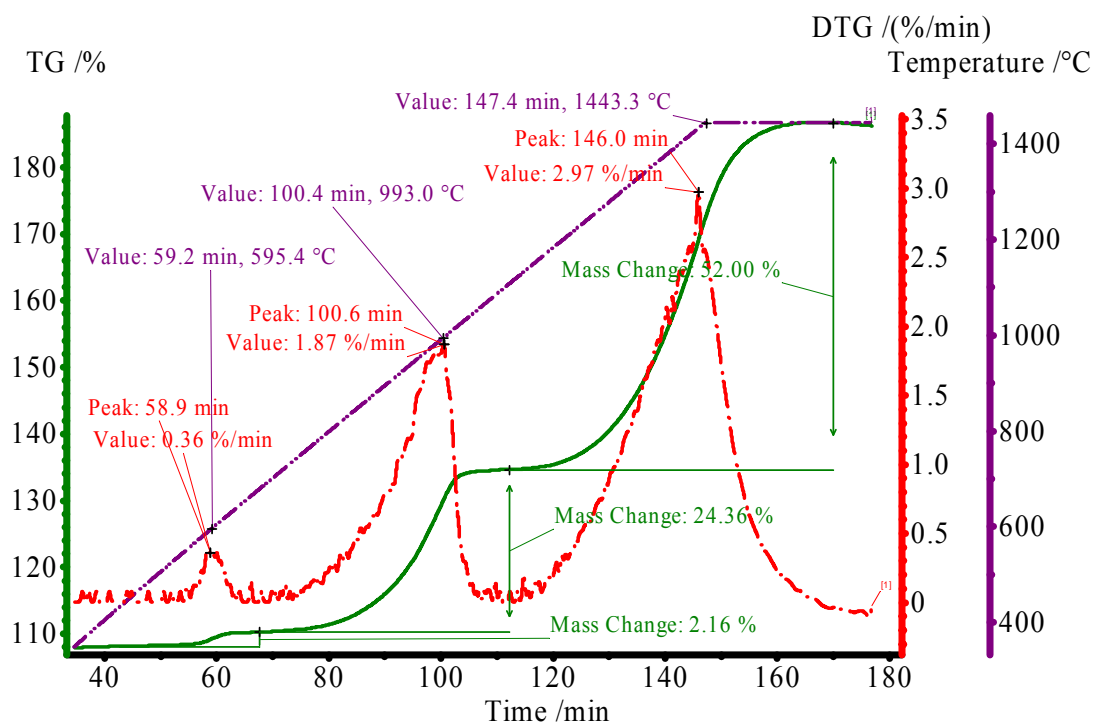


Figure E.3d – 4.5-7 $\mu$ m Al + O<sub>2</sub> TGA and DTG Curves (10Kpm)

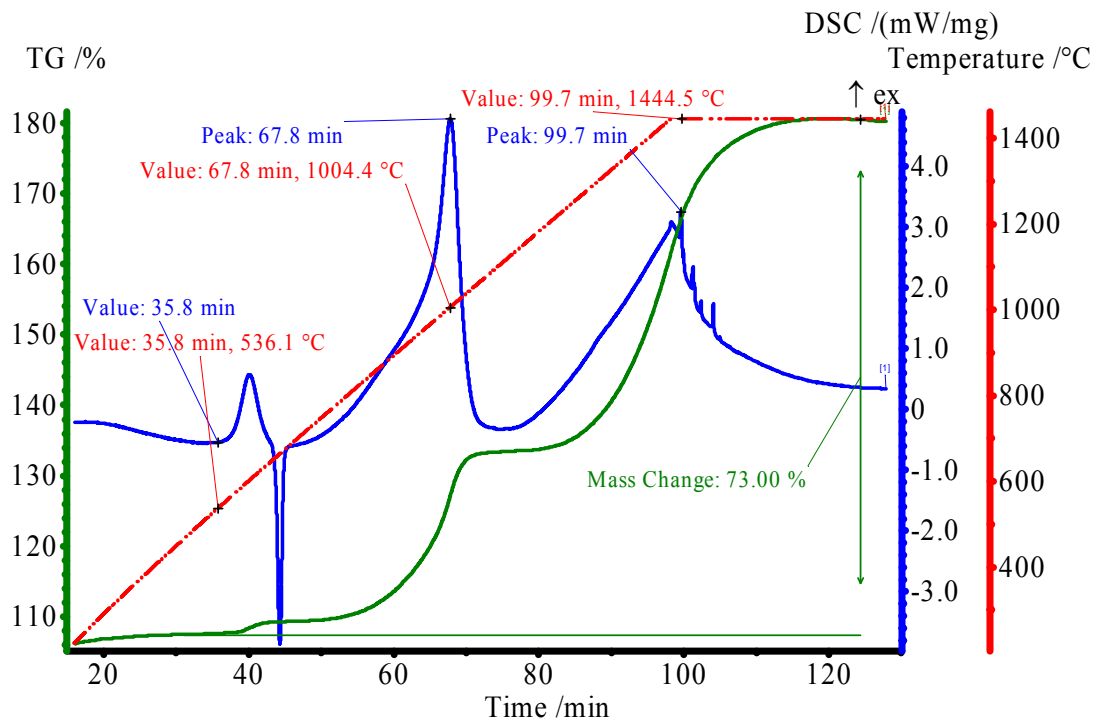


Figure E.3e – 4.5-7 $\mu$ m Al + O<sub>2</sub> DSC/TGA Curves (15Kpm)

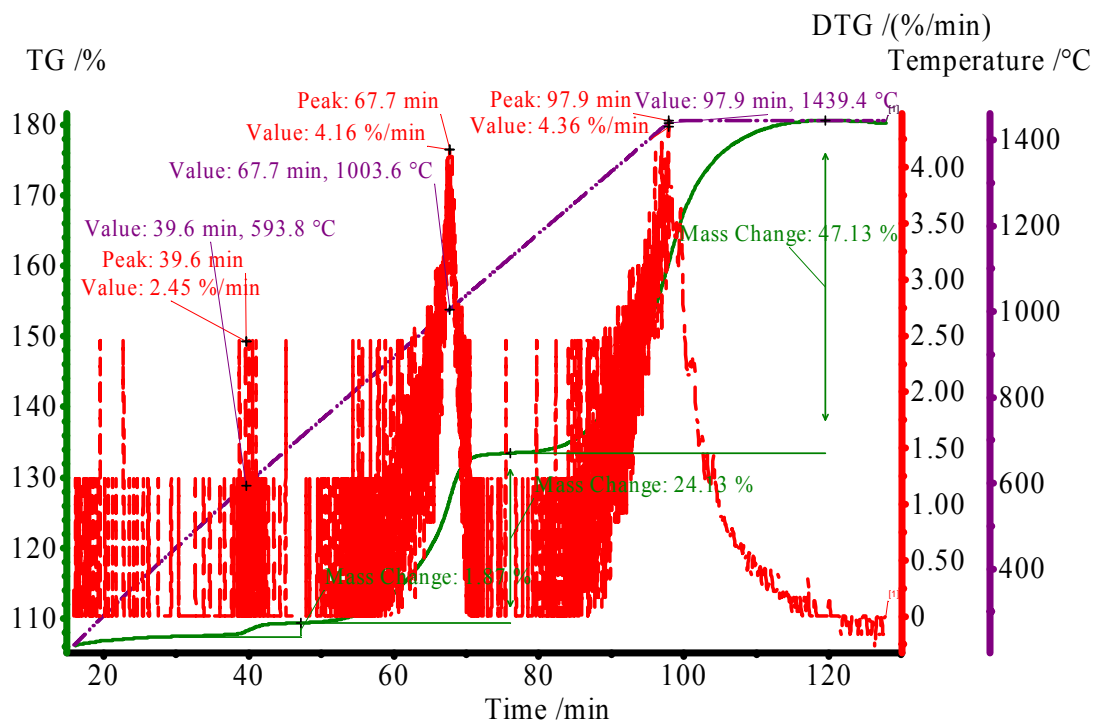


Figure E.3f – 4.5-7 $\mu$ m Al + O<sub>2</sub> TGA and DTG Curves (15Kpm)

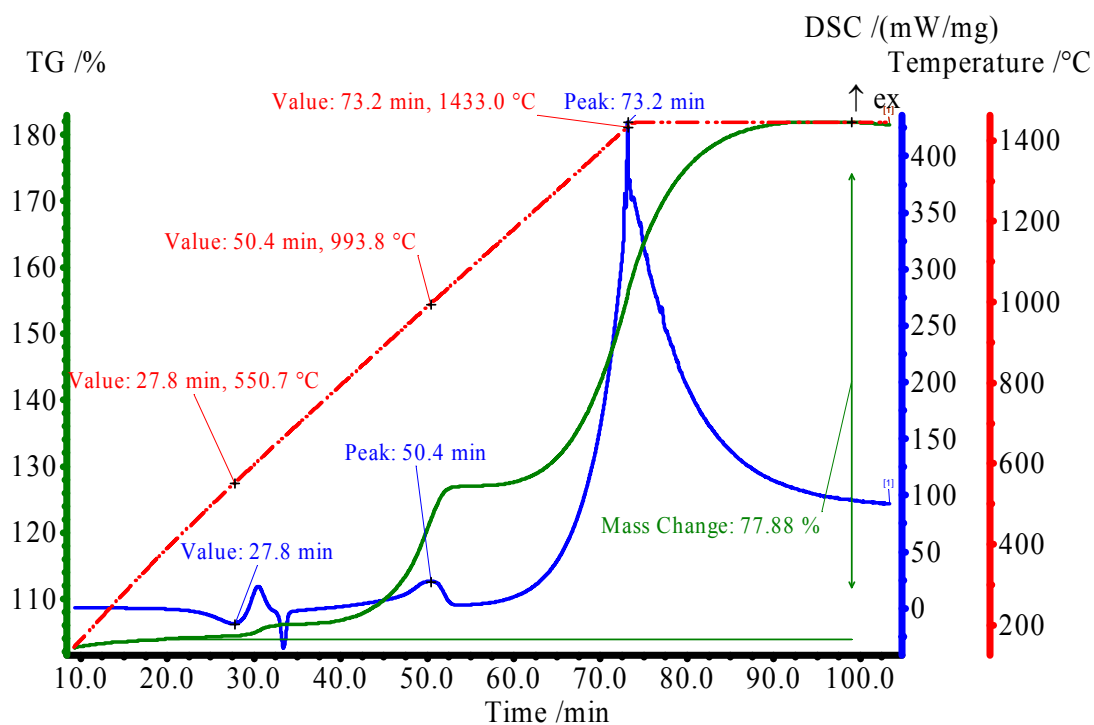


Figure E.3g – 4.5-7 $\mu$ m Al + O<sub>2</sub> DSC/TGA Curves (20Kpm)

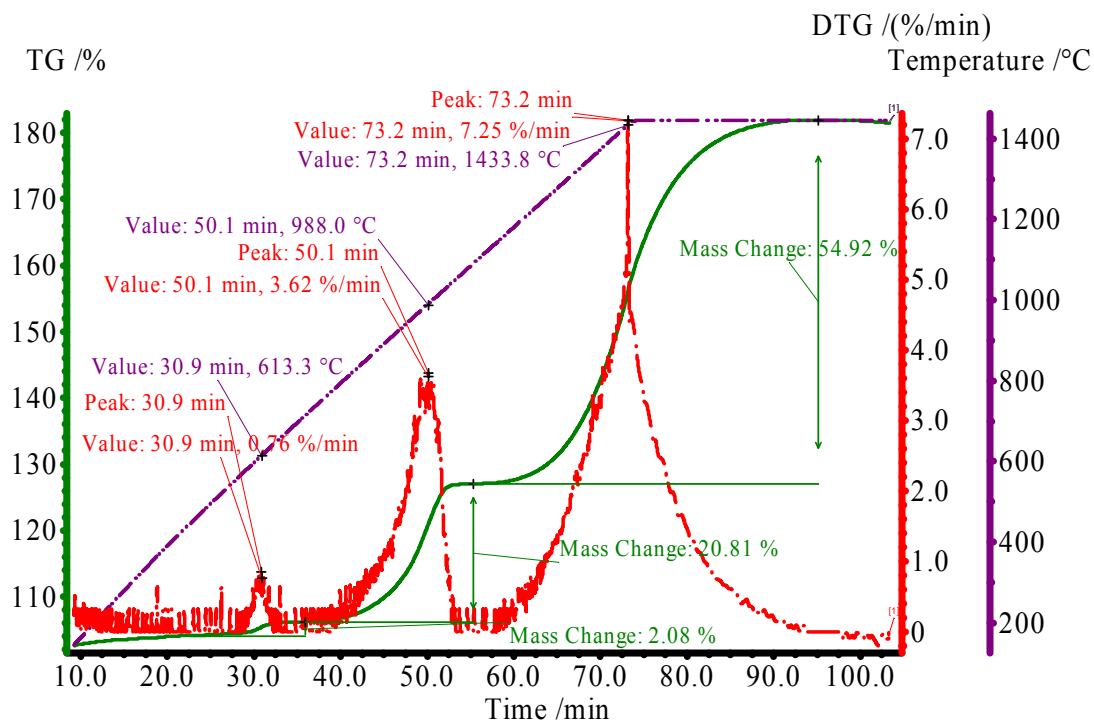


Figure E.3h – 4.5-7 $\mu$ m Al + O<sub>2</sub> TGA and DTG Curves (20Kpm)

#### E.4 20 $\mu$ m Al + O<sub>2</sub> Gas

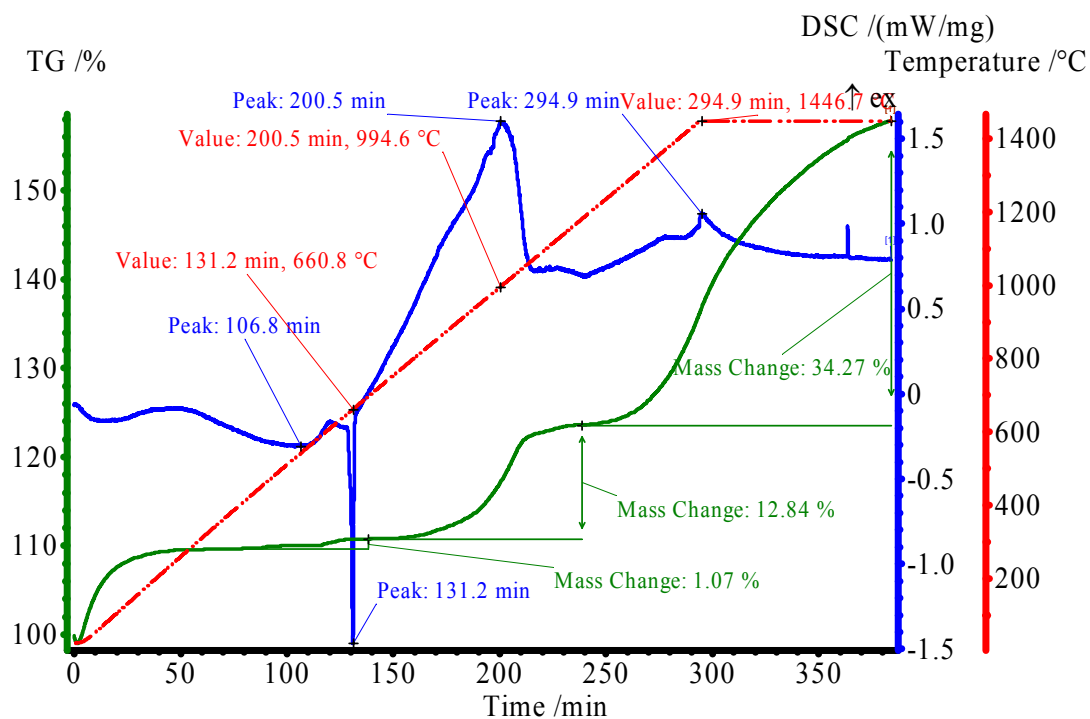


Figure E.4a – 20 $\mu$ m Al + O<sub>2</sub> DSC/TGA Curves (5Kpm)

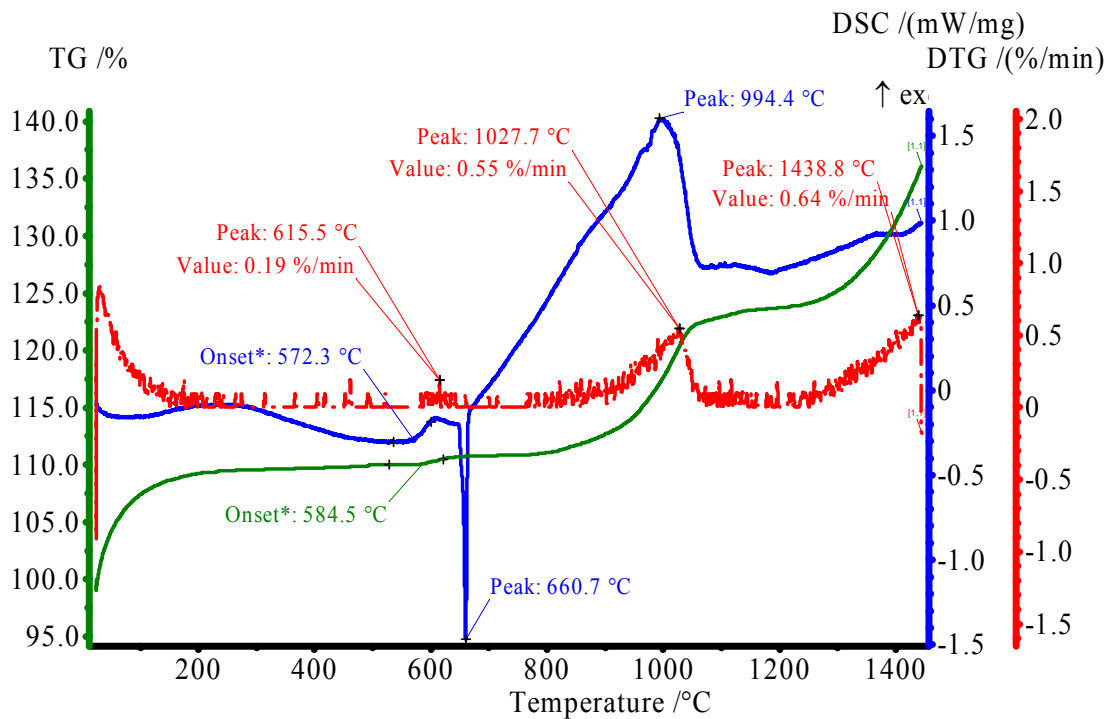


Figure E.4b – 20 $\mu$ m Al + O<sub>2</sub> DSC/TGA Curves (5Kpm)

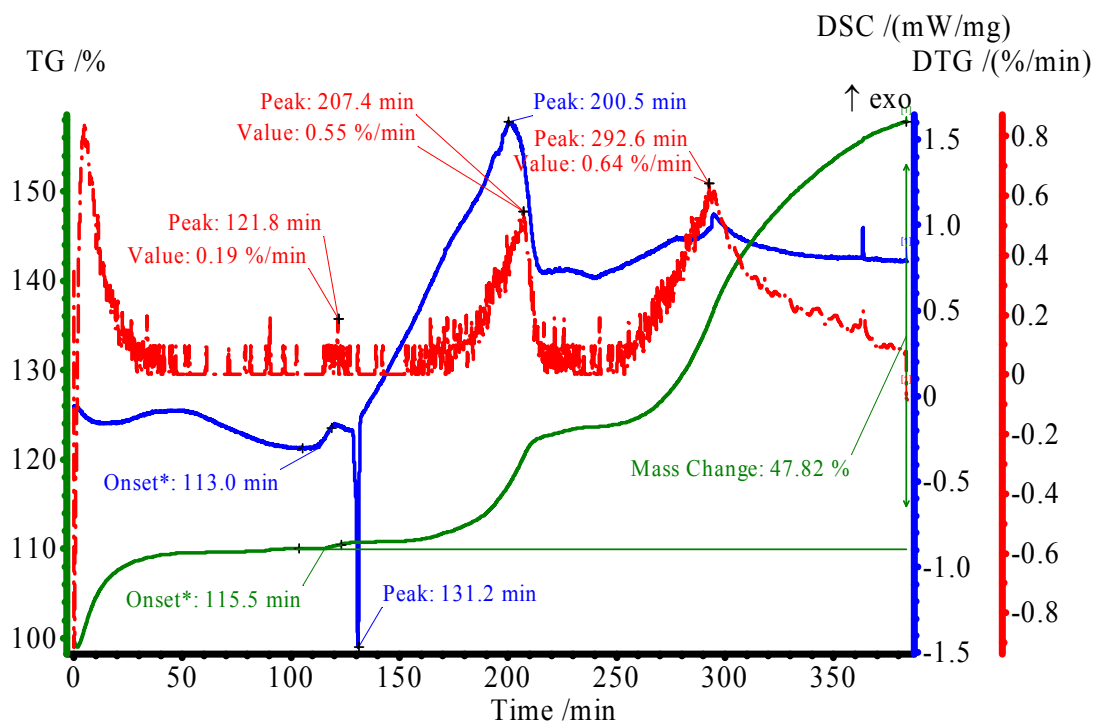


Figure E.4c – 20µm Al + O<sub>2</sub> DSC/TGA Curves (5Kpm)

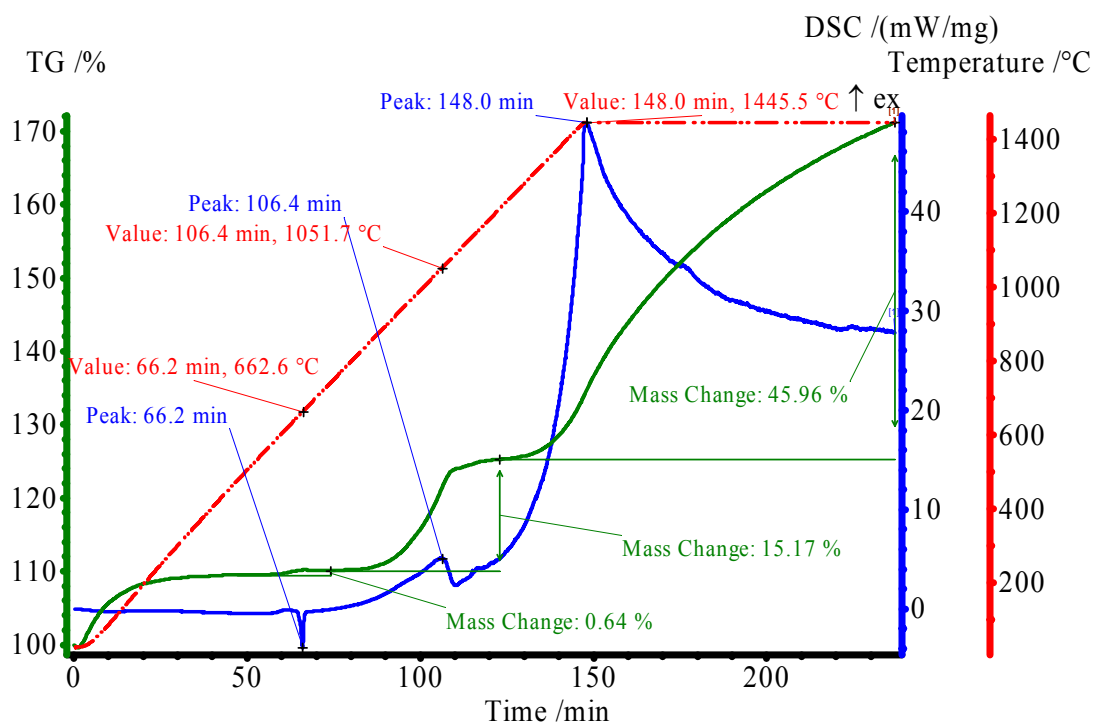


Figure E.4d – 20µm Al + O<sub>2</sub> DSC/TGA Curves (10Kpm)

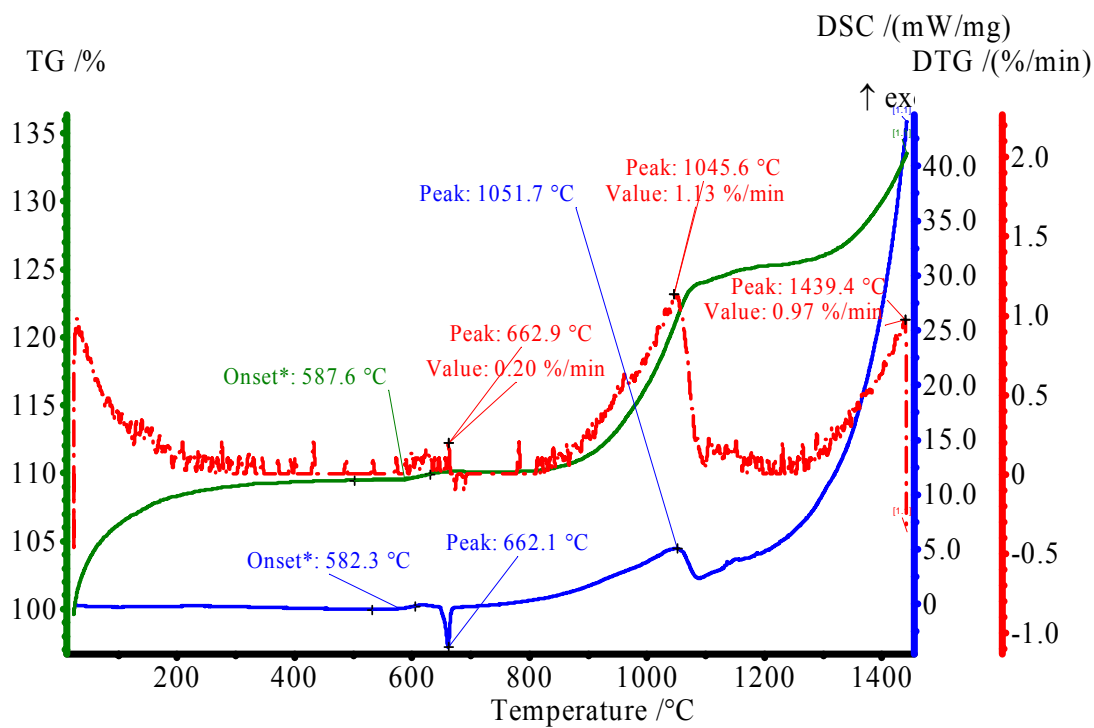


Figure E.4e – 20µm Al + O<sub>2</sub> DSC/TGA Curves (10Kpm)

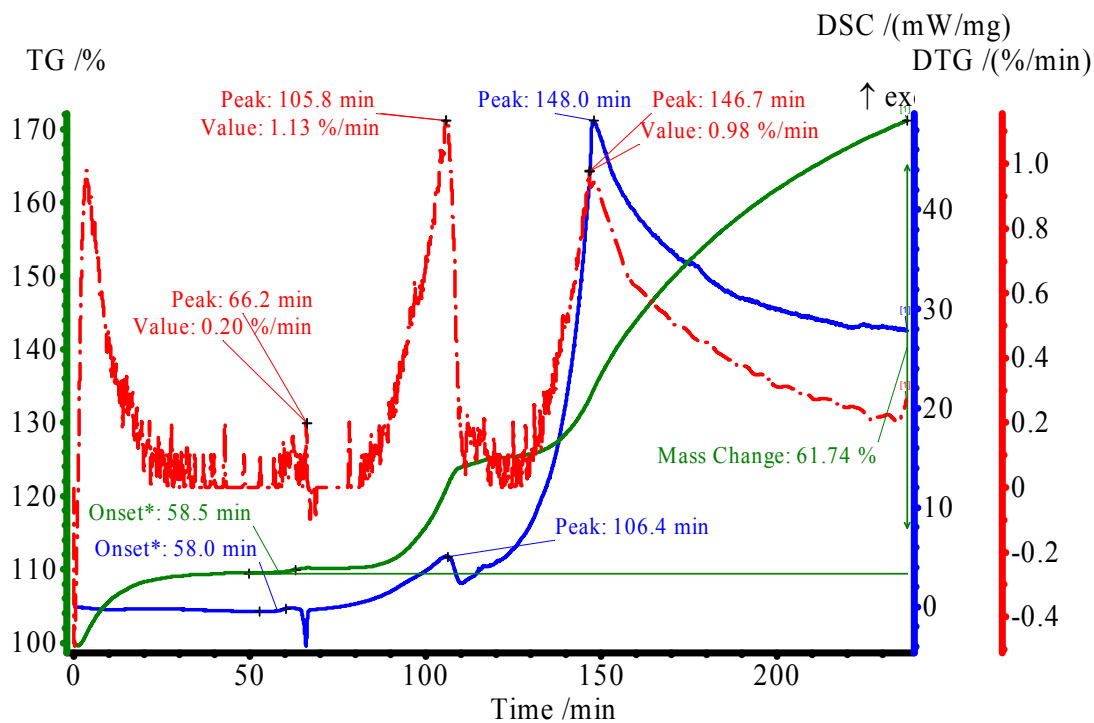


Figure E.4f – 20µm Al + O<sub>2</sub> DSC/TGA Curves (10Kpm)

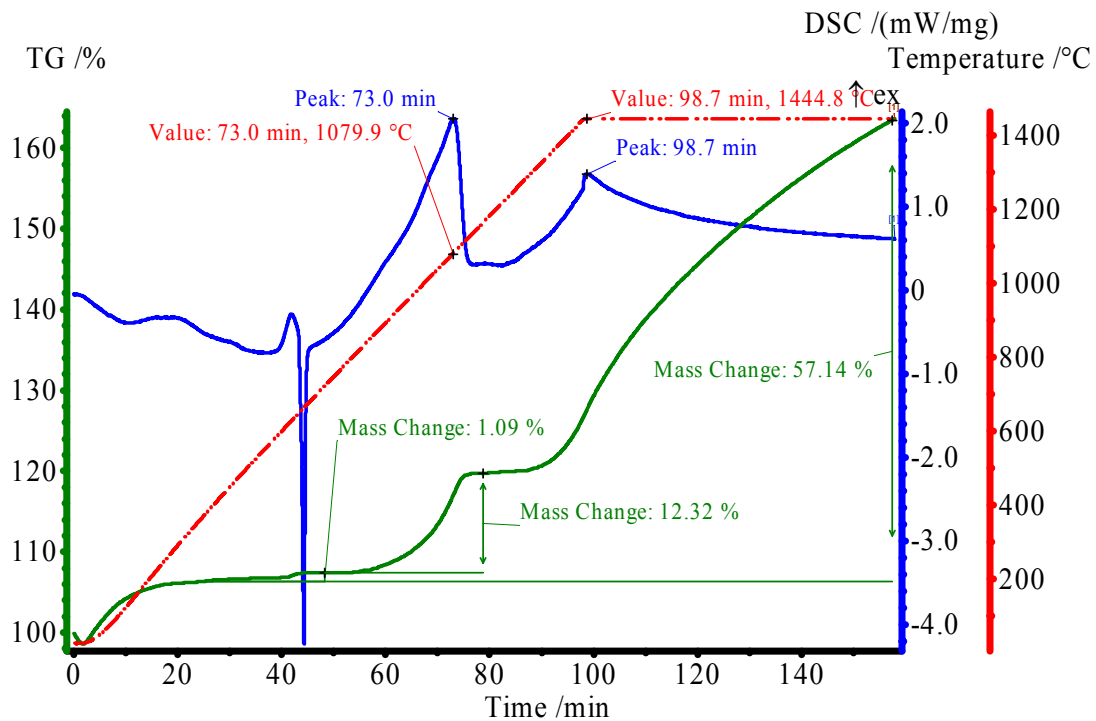


Figure E.4g – 20µm Al + O<sub>2</sub> DSC/TGA Curves (15Kpm)

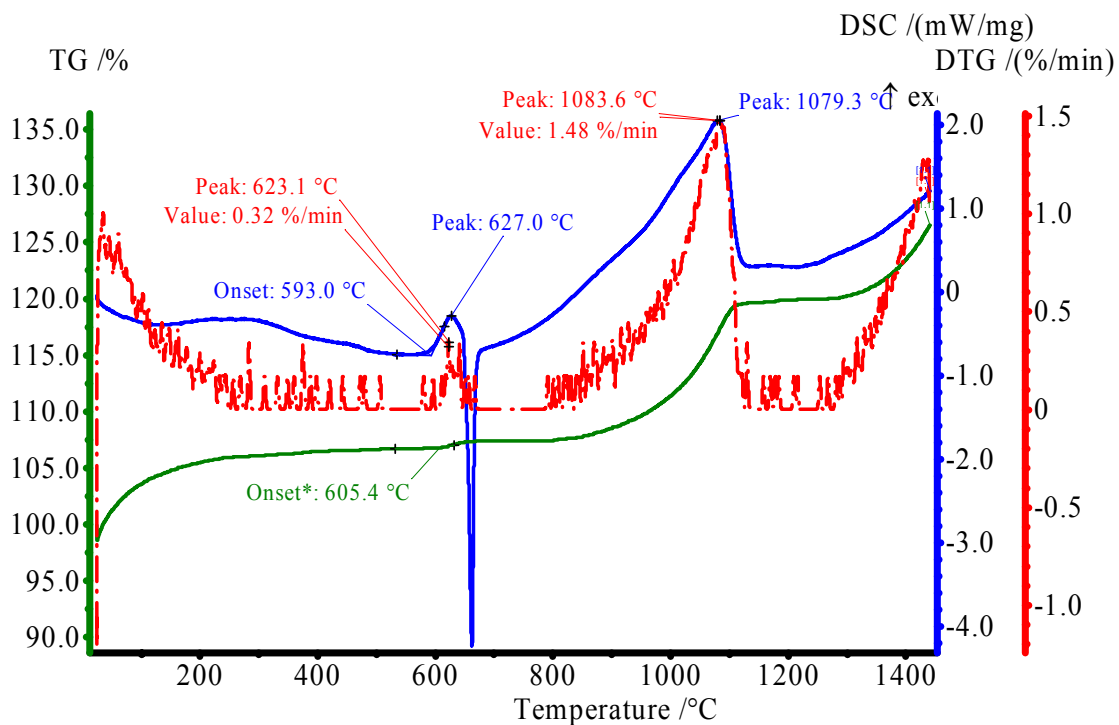


Figure E.4h – 20µm Al + O<sub>2</sub> DSC, TGA and DTG Curves (15Kpm)

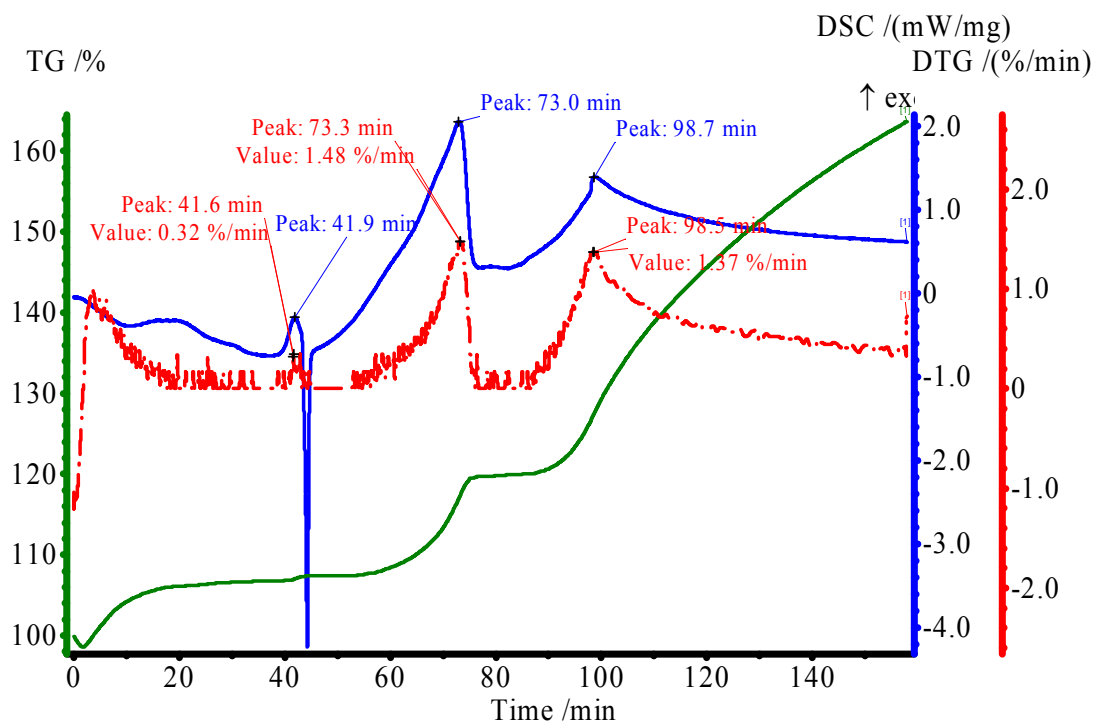


Figure E.4i – 20µm Al + O<sub>2</sub> DSC, TGA and DTG Curves (with isothermal data-15Kpm)

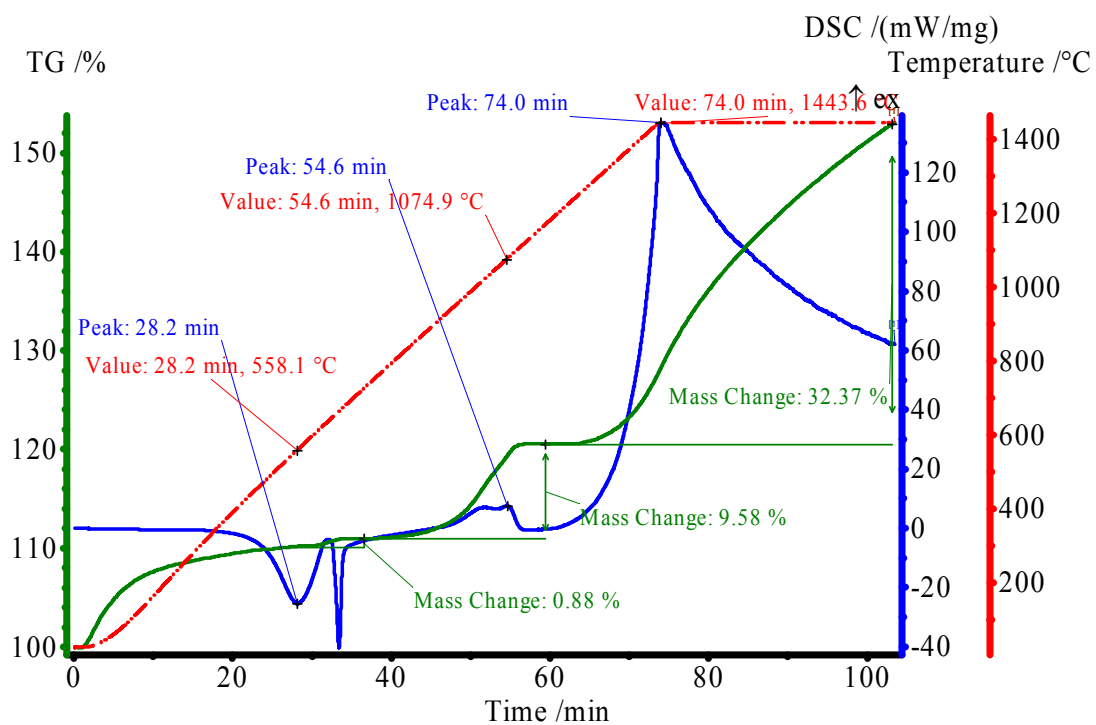


Figure E.4j – 20µm Al + O<sub>2</sub> DSC/TGA Curves (20Kpm)



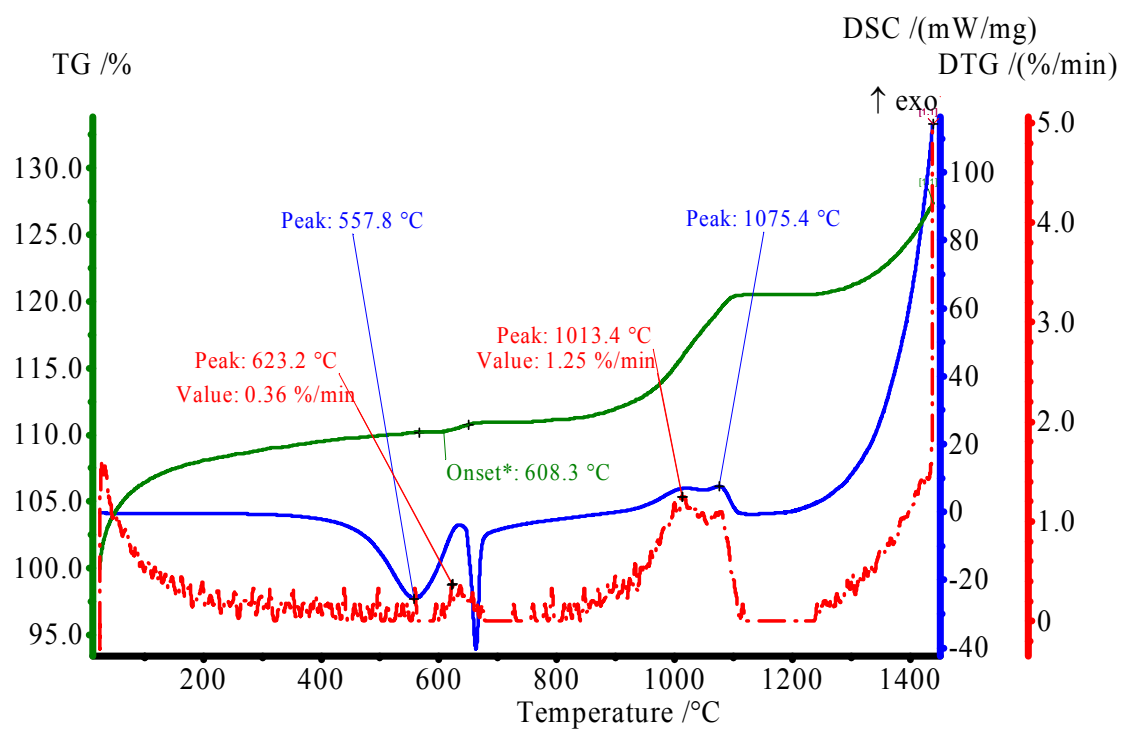


Figure E.4k – 20µm Al + O<sub>2</sub> DSC,TGA and DTG Curves (20Kpm)

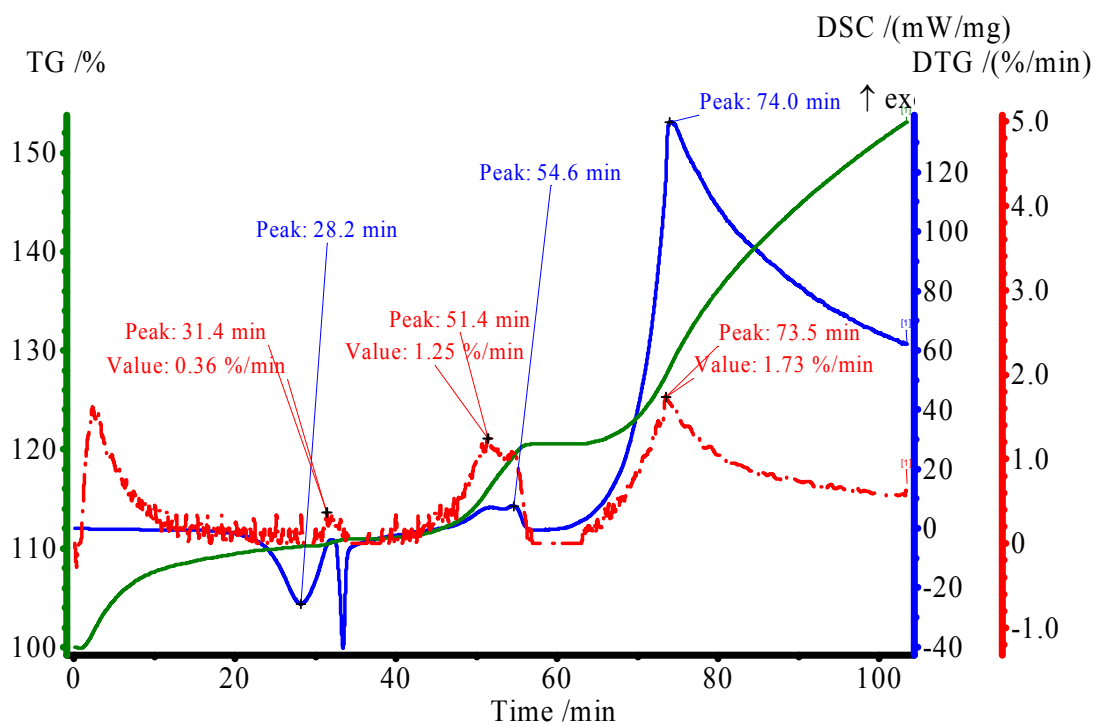


Figure E.4l – 20µm Al + O<sub>2</sub> DSC, TGA and DTG Curves (with isothermal data-20Kpm)

F. Aluminum Oxidation DSC/TGA Results Plotted by  $\beta$

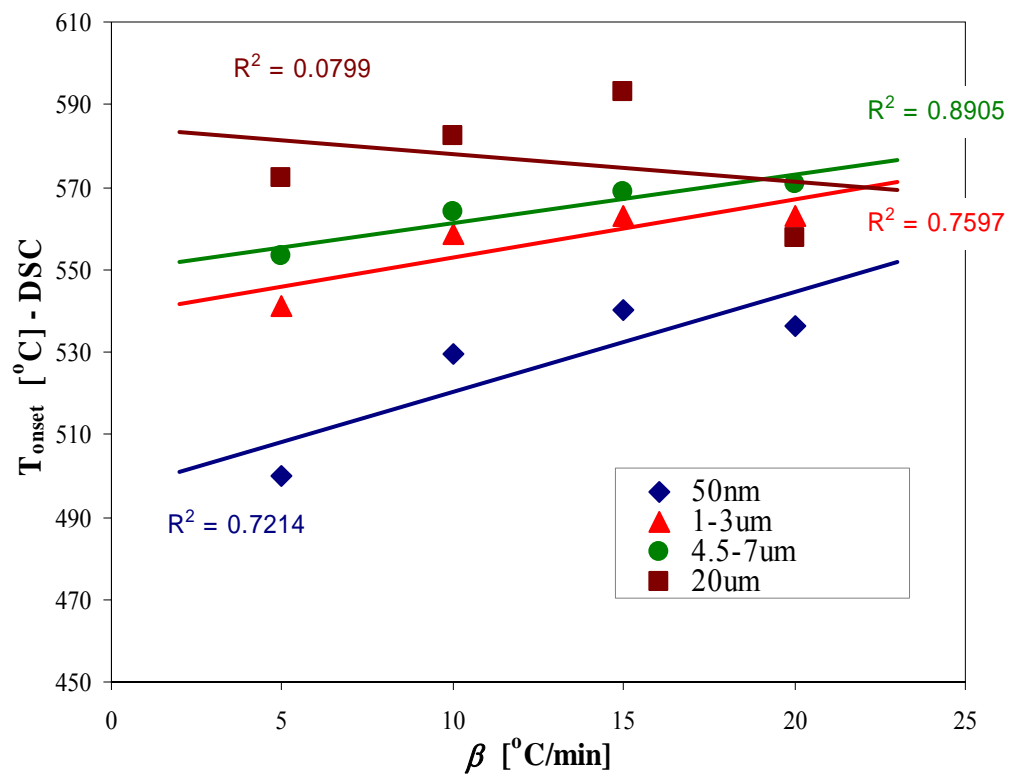


Figure F.1 – DSC Onset temperature as a function of  $\beta$

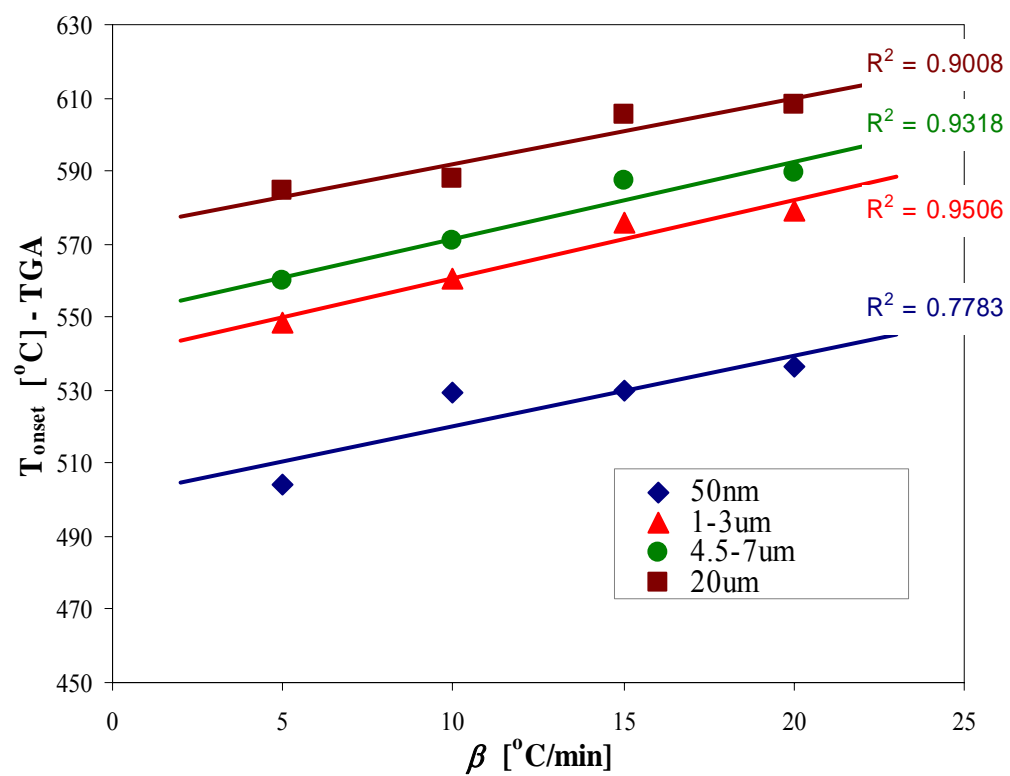


Figure F.2 – TGA Onset temperature as a function of  $\beta$

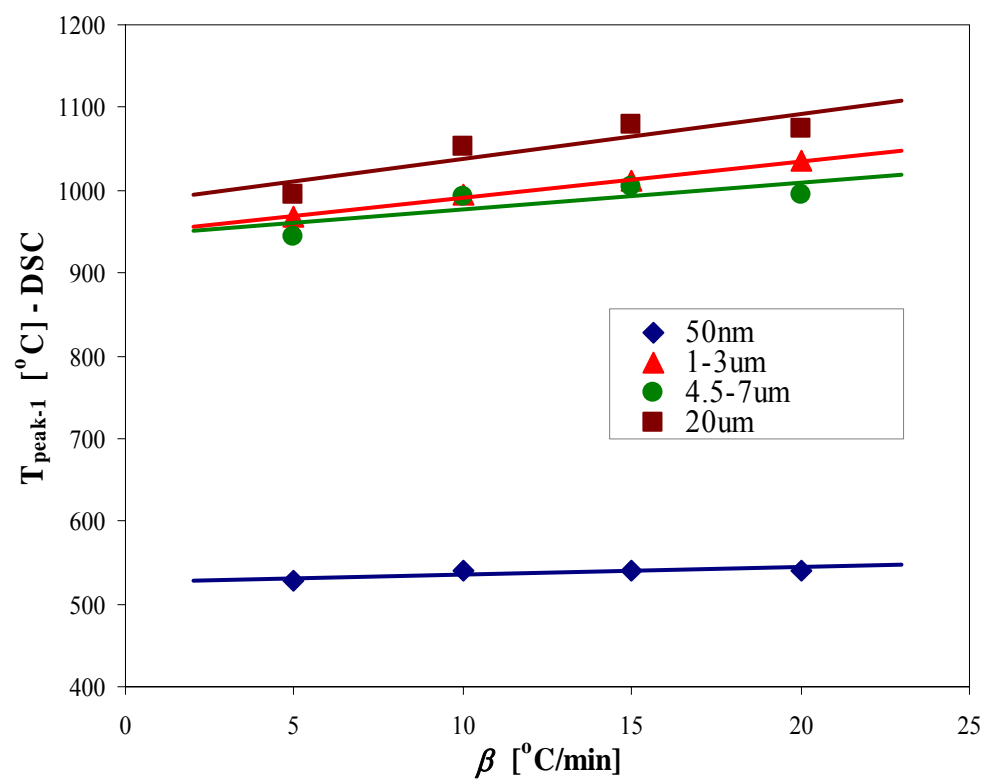


Figure F.3 – Peak-1 DSC temperature as a function of  $\beta$

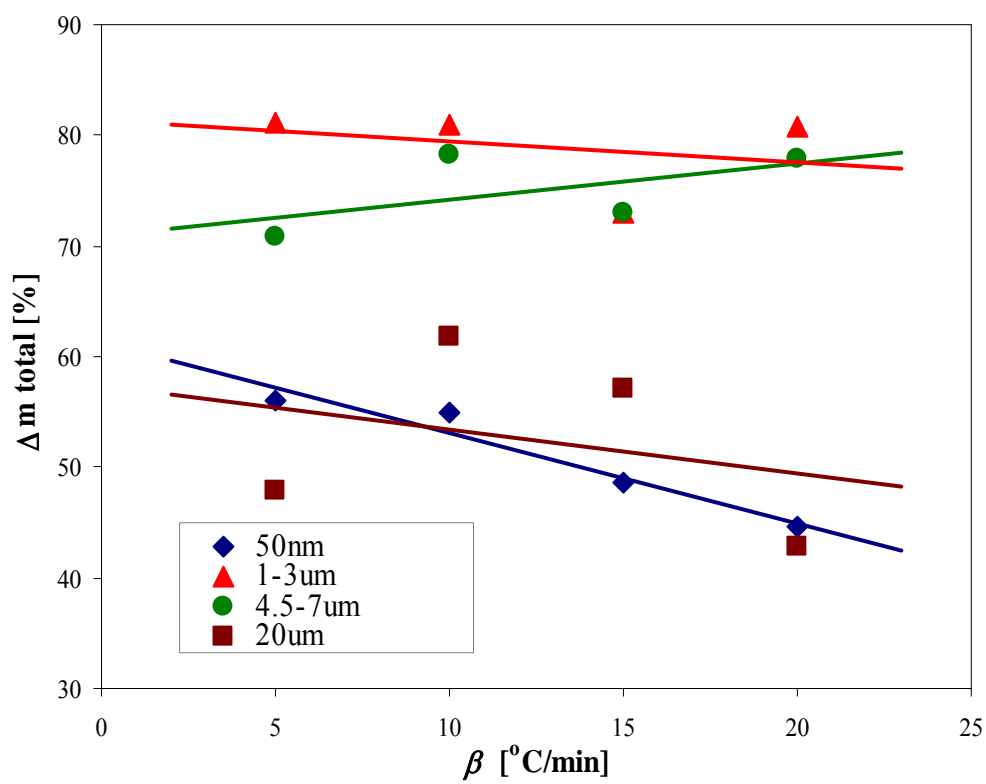


Figure F.4 – Total mass gain as a function of  $\beta$

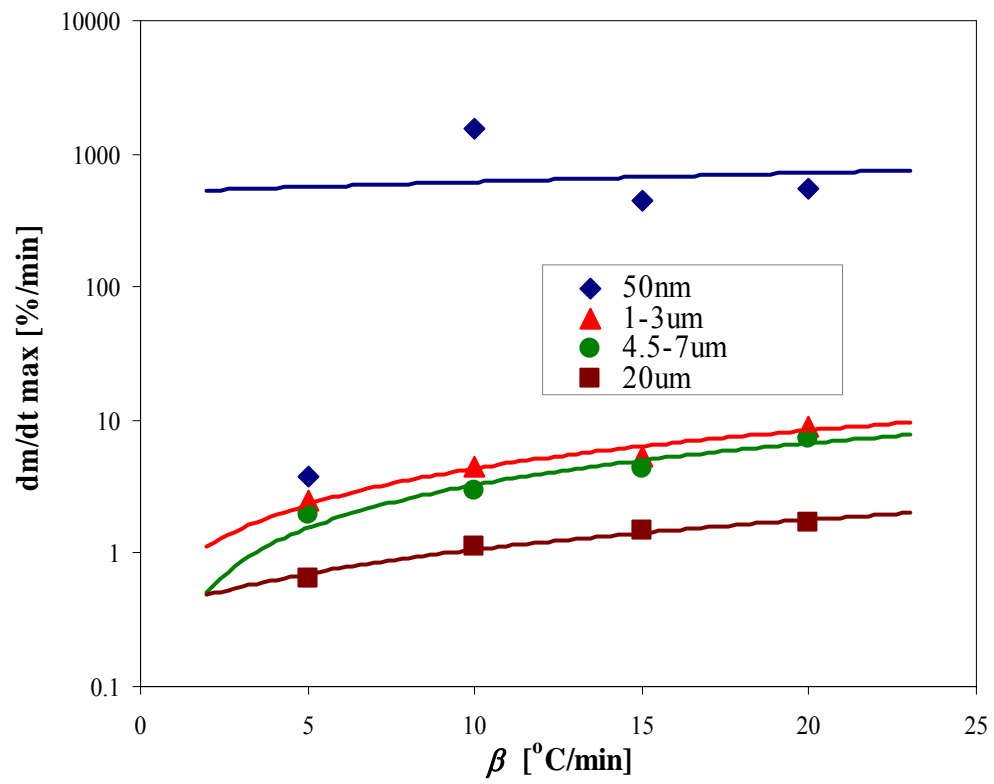


Figure F.5 – Peak mass rate of change ( $\text{dm}/\text{dt}$ ) as a function of  $\beta$

G.

### Aluminum + Molybdenum Trioxide Thermite DSC Curves

TG curves are not shown since the mass change is negligible in a solid-solid reaction.

Table G.1 - 80nm Al + MoO<sub>3</sub> DSC Data from Figures 7.3 and 8.1 used for Figure 8.2

HR ( $\beta$ ) [Kpm]	Reaction Start [min]	Reaction Stop [min]	Duration [min]	Reaction Energy [J/mg]
2.5	146.9	260.8	113.9	3430
5	72.2	135.6	63.4	1604
10	27.2	70.8	43.6	1659
15	26.3	50.3	24.0	2192
20	19.5	38.4	18.9	2281

G.1 50nm Al + MoO<sub>3</sub>

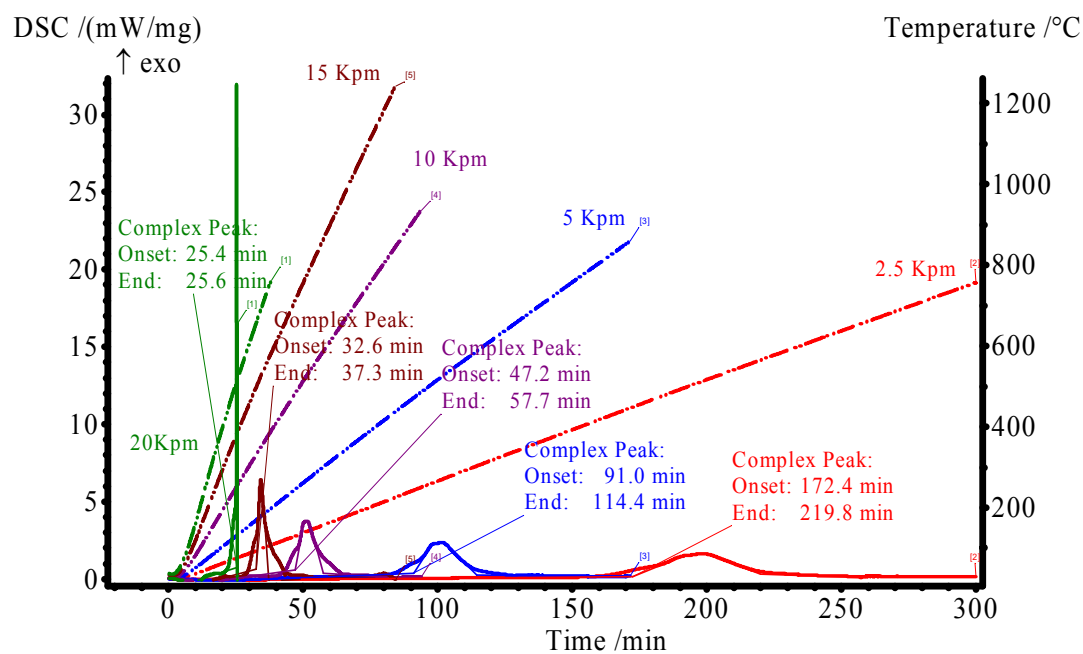


Figure G.1a - 50 nm Al + MoO<sub>3</sub> DSC Curves

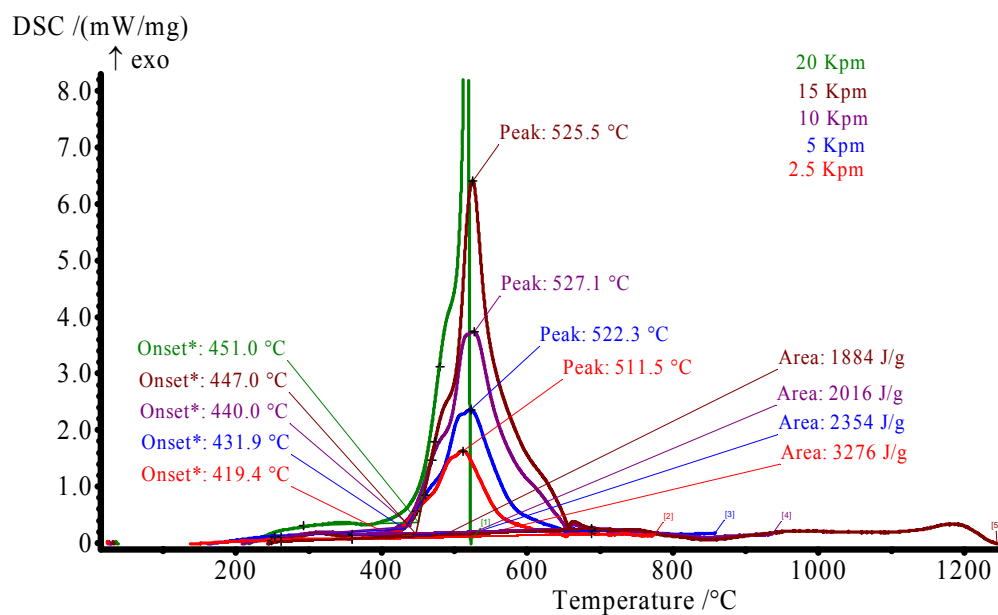


Figure G.1b - 50 nm Al + MoO<sub>3</sub> DSC Curves



G.2 80nm Al + MoO<sub>3</sub>

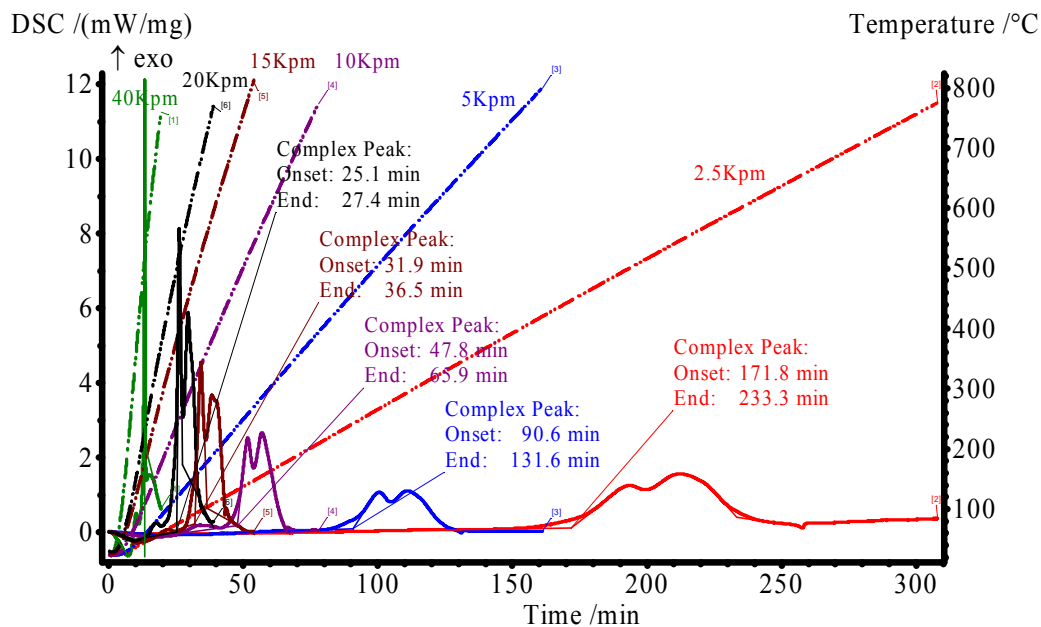


Figure G.2a - 80 nm Al + MoO<sub>3</sub> DSC Curves (More detailed information for Figure 8.1)

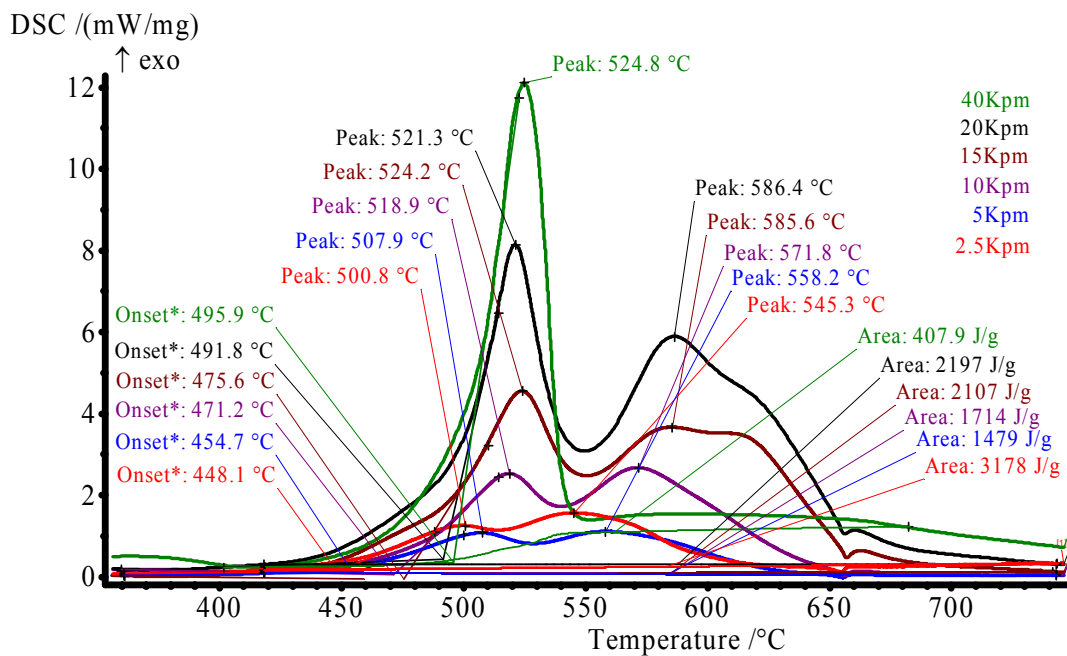


Figure G.2b - 80 nm Al + MoO<sub>3</sub> DSC Curves

### G.3 120nm Al + MoO<sub>3</sub>

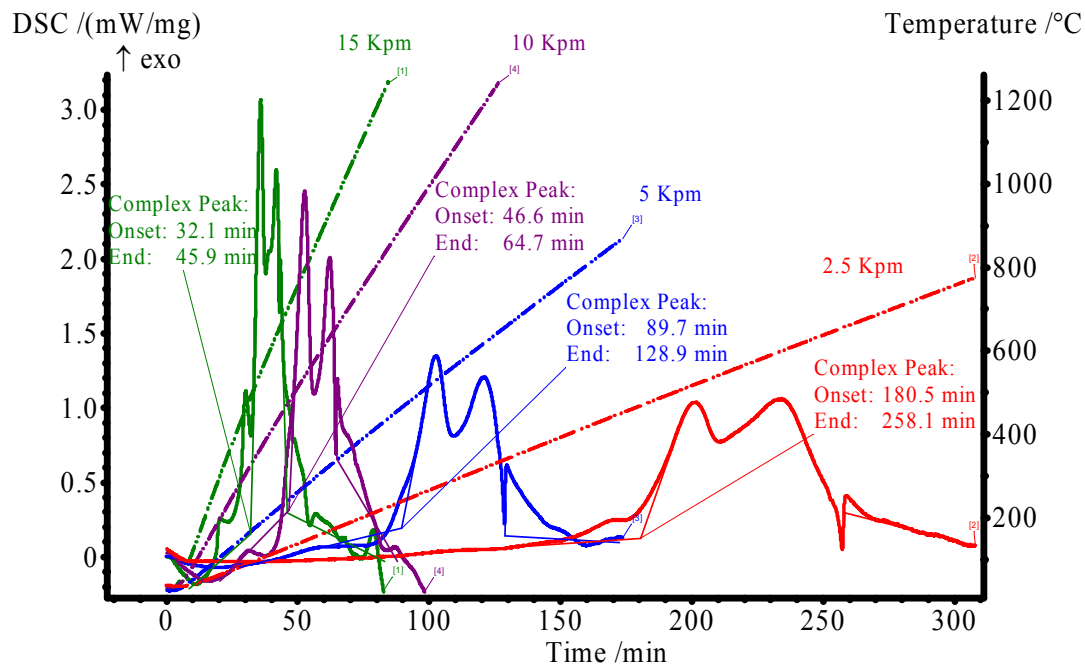


Figure G.3a - 120 nm Al + MoO<sub>3</sub> DSC Curves

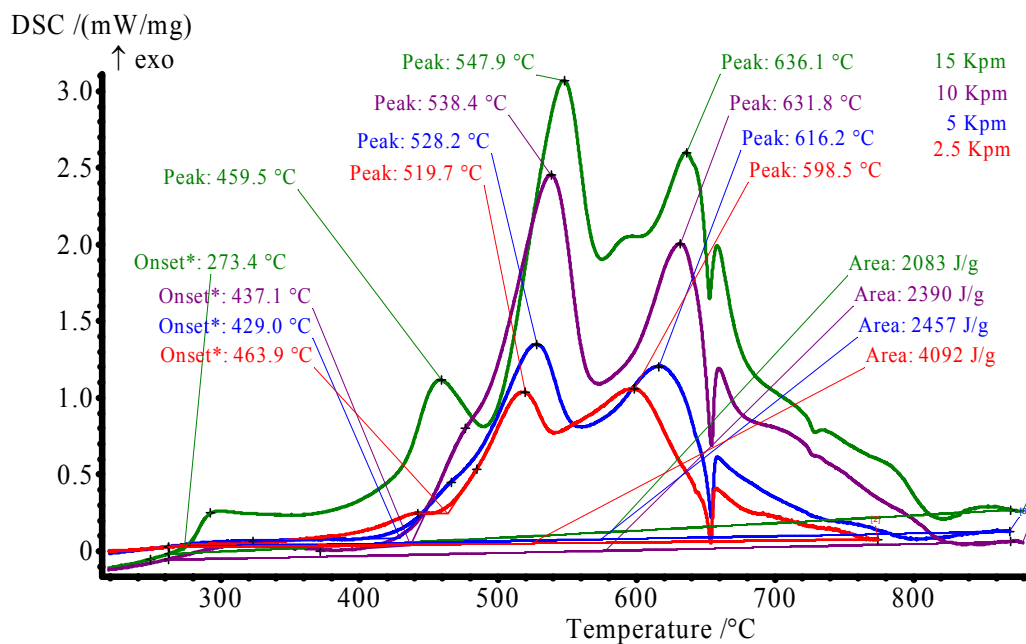


Figure G.3b - 120 nm Al + MoO<sub>3</sub> DSC Curves

G.4 1-3 $\mu\text{m}$  Al + MoO<sub>3</sub>

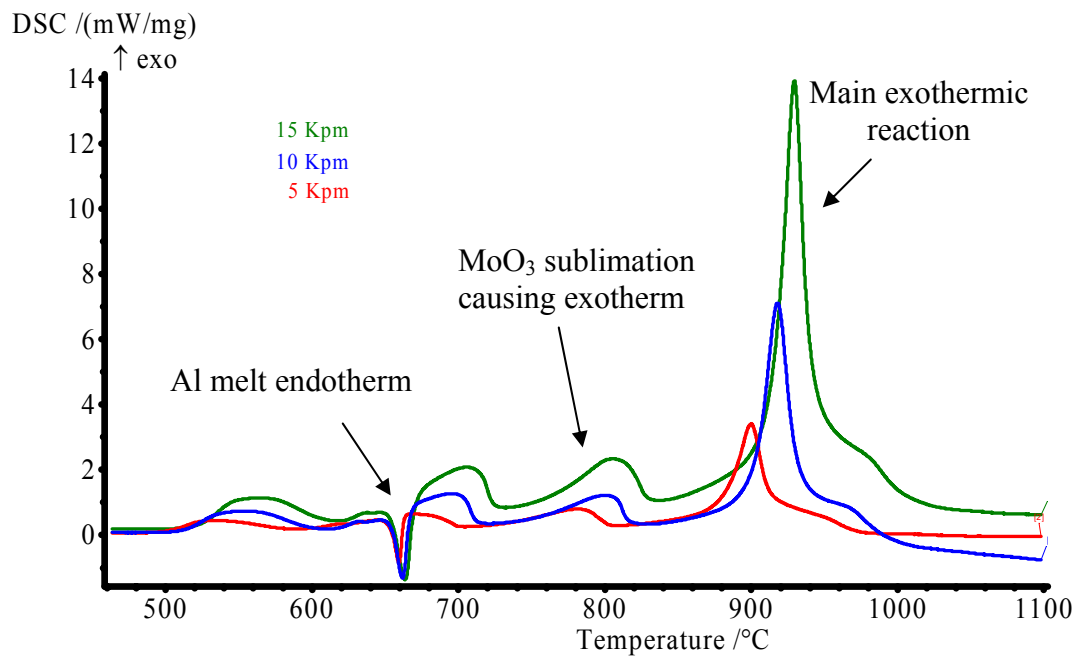


Figure G.4a - 1-3 $\mu\text{m}$  Al + MoO<sub>3</sub> DSC and TGA Curves (5, 10 and 15 Kpm)

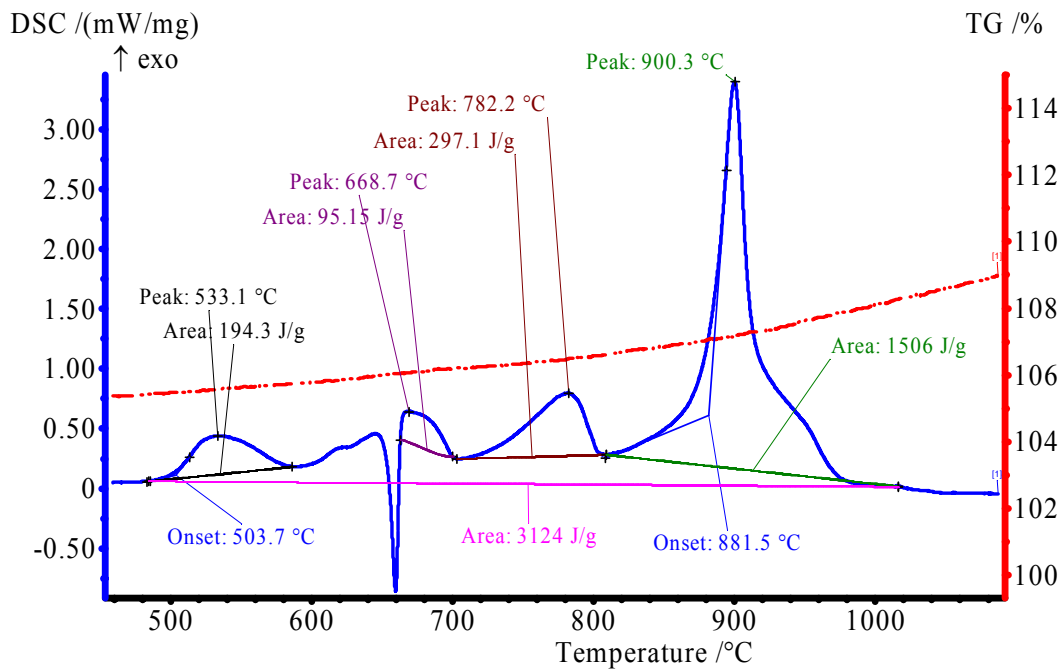


Figure G.4b - 1-3 $\mu\text{m}$  Al + MoO<sub>3</sub> DSC and TGA Curves (5 Kpm)

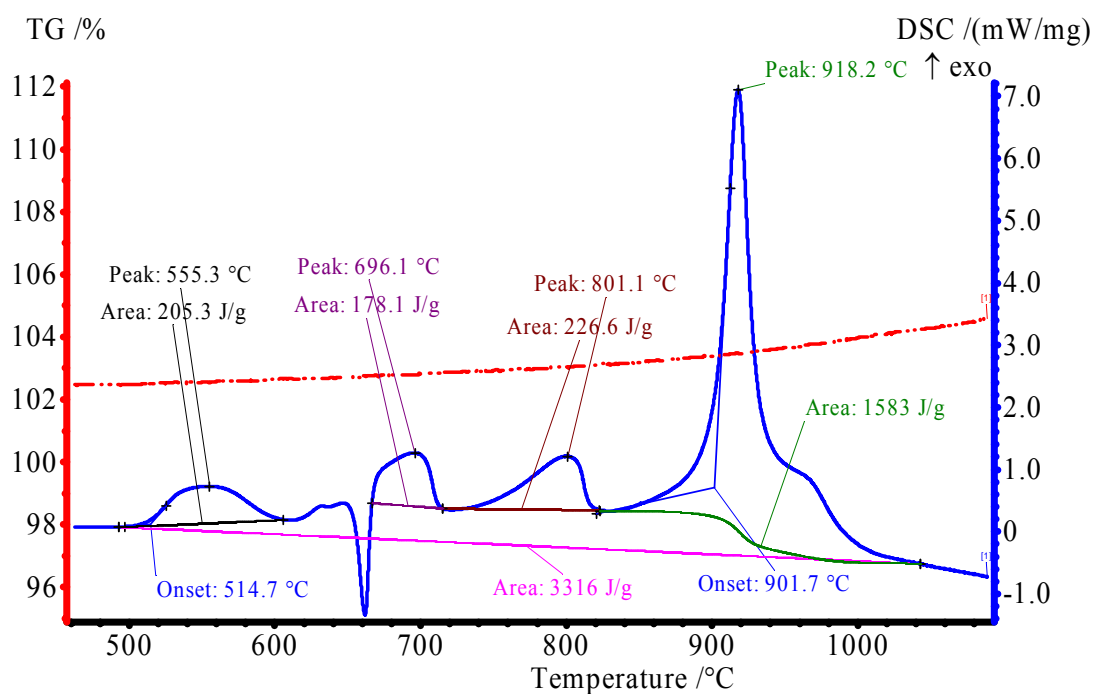


Figure G.4c - 1-3µm Al + MoO<sub>3</sub> DSC and TGA Curves (10 Kpm)

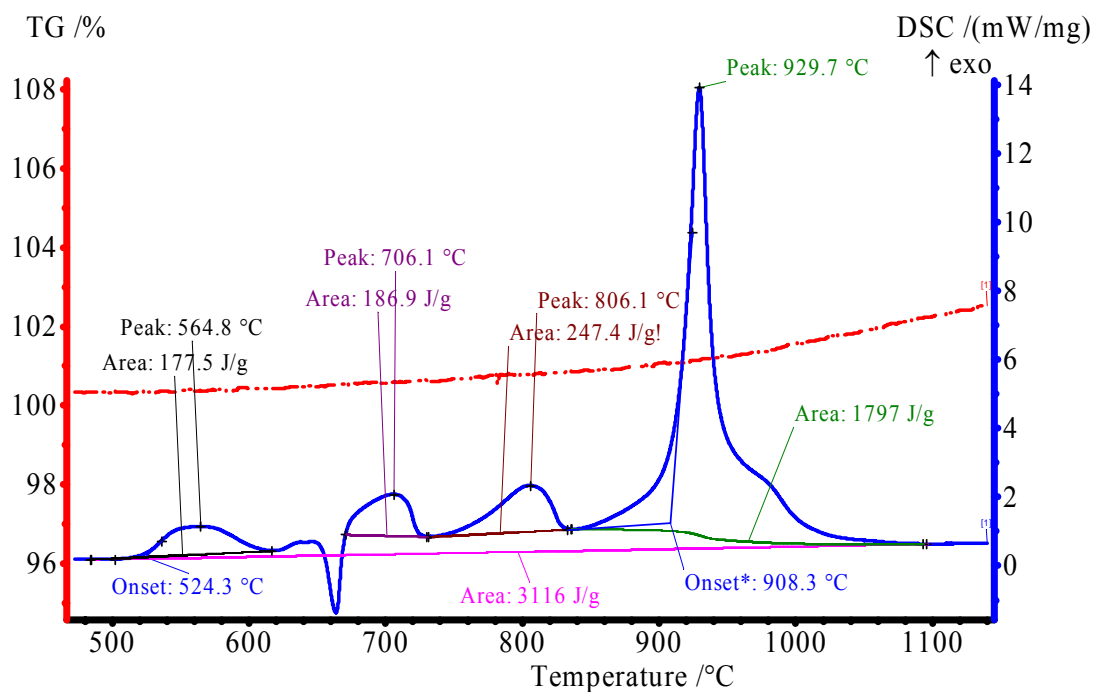


Figure G.4d - 1-3µm Al + MoO<sub>3</sub> DSC and TGA Curves (15 Kpm)

G.5 3-4 $\mu$ m Al + MoO<sub>3</sub>

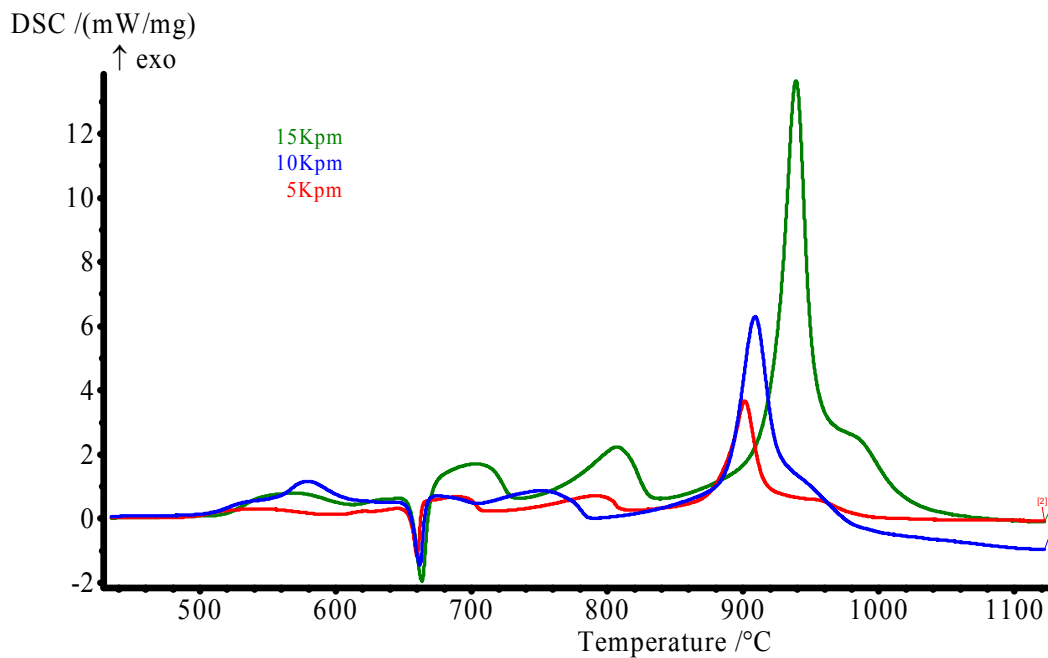


Figure G.5a – 3-4 $\mu$ m Al + MoO<sub>3</sub> DSC Curves (5, 10 and 15 Kpm)

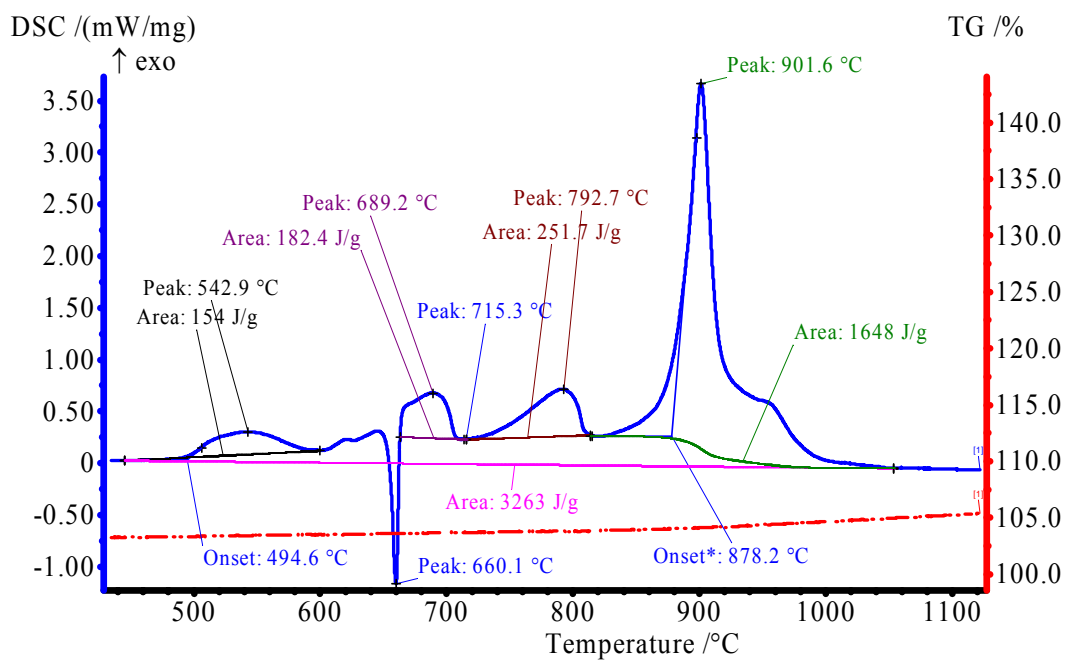


Figure G.5b – 3-4 $\mu$ m Al + MoO<sub>3</sub> DSC Curves (5Kpm)

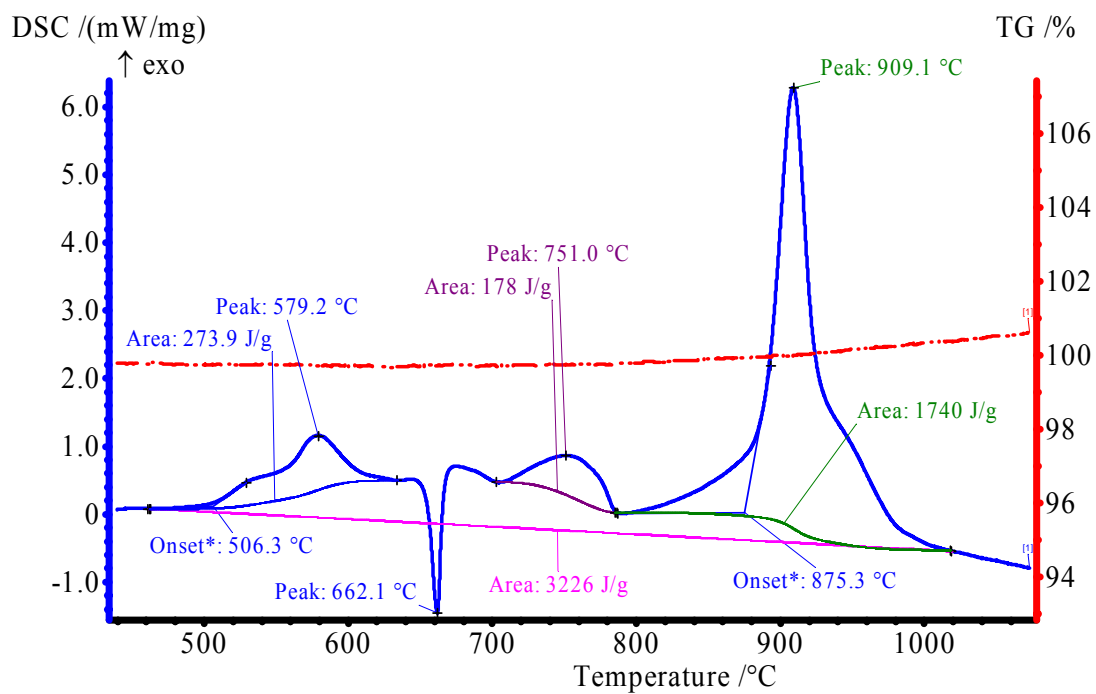


Figure G.5c – 3-4μm Al + MoO<sub>3</sub> DSC Curves (10Kpm)

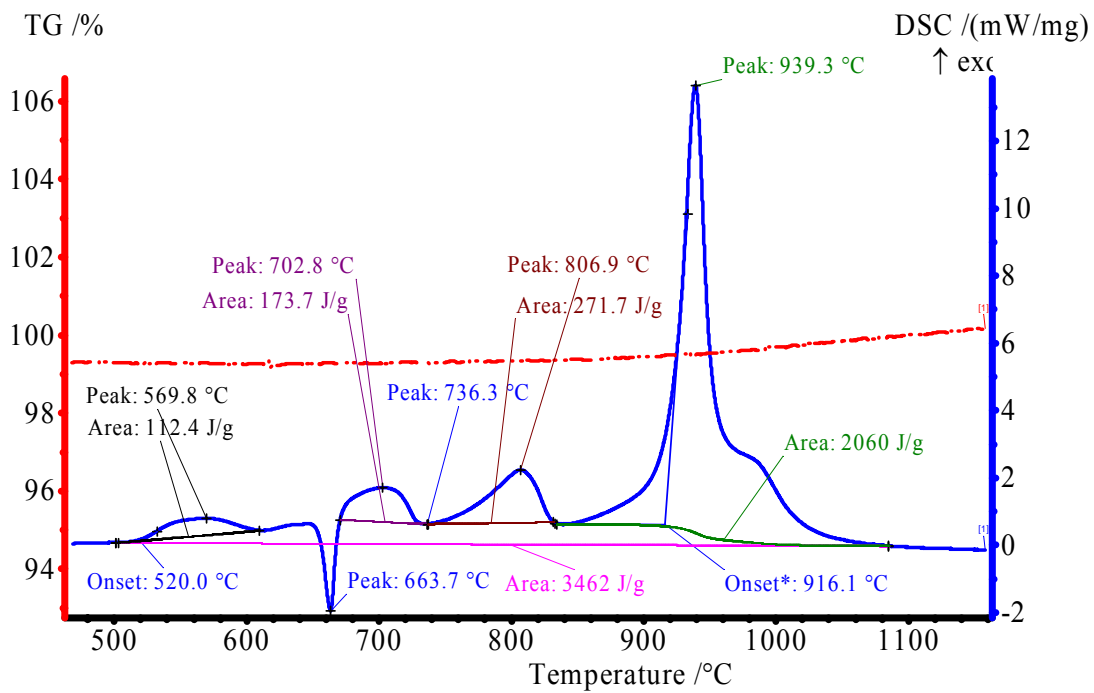


Figure G.5d – 3-4μm Al + MoO<sub>3</sub> DSC Curves (15Kpm)

G6 4.5-7 $\mu$ m Al + MoO<sub>3</sub>

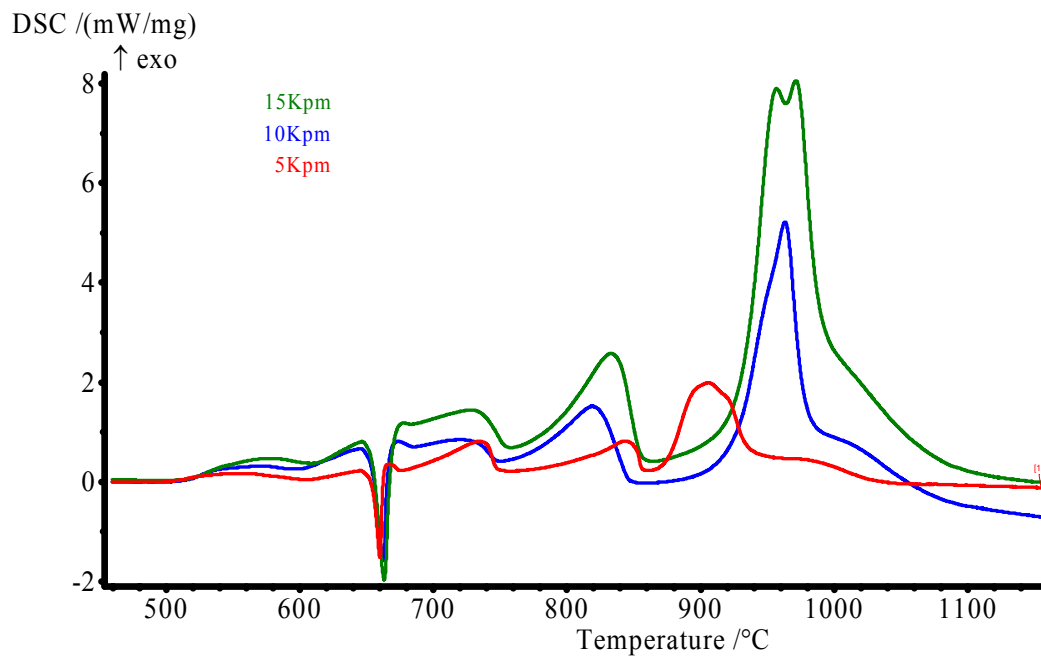


Figure G.6a - 4.5-7 $\mu$ m Al + MoO<sub>3</sub> DSC Curves (5, 10 , 15 Kpm)

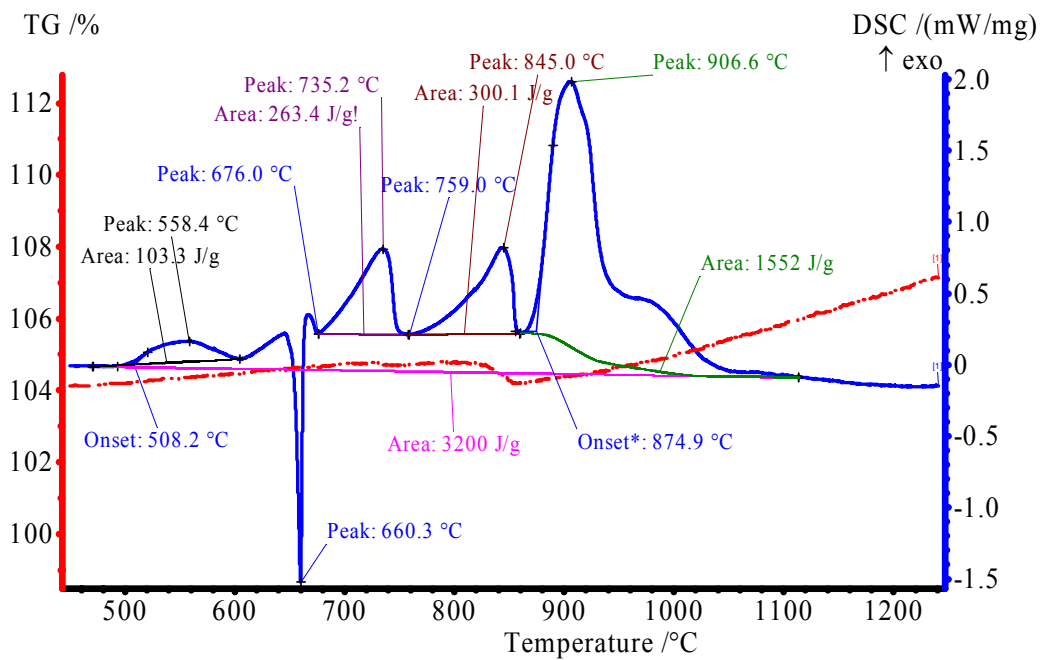


Figure G.6b - 4.5-7 $\mu$ m Al + MoO<sub>3</sub> DSC and TGA Curves (5Kpm)

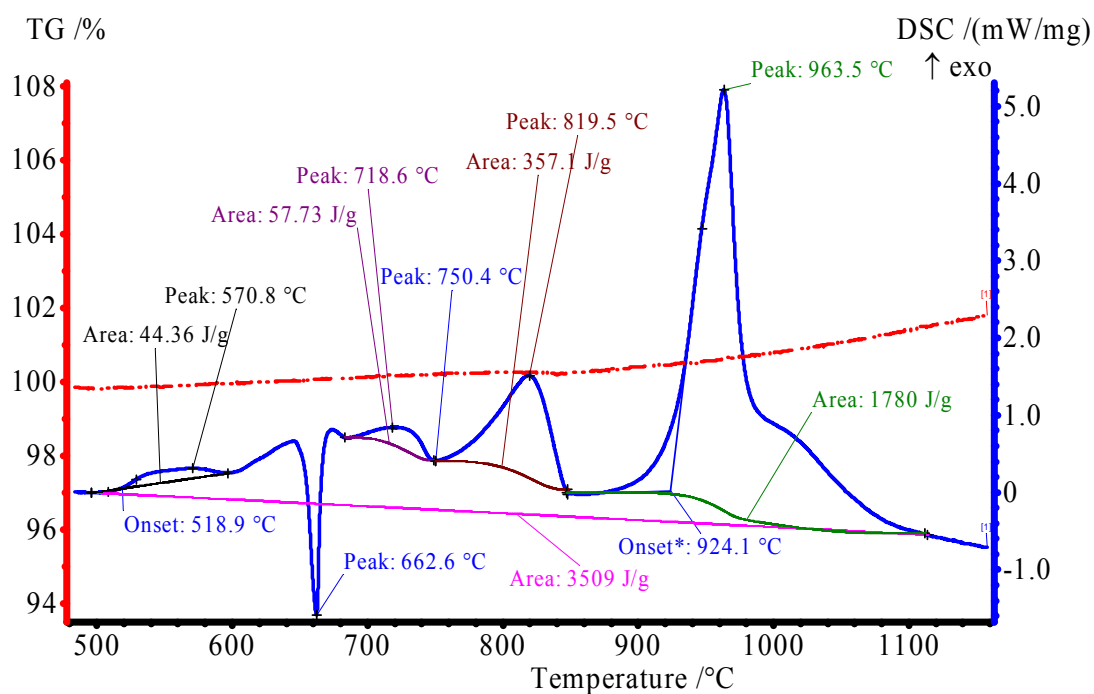


Figure G.6c - 4.5-7 $\mu$ m Al + MoO<sub>3</sub> DSC and TGA Curves (10Kpm)

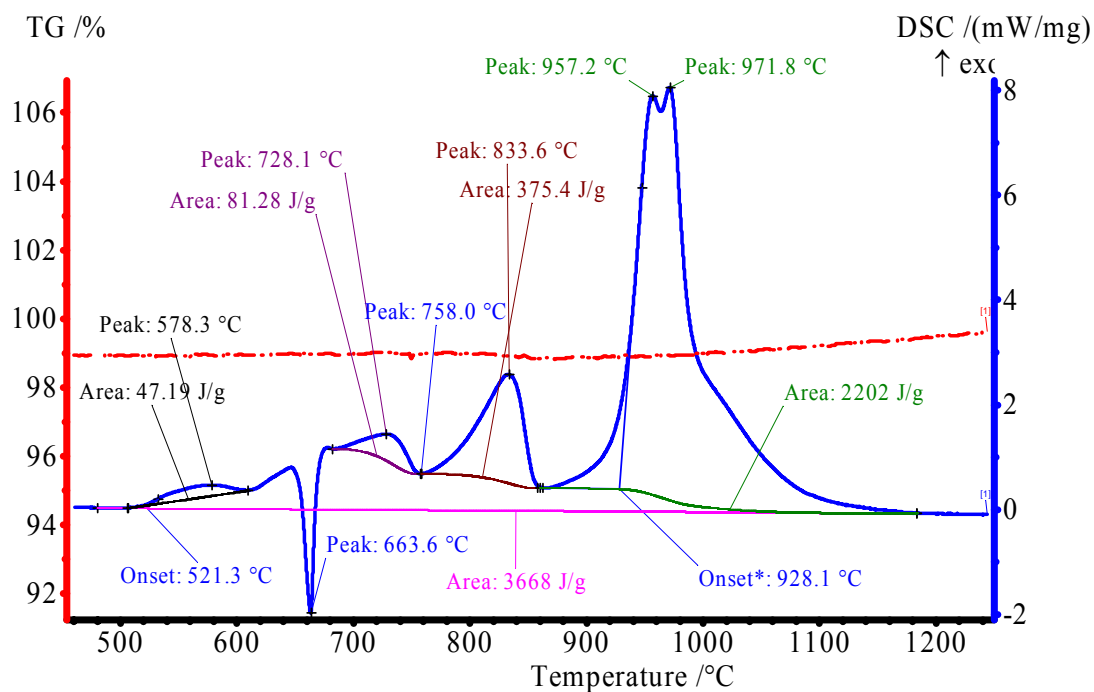


Figure G.6d - 4.5-7 $\mu$ m Al + MoO<sub>3</sub> DSC and TGA Curves (15Kpm)



G.7 10-14 $\mu$ m Al + MoO<sub>3</sub>

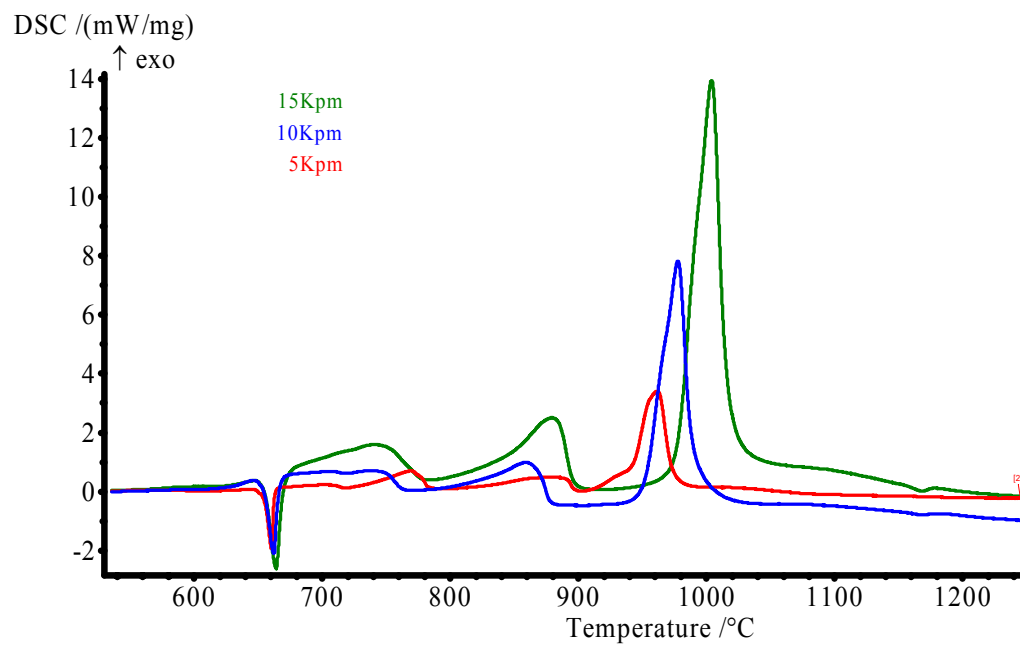


Figure G.7a – 10-14 $\mu$ m Al + MoO<sub>3</sub> DSC and TGA Curves (5, 10 and 15 Kpm)

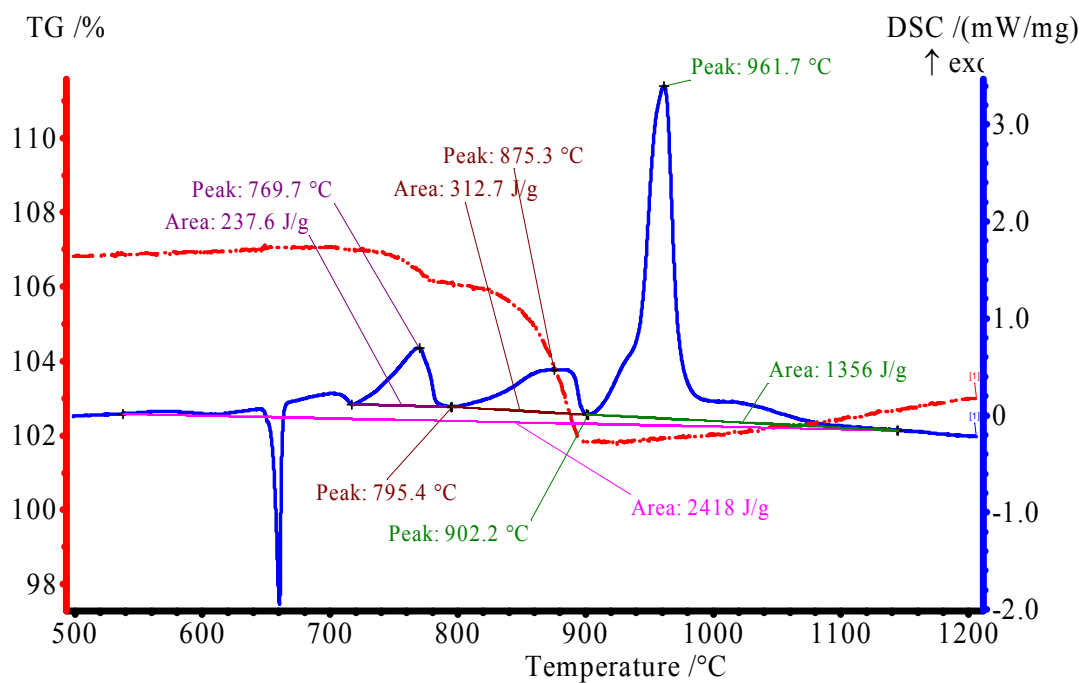


Figure G.7b – 10-14µm Al + MoO<sub>3</sub> DSC and TGA Curves (5Kpm)

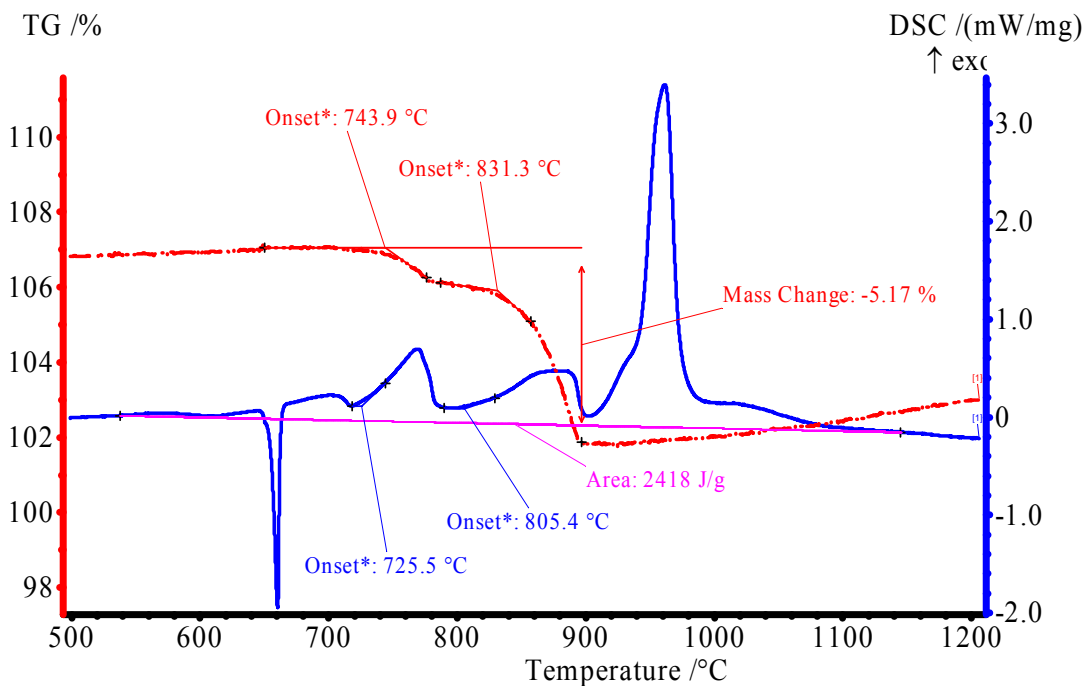


Figure G.7c – 10-14µm Al + MoO<sub>3</sub> DSC and TGA Curves with Mass Loss (5Kpm)

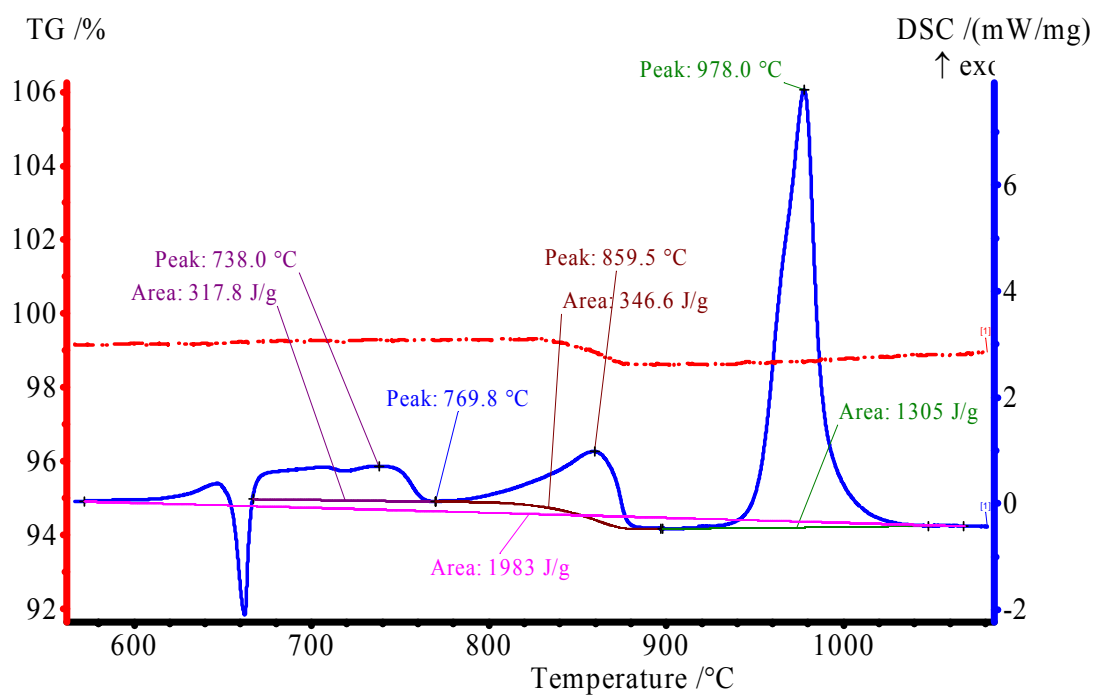


Figure G.7d – 10-14µm Al + MoO<sub>3</sub> DSC and TGA Curves (10Kpm)

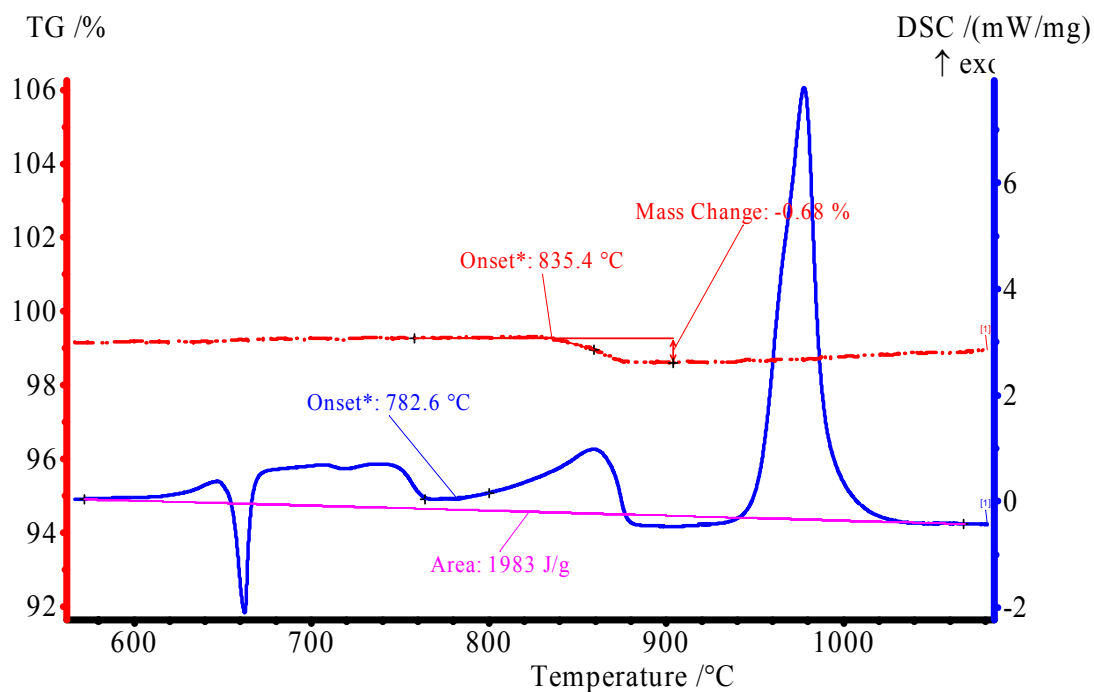


Figure G.7e – 10-14µm Al + MoO<sub>3</sub> DSC and TGA Curves with Mass Loss (10Kpm)

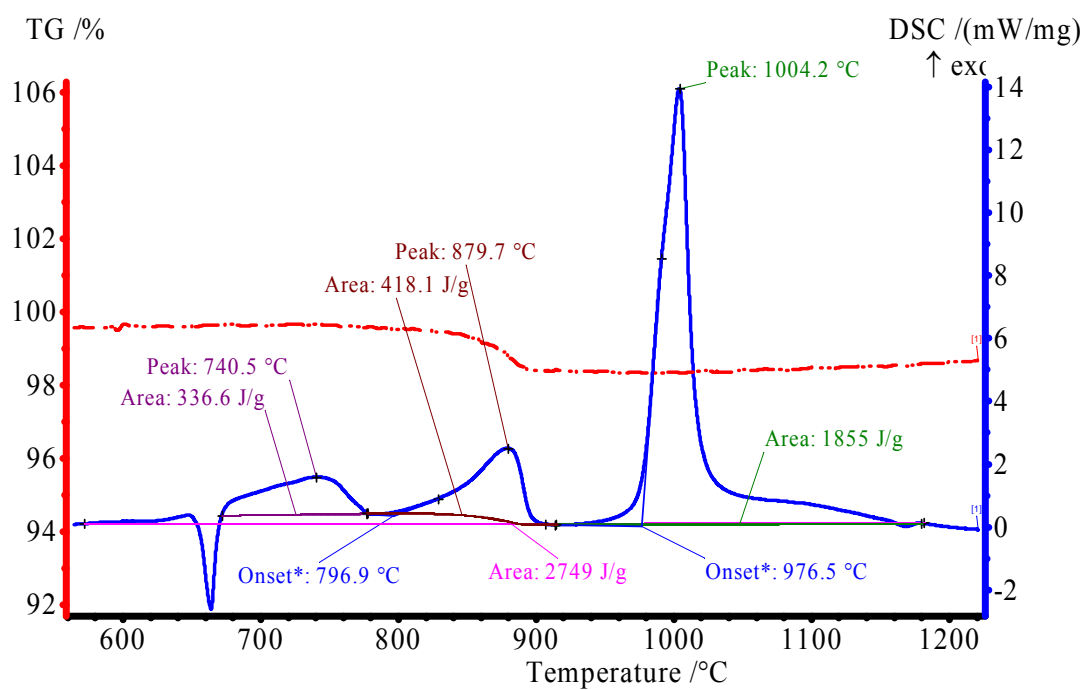


Figure G.7f – 10-14µm Al + MoO<sub>3</sub> DSC and TGA Curves (15Kpm)

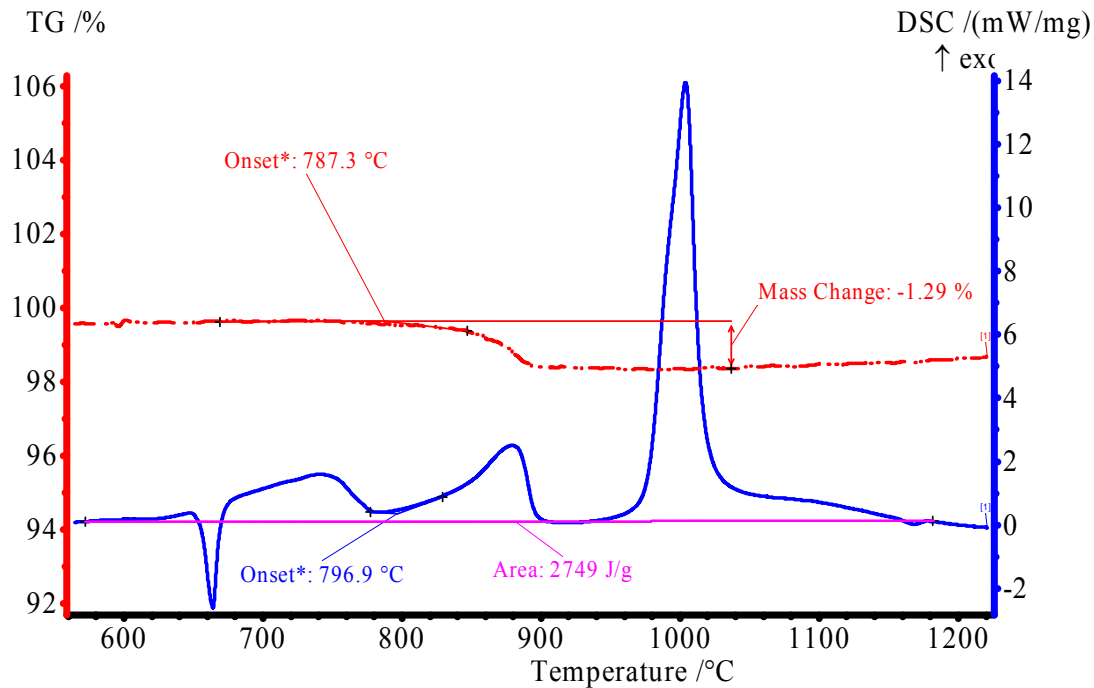


Figure G.7g – 10-14µm Al + MoO<sub>3</sub> DSC and TGA Curves with Mass Loss (15Kpm)

G8  $20\mu\text{m Al} + \text{MoO}_3$

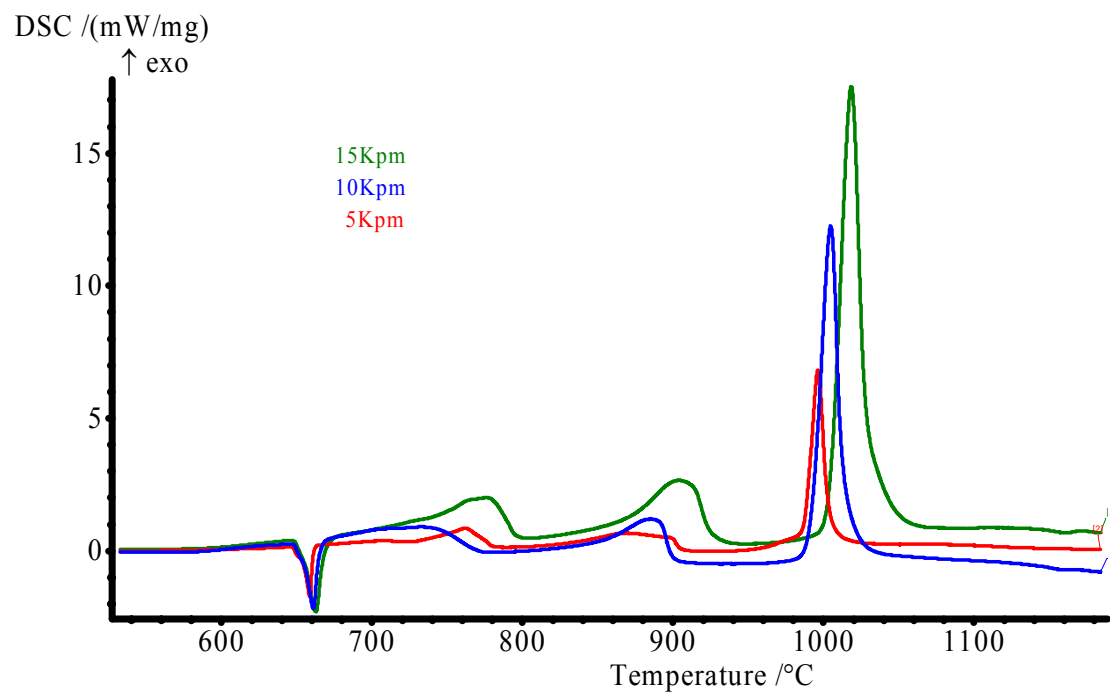


Figure G.8a -  $20\mu\text{m Al} + \text{MoO}_3$  DSC Curves (5, 10 and 15 Kpm)

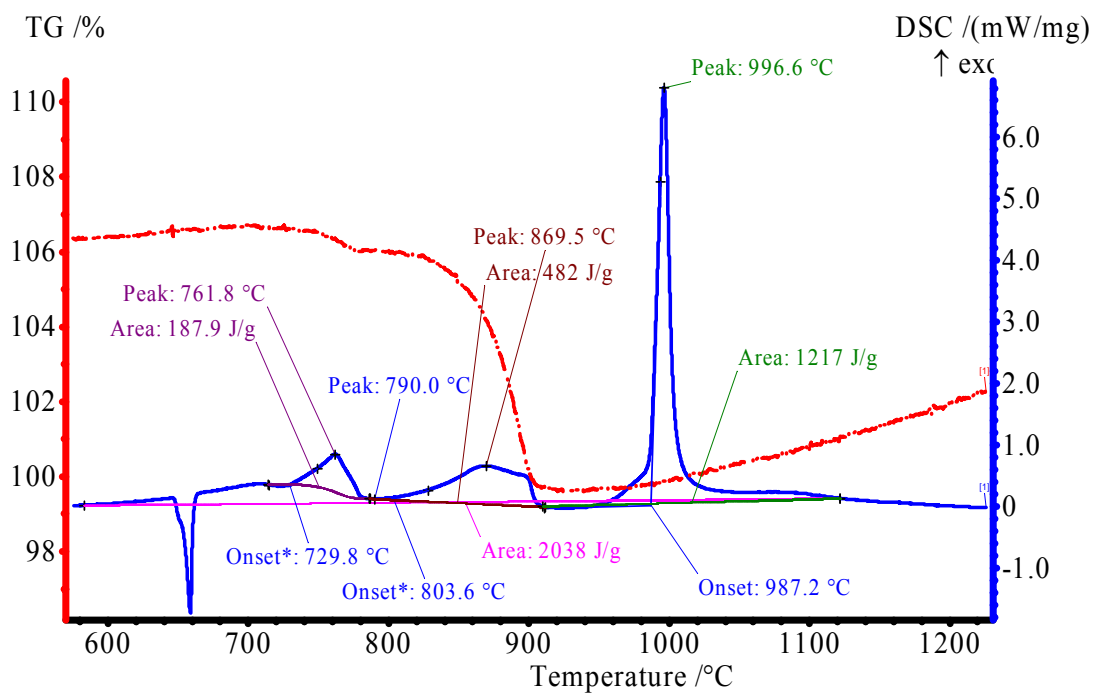


Figure G.8b - 20µm Al + MoO<sub>3</sub> DSC and TGA Curves (5Kpm)

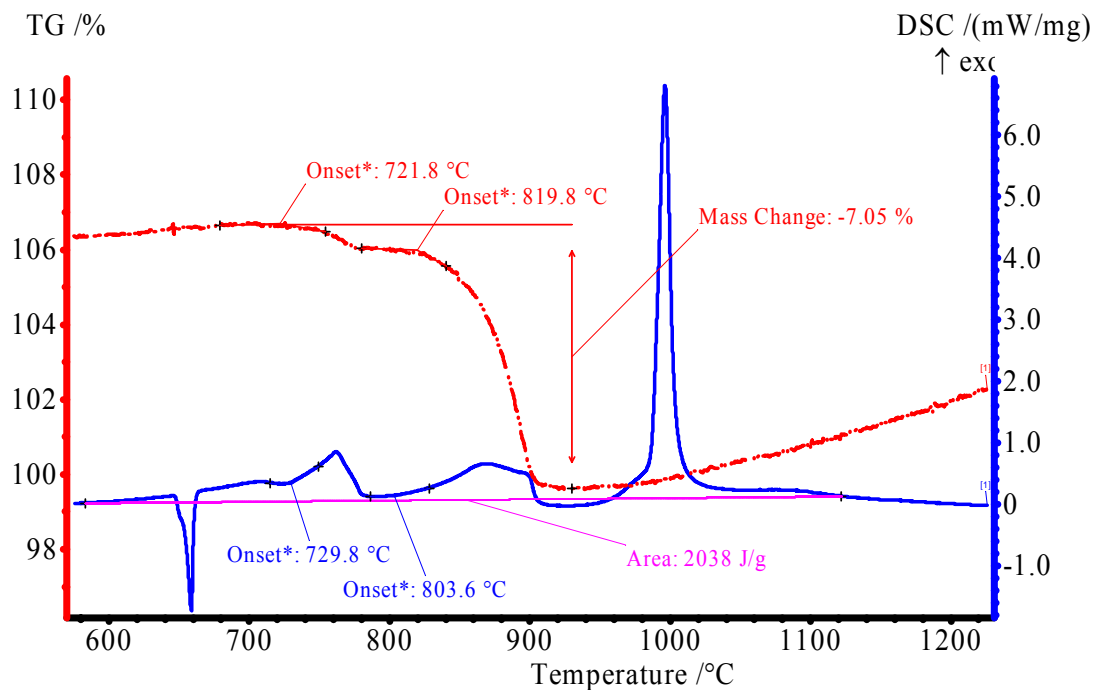


Figure G.8c - 20µm Al + MoO<sub>3</sub> DSC and TGA Curves with Mass Loss (5Kpm)

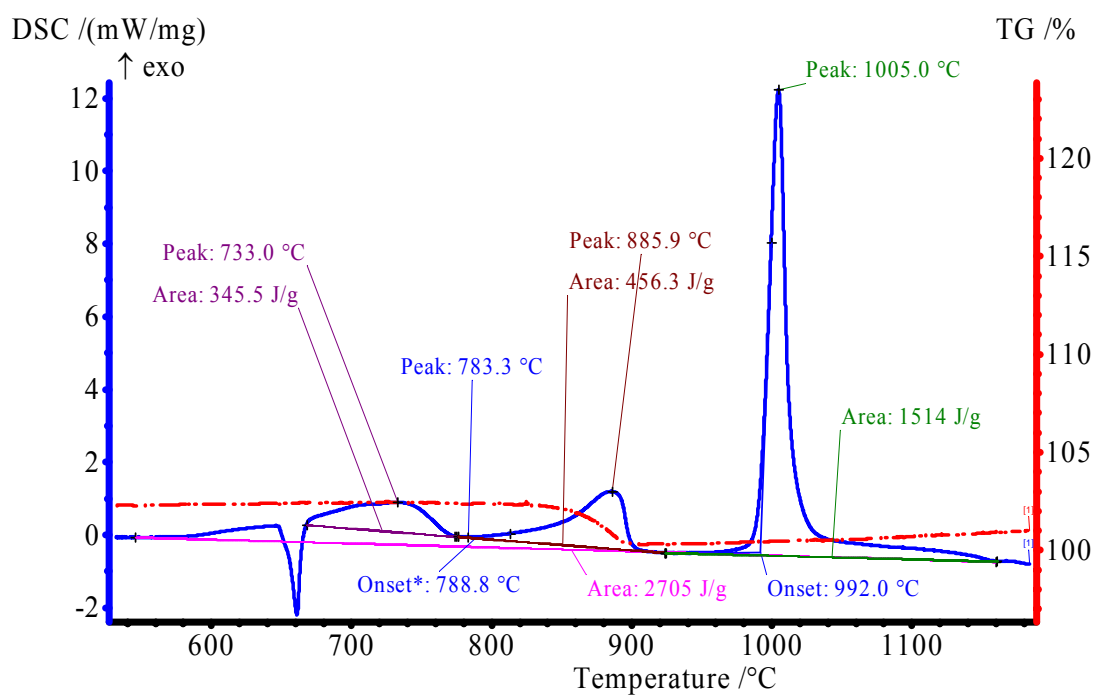


Figure G.8d - 20µm Al + MoO<sub>3</sub> DSC and TGA Curves (10Kpm)

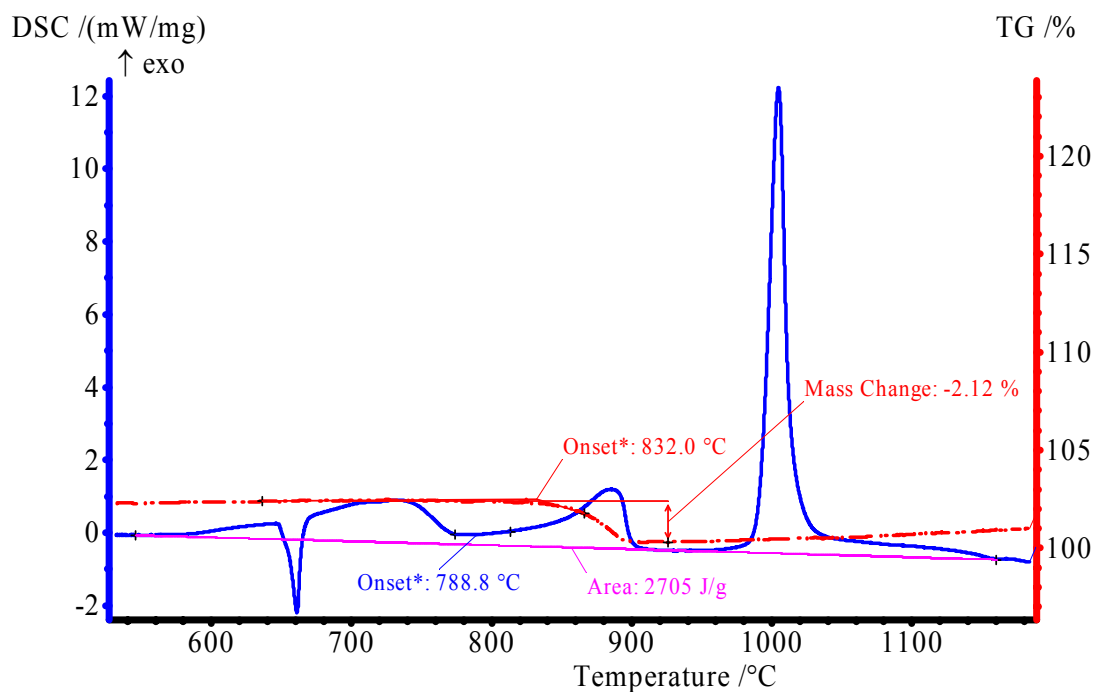


Figure G.8e - 20µm Al + MoO<sub>3</sub> DSC and TGA Curves with Mass Loss(10Kpm)

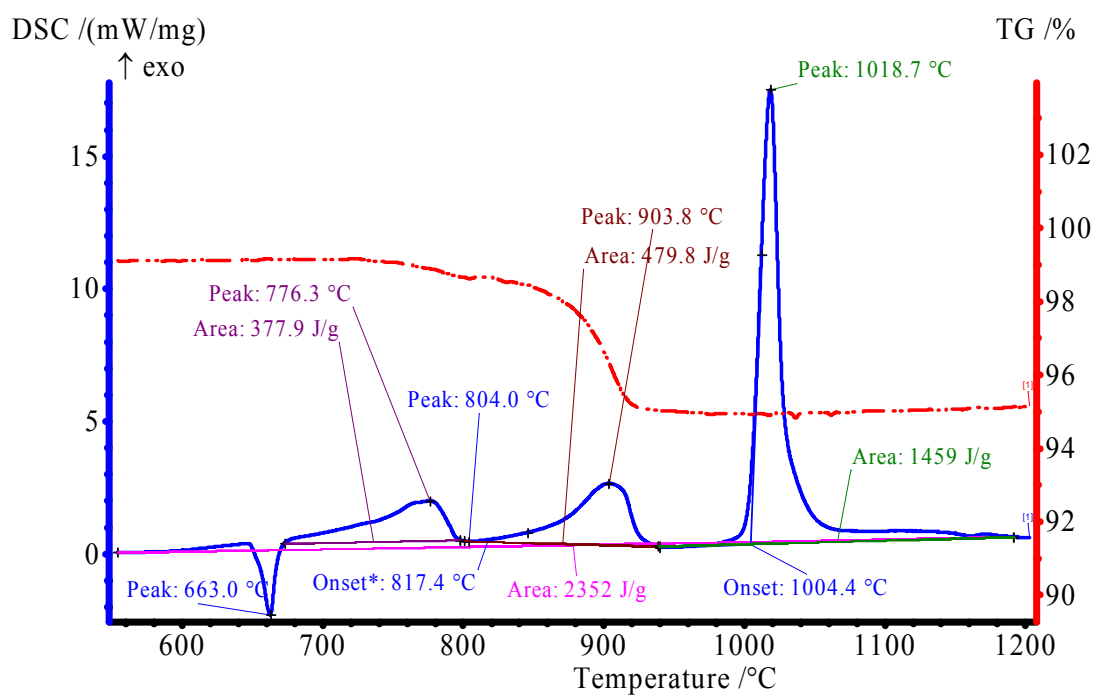


Figure G.8f - 20µm Al + MoO<sub>3</sub> DSC and TGA Curves (15Kpm)

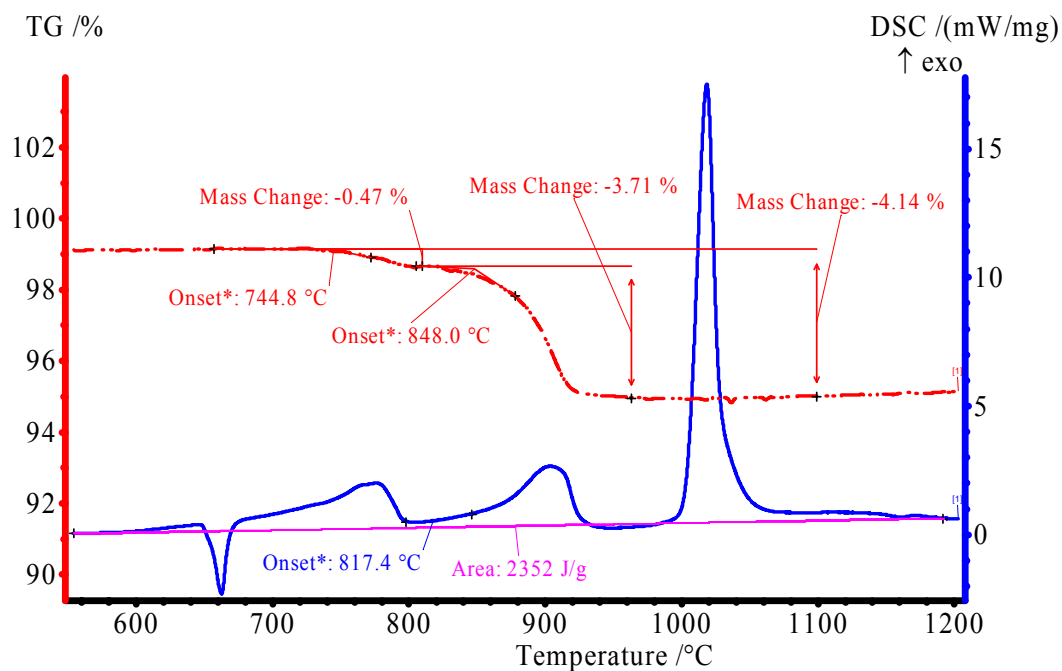
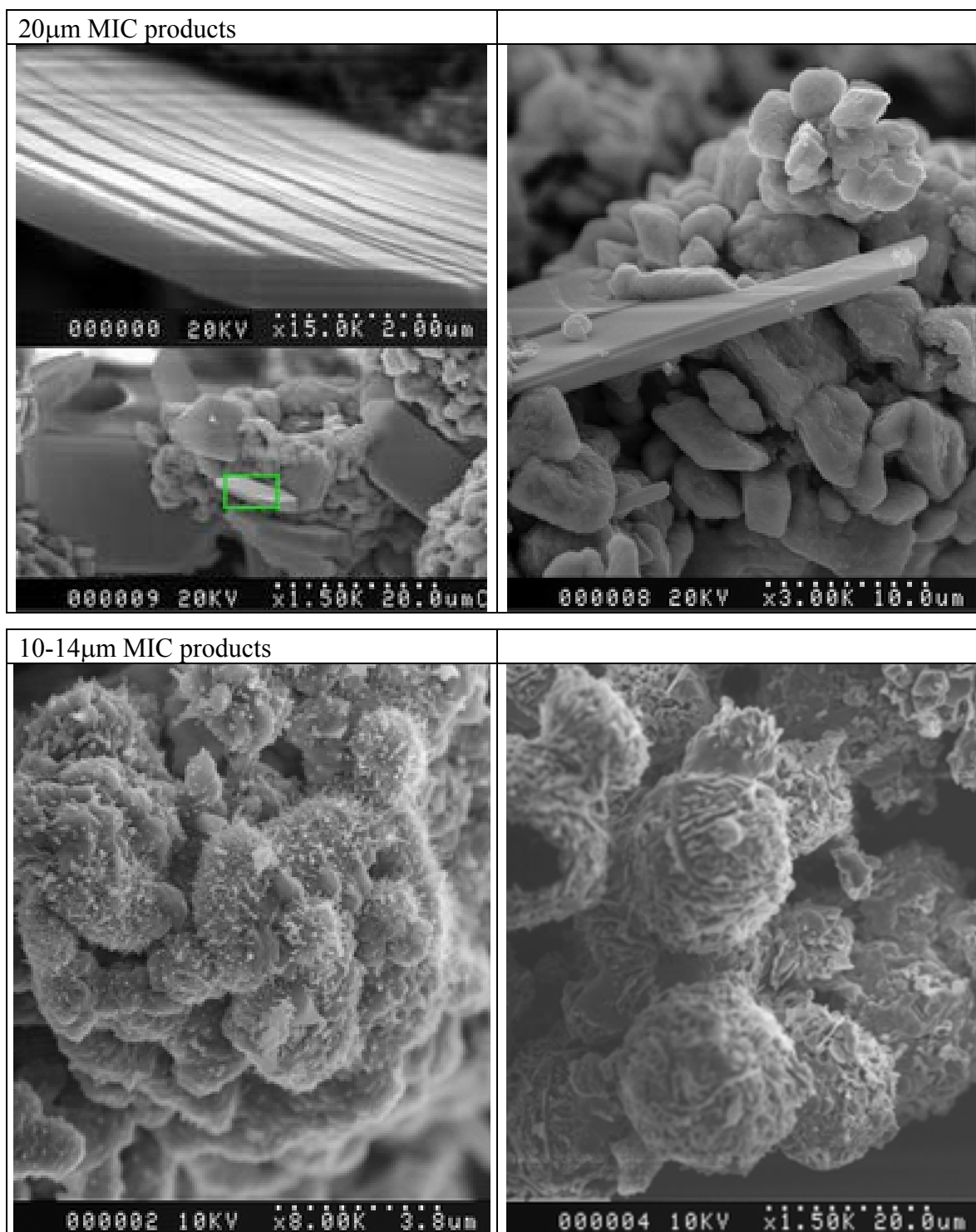


Figure G.8g - 20µm Al + MoO<sub>3</sub> DSC and TGA Curves with Mass Loss(15Kpm)



## H. SEM Images of DSC Samples



I. 2-Drop Calorimeter Calibration Data

Table .1 – Resistor Pulse Calibration Data

<b>Sample</b>	<b>Sample Number</b>	<b>Pulse 1 (Cal)</b>	<b>Result (Cal)</b>	<b>% Recovery</b>	<b>Pulse 2 (Cal)</b>	<b>Result (Cal)</b>	<b>% Recovery</b>
Nichrome Blank	1	1	1.015	101.5	5	5.029	100.6
Nichrome Blank	2	1	1.013	101.3	5	5.026	100.5
Nichrome Blank	3	1	1.013	101.3	5	5.024	100.5
40nm Al + MoO <sub>3</sub>	1	5	5.036	100.7	25	25.12	100.5
40nm Al + MoO <sub>3</sub>	4	5	5.039	100.8	25	25.08	100.3
40nm Al + MoO <sub>3</sub>	7	5	5.045	100.9	25	25.15	100.6
3-4mm Al + MoO <sub>3</sub>	2	5	5.04	100.8	25	25.1	100.4
3-4mm Al + MoO <sub>3</sub>	5	5	5.039	100.8	25	25.15	100.6
3-4mm Al + MoO <sub>3</sub>	8	5	5.032	100.6	25	25.15	100.6
10-14mm Al + MoO <sub>3</sub>	3	5	5.038	100.8	25	25.12	100.5
10-14mm Al + MoO <sub>3</sub>	6	5	5.036	100.7	25	25.08	100.3
10-14mm Al + MoO <sub>3</sub>	9	5	5.028	100.6	25	25.1	100.4